The Dissertation Committee for Rouzbeh Ghanbarnezhad Moghanloo
Certifies that this is the approved version of the following dissertation:

Modeling the Fluid Flow of Carbon Dioxide through Permeable Media

Committee:

Larry W. Lake, Supervisor

Steven L. Bryant

David DiCarlo

Russell T. Johns

Kamy Sepehrnoori

Modeling the Fluid Flow of Carbon Dioxide through Permeable Media

by

Rouzbeh Ghanbarnezhad Moghanloo, B.S.; M.S.

Dissertation

Presented to the Faculty of the Graduate School of

The University of Texas at Austin

in Partial Fulfillment

of the Requirements

for the Degree of

Doctor of Philosophy

The University of Texas at Austin

May 2012

Dedication

I dedicate this dissertation to

My beautiful wife, Maryam, for her love, support, patience, and understanding

My wonderful parents, Ali and Shahnaz, for their unconditional love and support

and

My lovely Sonia

Acknowledgments

I would like to express my sincere gratitude to my supervising professor, Dr. Larry Lake, for his continuous guidance, support, and encouragement. I have learned a lot from his profound insight, keen observations, and vast knowledge. I am privileged to have had an opportunity to work with him.

I appreciate the time, valuable comments, and feedback of my committee members, Dr. Steve Bryant, Dr. David DiCarlo, Dr. Russell Johns, and Dr. Kamy Sepehrnoori.

I would like to acknowledge the staff of the Petroleum and Geosystems Engineering Department at The University of Texas at Austin, Michelle Mason, Joanna Castillo, Cheryl Kruzie, Frankie Hart, Mary Pettengill, Shelette Paulino, and Nina Schenck for their technical and administrative support.

Special thanks to my friends Drs. Abraham John, Gholamreza Garmeh, Maylin Carrizales, Javad Behseresht, Ahmad Sakhaee Pour, Ashwin Venkatraman, Lokendra Jain, and Olaoluwa Adepoju for their valuable technical discussions and suggestions.

I sincerely thank the financial support provided by the Gas Flooding JIP.

Modeling the Fluid Flow of Carbon Dioxide through Permeable Media

Rouzbeh Ghanbarnezhad Moghanloo, Ph.D.

The University of Texas at Austin, 2012

Supervisor: Larry W. Lake

This dissertation presents analytical solutions to address several unresolved issues on the modeling of CO_2 flow in permeable media. Analytical solutions are important as numerical simulations do not yield explicit expressions in terms of the model parameters. In addition, simulations that provide the most comprehensive solutions to multiphase flow problems are computationally intensive. Accordingly, we address the following topics in this dissertation.

The method of characteristics (MOC) solution of the overall mass conservation equation of CO_2 in two-phase flow through permeable media is derived in the presence of compressibility. The formally developed MOC solutions rely on the incompressible fluid and rock assumptions that are rarely met in practice; hence, the incompressible assumption is relaxed and the first semi-analytic MOC solution for compressible flow is derived. The analytical solution is verified by simulation results.

Fractional flow theory is applied to evaluate the CO_2 storage capacity of one-dimensional (1D) saline aquifers. Lack of an accurate estimation of the CO_2 storage capacity stands in the way of the fully implementation of CO_2 storage in aquifers. The notion of optimal solvent-water-slug size is incorporated into the graphical solution of combined geochemical front propagation and fractional flow theory to determine the CO_2 storage capacity of aquifers. The analytical solution is verified by simulation results.

The limits of the Walsh and Lake (WL) method to predict the performance of CO_2 injection is examined when miscibility is not achieved. The idea of an analogous first-contact miscible flood is implemented into the WL method to study miscibly-degraded simultaneous water and gas (SWAG) displacements. The simulation verifies the WL solutions. For the two-dimensional (2D) displacements, the predicted optimal SWAG ratio is accurate when the permeable medium is fairly homogeneous with a small cross-flow or heterogeneous with a large lateral correlation length (the same size or greater than the interwell spacing). We conclude that the WL solution is accurate when the mixing zone grows linearly with time.

We examine decoupling of large and small-scale heterogeneity in multilayered reservoirs. In addition, using an analytical solution derived in this research, the fraction of layers in which the channeling occurs is determined as a function of the Koval factor and input dispersivity.

We successfully present a simulation configuration to verify the off-diagonal elements of the numerical dispersion tensor. Numerical dispersion is inevitably introduced into the finite difference approximations of the 2D convection-dispersion equation. We show that

the off-diagonal elements of the numerical dispersion tensor double when the flow velocity changes with distance. In addition, the simulation results reveal that the flow becomes more dispersive with distance travelled if there is convective cross-flow. In addition, local mixing increases with the convective cross-flow between layers.

A numerical indicator is presented to describe the nature of CO_2 miscible displacements in heterogeneous permeable media. Hence, the quantitative distinction between flow patterns becomes possible despite the traditionally qualitative approach. The correlation coefficient function is adopted to assign numerical values to flow patterns. The simulation results confirm the accuracy of the descriptive flow pattern values.

The order-of-one scaling analysis procedure is implemented to provide a unique set of dimensionless scaling groups of 2D SWAG displacements. The order-of-one scaling analysis is a strong mathematical approach to determine approximations that are allowed for a particular transport phenomenon. For the first time, we implement the scaling analysis of miscible displacements while considering effects of water salinity, dissolution of CO_2 in the aqueous phase, and complex configurations of injection and production wells.

Table of Contents

List of Tables

List of Figures

Chapter 1: Introduction

This dissertation is divided into two parts. The method of characteristics (MOC) solutions of the mass conservation equation under incompressible/compressible flow and their applications in reservoir engineering are discussed in Part I.

Chapter 2 gives the development of the MOC solution in the presence of compressibility. The following hypothesis is tested: if the compressibility can be properly represented by constant values, then the MOC solution of the mass conservation equation can properly predict the performance of compressible flows.

Chapter 3 determines the CO_2 storage capacity of aquifers using fractional flow theory. The following hypothesis is verified: if the capillary snap-off phenomenon can be properly captured through hysteresis between the relative permeability curves of imbibition and drainage displacements, then the CO_2 storage capacity of one-dimensional aquifers can be determined using fractional flow theory.

In Chapter 4, the Walsh and Lake method is applied to predict the performance of degraded miscible displacements through implementing the idea of analogues first-contact-miscible flood. The following hypothesis is verified: if the corresponding degraded miscible residual oil saturation is known, the Walsh-Lake method applies to solvent floods in which miscibility does not completely develop (because of the dispersion and/or insufficient local pressure).

Part II of this dissertation describes the impact of dispersion on the performance of miscible displacement in the presence of large-scale heterogeneity.

Chapter 5 examines decoupling of the local heterogeneity and permeability variation in multi-layered reservoirs in the absence of cross-flow between layers. The following hypothesis is verified: if the large- and local-scale heterogeneities can be decoupled properly, their representing parameters will be scale-independent.

Chapter 6 presents a specific simulation configuration is examined successfully to verify the off-diagonal coefficients. Furthermore, the numerical dispersion coefficients are derived when flow velocity varies with distance and verified with simulation. In addition, simulation results in Chapter 6 suggest that the flow becomes more dispersive with distance travelled if there is convective cross-flow. In addition, local mixing increases with the convective cross-flow between layers (Chapter 6).

Chapter 7 introduces a flow regime indicator that eliminates the need for different terminology to describe the nature of a miscible displacement such as dispersive, gravity override, and channeling. The following hypothesis is verified: if the development pattern of the mixing zone is known, then interplay between effects is summarized into a single numerical value called the flow pattern value.

Chapter 8 presents the contributions and the recommendations for future research. In addition, a unique set of dimensionless scaling groups are obtained for degraded CO_2 miscible displacements using order-of-one scaling analysis in Appendix C.

Chapter 2: Applying the Method of Characteristics to Model the Flow of Compressible CO_2 in Aquifers

Deep aquifers are attractive geological formations for the injection and long-term storage of CO_2. This chapter presents the first semi- analytic solution of two-phase compressible flow in permeable media using method of characteristics (MOC). For the first time, the method of characteristics is used to solve the overall composition balance equation of CO_2 with no restriction on the compressibility. The following assumptions are considered: one-dimensional (1D), two-phase flow (aqueous and gaseous), a small compressibility of fluids and rock, and mutual solubility of CO_2 and water in the aqueous and gaseous phases.

A simulation approach is used to verify the derived analytical solutions. The simulation models consist of a vertical injection well and a producer located at the ends of a 1D grid. The pace at which specific gas saturations propagate along the permeable medium are compared with the gas saturation profiles obtained when no compressibility is involved.

The results suggest that the velocity of a wave, which is associated with the transport of a certain mass of CO_2 along the permeable medium, is a function of the gas saturation, compressibility of the rock and fluids, and the pressure gradient. The results suggest that the wave velocity will only be a function of the gas saturation and pressure gradient if the compressibility of the rock is negligible compared to that of CO_2. Hence, the waves' velocity will only depend on saturation, as is for an incompressible flow system, when changes in pressure gradient are minimal.

Thus, this section explains how fast a compressible CO_2 plume will travel along the aquifers length. In practice, the fate of the injected CO_2 plume is essential to determine the storage capacity of aquifers and to evaluate the risk associated with the CO_2 sequestration projects.

2.1 INTRODUCTION

Despite extensive research on the analytical modeling of CO_2 sequestration in deep saline aquifers, CO_2 has been always considered as an incompressible fluid. Analytical solutions are interesting, as numerical simulations do not yield explicit expressions in terms of the model parameters. Furthermore, simulations that provide the most comprehensive solutions to multiphase flow problems are computationally intensive.

We derive the method of characteristics (MOC) solution of the overall composition balance equation of CO_2 to model 1D two-phase flow in the horizontal direction in the presence of compressibility. In the following study, the incompressible assumption is relaxed as there is no incompressible fluid in practice. With zero compressibility, it is impossible to inject more than the discharge rate in an aquifer. Thus, the total flow velocity (gaseous + aqueous) stays constant with distance when compressibility is absent; on the contrary, it can vary in the presence of compressibility. The continuity equation necessitates this argument as described in the remainder of this chapter.

However, the gas density may still be considered “constant” along a vertical cross-section owing to the interplay between compressibility and thermal expansion

(Juanes, 2010). This is because the temperature affects CO_2 density and, thus, CO_2 storage capacity. All other conditions being equal, the storage capacity is less for deeper formations with a high temperature owing to the geothermal gradient. On the contrary, the capacity is increased for larger CO_2 density as is in deep aquifers because of the pressure gradient. Thus, for shallower depths, the storage capacity is smaller as a result of lower pressure and lower CO_2 density. Bachu (2003) showed that the effects of compressibility and thermal expansion counteract each other and yield a constant CO_2 density across the depth of the aquifer.

The process considered here is based on the following premises: (1) the aquifer is assumed as a 1D uniform and homogeneous medium; (2) the aquifer is initially filled with water; (3) the outlet boundary of the aquifer is modeled through a production well with a constant pressure constraint; (4) two-component two-phase flow takes place; (5) neither sorption nor reaction occurs; (6) the fluids and rock compressibilities are represented by constant values; (7) the phases are, thermodynamically, in equilibrium everywhere; (8) dispersive transport and the capillary effects are negligible; (9) injection takes place using either a constant bottomhole pressure or a constant rate constraint; and (10) mutual solubility of CO_2 and water occurs in the aqueous and gaseous phases, respectively. We also assume that the Riemann problem boundary conditions apply: uniform initial saturation and the step-wise changes of the injection condition at the origin of the distance-time plot.

The pressure disturbance created at the injection inlet travels through the permeable medium. We treat the pressure propagations as two distinct categories:

pressure waves accompanied by the changes in saturation and those traveling fast without coupling with the saturation change. As will be described later, the injection and the production rates will become equal when the fast pressure disturbance, which is not associated with the saturation change, reaches the distant boundary of the permeable medium. This fast pressure disturbance is followed by the coupled saturation and pressure front traveling from the injection well into the aquifer. The fast disturbance is mainly dominated by the pressure disturbance while the slower one is caused by sharp changes in both pressure and saturation. In addition, a third pressure wave starts traveling from the producer toward the injector when the injected CO_2 breaks through.

We derive an expression for the velocity of the coupled propagation of the saturation and pressure front that can be solved semi-analytically. The pressure field obtained from finite-difference/streamline simulations is incorporated into the analytical expression from which saturation is determined. See Vasco (2011) for more information on the coupled propagation of saturation and pressure front.

Even though flow is never limited to 1D in CO_2 injection applications, the insight obtained from the MOC solution derived in this study can be effectively incorporated with streamline simulations. In other words, the pressure field can be calculated through streamline representations of the flow in heterogeneous reservoirs and from that, saturation is determined analytically using the analytical solution derived in this study. For more details on the coupling of streamline simulations and 1D theoretical solutions, see Batycky (1997), Thiele (1994), and Jessen *et al.* (2002).

2.2 THE METHOD OF CHARACTERISTICS

The method of characteristics (Courant and Hilbert, 1962) is a robust technique to solve first-order, strictly hyperbolic, partial differential equations (PDE) such as the mass conservation equation. The goal of method of characteristics (MOC) is to convert the original PDE into a set of ordinary differential equations (ODE) along certain curves called characteristics. For a detailed description on MOC applications to chromatography problems associated with binary displacements see Rhee *et al.* (1986).

In general, the conservation equations are nonlinear. The nonlinearity in the mass conservation equation lies in the relationship between the overall flux and the overall concentration of each component. If the coherent condition applies, these wave velocities become constant; hence, the flow problem will be solved through finding those overall concentrations and the associated waves' velocities. The MOC solution is a unique set of overall concentration waves traveling through distance and time (independent variables). To restore the solution uniqueness, some additional reasoning called velocity constraints and entropy conditions often are applied; see Helfferich (1970) and Lake (1989).

2.3 CONCEPT OF COHERENCE

The notion of coherence was originally developed in 1963 by Helfferich to provide insight into multicomponent fixed-bed chromatography. The concept of coherence describes a state in which the velocity of waves that are associated with dependent variables becomes the same at any point within the problem domain. In other words, a complete set of compositions (dependent variables in this study) travel together in the same direction and the same velocity if the wave is coherent (Hankins *et al*., 2004).

Incorporating the concept of coherence into problems, which involve wave propagation, yields a robust solution. Using the method of characteristics, Helfferich (1981) showed that implementing uniform initial and boundary conditions (called Riemann problem conditions) leads to solutions that can be described using coherent waves. Major extensions were performed to apply the coherence into enhanced oil recovery (EOR) applications (Helfferich, 1981; Lake, 1989).

2.4 THE MOC SOLUTION WHEN NO COMPRESSIBILITY IS INVOLVED

To evaluate the MOC solution when compressibility is present, it is worthwhile to compare it with the solution in which no compressibility is considered. Hence, we first assume that fluid properties and pore space are independent of the pressure changes and consider the following premises for Part I: (1) the aquifer is assumed as a 1D uniform and homogeneous medium; (2) the aquifer is initially filled with water; (3) the outlet boundary of the aquifer is modeled through a production well with a constant constraint; (4) two-component two-phase flow takes place; (5) neither sorption nor reaction occurs; (6) the phases are thermodynamically, in equilibrium everywhere; (7) dispersive transport and the capillary effects are negligible; (8) a constant mutual solubility of CO_2 and water occurs in the aqueous and gaseous phases, respectively (displacement along a tie-line); (9) the phase compositions, viscosities, and densities are fixed and the relative permeabilities depend only on the saturations.

The overall mass conservation equations for (1) water and (2) CO_2 components under no sorption or chemical reaction can be written as (Dumore, 1984; Lake, 1989):

$$\frac{\partial\overbrace{\left(\phi S_1\rho_1\omega_{11}+\phi(1-S_1)\rho_2\omega_{12}\right)}^{G_1}}{\partial t}+\frac{\partial\overbrace{\left(\rho_1\omega_{11}u_1+\rho_2\omega_{12}u_2\right)}^{H_1}}{\partial x}=0, \tag{2.1}$$

$$\frac{\partial\overbrace{\left(\phi S_1\rho_1\omega_{21}+\phi(1-S_1)\rho_2\omega_{22}\right)}^{G_2}}{\partial t}+\frac{\partial\overbrace{\left(\rho_1\omega_{21}u_1+\rho_2\omega_{22}u_2\right)}^{H_2}}{\partial x}=0, \tag{2.2}$$

where ω_{ij} represent the mass fraction of component *i* in phase *j*. The sum of mass fractions of component *i* over all phases is equal to one. We sum Eqs. (2.1) and (2.2) under the assumption of incompressible fluids and constant pore space to obtain the equation of continuity (the conservation of total mass):

$$\frac{d}{dx}\overbrace{\left(u_1+u_2\right)}^{u_t}=0, \tag{2.3}$$

where u_t is the total local flow velocity (gas + water). Equation (2.3) implies that total flow velocity is constant with distance when no compressibility is involved.

Rewriting Eqs. (2.1) and Eq. (2.2) in terms of G_i and H_i, gives

$$\frac{\partial G_1}{\partial t}+\frac{\partial H_1}{\partial x}=0. \tag{2.4}$$

$$\frac{\partial G_2}{\partial t}+\frac{\partial H_2}{\partial x}=0. \tag{2.5}$$

where G_i and H_i show the accumulation and flux terms in the overall mass conservation of component *i*. Lake (1989) showed that the overall compositional equations expressed in terms of fractional flow terms can be obtained from Eqs. (2.4) and (2.5):

$$\frac{\partial C_1}{\partial t_D}+\frac{\partial F_1}{\partial x_D}=0. \tag{2.6}$$

$$\frac{\partial C_2}{\partial t_D}+\frac{\partial F_2}{\partial x_D}=0, \tag{2.7}$$

where C_i is the overall volume fraction of component i given by

$$C_i = \sum_{j=1}^{N_p} C_{ij} S_j \qquad i=1, 2 \text{ and } j=1, 2 \tag{2.8}$$

and C_{ij} is the volume fraction of component in in phase j; F_i is the overall volumetric flow of component i given by

$$F_i = \sum_{j=1}^{N_p} C_{ij} f_j \qquad i=1, 2 \tag{2.9}$$

$$x_D = \frac{x}{L} \ . \tag{2.10}$$

$$t_D = \frac{u_{tot} t}{\phi L} . \tag{2.11}$$

Considering the fact that F_i is only a function of C_i (because the phase compositions, viscosities, and densities are fixed and the relative permeabilities depend only on the saturations), Eqs. (2.6) and (2.7) can be written as

$$\frac{\partial C_1}{\partial t_D} + \frac{dF_1}{dC_1} \frac{\partial C_1}{\partial x_D} = 0 . \tag{2.12}$$

$$\frac{\partial C_2}{\partial t_D} + \frac{dF_2}{dC_2} \frac{\partial C_2}{\partial x_D} = 0 . \tag{2.13}$$

However, we keep only one of the Equations (2.12) and (2.13) and discard the other one, because there are only two components and the summation of C_1 and C_2 becomes unity. As C_2 is only a function of x_D and t_D, we can write the following expression for the total derivative of C_2 over smooth changes (considering that C_2 is at least piecewise continuous over x_D and t_D domains):

$$dC_2 = \frac{\partial C_2}{\partial t_D} dt_D + \frac{\partial C_2}{\partial x_D} dx_D = 0 . \tag{2.14}$$

Therefore, the ordinary derivative of C_2 becomes

$$\frac{dC_2}{d\eta} = \frac{\partial C_2}{\partial t_D}\frac{dt_D}{d\eta} + \frac{\partial C_2}{\partial x_D}\frac{dx_D}{d\eta} = 0\,, \tag{2.15}$$

where η is parametric parameter. A term by term comparison of Eq. (2.12) with Eq. (2.15) indicates that

$$\frac{dC_2}{d\eta} = 0\,. \tag{2.16}$$

$$\frac{dt_D}{d\eta} = 1.0\,. \tag{2.17}$$

$$\frac{dx_D}{d\eta} = \frac{dF_2}{dC_2}\,. \tag{2.18}$$

Equations(2.16), (2.17), and (2.18) are known as the characteristic equations. The elimination of η from the characteristics equations yields a relationship between x_D and t_D; hence, the graphical representation of the solution in the distance-time plot occurs on the characteristic curve along which C_2 is constant (note that $\frac{dC_2}{d\eta} = 0$). Note that the solution of Eq. (2.16) shows that the C_1 is fixed along the characteristics as its derivative is zero; furthermore, the solution of Eq. (2.17) implies that t_D is equal to η and, thus, they can be used interchangeably.

From this representation, it follows the wave velocity associated with a constant concentration, C_2, in distance-time space is

$$\frac{dx_D}{dt_D} = \frac{dF_2}{dC_2}\Big|_{C_2}\,. \tag{2.19}$$

Differentiation of Eq. (2.9) with respect to C_2 shows that

$$\frac{dF_2}{dC_2} = (C_{22} - C_{21})\frac{df_2}{dC_2} \quad . \tag{2.20}$$

Applying the chain rule and differentiation of Eq. (2.8) with respect to $S_{2,}$ give,

$$\frac{dF_2}{dC_2} = (C_{22} - C_{21})\left(\frac{df_2}{dS_2}\frac{dS_2}{dC_2}\right) = \frac{df_2}{dS_2} \quad . \tag{2.21}$$

Thus, the velocity at which a specific overall volume fraction of component 2 propagates in a semi-miscible displacement is equal to the corresponding saturation wave velocity as if the displacement is completely immiscible.

It is important to distinguish the difference between the flow velocity and the wave velocity; the former is the total volumetric flow rate of all phases per unit area, whereas the latter is the velocity at which a given composition travels along the permeable medium.

2.5 THE MOC SOLUTION WHEN COMPRESSIBILITY IS CONSIDERED

In this section, the overall mass conservation equation of CO_2 is solved by the method of characteristics when there is no restriction involved for compressibility. Despite Part I, we lift the restrictions on compressibility and the dependency of the fluids' properties on pressure. In other words, fluid's volume and the pore space may change as local pressure varies. All other assumptions apply accordingly.

As will be discussed, two various pressure disturbances are formed and propagated through the permeable medium before the injected fluid breaks through: fast and slow; however, only one of those pressure disturbances (slow) is associated with the saturation change.

2.5.1 The General Form of the Solution

We apply the method of characteristics to solve the overall mass conservation equation of CO_2, Eq. (2.5). Thus, the definitions of G_2 and H_2 become

$$G_2 = \phi(1-S_2)\rho_1\omega_{21} + \phi\rho_2 S_2\omega_{22}, \tag{2.22}$$

$$H_2 = \rho_1\omega_{21}u_1 + \rho_2\omega_{22}u_2. \tag{2.23}$$

Incorporating the Darcy's law into the definition of H_2 while discarding the capillary pressure term gives

$$G_2 = \phi(1-S_2)\rho_1\omega_{21} + \phi\rho_2 S_2\omega_{22}, \tag{2.24}$$

$$H_2 = \rho_1\omega_{21}\left(\frac{kk_{r1}}{\mu_1}\frac{\partial P}{\partial x}\right) + \rho_2\omega_{22}\left(\frac{kk_{r2}}{\mu_2}\frac{\partial P}{\partial x}\right). \tag{2.25}$$

Note that we incorporate the negative sign in Darcy's law into the definition of the pressure gradient and the absolute (positive) value of pressure gradient is used through derivations in the remainder of this section.

Furthermore, we introduce the exponential form of gas-water relative permeability into the expression of H_2 (Lake, 1989):

$$H_2 = \rho_1\omega_{21}\left(\frac{k\left(\frac{S_1 - S_{1r}}{1-S_{1r}-S_{2r}}\right)^n}{\mu_1}\frac{\partial P}{\partial x}\right) + \rho_2\omega_{22}\left(\frac{k\left(\frac{S_2 - S_{2r}}{1-S_{1r}-S_{2r}}\right)^n}{\mu_2}\frac{\partial P}{\partial x}\right). \tag{2.26}$$

The substitution of S_1, and considering that the fluid saturations sum to unity, yields

$$H_2 = \rho_1\omega_{21}\left(\frac{k\left(\frac{1-S_2-S_{1r}}{1-S_{1r}-S_{2r}}\right)^n}{\mu_1}\frac{\partial P}{\partial x}\right) + \rho_2\omega_{22}\left(\frac{k\left(\frac{S_2 - S_{2r}}{1-S_{1r}-S_{2r}}\right)^n}{\mu_2}\frac{\partial P}{\partial x}\right). \tag{2.27}$$

We assume that H_2 and G_2 are functions of time and distance through their dependencies on saturation and pressure:

$$H_2 = f(S_2, P), \tag{2.28}$$

$$G_2 = f(S_2, P). \tag{2.29}$$

The derivative of H_2 with respect to G_2 can be written as

$$\frac{\partial H_2}{\partial G_2} = \left(\frac{\partial H_2}{\partial S_2}\right)_P \frac{\partial S_2}{\partial G_2} + \left(\frac{\partial H_2}{\partial P}\right)_{S_2} \frac{\partial P}{\partial G_2}. \tag{2.30}$$

Furthermore, we assume that under specific conditions that will be discussed later in the verification part (section 2.6), H will be only function of G; thus, Eq. (2.5) can be written as:

$$\frac{\partial G_2}{\partial t} + \frac{dH_2}{dG_2}\frac{\partial G_2}{\partial x} = 0. \tag{2.31}$$

The substitution of Eq. (2.30) into Eq. (2.31) gives

$$\frac{\partial G_2}{\partial t} + \left(\frac{\partial H_2}{\partial S_2}\frac{\partial S_2}{\partial G_2} + \frac{\partial H_2}{\partial P}\frac{\partial P}{\partial G_2}\right)\frac{\partial G_2}{\partial x} = 0. \tag{2.32}$$

Furthermore, the ordinary derivative of G_2 becomes

$$\frac{\partial G_2}{\partial t}\frac{dt}{d\eta} + \frac{\partial G_2}{\partial x}\frac{dx}{d\eta} = \frac{dG_2}{d\eta}, \tag{2.33}$$

where η is a variable. A term by term comparison of Eq. (2.32) with Eq. (2.33) yields the characteristics equations as

$$\frac{dG_2}{d\eta} = 0, \tag{2.34}$$

$$\frac{dt}{d\eta} = 1.0 \quad , \tag{2.35}$$

$$\frac{dx}{d\eta} = \frac{dH_2}{dG_2} \quad . \tag{2.36}$$

Note that the solution of Eq. (2.34) shows that the G_2 is fixed along the characteristics as its derivative is zero; furthermore, the solution of Eq. (2.35) implies that t is equal to η (assuming the integral constant to be zero) and, thus, they can be used interchangeably. In addition, Eq. (2.36) indicates that the wave velocity associated with specific mass of CO_2, G_2, in distance-time space is equal to the derivative of H_2 with respect to G_2. However, there is no explicit expression of H_2 as a function of G_2; therefore, we use the chain rule to take this derivative as shown in Eq. (2.30).

Thus, the differentiation of Eq. (2.27) with respect to s_2 gives

$$\frac{\partial H_2}{\partial S_2} = \frac{-n\rho_1\omega_{21}}{\left(1-S_{1r}-S_{2r}\right)^n}\left(1-S_2-S_{1r}\right)^{n-1}\left(\frac{k}{\mu_1}\frac{\partial P}{\partial x}\right) + \rho_2\frac{n\omega_{22}}{\left(1-S_{1r}-S_{2r}\right)^n}\left(S_2-S_{2r}\right)^{n-1}\left(\frac{k}{\mu_2}\frac{\partial P}{\partial x}\right) \quad . \tag{2.37}$$

Furthermore, the differentiation of Eq. (2.27) with respect to pressure yields

$$\begin{aligned}\frac{\partial H_2}{\partial P} = {} & \rho_1\omega_{21}\left(\frac{1-S_2-S_{1r}}{1-S_{1r}-S_{2r}}\right)^n\left(\frac{k}{\mu_1}\frac{\partial\left(\frac{\partial P}{\partial x}\right)}{\partial P}\right) + \frac{d\rho_1}{dP}\omega_{21}\left(\left(\frac{k}{\mu_1}\frac{1-S_2-S_{1r}}{1-S_{1r}-S_{2r}}\right)^n\frac{\partial P}{\partial x}\right) \\ & + \rho_1\frac{d\omega_{21}}{dP}\left(\frac{1-S_2-S_{1r}}{1-S_{1r}-S_{2r}}\right)^n\left(\frac{k}{\mu_1}\frac{\partial P}{\partial x}\right) + \frac{d\rho_2}{dP}\omega_{22}\left(\frac{S_2-S_{2r}}{1-S_{1r}-S_{2r}}\right)^n\left(\frac{k}{\mu_2}\frac{\partial P}{\partial x}\right) \\ & + \rho_2\frac{d\omega_{22}}{dP}\left(\frac{S_2-S_{2r}}{1-S_{1r}-S_{2r}}\right)^n\left(\frac{k}{\mu_2}\frac{\partial P}{\partial x}\right) + \rho_2\omega_{22}\left(\frac{S_2-S_{2r}}{1-S_{1r}-S_{2r}}\right)^n\left(\frac{k}{\mu_2}\frac{\partial\left(\frac{\partial P}{\partial x}\right)}{\partial P}\right) \\ & - \rho_1\omega_{21}k\left(\frac{1-S_2-S_{1r}}{1-S_{1r}-S_{2r}}\right)^n\frac{\partial P}{\partial x}\frac{\left(\frac{\partial\mu_1}{\partial P}\right)}{\mu_1^2} - \rho_2\omega_{22}k\left(\frac{S_2-S_{1r}}{1-S_{1r}-S_{2r}}\right)^n\frac{\partial P}{\partial x}\frac{\left(\frac{\partial\mu_2}{\partial P}\right)}{\mu_2^2}\end{aligned} \quad . \tag{2.38}$$

Similarly, the differentiation of Eq. (2.24) with respect to saturation and distance gives

$$\frac{\partial G_2}{\partial S_2} = -\phi\rho_1\omega_{21} + \phi\rho_2\omega_{22} \quad , \tag{2.39}$$

$$\begin{aligned}\frac{\partial G_2}{\partial P} &= \phi(1-S_2)\rho_1\frac{d\omega_{21}}{dP} + \phi\left(1-S_2\right)\omega_{21}\frac{d\rho_1}{dP} \\ &+ \phi\frac{d\rho_2}{dP}S_2\omega_{22} + \phi\rho_2 S_2\frac{d\omega_{22}}{dP} + \frac{d\phi}{dP}(1-S_2)\rho_1\omega_{21} + \frac{d\phi}{dP}\rho_2 S_2\omega_{22}\end{aligned} \quad . \tag{2.40}$$

The substitution of Eqs. (2.37), (2.38), (2.39), and (2.40) into Eq. (2.36) yields

$$\begin{aligned}\frac{dx}{dt} = &\frac{\dfrac{-n\rho_1\omega_{21}}{\left(1-S_{1r}-S_{2r}\right)^n}\left(1-S_2-S_{1r}\right)^{n-1}\left(\dfrac{k}{\mu_1}\dfrac{\partial P}{\partial x}\right) + \rho_2\dfrac{n\omega_{22}}{\left(1-S_{1r}-S_{2r}\right)^n}\left(S_2-S_{2r}\right)^{n-1}\left(\dfrac{k}{\mu_2}\dfrac{\partial P}{\partial x}\right)}{-\phi\rho_1\omega_{21}+\phi\rho_2\omega_{22}} \\ &+ \frac{\rho_1\omega_{21}\left(\dfrac{1-S_2-S_{1r}}{1-S_{1r}-S_{2r}}\right)^n\left(\dfrac{k}{\mu_1}\dfrac{\partial\left(\dfrac{\partial P}{\partial x}\right)}{\partial P}\right) + \dfrac{d\rho_1}{dP}\omega_{21}\left(\left(\dfrac{k}{\mu_1}\dfrac{1-S_2-S_{1r}}{1-S_{1r}-S_{2r}}\right)^n\dfrac{\partial P}{\partial x}\right) + \rho_1\dfrac{d\omega_{21}}{dP}\left(\dfrac{1-S_2-S_{1r}}{1-S_{1r}-S_{2r}}\right)^n\left(\dfrac{k}{\mu_1}\dfrac{\partial P}{\partial x}\right)}{\phi(1-S_2)\rho_1\dfrac{d\omega_{21}}{dP}+\phi\left(1-S_2\right)\omega_{21}\dfrac{d\rho_1}{dP}+\phi\dfrac{d\rho_2}{dP}S_2\omega_{22}+\phi\rho_2S_2\dfrac{d\omega_{22}}{dP}+\dfrac{d\phi}{dP}(1-S_2)\rho_1\omega_{21}+\dfrac{d\phi}{dP}\rho_2S_2\omega_{22}} \\ &+ \frac{\dfrac{d\rho_2}{dP}\omega_{22}\left(\dfrac{S_2-S_{2r}}{1-S_{1r}-S_{2r}}\right)^n\left(\dfrac{k}{\mu_2}\dfrac{\partial P}{\partial x}\right) + \rho_2\dfrac{d\omega_{22}}{dP}\left(\dfrac{S_2-S_{2r}}{1-S_{1r}-S_{2r}}\right)^n\left(\dfrac{k}{\mu_2}\dfrac{\partial P}{\partial x}\right) + \rho_2\omega_{22}\left(\dfrac{S_2-S_{2r}}{1-S_{1r}-S_{2r}}\right)^n\left(\dfrac{k}{\mu_2}\dfrac{\partial\left(\dfrac{\partial P}{\partial x}\right)}{\partial P}\right)}{\phi(1-S_2)\rho_1\dfrac{d\omega_{21}}{dP}+\phi\left(1-S_2\right)\omega_{21}\dfrac{d\rho_1}{dP}+\phi\dfrac{d\rho_2}{dP}S_2\omega_{22}+\phi\rho_2S_2\dfrac{d\omega_{22}}{dP}+\dfrac{d\phi}{dP}(1-S_2)\rho_1\omega_{21}+\dfrac{d\phi}{dP}\rho_2S_2\omega_{22}} \\ &+ \frac{-\rho_1\omega_{21}k\left(\dfrac{1-S_2-S_{1r}}{1-S_{1r}-S_{2r}}\right)^n\dfrac{\partial P}{\partial x}\dfrac{\left(\dfrac{\partial\mu_1}{\partial P}\right)}{\mu_1^2} - \rho_2\omega_{22}k\left(\dfrac{S_2-S_{1r}}{1-S_{1r}-S_{2r}}\right)^n\dfrac{\partial P}{\partial x}\dfrac{\left(\dfrac{\partial\mu_2}{\partial P}\right)}{\mu_2^2}}{\phi(1-S_2)\rho_1\dfrac{d\omega_{21}}{dP}+\phi\left(1-S_2\right)\omega_{21}\dfrac{d\rho_1}{dP}+\phi\dfrac{d\rho_2}{dP}S_2\omega_{22}+\phi\rho_2S_2\dfrac{d\omega_{22}}{dP}+\dfrac{d\phi}{dP}(1-S_2)\rho_1\omega_{21}+\dfrac{d\phi}{dP}\rho_2S_2\omega_{22}}\end{aligned} \tag{2.41}$$

Equation (2.41) shows the velocity of CO_2 waves traveling through the aquifer. In the following sections, we restrict our solution to special cases with additional assumptions

to the derivative of pressure gradient and also the derivative of equilibrium concentration (ω_{21}) with respect to pressure.

2.5.2 Constant Mutual Solubility (Displacement Along a Single Tie Line)

Typical phase diagram for a binary mixture (water-CO_2) consists of several tie lines, each connecting the equilibrium concentrations (solubility values in this study). If the displacement occurs across a tie line, solubilities stay constant. Thus, we apply the same treatment as used in the previous section except that the derivative of mass fraction terms (ω_{21} and ω_{22}) with respect to pressure becomes zero .

Taking derivative of Eq. (2.27) with respect to saturation gives

$$\frac{\partial H_2}{\partial S_2} = \frac{-n\rho_1\omega_{21}}{\left(1-S_{1r}-S_{2r}\right)^n}\left(1-S_2-S_{1r}\right)^{n-1}\left(\frac{k}{\mu_1}\frac{\partial P}{\partial x}\right)+\rho_2\frac{n\omega_{22}}{\left(1-S_{1r}-S_{2r}\right)^n}\left(S_2-S_{2r}\right)^{n-1}\left(\frac{k}{\mu_2}\frac{\partial P}{\partial x}\right) \tag{2.42}$$

Taking derivative of Eq. (2.42) with respect to pressure yields

$$\begin{aligned}\frac{\partial H_2}{\partial P} = {} & \rho_1\omega_{21}\left(\frac{1-S_2-S_{1r}}{1-S_{1r}-S_{2r}}\right)^n\left(\frac{k}{\mu_1}\frac{\partial\left(\frac{\partial P}{\partial x}\right)}{\partial P}\right)+\frac{d\rho_1}{dP}\omega_{21}\left(\left(\frac{k}{\mu_1}\frac{1-S_2-S_{1r}}{1-S_{1r}-S_{2r}}\right)^n\frac{\partial P}{\partial x}\right)\\ & +\frac{d\rho_2}{dP}\omega_{22}\left(\frac{S_2-S_{2r}}{1-S_{1r}-S_{2r}}\right)^n\left(\frac{k}{\mu_2}\frac{\partial P}{\partial x}\right)+\rho_2\omega_{22}\left(\frac{S_2-S_{2r}}{1-S_{1r}-S_{2r}}\right)^n\left(\frac{k}{\mu_2}\frac{\partial\left(\frac{\partial P}{\partial x}\right)}{\partial P}\right)\\ & -\rho_1\omega_{21}k\left(\frac{1-S_2-S_{1r}}{1-S_{1r}-S_{2r}}\right)^n\frac{\partial P}{\partial x}\frac{\left(\frac{\partial\mu_1}{\partial P}\right)}{\mu_1^2}-\rho_2\omega_{22}k\left(\frac{S_2-S_{1r}}{1-S_{1r}-S_{2r}}\right)^n\frac{\partial P}{\partial x}\frac{\left(\frac{\partial\mu_2}{\partial P}\right)}{\mu_2^2}\end{aligned} \tag{2.43}$$

Taking derivative of Eq. (2.24) with respect to saturation gives

$$\frac{\partial G_2}{\partial S_2} = -\phi\rho_1\omega_{21} + \phi\rho_2\omega_{22}\,. \tag{2.44}$$

Taking derivative of Eq. (2.24) with respect to pressure gives

$$\frac{\partial G_2}{\partial P} = \phi\left(1-S_2\right)\omega_{21}\frac{d\rho_1}{dP} + \phi\frac{d\rho_2}{dP}S_2\omega_{22} + \frac{d\phi}{dP}(1-S_2)\rho_1\omega_{21} + \frac{d\phi}{dP}\rho_2 S_2\omega_{22}\,. \tag{2.45}$$

Therefore, the velocity of waves (associated with certain mass of CO_2) traveling along a tie-line has the form of

$$\frac{dx}{dt}=\frac{\dfrac{-n\rho_1\omega_{21}}{\left(1-S_{1r}-S_{2r}\right)^n}\left(1-S_2-S_{1r}\right)^{n-1}\left(\dfrac{k}{\mu_1}\dfrac{\partial P}{\partial x}\right)+\rho_2\dfrac{n\omega_{22}}{\left(1-S_{1r}-S_{2r}\right)^n}\left(S_2-S_{2r}\right)^{n-1}\left(\dfrac{k}{\mu_2}\dfrac{\partial P}{\partial x}\right)}{-\phi\rho_1\omega_{21}+\phi\rho_2\omega_{22}}$$

$$+\frac{\rho_1\omega_{21}\left(\dfrac{1-S_2-S_{1r}}{1-S_{1r}-S_{2r}}\right)^n\left(\dfrac{k}{\mu_1}\dfrac{\partial\left(\dfrac{\partial P}{\partial x}\right)}{\partial P}\right)+\dfrac{d\rho_1}{dP}\omega_{21}\left(\left(\dfrac{k}{\mu_1}\dfrac{1-S_2-S_{1r}}{1-S_{1r}-S_{2r}}\right)^n\dfrac{\partial P}{\partial x}\right)}{\phi\left(1-S_2\right)\omega_{21}\dfrac{d\rho_1}{dP}+\phi\dfrac{d\rho_2}{dP}S_2\omega_{22}+\dfrac{d\phi}{dP}(1-S_2)\rho_1\omega_{21}+\dfrac{d\phi}{dP}\rho_2S_2\omega_{22}}$$

$$+\frac{\dfrac{d\rho_2}{dP}\omega_{22}\left(\dfrac{S_2-S_{2r}}{1-S_{1r}-S_{2r}}\right)^n\left(\dfrac{k}{\mu_2}\dfrac{\partial P}{\partial x}\right)+\rho_2\omega_{22}\left(\dfrac{S_2-S_{2r}}{1-S_{1r}-S_{2r}}\right)^n\left(\dfrac{k}{\mu_2}\dfrac{\partial\left(\dfrac{\partial P}{\partial x}\right)}{\partial P}\right)}{\phi\left(1-S_2\right)\omega_{21}\dfrac{d\rho_1}{dP}+\phi\dfrac{d\rho_2}{dP}S_2\omega_{22}+\dfrac{d\phi}{dP}(1-S_2)\rho_1\omega_{21}+\dfrac{d\phi}{dP}\rho_2S_2\omega_{22}}$$

$$-\frac{\rho_1\omega_{21}k\left(\dfrac{1-S_2-S_{1r}}{1-S_{1r}-S_{2r}}\right)^n\dfrac{\partial P}{\partial x}\dfrac{\left(\dfrac{\partial\mu_1}{\partial P}\right)}{\mu_1^2}+\rho_2\omega_{22}k\left(\dfrac{S_2-S_{1r}}{1-S_{1r}-S_{2r}}\right)^n\dfrac{\partial P}{\partial x}\dfrac{\left(\dfrac{\partial\mu_2}{\partial P}\right)}{\mu_2^2}}{\phi\left(1-S_2\right)\omega_{21}\dfrac{d\rho_1}{dP}+\phi\dfrac{d\rho_2}{dP}S_2\omega_{22}+\dfrac{d\phi}{dP}(1-S_2)\rho_1\omega_{21}+\dfrac{d\phi}{dP}\rho_2S_2\omega_{22}}. \tag{2.46}$$

2.5.3 No Mutual Solubility

Next, we investigate the solution for cases in which the solubility of components is negligible. Thus, the definitions of G_2 and H_2 become

$$G_2=\phi\rho_2S_2, \tag{2.47}$$

$$H_2=\rho_2u_2. \tag{2.48}$$

Substitution of ρ_2 into Eq. (2.47) gives

$$G_2=\phi\rho_2S_2. \tag{2.49}$$

Substitution of ρ_2 and u_2 into Eq. (2.48) gives

$$H_2 = \rho_2 \left(\frac{k k_{r2}}{\mu_2} \frac{\partial P}{\partial x} \right). \tag{2.50}$$

Introducing the exponential form of the gas-water relative permeability into Eq. (2.50),

$$H_2 = \rho_2 \left(\frac{k \left(\frac{S_2 - S_{2r}}{1 - S_{1r} - S_{2r}} \right)^n}{\mu_2} \frac{\partial P}{\partial x} \right). \tag{2.51}$$

Thus, derivitives of H_2 with respect to pressure and saturation become

$$\frac{\partial H_2}{\partial S_2} = \rho_2 \frac{n}{\left(1 - S_{1r} - S_{2r}\right)^n} \left(S_2 - S_{2r}\right)^{n-1} \left(\frac{k}{\mu_2} \frac{\partial P}{\partial x} \right). \tag{2.52}$$

$$\frac{\partial H_2}{\partial P} = \frac{d\rho_2}{dP} \left(\frac{S_2 - S_{2r}}{1 - S_{1r} - S_{2r}} \right)^n \left(\frac{k}{\mu_2} \frac{\partial P}{\partial x} \right) + \rho_2 \left(\frac{S_2 - S_{2r}}{1 - S_{1r} - S_{2r}} \right)^n \left(\frac{k}{\mu_2} \frac{\partial \left(\frac{\partial P}{\partial x} \right)}{\partial P} \right) - \rho_2 k \left(\frac{S_2 - S_{1r}}{1 - S_{1r} - S_{2r}} \right)^n \frac{\partial P}{\partial x} \frac{\left(\frac{\partial \mu_2}{\partial P} \right)}{\mu_2^2}. \tag{2.53}$$

Similarly, for G_2,

$$\frac{\partial G_2}{\partial S_2} = \phi \rho_2 . \tag{2.54}$$

$$\frac{\partial G_2}{\partial P} = \phi \frac{d\rho_2}{dP} S_2 + \frac{d\phi}{dP} \rho_2 S_2 . \tag{2.55}$$

Therefore, the wave velocity becomes

$$\frac{dx}{dt}=\frac{\rho_2\frac{n}{(1-S_{1r}-S_{2r})^n}(S_2-S_{2r})^{n-1}\left(\frac{k}{\mu_2}\frac{\partial P}{\partial x}\right)}{\phi\rho_2}+\frac{\frac{d\rho_2}{dP}\left(\frac{S_2-S_{2r}}{1-S_{1r}-S_{2r}}\right)^n\left(\frac{k}{\mu_2}\frac{\partial P}{\partial x}\right)+\rho_2\left(\frac{S_2-S_{2r}}{1-S_{1r}-S_{2r}}\right)^n\left(\frac{k}{\mu_2}\frac{\partial\left(\frac{\partial P}{\partial x}\right)}{\partial P}\right)}{\phi\frac{d\rho_2}{dP}S_2+\frac{d\phi}{dP}\rho_2S_2}$$

$$+\frac{-\rho_2k\left(\frac{S_2-S_{1r}}{1-S_{1r}-S_{2r}}\right)^n\frac{\partial P}{\partial x}\frac{\left(\frac{\partial\mu_2}{\partial P}\right)}{\mu_2^2}}{\phi\frac{d\rho_2}{dP}S_2+\frac{d\phi}{dP}\rho_2S_2} \qquad (2.56)$$

.

Rearranging,

$$\frac{dx}{dt}=\frac{n}{\phi(1-S_{1r}-S_{2r})^n}(S_2-S_{2r})^{n-1}\left(\frac{k}{\mu_2}\frac{\partial P}{\partial x}\right)+$$

$$\frac{\frac{d\rho_2}{dP}\left(\frac{S_2-S_{2r}}{1-S_{1r}-S_{2r}}\right)^n\left(\frac{k}{\mu_2}\frac{\partial P}{\partial x}\right)+\rho_2\left(\frac{S_2-S_{2r}}{1-S_{1r}-S_{2r}}\right)^n\left(\frac{k}{\mu_2}\frac{\partial\left(\frac{\partial P}{\partial x}\right)}{\partial P}\right)}{\phi\frac{d\rho_2}{dP}S_2+\frac{d\phi}{dP}\rho_2S_2}-\frac{\rho_2k\left(\frac{S_2-S_{1r}}{1-S_{1r}-S_{2r}}\right)^n\frac{\partial P}{\partial x}\frac{\left(\frac{\partial\mu_2}{\partial P}\right)}{\mu_2^2}}{\phi\frac{d\rho_2}{dP}S_2+\frac{d\phi}{dP}\rho_2S_2}$$

. (2.57)

The above equation suggests that the velocity of CO_2 waves are a function of saturation, pressure gradient, compressibilities, and the derivative of pressure gradient. In addition, it is often difficult to analytically determine the derivative of pressure gradient with respect to pressure during displacement. Therefore, we limit our analysis to cases in which the change in pressure gradient is minimal and, thus, its derivative vanishes.

2.5.4 Locally Constant Pressure Gradient and No Mutual Solubility

We limit our analysis to circumstances in which the $\frac{dP}{dx}$ pressure gradient varies insignificantly at upstream of the gas front; consequently, Eq. (2.57) can be expressed as

$$\frac{dx}{dt}=\frac{n}{\phi\left(1-S_{1r}-S_{2r}\right)^{n}}\left(S_2-S_{2r}\right)^{n-1}\left(\frac{k}{\mu_2}\frac{\partial P}{\partial x}\right)+\frac{\frac{d\rho_2}{dP}\left(\frac{S_2-S_{2r}}{1-S_{1r}-S_{2r}}\right)^{n}\left(\frac{k}{\mu_2}\frac{\partial P}{\partial x}\right)}{\phi\frac{d\rho_2}{dP}S_2+\frac{d\phi}{dP}\rho_2 S_2}-\frac{\rho_2 k\left(\frac{S_2-S_{1r}}{1-S_{1r}-S_{2r}}\right)^{n}\frac{\partial P}{\partial x}\frac{\left(\frac{\partial\mu_2}{\partial P}\right)}{\mu_2^2}}{\phi\frac{d\rho_2}{dP}S_2+\frac{d\phi}{dP}\rho_2 S_2} \quad . \quad (2.58)$$

Furthermore, if we neglect the variation of viscosity with pressure, Eq. (2.58)becomes

$$\frac{dx}{dt}=\frac{n}{\phi\left(1-S_{1r}-S_{2r}\right)^{n}}\left(S_2-S_{2r}\right)^{n-1}\left(\frac{k}{\mu_2}\frac{\partial P}{\partial x}\right)+\frac{\frac{d\rho_2}{dP}\left(\frac{S_2-S_{2r}}{1-S_{1r}-S_{2r}}\right)^{n}\left(\frac{k}{\mu_2}\frac{\partial P}{\partial x}\right)}{\phi\frac{d\rho_2}{dP}S_2+\frac{d\phi}{dP}\rho_2 S_2} \quad . \quad (2.59)$$

In addition, the compressibility of fluids at a constant temperature is defined by the relative change in volume per unit pressure variation:

$$c_j=-\frac{1}{V}\left(\frac{\partial V}{\partial P}\right)_{Temp} \quad . \quad (2.60)$$

In terms of density, the fluid compressibility at constant temperature, *T*, can be expressed as

$$c_j=\frac{1}{\rho}\left(\frac{\partial \rho}{\partial P}\right)_{Temp} \quad . \quad (2.61)$$

However, it is customary to report *z*, the gas compressibility factor, in the tables; hence, a relation between *c* and *z* is needed for the gas phase. Following from the real gas law:

$$PV = zRT. \tag{2.62}$$

Differential form of the above equation for an isothermal process is expressed as

$$VdP + PdV = RTdz. \tag{2.63}$$

Rearranging,

$$V + P\frac{dV}{dP} = RT\frac{dz}{dP}. \tag{2.64}$$

Dividing Eq. (2.64) by *V* gives

$$1 + P\frac{dV}{VdP} = \frac{RT}{V}\frac{dz}{dP}. \tag{2.65}$$

Rearranging,

$$P\left(-\frac{1}{V}\frac{dV}{dP}\right) = 1 - \frac{RT}{V}\frac{dz}{dP}. \tag{2.66}$$

Incorporating Eq. (2.60) into Eq. (2.66) gives

$$c_j = \frac{1}{P} - \frac{RT}{PV}\frac{dz}{dP}. \tag{2.67}$$

$$c_j = \frac{1}{P} - \frac{1}{z}\frac{dz}{dP}. \tag{2.68}$$

$$c_j = \frac{1}{P} - \frac{d\ln z}{dP}. \tag{2.69}$$

Eq. (2.69) shows the relation between *z* and *c*. We also consider the compressibility of pore space at constant temperature, *T*, as

$$c_r = \frac{1}{\phi}\left(\frac{\partial\phi}{\partial P}\right)_{Temp}. \tag{2.70}$$

Incorporating the definitions of rock and fluid compressibility into Eq.(2.59), yields

$$\frac{dx}{dt}=\frac{n}{\phi\left(1-S_{1r}-S_{2r}\right)^{n}}\left(S_2-S_{2r}\right)^{n-1}\left(\frac{k}{\mu_2}\frac{\partial P}{\partial x}\right)+\frac{c_2\rho_2\left(\frac{S_2-S_{2r}}{1-S_{1r}-S_{2r}}\right)^{n}\left(\frac{k}{\mu_2}\frac{\partial P}{\partial x}\right)}{\phi\rho_2 S_2\left(c_2+c_r\right)}. \tag{2.71}$$

Rearranging Eq. (2.71) yields the final form of the wave velocity as

$$\frac{dx}{dt}=\frac{n}{\phi\left(1-S_{1r}-S_{2r}\right)^{n}}\left(S_2-S_{2r}\right)^{n-1}\left(\frac{k}{\mu_2}\frac{\partial P}{\partial x}\right)+\frac{c_2\left(\frac{S_2-S_{2r}}{1-S_{1r}-S_{2r}}\right)^{n}\left(\frac{k}{\mu_2}\frac{\partial P}{\partial x}\right)}{\phi S_2\left(c_2+c_r\right)}. \tag{2.72}$$

The above equation suggests the velocity of the CO_2 waves is a function of saturation, rock and CO_2 compressibility, and the pressure gradient; however, the velocity of the CO_2 wave is only a function of saturation in the absence of compressibility.

If the rock compressibility is negligible compared to that of CO_2, the gas compressibility is canceled from the second term in Eq.(2.72); Therefore, the wave velocity will be only a function of the gas saturation and the pressure gradient. Hence, for a constant pressure gradient when the rock compressibility is negligible, the wave velocity only depends on gas saturation as is for incompressible fluids.

2.6 VERIFICATION

We first verify the assumption under which H is only function of G. We consider (1):constant compressibility values of 1.69 E-4 and 5E-5 (1/psi) for the gaseous phase and the rock; (2) uniform initial pressure and temperature values of 2000 psi and 150°F are assumed; (3) the exponent of relative permeability model (n) and the residual saturations are 2 and 0.2, respectively; (4) uniform porosity and the permeability values of 0.3 and 100 md; and (5) no mutual solubility in the following examples.

Using equations (2.22) and (2.23), H and G are calculated for the range of pressure between 2000 <P< 3000 psi and saturations between 0.2 <S_g<0.8 (Figure 2.1). It is clear from the figure that for every G there is one and only one value of H assigned along each curve that represents constant pressure gradient; In other words, H is only function of G along those curves even though pressure and saturation are varying. Hence, H will be only function of G if the pressure gradient is constant.

To verify Eq.(2.72), we use a simulation approach. The simulations are performed using STARS, CMG's three-phase multicomponent simulator. We choose STARS as assigning and changing the fluid properties (density, viscosity, and compressibility) are simple in it. The simulation model consists of two vertical wells located at the ends of a 1D grid with 1000 grid blocks. The top and bottom of the model are no flow boundary conditions. The injection well is assigned either a constant bottomhole pressure of 3000 psi (pressure constraint) or constant rate of 140 reservoir barrels per day (rate constraint). However, we consider a constant pressure constraint for the production well located at the end of model.

According to Eq. (2.72), the wave velocity will be only a function of the gas saturation if the change in the pressure gradient is negligible. However, displacing CO_2 has larger mobility (an order of magnitude) than the resident brine. This yields two regions with considerably different pressure drops along the aquifer length: (1) across the mixture of CO_2 and brine flowing upstream of the gas front and (2) across the resident brine downstream of the front. The latter yields the flow of resident brine toward the outlet boundary (Figure 2.8). Therefore, we investigate the wave propagation for three

different cases with the end-point mobility ratios ($M°$) of 0.1, 1, and 10. The end-point mobility ratio is defined as the ratio of the mobility of the injected phase to the the resident fluid when the end-point relative permeability values are used. We do not realize the end-point mobility ratios of 0.1 and 1 in practice for the CO_2 storage in an aquifer; however, the examples are for verification of the analytical solutions derived in this study that may be used for other applications.

2.6.1 The End-Point Mobility (M°) Ratio of 10

The first case we study is an isothermal CO_2 injection into an aquifer initially filled with water while $M°=10$. Figure 2.2 shows the pressure profile at the early stage of the displacement. The pressure perturbation travels very fast owing to small compressibility of the resident water and the rock (see early jumps in the pressure curve in Figures 2.5 and 2.6). Figure 2.2 can be translated into the propagation of the compressible zone along the aquifer. Similar to Bourdarot (1998), we define the compressible zone as part of the aquifer affected by the pressure perturbations as it travels along the permeable medium. When the compressible zone reaches the outlet boundary, the pressure perturbation vanish. The pressure perturbation travels very fast such that when it hits the outlet boundary, the injected gas has not gone far from the injector. Figure 2.3 illustrates the local flow velocity of the resident fluid as a function of distance at early times. The resident fluid moves toward the producer because of the local pressure gradient induced by the pressure wave. The velocity of the resident water changes significantly with distance at early stages of displacement because of the compressibility of water and the rock.

Figure 2.4 indicates the local fluid velocity at the inlet and outlet of the aquifer; *i.e.* grid blocks 1 and 1000. When the fast pressure pulse diminishes at around 92 days, the flow rates become equal at the two ends. Similar behavior is observed for other grid blocks.

The saturation and the local pressure at the mid-point of the aquifer (grid block 500) obtained from the simulation are shown in Figure 2.5. Note that a rapid increase in the local pressure occurs soon after the start of injection as the pressure wave passes through that grid block. This change in pressure (starts after day 10) is followed by the coupled saturation and pressure changes at around 13000 days. Note that there is another change in the pressure curve that occurs after the gas breakthrough at around 26000 days.

Figure 2.6 indicates the pressure and saturation changes at the aquifer's mid-point (grid block 500) when the injection well is assigned the pressure constraint. A similar behavior is observed for the pressure and saturation changes as Figure 2.5. An early pressure jump at 40 days followed by the coupled saturation and pressure changes at 7400 days is realized at the aquifer's mid-point. In addition, a late pressure change occurs at 12400 days that is created because of the gas breakthrough.

Figure 2.7 shows the pressure and saturation profiles depicted at 5450 days. The coupled front propagates along the permeable medium and displaces the resident water. The injector is assigned the rate constraint in this example. Furthermore, two saturation shocks are observed in the saturation profile: a leading shock accompanied by the pressure change and a trailing shock with zero velocity connecting the gas saturation of 0.8 to 0.75. The saturation of the leading front occurs at 0.44.

Figure 2.8 also suggests that there is constant pressure drops upstream and downstream of the gas front. Figure 2.8 shows the pressure gradient obtained from the simulation as a function of the aquifer's length depicted at 10000 days. For this example, the injector is assigned the constant rate constraint. Except for the gas front location, the pressure gradient curve is continuous over the length of the aquifer. However, upstream of the gas front, the pressure gradient varies linearly with distance at the slope of 5E-6 (psi/ft^2). This very small slope favors our assumption of the constant pressure gradient; As a result, the term consists the derivative of pressure gradient in Eq. (2.57) will be two orders of magnitude smaller than the other terms using the slope obtained from Figure 2.8. For more details about the pressure change along aquifer see Oruganti (2010). Oruganti (2010) semi-analytically studied the evolution of over pressure for CO_2 injection for different boundary conditions: constant pressure, no-flow and infinite acting boundary.

Figure 2.9 illustrates the solution route (wave velocities and associated saturations and the pressure gradients) obtained semi-analytically from Eq. (2.72). The pressure gradient at each location is obtained from the simulation and is incorporated into Eq. (2.72). Inserting compressibility values for the gas and the rock, we solve Eq. (2.72) for saturation. Note that we choose just the saturation values that are bounded between zero and one as the values beyond this range is non-physical. Starting from initial condition (I), the solution route consists of a shock between I and point A followed by spreading waves connecting A to B and eventually a trailing shock from B toward injection

condition (J). This solution route is consistent with saturation profile in Figure 2.9 obtained from the simulation.

Furthermore, Figure 2.10 implies that the wave velocity along the solution route decreases monotonically from I to J. This observation is consistent with the entropy condition as described in Lake (1989). The solution route intersects the curves along which the absolute pressure gradient is constant. Larger pressure gradients occur downstream of the gas front filled with water; because the resident brine has less mobility compared to the upstream fluids.

At early stage of displacement, fast pressure waves occur along which only pressure disturbance is traveling; they are not accompanied by the change in saturation and, consequently, all are located along y-axis; *i.e.* no saturation change is associated.

However, another set of pressure waves travel at later times that are associated with change in saturation. The change in saturation, though, is not continuous; in this example, we have two separate saturation jumps (shocks) consistent with figures 2.7 and 2.9.

2.6.2 The End-Point Mobility (M°) Ratio of 1

Next, we study an isothermal injection of a hypothetical gas into a permeable medium initially filled with a resident fluid such that $M°=1$. The saturation and the pressure changes at the mid-point of the aquifer (grid block 500) obtained from the simulation are shown in Figure 2.11. Note that pressure changes at that grid block occur soon after the start of injection. The early change in pressure (with a peak at 24 days) is

followed by the coupled saturation and pressure changes at around 17500 days. There is another change in the pressure that occurs after the gas breakthrough at 35500 days.

Figure 2.12 indicates the pressure and saturation changes when the injection well is assigned the constant pressure constraint of 3000 psi. A similar characteristic is observed for the pressure and saturation change as in Figure 2.11. An early pressure increase occurs at 16 days and the coupled saturation and pressure changes reach the aquifer's mid-point at 2850 days. Furthermore, a late pressure change occurs at 5850 days created because of the gas breakthrough.

Figure 2.13 shows the pressure and saturation profiles depicted at 8200 days. The coupled front propagates along the permeable medium and displaces the resident water. Note that the injector is assigned the constant rate constraint. Furthermore, only one saturation shock is observed that is accompanied by the pressure change. The front saturation occurs at 0.66.

Figure 2.14 illustrates solution route obtained semi-analytically from Eq. (2.72). The pressure gradient at each location is obtained from the simulation and is incorporated into Eq.(2.72). The solution route consists of a shock between I and point A followed by spreading waves connecting A to J. The wave velocity along the solution route decreases monotonically from I toward J. The solution route intersects the curves along which the absolute pressure gradient is constant. Therefore, pressure gradients are small in general.

2.6.3 The End-Point Mobility (M°) Ratio of 0.1

Finally, we study an isothermal injection of a hypothetical gas into a permeable medium initially filled with a resident fluid such that $M°$=0.1. The saturation and the

pressure changes at the mid-point of the aquifer (grid block 500) obtained from the simulation are shown in Figure 2.15. Note that pressure changes at that grid block occur soon after the start of injection. The early change in pressure (with a peak at around 32 days) is followed by the coupled saturation and pressure changes at around 19500 days.

Figure 2.16 indicates the pressure and saturation changes when the injection well is assigned the constant pressure constraint. A similar characteristic is observed for the pressure and saturation change as Figure 2.14. An early pressure increase occurs at 8 days and the coupled saturation and pressure changes reach the aquifer's mid-point at 5450 days.

Figure 2.17 shows the pressure and saturation profiles depicted at 9500 days. The coupled front propagates along the permeable medium and displaces the resident water. Note that the injector is assigned the constant rate constraint. Also note that only one saturation shock is observed that is accompanied by the pressure change. The front saturation occurs at 0.78.

Figure 2.18 illustrates solution route obtained semi-analytically from Eq. (2.72). The pressure gradient at each location is obtained from the simulation and is incorporated into Eq.(2.72). The solution route consists of a shock between I and point A followed by spreading waves connecting A to J. The wave velocity along the solution route decreases monotonically from I toward the injection condition, J. The solution route intersects the curves along which the absolute pressure gradient is constant.

2.6.4 Impact of Rock Compressibility

Next, we evaluate the impact of rock compressibility on the wave velocity using Eq.(2.89). As it was mentioned in the previous section, the wave velocity is expected to be indifferent with respect to fluid compressibility if the rock compressibility is negligible compared to that of fluid. To test this hypothesis, we consider four cases with different fluid compressibility values and no rock compressibility. The objective is to show that all cases produce the same saturation profile at a given time. We assign the constant injection rate constraint and the end point mobility ratio of 10. We keep the other properties as the previous examples.

Figure 2.19 shows the cumulative produced fluid as a function of time. Note that the amount of water discharged from the aquifer is not the same for all cases. This is because of the compressibility of the gas. Hence, we cannot use dimensionless time as defined by Lake (1989), because the injection and production rates are no longer equal owing to the gas compressibility. Hence, we use actual time in days in our analysis rather than the dimensionless form of it.

We set 1,000,000 reservoir barrels as the reference volume and determine the time required for each case to produce this amount. Figure 2.20 compares the saturation profiles depicted as a function of distance. As shown, all curves coincide demonstrating that the fluid compressibility becomes unimportant in the absence of rock compressibility; this is in agreement with the theory as described in the previous sections.

Furthermore, Figure 2.21 compares the saturation profiles depicted at different times representing the production of the same amount of fluid for three cases. In two

cases, the rock compressibility is in the same order as the gas (only to verify the prediction of the analytical solution); therefore, different values of the gas compressibility yield different wave velocities as the compressibility terms are not dropped from Eq.(2.72). However, in the third case no compressibility is involved and the saturation profile is behind the two others.

2.6.5 IMPACT OF INITIAL GAS SATURATION

In this section, the impact of a non-zero initial gas saturation is investigated on the saturation profile while all other parameters are the same as the simulation model used in the part 2.6.1 of this dissertation.

Figure 2.22 shows the changes in saturation and pressure as a function of distance (normalized by the aquifer length) depicted at 5000 days obtained from the simulation. Two saturation shocks are observed: a leading shock accompanied by the pressure change and a trailing shock with zero velocity connecting the gas saturation of 0.8 to 0.75. The saturation of the leading front occurs at 0.34 (located at x_D=0.36) accompanied by the pressure shock.

Figure 2.23 shows pressure gradient as a function of saturation obtained from simulation when initial gas saturation is 0.2 (S_g =0.2). Similar behavior Figure (2.10) is observed : at early stage of displacement, fast pressure waves occur along which only pressure disturbance is traveling. These fast pressure waves are followed by slow pressure waves that are associated with the change in saturation.

2.6.6 IMPACT OF LARGE COMPRESSIBILITY

In this section, the impact of a larger gas saturation (100 times greater than CO_2 is investigated on the saturation profile while all other parameters are the same as the simulation model used in the part 2.6.5 of this dissertation. \

Figure 2.24 shows pressure gradient as a function of saturation obtained from simulation when initial gas saturation is 0.2 (S_g =0.2) and the compressibility of gas is 100 times greater than CO_2. Despite Figure (2.23), fast pressure waves reduce the initial gas saturation (as a result of large gas compressibility and more sensitivity to pressure drop) as it travels along the length of the aquifer. These fast pressure waves are followed by slow pressure waves that are similar to those in Figure (2.23). However, the gas saturation vanishes downstream of the slow pressure waves because of the large gas compressibility in this case.

Figure 2.25 illustrates the changes in saturation and pressure as a function of distance (normalized by the aquifer length) depicted at 2500 days obtained from the simulation. Three distinct regions are identified (1): initial condition, where pressure and saturation occur at their original values; (2) region under influence of the fast pressure waves, where the gas saturation decreases because of the applied pressure disturbance; and (3) Buckley and Leverett solution. The saturation of the leading front occurs at 0.39 (located at x_D=0.23) accompanied by the slow pressure wave.

Figure 2.26 shows the changes in saturation and pressure as a function of distance (normalized by the aquifer length) depicted at 8000 days obtained from the simulation. Fast pressure waves have reached upon the aquifer's outlet boundary and, hence, no

initial condition is realized. Because of the large gas compressibility, the initial gas have been pushed toward the producer by the fast pressure wave. The saturation of the leading front occurs at 0.39 (located at x_D=0.63) accompanied by the slow pressure wave.

2.7 Discussion and Conclusions

The main outcome of the analytical developments presented here is the MOC solution for two-phase, two-component flow with constant compressibility values. Semi-analytical solutions, Equations (2.41), (2.46), and (2.72) are introduced to determine the wave velocity for different cases. Furthermore, semi-analytical solutions, Eqs (2.89) and (2.90), are introduced to evaluate the velocity of the saturation waves. The simulation results confirm the accuracy of Eq.(2.72).

1. The velocity of the saturation waves increases when the pressure gradient increases despite when the compressibility is absent.
2. The wave velocities increase from J to I, consistent with the entropy condition as defined to evaluate the MOC solutions in incompressible displacements.
3. If the pressure gradient for each location is known from the simulation, the saturations can be determined accurately using the solutions derived in this work.
4. The wave velocity becomes independent of the fluid compressibility in the absence of the rock compressibility.
5. The simplicity of the solution yields an efficient and quick method to investigate how fast CO_2 propagates along the aquifer length.
6. For very large gas compressibility values (100 times greater than CO_2), fast pressure wave reduces the initial gas saturation (because of the compression) as it

travels through the aquifer. The fast pressure wave pushes the bulk of compressed gas toward the outlet of the aquifer. As a result, the initial existing gas is compressed nearby the producer.

NOMENCLATURE

P= pressure, psi

F_i= overall flux of component i

H_i=mass flux of component i

G_i=mass of component i in the bulk volume

f_j= fractional flow of phase j

C_i= overall concentration of component i

c_r= isothermal rock compressibility

c_{ij}=volume fraction of component i in phase j

ω_{ij}=mass fraction of component i in phase j

c_w= isothermal compressibility of the resident water

S_j= saturation of phase j

x_D== dimensionless distance

t_D== dimensionless time

ρ_j= density of phase j, lb/ft^3

μ_j=viscosity of phase j, cp

k= permeability, md

L=aquifer length, ft

$M°$= End point mobility ratio

V= volume, ft^3

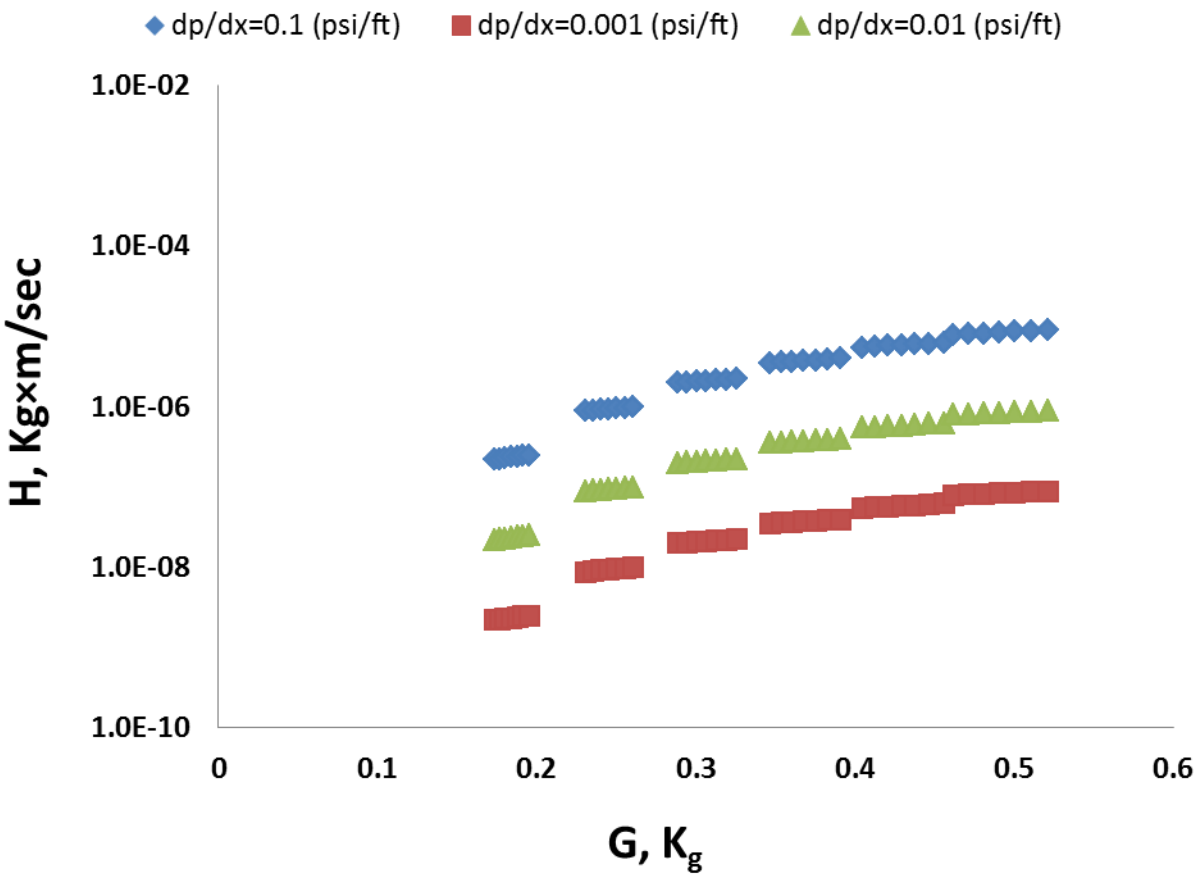

Figure 2.1: H as a function of G for various pressure gradients.

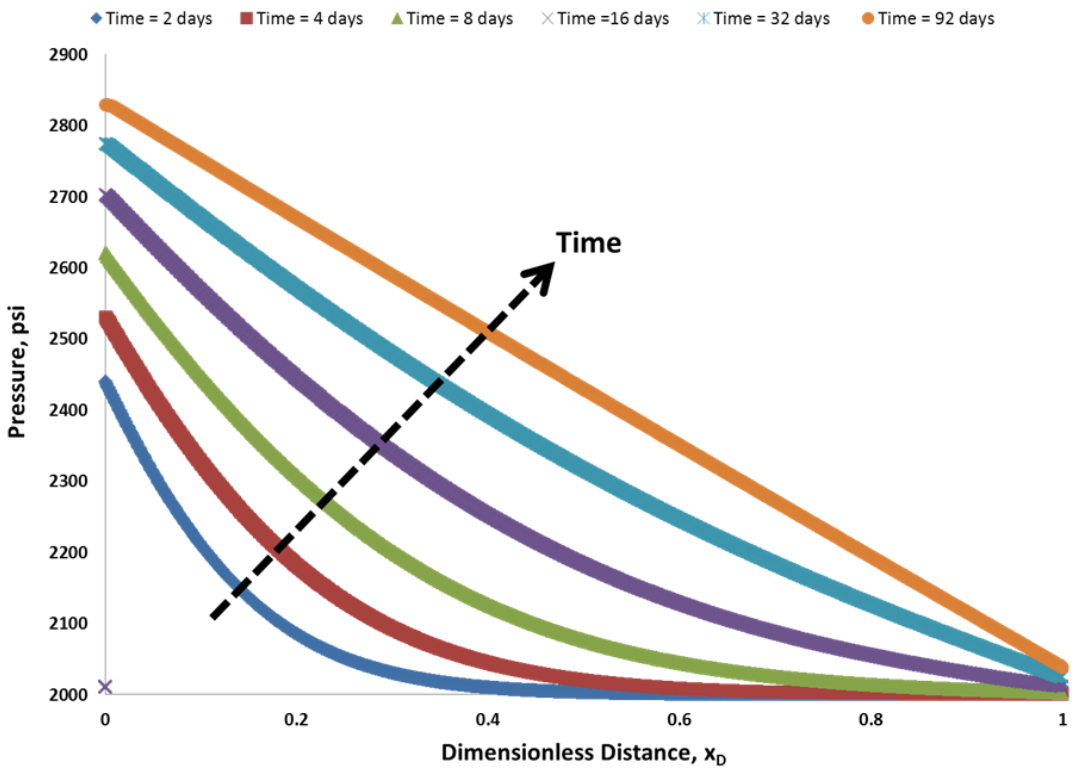

Figure 2.2: Pressure profiles (pressure as a function of distance normalized by the length of the aquifer) at early times of the displacement obtained from simulation. Note that when the pressure disturbance reaches the outlet boundary after 92 days, steady-state condition is established temporarily with respect to time (orange curve); however, this state is disrupted later by propagation of the coupled saturation and pressure front as two different pressure gradients are realized (see Figure 2.8). The pressure constraint is applied for the injector in this example.

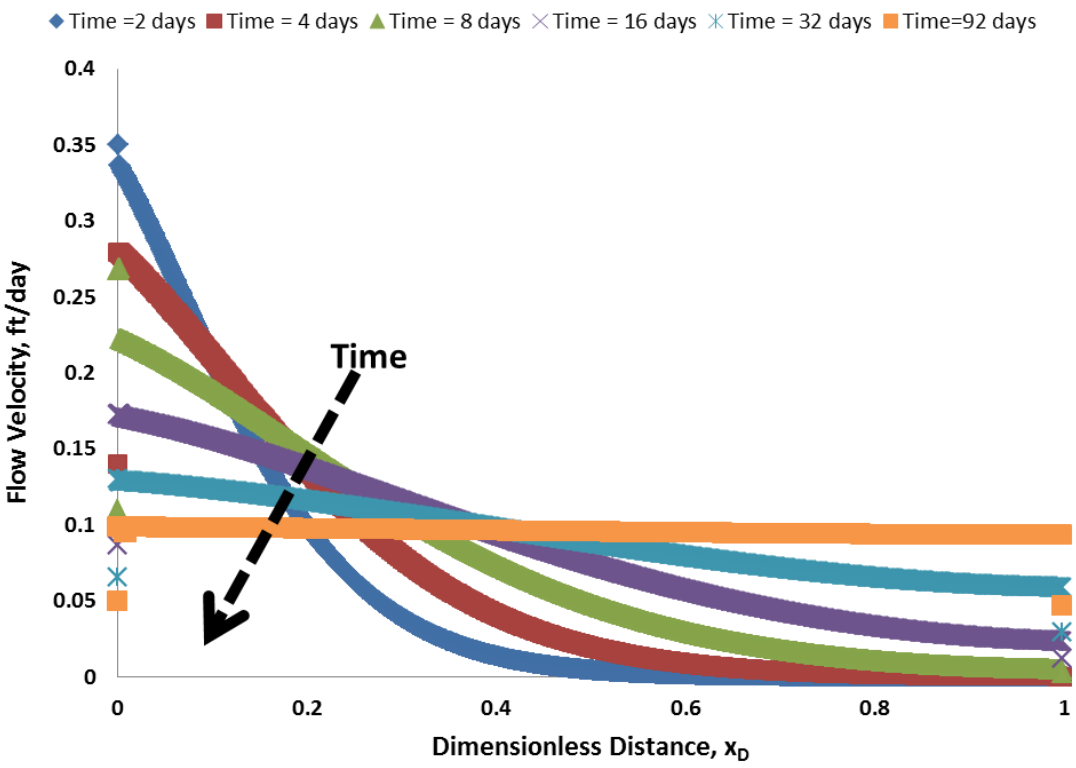

Figure 2.3: Local flow velocity as a function of distance (normalized by the length of the aquifer) for early stages of the displacement obtained from the simulation. When the compressible zone reaches the outlet boundary, steady-state condition is established temporarily with respect to time (orange curve); however, this state is disrupted by propagation of the coupled saturation and pressure front as two different pressure gradients are realized. Each curve in this plot corresponds to the similar curve in Figure 2.2.

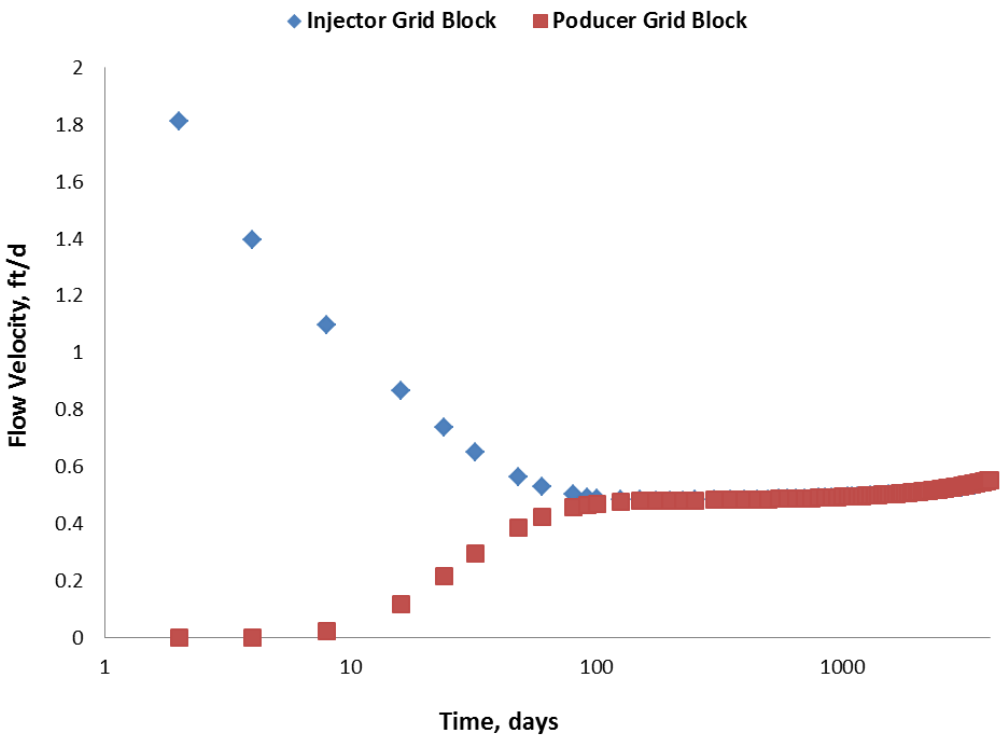

Figure 2.4: Local flow velocity at the two ends of the aquifer. When the fast pressure perturbation hits the outlet boundary (after 92 days), the flow velocity becomes equal at the injector and the producer. The injector is assigned the pressure constraint in this example.

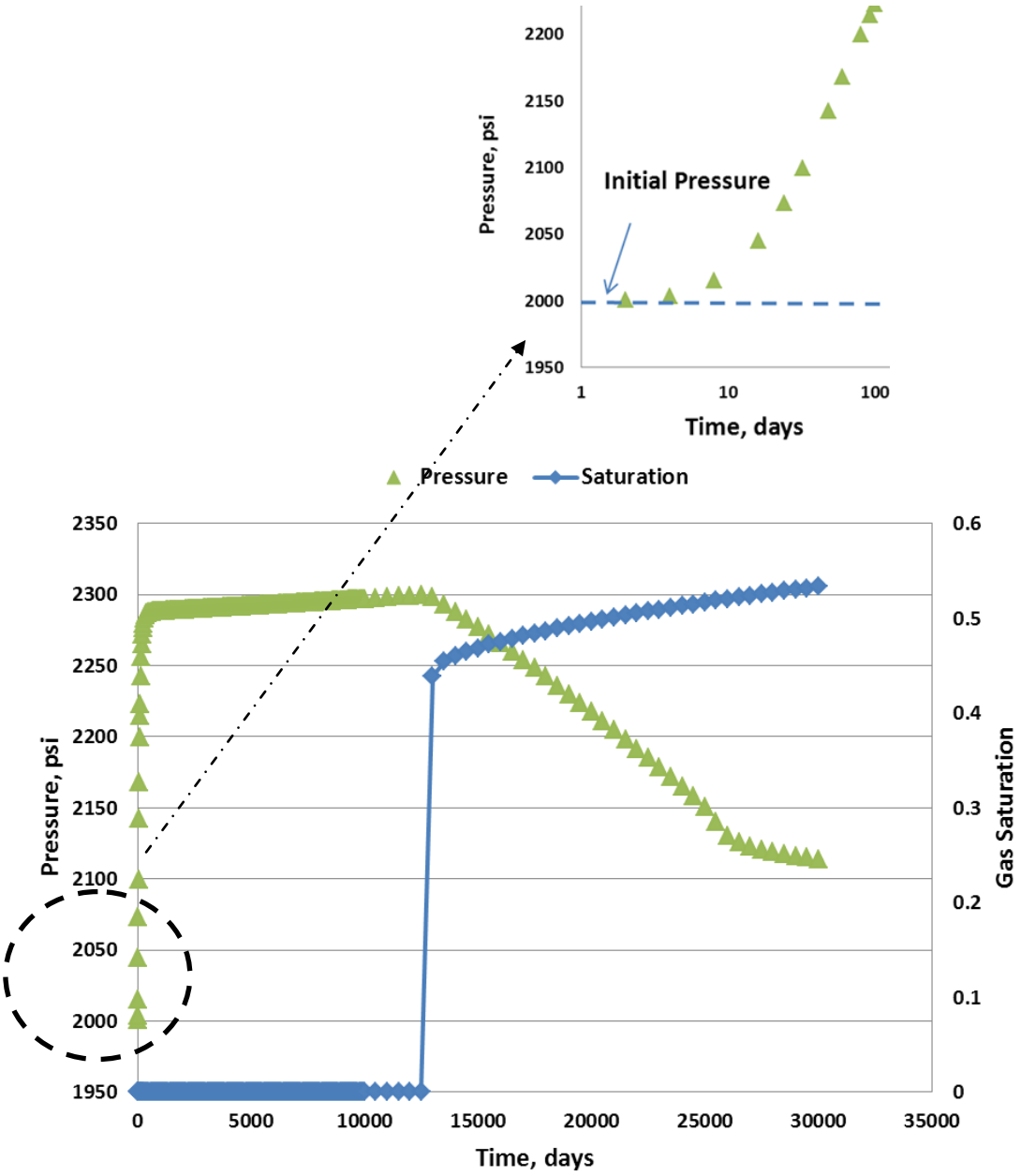

Figure 2.5: The saturation and pressure changes that occur at the aquifer's mid-point obtained from the simulation. For this example, the injector is assigned the constant rate constraint and M°=10. There are three points at which the slope of pressure curve changes but only one of them (at 13000 days) is coupled with the saturation shock. The early pressure jump occurs only after 10 days injection. The late pressure change that occurs at around 26000 days is related to the gas breakthrough.

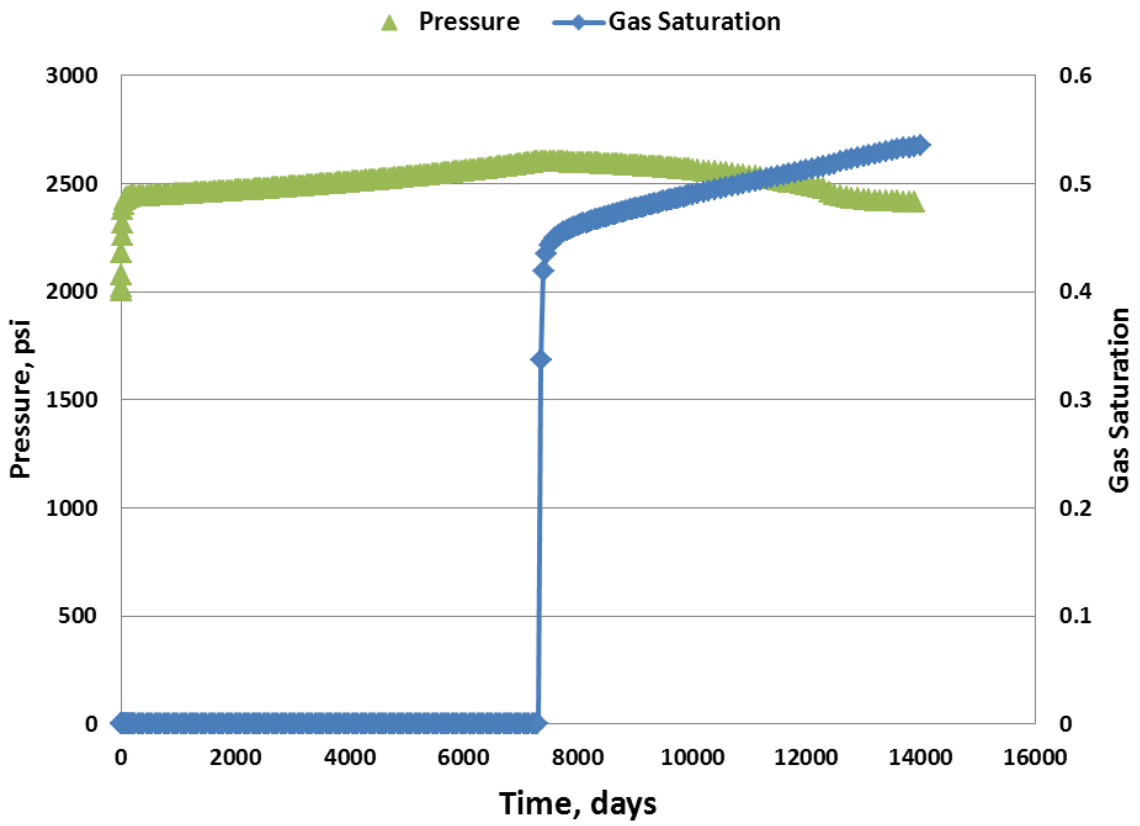

Figure 2.6: The saturation and pressure changes occur at the aquifer's mid-point (grid block 500) obtained from the simulation. For this example, M°=10 and the injector is assigned the constant pressure constraint of 3000 psi. There are three points at which the slope of pressure curve changes but only one of them is coupled with the saturation shock (at 7400 days). The late pressure change that occurs at around 12500 days is related to the gas breakthrough.

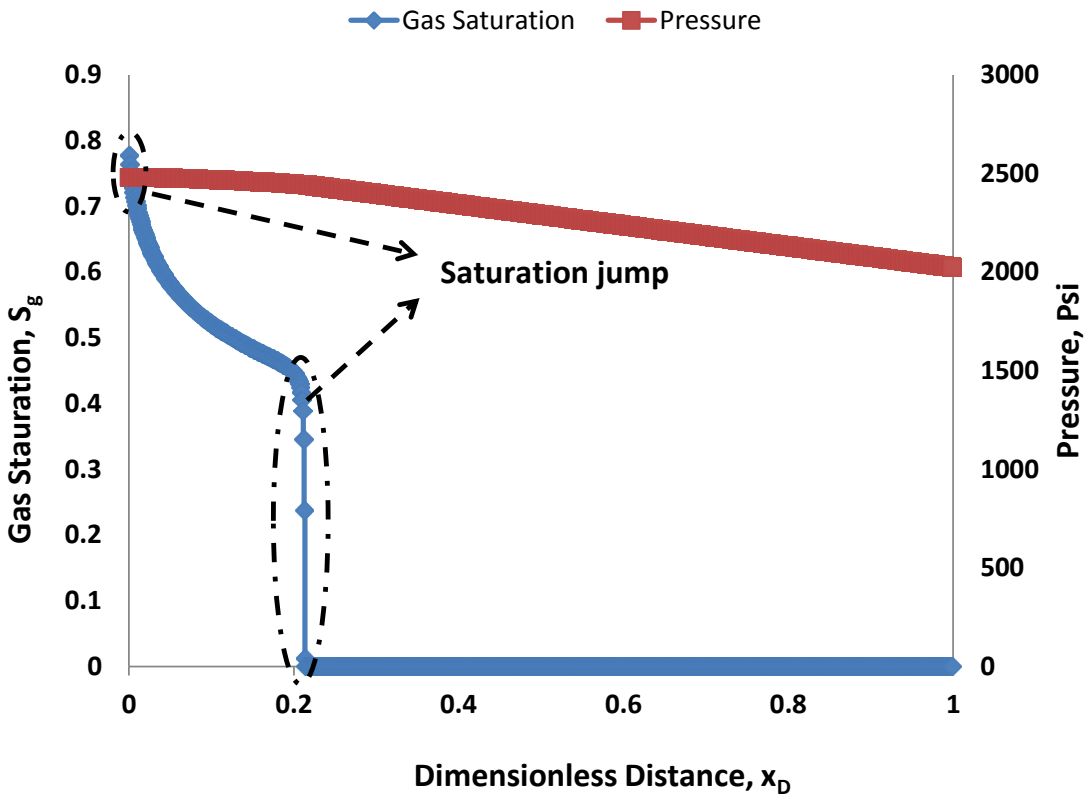

Figure 2.7: The changes in saturation and pressure as a function of distance (normalized by the aquifer length) depicted at 5450 days obtained from the simulation. For this example, the constant rate constraint is assigned to the injector and M°=10. Two saturation shocks are observed: a leading shock accompanied by the pressure change and a trailing shock with zero velocity connecting the gas saturation of 0.8 to 0.75. The saturation of the leading front occurs at 0.44 (located at x_D=0.21) accompanied by the pressure shock.

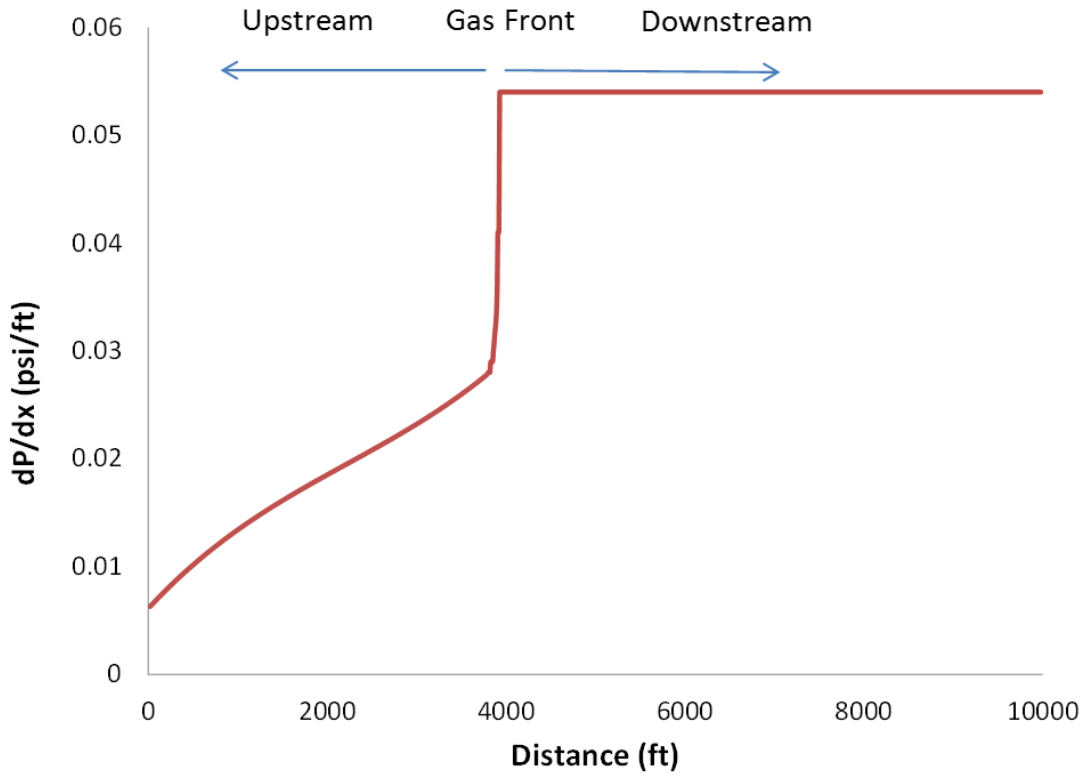

Figure 2.8: Pressure gradient (obtained from the simulation) as a function of the aquifer's length depicted at t=10000 days. For this example, the constant rate constraint is assigned to the injector and M°=10. Except for the gas front location, the pressure gradient curve is continuous over the length of the aquifer. However, the upstream of the gas front, the pressure gradient varies linearly with distance at the slope is 5E-6 psi/ft^2.

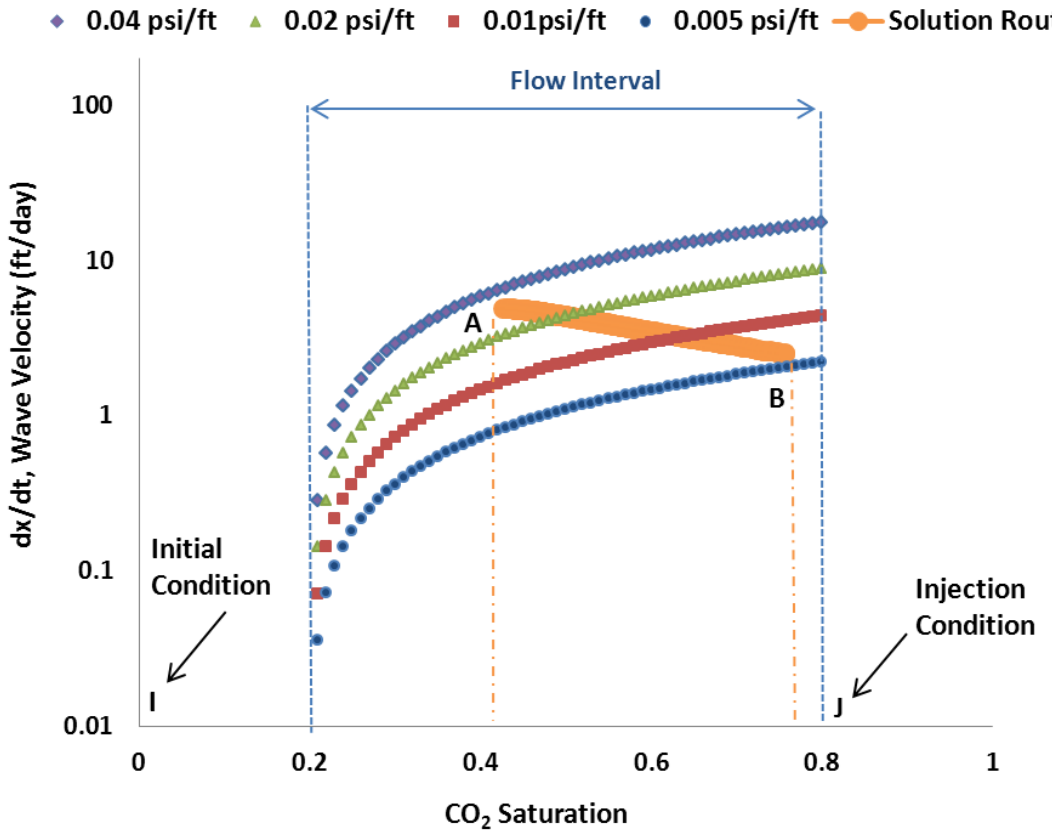

Figure 2.9: Solution route obtained semi-analytically from Eq.(2.72) when the injector is assigned a constant rate. The pressure gradient at each location is obtained from the simulation and is incorporated into Eq. (2.72). The solution consists of a shock between I and point A followed by spreading waves connecting A to B and eventually a trailing shock from B toward injection condition (J). Note that saturation residuals are 0.2. The wave velocity along the solution route decreases monotonically from I to J. For this example, the constant rate constraint is assigned to the injector and M°=10. Therefore, larger pressure gradient occurs downstream of the gas front located at point A.

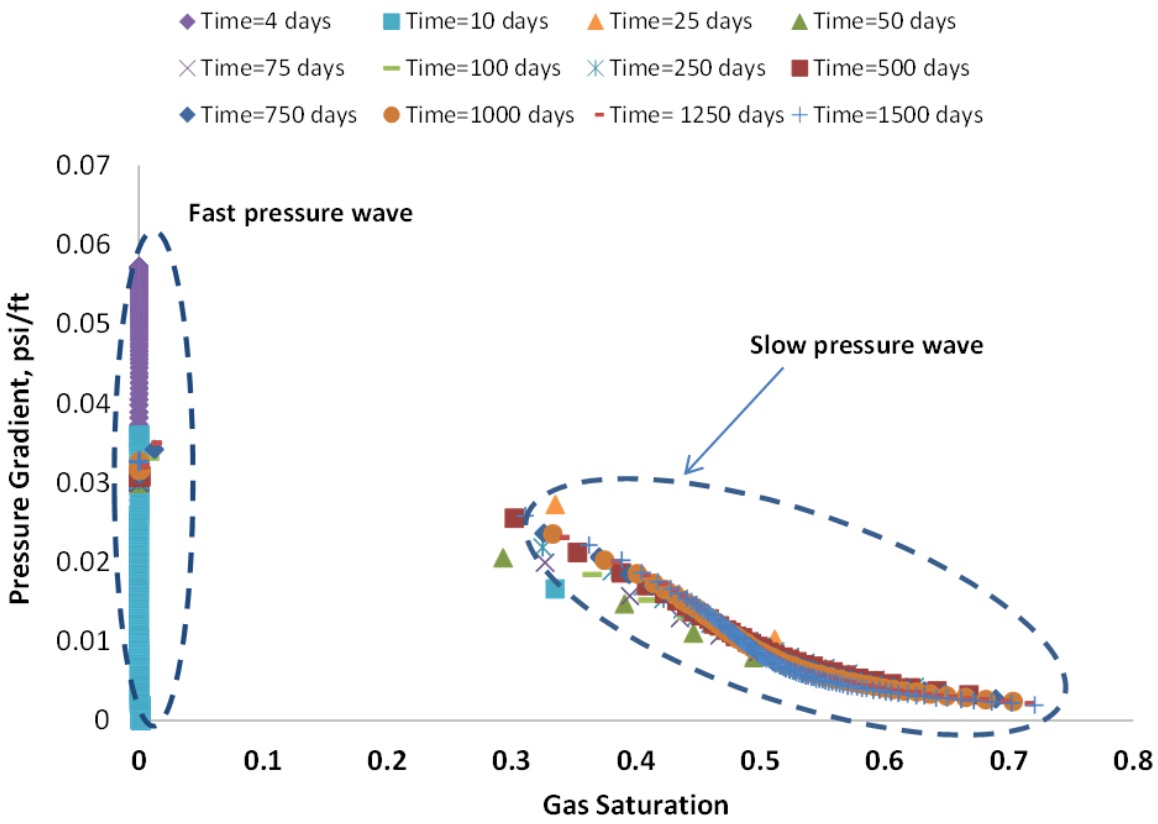

Figure 2.10: Pressure gradient as a function of saturation obtained from simulation. At early stage of displacement, fast pressure waves occur along which only pressure disturbance is traveling. These fast pressure waves are followed by slow pressure waves that are associated with the change in saturation. For this example, the constant rate constraint is assigned to the injector and M°=10.

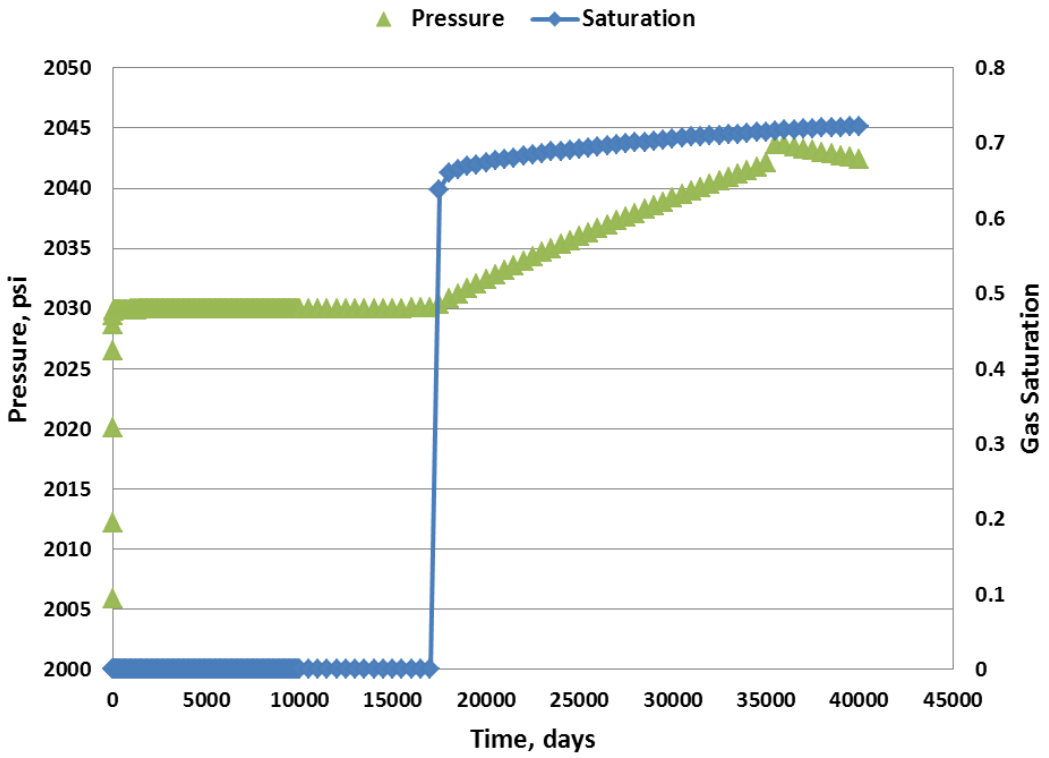

Figure 2.11: The saturation and pressure changes that occur at the aquifer's mid-point (grid block 500) obtained from the simulation. For this example, the constant rate constraint is assigned to the injector and M°=1.0. There are three points at which the slope of pressure curve changes but only one of them is coupled with the saturation shock (at 17500 days).

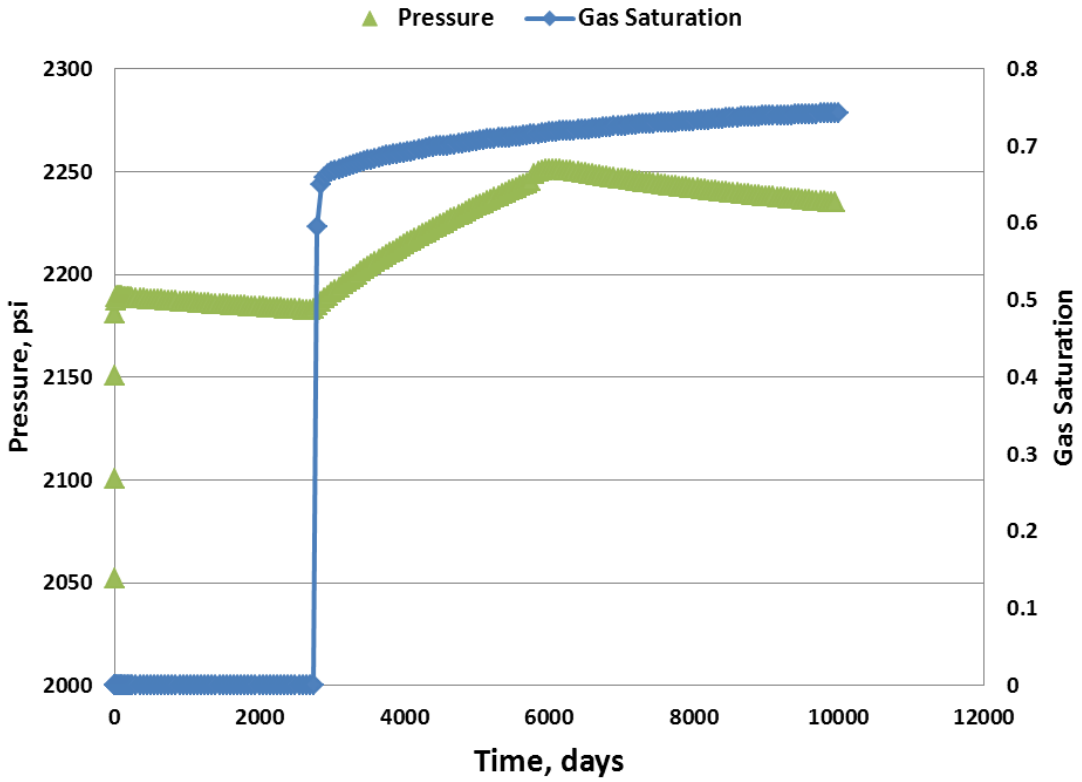

Figure 2.12: The saturation and pressure changes occur at the aquifer's mid-point (grid block 500) obtained from the simulation. For this example, M°=1 and the constant pressure constraint is assigned to the injector. There are three points at which the slope of pressure curve changes but only one of them is coupled with the saturation shock (at 2850 days).

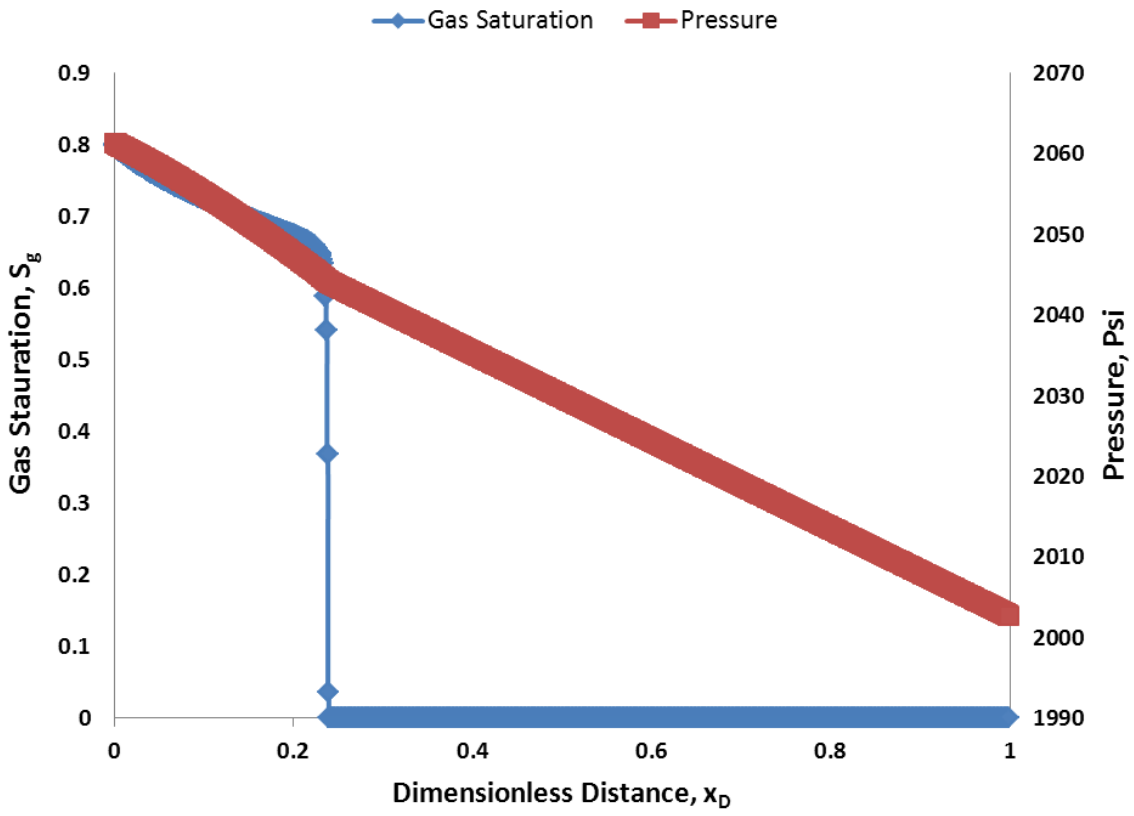

Figure 2.13: The changes in saturation and pressure as a function of distance (normalized by the length of the aquifer) depicted at 8200 days (obtained from the simulation). In this example, the constant rate constraint is assigned to the injector and M° =1. Note that only one saturation shock. The saturation of the gas front occurs at 0.66 (which is located at x_D=0.24).

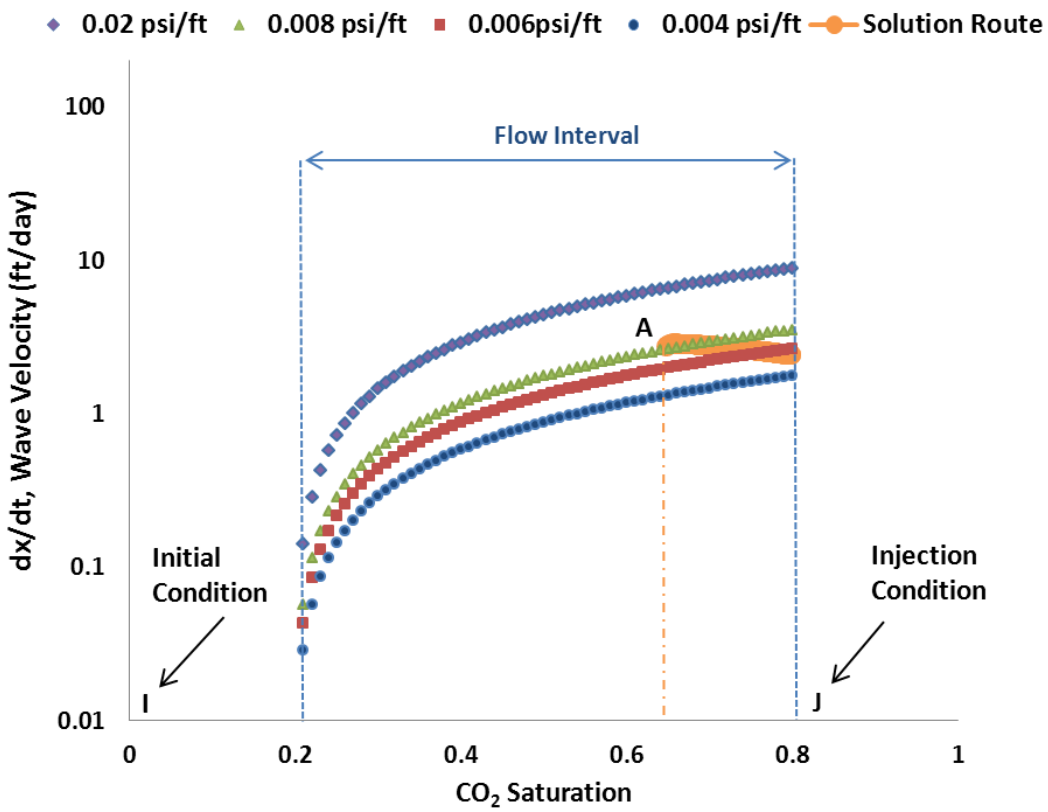

Figure 2.14: Solution route obtained semi-analytically from Eq. (2.72) when the injector is assigned a constant rate. The pressure gradient at each location is obtained from the simulation and is incorporated into Eq. (2.72). The solution consists of a shock between I and point A followed by spreading waves connecting A to J along the orange curve. Note that saturation residuals are 0.2. The wave velocity along the solution route decreases monotonically from I to J. For this example, the constant rate constraint is assigned to the injector and M°=1. Therefore, pressure gradients are small in general.

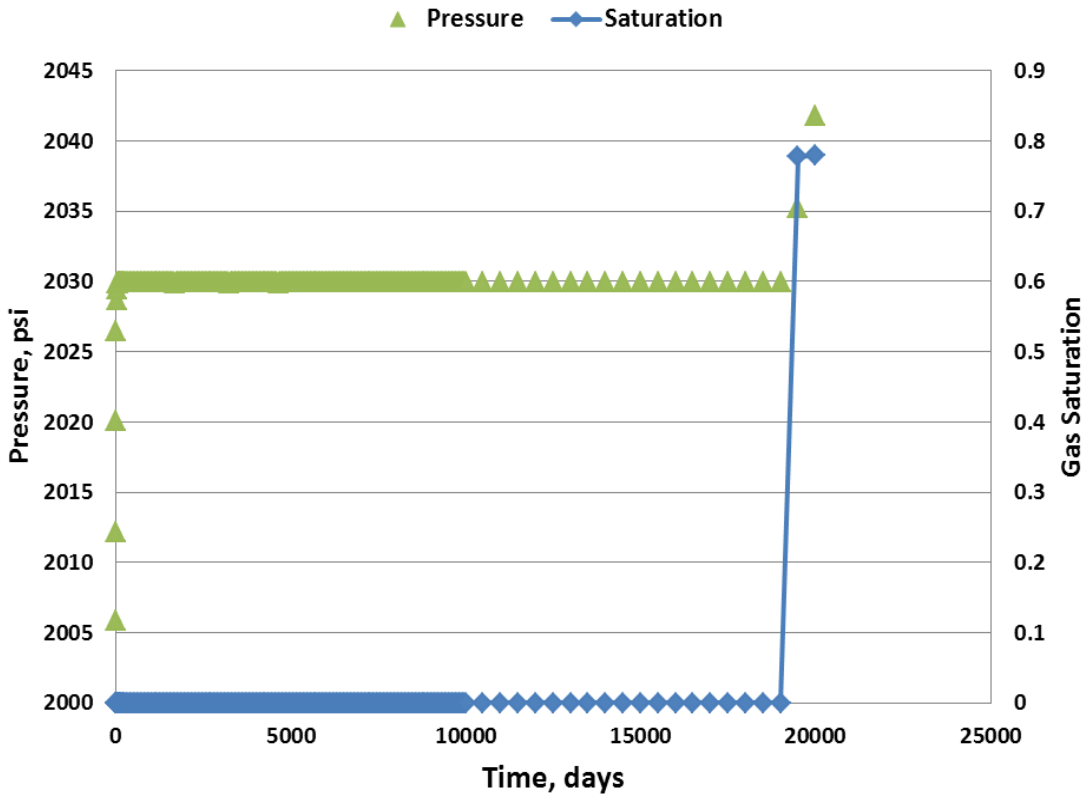

Figure 2.15: The saturation and pressure changes that occur at the aquifer's mid-point (grid block 500) obtained from the simulation. For this example, the constant rate constraint is assigned to the injector and M°=0.1. There are two points at which the slope of pressure curve changes but only one of them is coupled with the saturation shock (at 19500 days).

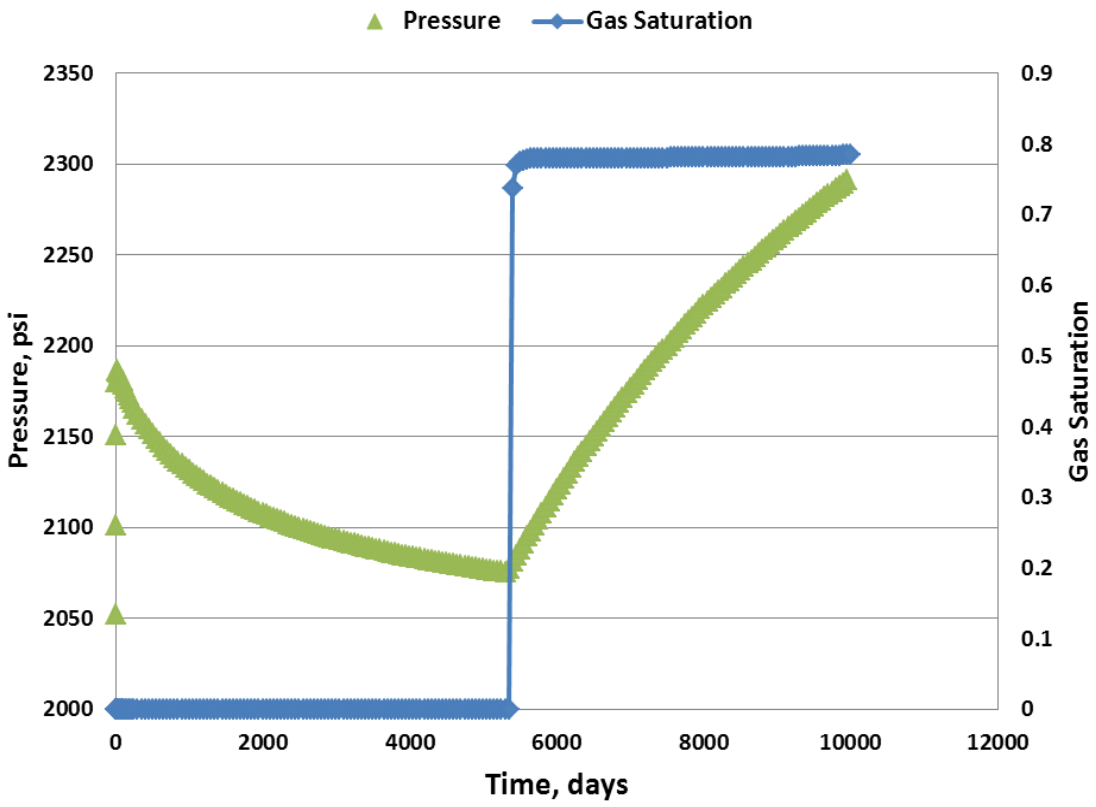

Figure 2.16: The saturation and pressure changes occur at the aquifer's mid-point obtained from the simulation. For this example, M°=0.1 and the constant rate constraint is assigned to the injector. There are two points at which the slope of pressure curve changes but only one of them (at 5450 days) is coupled with the saturation shock.

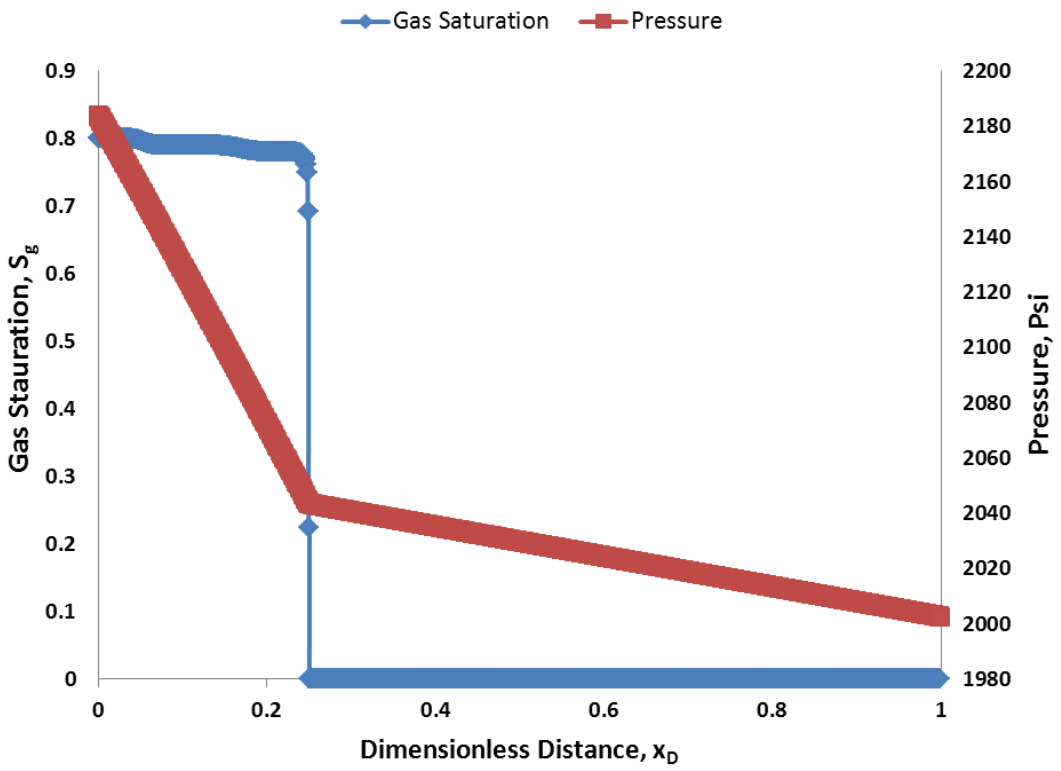

Figure 2.17: The changes in saturation and pressure as a function of distance (normalized by the length of the aquifer) depicted at 9500 days (obtained from the simulation). For this example, the constant rate constraint is assigned to the injector and M° = 0.1. Note that only one saturation shock occurs. The saturation of the gas front occurs at 0.78 (which is located at x_D=0.25).

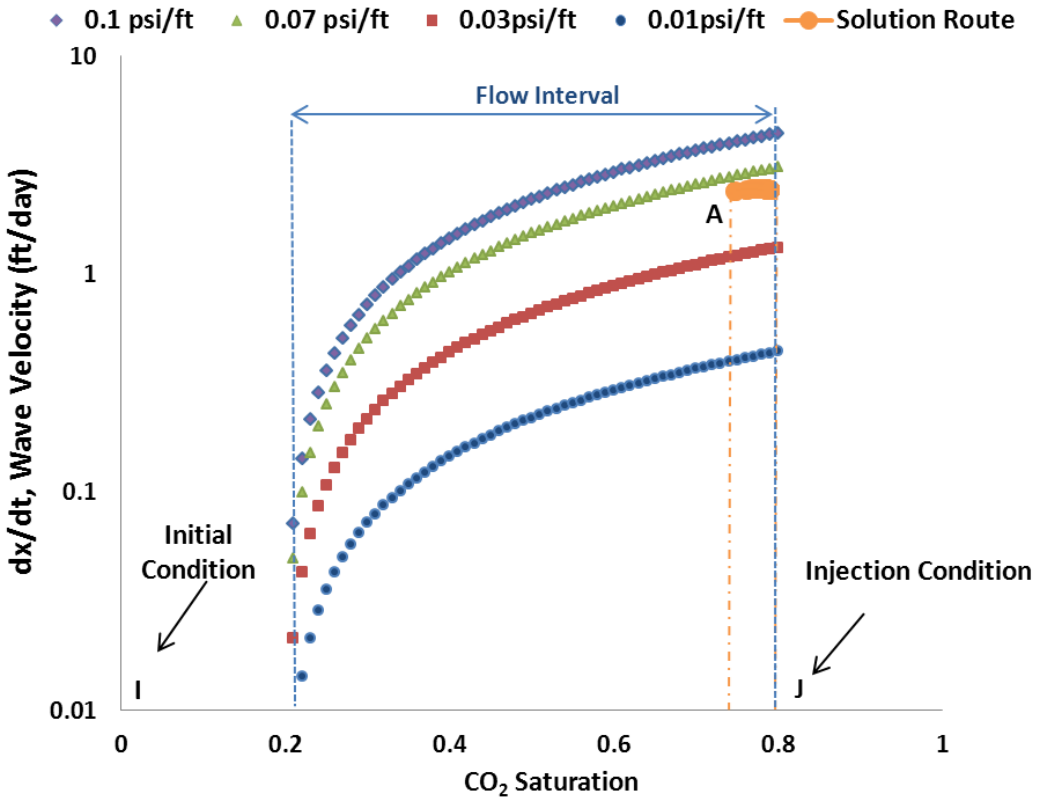

Figure 2.18: Solution route obtained semi-analytically from Eq. (2.72) when the injector is assigned a constant rate. The pressure gradient at each location is obtained from the simulation and is incorporated into Eq. (2.72). The solution consists of a shock between I and point A followed by spreading waves connecting A to J along the orange curve. Note that saturation residuals are 0.2. The wave velocity along the solution route decreases monotonically from I to J. For this example, the constant rate constraint is assigned to the injector and M°=0.1. Therefore, pressure gradients are small in general.

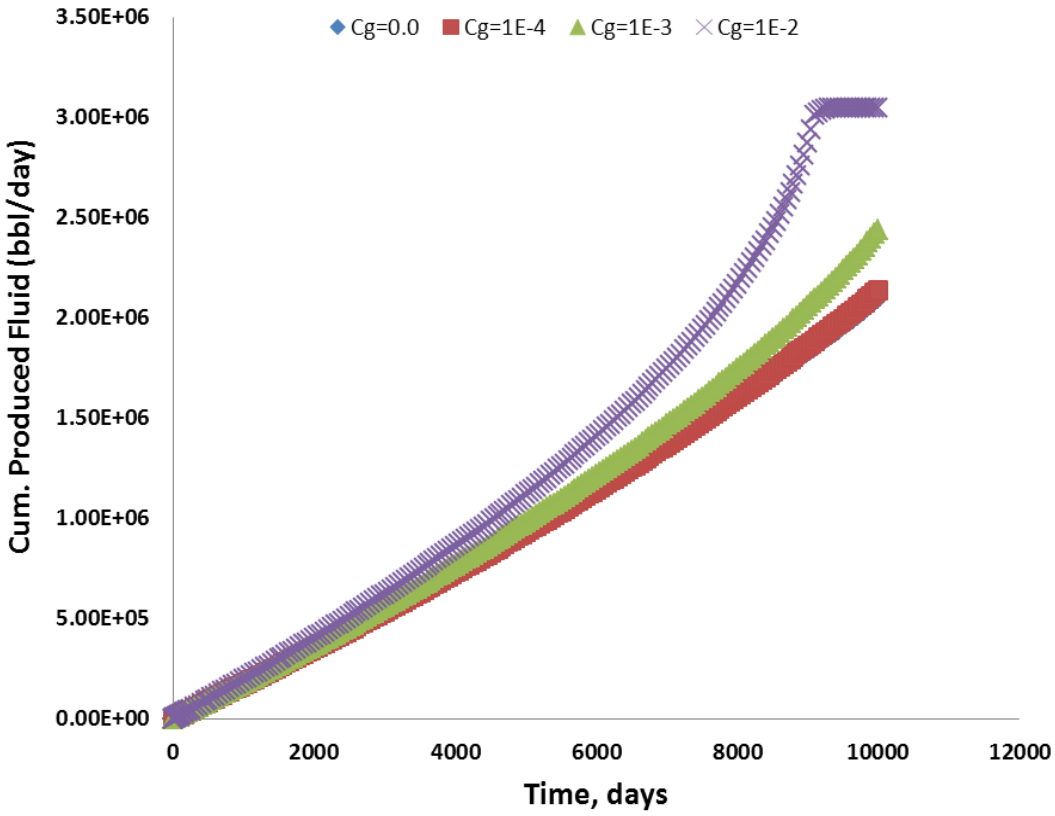

Figure 2.19: Cumulative volume of the produced water as a function of time for cases with different fluid compressibility values of 0.0001, 0.001, 0.01 and zero (incompressible). Curves representing the fluid compressibility of 0.0001 and incompressible fluid coincide.

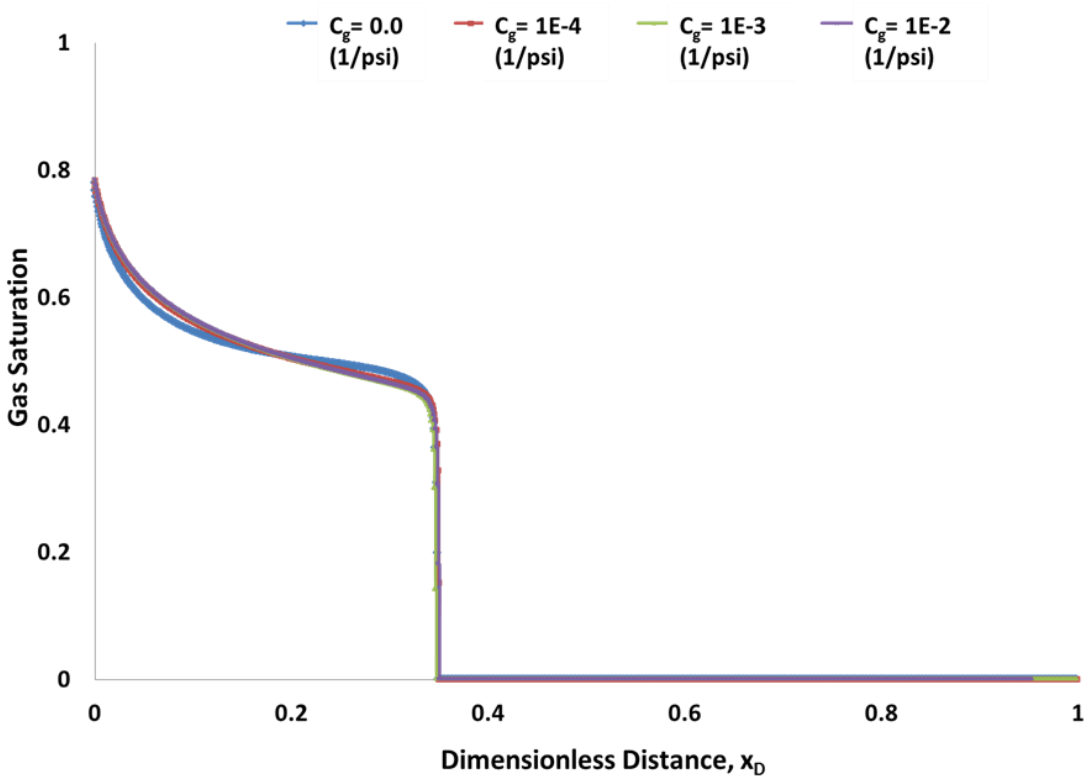

Figure 2.20: Saturation profiles depicted at the corresponding time to production of 1E+6 barrels of water. All curves coincide showing that fluid compressibility is no longer a factor to determine the wave velocity in the absence of rock compressibility.

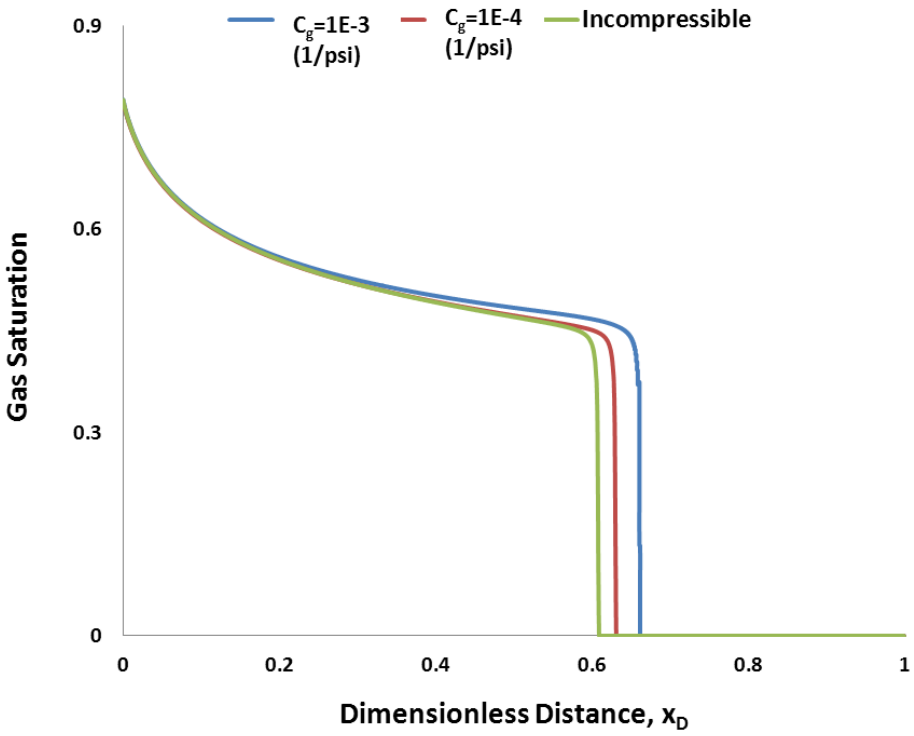

Figure 2.21: Saturation profiles depicted at the corresponding time to production of 2E+6 barrels of water. Note that despite Figure 2.20, saturation profiles do not coincide as (in this example) the rock compressibility is in the same order of the gas compressibility; hence, different values of the gas compressibility yield different wave velocities as the compressibility terms are not dropped from Eq. (2.72). The rock compressibility is 0.00001 (1/psi). However, the green curve shows the case in which no compressibility involved.

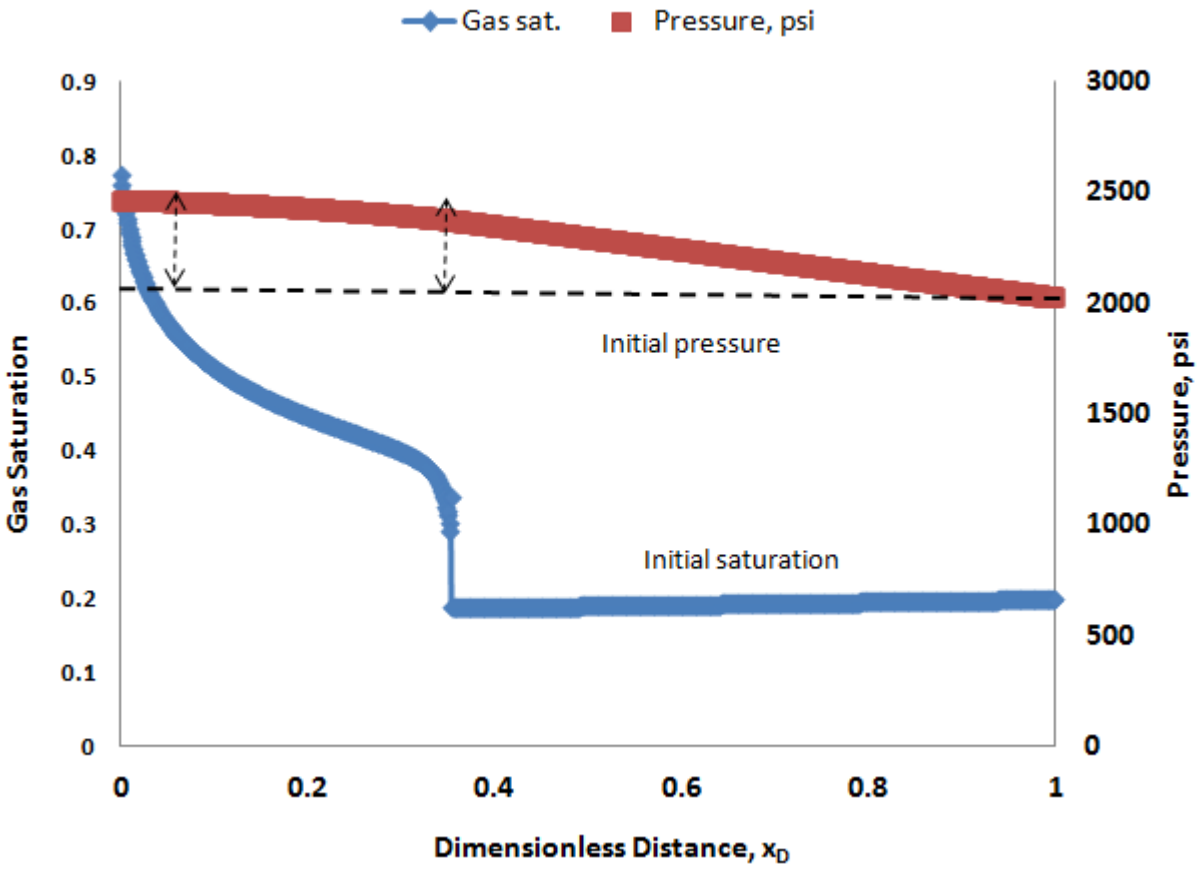

Figure 2.22: The changes in saturation and pressure as a function of distance (normalized by the aquifer length) depicted at 5000 days obtained from the simulation. For this example, the constant rate constraint is assigned to the injector, initial gas saturation is 0.2, and M°=10. Two saturation shocks are observed: a leading shock accompanied by the pressure change and a trailing shock with zero velocity connecting the gas saturation of 0.8 to 0.75. The saturation of the leading front occurs at 0.34 (located at x_D=0.36) accompanied by the pressure shock.

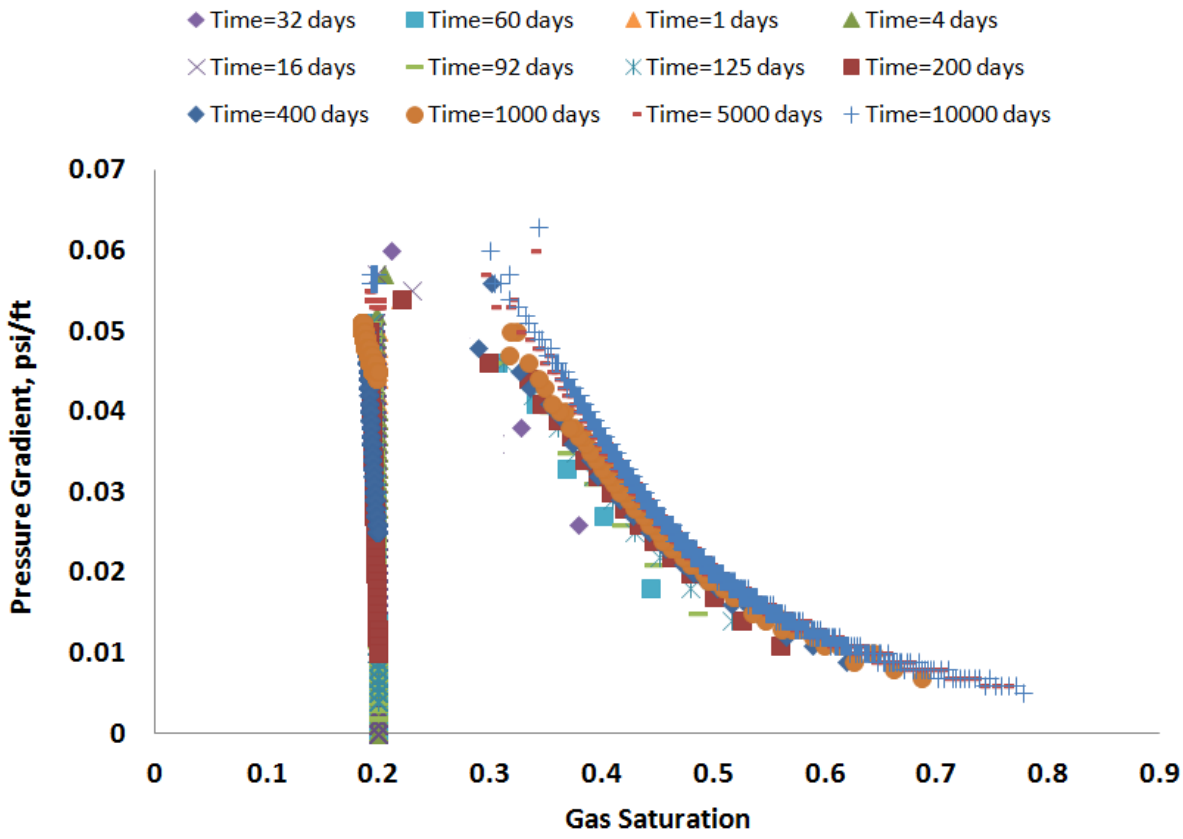

Figure 2.23: Pressure gradient as a function of saturation obtained from simulation when initial gas saturation is 0.2 (S_g =0.2). Similar behavior Figure (2.10) is observed : at early stage of displacement, fast pressure waves occur along which only pressure disturbance is traveling. These fast pressure waves are followed by slow pressure waves that are associated with the change in saturation. For this example, the constant rate constraint is assigned to the injector and M°=10.

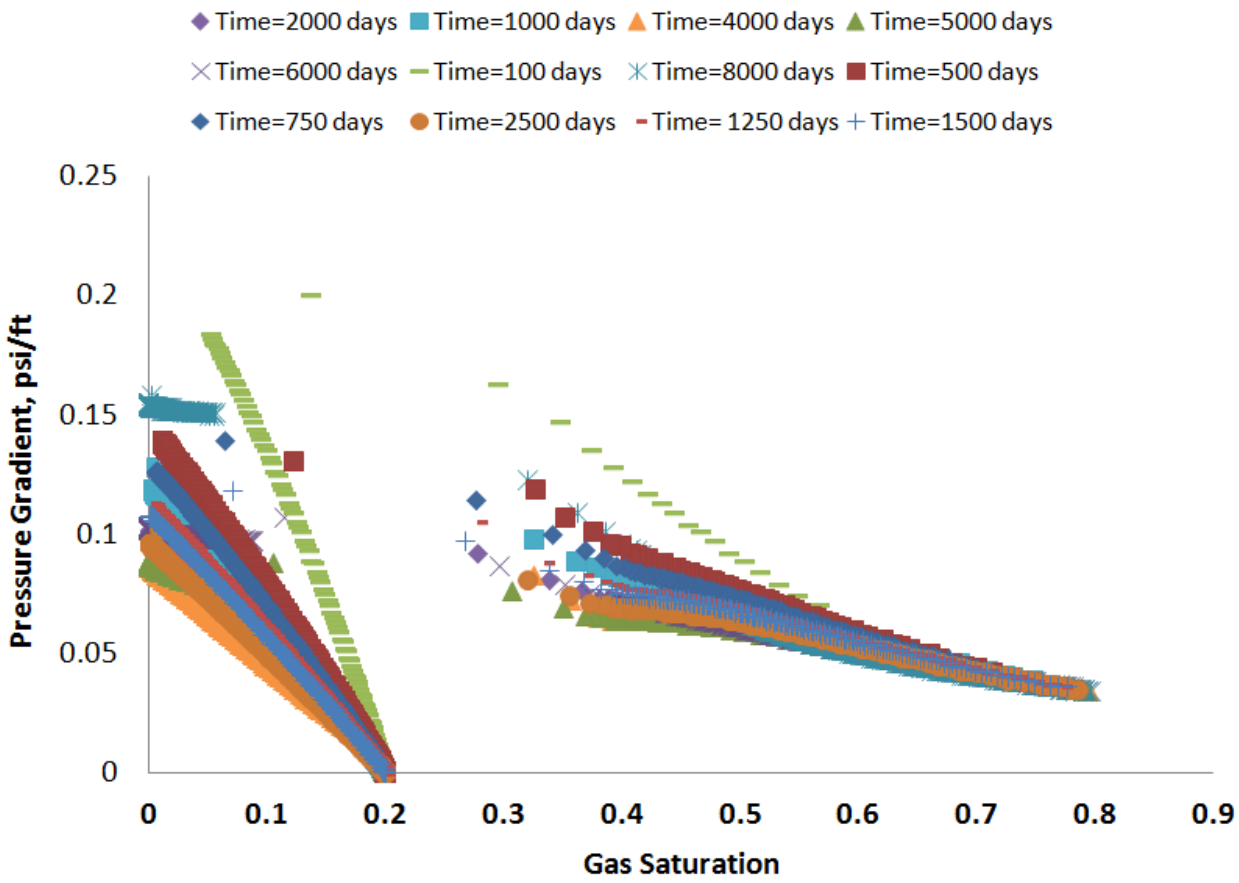

Figure 2.24: Pressure gradient as a function of saturation obtained from simulation when initial gas saturation is 0.2 (S_g =0.2) and the compressibility of gas is 100 times greater than CO_2. Despite Figure (2.23), fast pressure waves reduce the initial gas saturation (as a result of large gas compressibility and more sensitivity to pressure drop) as it travels along the length of the aquifer. These fast pressure waves are followed by slow pressure waves that are similar to those in Figure (2.23). However, the gas saturation vanishes downstream of the slow pressure waves because of the large gas compressibility in this example. For this example, the constant rate constraint is assigned to the injector and M°=10.

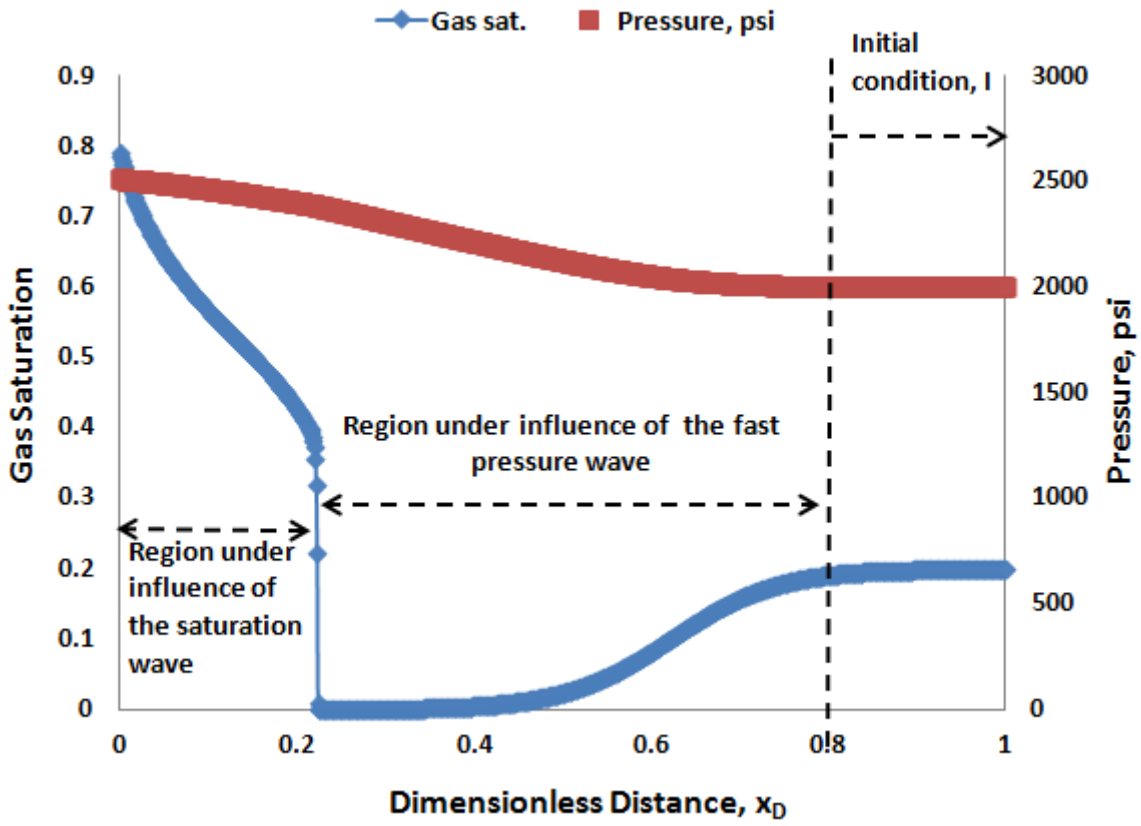

Figure 2.25: The changes in saturation and pressure as a function of distance (normalized by the aquifer length) depicted at 2500 days obtained from the simulation. For this example, the constant rate constraint is assigned to the injector, initial gas saturation is 0.2, the gas compressibility is two orders of magnitude greater than CO_2, and M°=10. Three distinct regions are identified (1): initial condition, where pressure and saturation occur at their original values; (2) region under influence of the fast pressure waves, where the gas saturation decreases because of the applied pressure disturbance; and (3) Buckley and Leverett solution. The saturation of the leading front occurs at 0.39 (located at x_D=0.23) accompanied by the slow pressure wave.

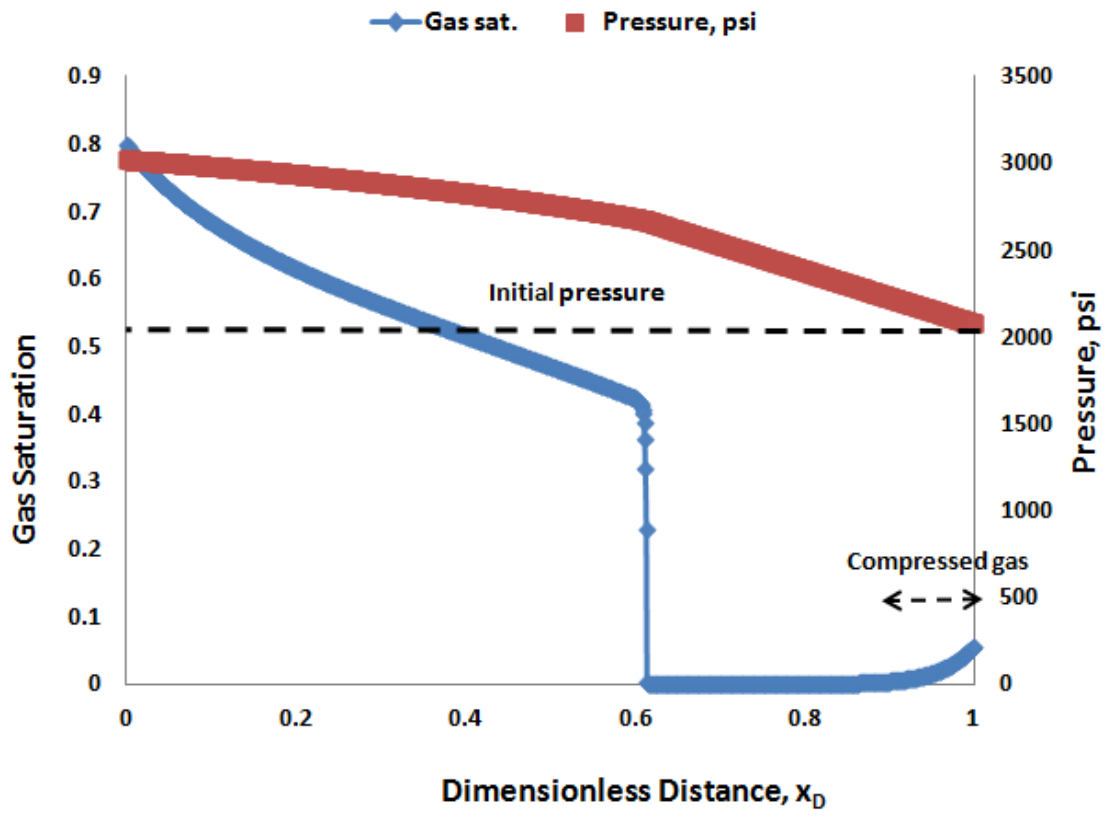

Figure 2.26: The changes in saturation and pressure as a function of distance (normalized by the aquifer length) depicted at 8000 days obtained from the simulation. For this example, the constant rate constraint is assigned to the injector, initial gas saturation is 0.2, the gas compressibility is two orders of magnitude greater than CO_2, and M°=10. Fast pressure waves have reached upon the aquifer's outlet boundary and, hence, no initial condition is realized. Because of the large gas compressibility, the initial gas have been pushed toward the producer by the fast pressure wave. The saturation of the leading front occurs at 0.39 (located at x_D=0.63) accompanied by the slow pressure wave.

Chapter 3: Applying Fractional Flow Theory to Determine the CO_2 Storage Capacity of an Aquifer

In this chapter, fractional flow theory is used to determine the CO_2 storage capacity of an aquifer. Capillary snap-off and dissolution into the aqueous phase are two major trapping mechanisms of the CO_2 sequestration in intermediate time-scales (Juanes *et. al* 2010).

In practice, numerical simulations are used to assess the storage capacity of a geological formation and to evaluate various trapping mechanisms; however, the simulations are complex and time-consuming as the mechanisms act simultaneously with various rates on different time-scales. Furthermore, these simulations require detailed inputs and, hence, are limited to site-specific studies.

We adopt the notion of the optimal solvent-water-slug size (see Chapter 4) and use the graphical solution of multiple geochemical front propagation and fractional flow theory developed by Noh *et. al* (2007) to determine the CO_2 storage capacity. In this work, the storage capacity is limited to capillary snap-off and dissolution trapping mechanisms. The optimal slug size should represent the CO_2 storage capacity of the aquifer as injecting larger slugs causes the CO_2 to breakthrough at the distant boundary and injecting smaller slugs leaves the aquifer unfilled. These cases represent overcapacity and under-capacity storage, respectively. We use numerical simulation to verify the accuracy of the predicted optimal slug size and simulation results confirm the accuracy of the predicted values.

In practice, the proposed method provides an efficient screening method to assess the CO_2 storage capacity of aquifers. Moreover, it significantly reduces the simulation costs while providing useful insight.

3.1 INTRODUCTION

CO_2 capture and geological storage (CCGS) is a promising method for long-term storage of CO_2 to mitigate its accumulation in the atmosphere and, thus, detrimental impacts on the climate. However, a general lack of knowledge about storage capacity of deep saline aquifers stands in the way of an immediate full-scale implementation of CCGS (IPCC, 2005; Bradshaw *et al.,* 2007). In this study, we focus on the storage capacity of saline aquifers as they are widely distributed (Bachu *et al*., 1994).

The evaluation of the CO_2 storage capacity in deep saline aquifers is very complex as there are multiple trapping mechanisms acting simultaneously at different rates. In the context of CO_2 storage in aquifers, the involved trapping mechanisms are:

1. Structural (hydrodynamic) trapping, where the upward migrating buoyant CO_2 is suppressed by an impermeable cap rock (Bachu *et al*., 1994)
2. Capillary snap-off trapping, where injected CO_2 breaks up into immobile ganglia (Kumar *et al*., 2005; Juanes *et al.,* 2006)
3. Solubility trapping, where CO_2 dissolution occurs in the resident aqueous phase (Ennis-King and Paterson, 2005; Riaz *et al*., 2006)
4. Mineral trapping, where dissolved CO_2 reacts with rock minerals and yields carbonate mineral precipitation (Gunter *et al.,* 1997)

5. Local capillary trapping, where upward migrating CO_2 is accumulated beneath a region with a higher capillary entry pressure than average (Saadatpoor *et al.*, 2010)

This study focuses on two trapping mechanisms that are likely to be effective on an intermediate time-scale: capillary snap-off and dissolution trapping (Sifuentes *et al.*, 2009; Juanes *et al.*, 2010). Injected CO_2 in an aquifer displaces the resident water under a drainage mechanism (assuming the gas phase is non-wetting), while resident or post-injection water displaces CO_2 through an imbibition process. The hysteresis in gas relative permeability that manifests the snap-off trapping mechanism occurs at the pore-scale. In addition, CO_2 dissolves into brine at any contact between the aqueous and gas phases.

Numerical simulations calculate the CO_2 capacity with reasonable accuracy; however, large scale simulations are time-consuming as they require detailed geological information about the aquifer. Szulczewski *et al.* (2009) introduced an analytical model to predict the basin-scale CO_2 storage capacity of an aquifer while considering gravity override and capillary trapping; however, their model does not account for the solubility of CO_2 in the brine nor mineral trapping.

We adopt the notion of the optimal solvent-water slug size and use the graphical solution of combined geochemical front propagation and fractional flow theories (Noh *et al.*, 2007) to define the CO_2 storage capacity of aquifers. According to Walsh and Lake (1989), the optimal solvent slug size expressed in total pore volume (P.V.), occurs when

the fastest waves of the chase water (the imbibition front in our study) and injected CO_2 (drainage front) coincide at the outlet boundary (distant boundary of the aquifer).

The objective of this study is to determine the largest (optimal) slug of CO_2 such that no CO_2 breakthrough occurs while the aquifer is filled to its capacity. Hence, all other slug sizes are unfavorable except the optimal as they either yield over- or under-capacity conditions. Hence, the optimal slug size represents the CO_2 storage capacity of the aquifer because of capillary and dissolution mechanisms. To verify the analytical solution, we compare the analytical and the simulation results.

3.2 DESCRIPTION

We study a pair of consecutive displacements: injection of CO_2 into an aquifer to displace resident water (drainage process) followed by injection of post-flood aqueous phase to displace CO_2 (imbibition process). These processes are studied under the following assumptions, of which most are common in the fractional flow theory:

1. The flow is one-dimensional (1D) governed by Darcy's law for multiphase flow.
2. Large-scale capillary effects associated to the flow (appeared in the mass conservation equation) and dispersion are negligible, *i.e.*, conservation of an individual component leads to a first-order strictly hyperbolic partial differential equation. However, local-scale capillary effect because of the snap-off process is modeled using relative permeability hysteresis.
3. The fractional flow of each phase does not depend on a position other than through a saturation change.

4. There are two flowing phases (the aqueous and non-aqueous phase).
5. Mixing in the fluid phases is ideal, *i.e.*, we assume constant partial molar volume and no change in total volume upon mixing and transfer of components from one phase to another.
6. Fluid viscosities, aquifer pore space, and densities are independent of pressure. Relative permeabilities are monotonic and differentiable with respect to saturation.
7. Local-equilibrium applies.
8. Neither sorption nor any chemical reaction occurs.
9. Injected CO_2 is saturated with the brine, *i.e.*, no water vaporization occurs.

Figure 3.1 shows a schematic of a typical gas saturation profile for a brine displacing CO_2 as followed by an imbibition displacement. If unsaturated CO_2 is injected, the residual water around the injection well is vaporized into the gaseous phase. Eventually, if the injection lasts long enough, region J (dry region) develops (Zuluaga, 2008).

3.3 MATHEMATICAL MODEL

The governing equations are the material balances for each component *i*:

$$\frac{\partial C_i}{\partial t_D} + \frac{\partial F_i}{\partial x_D} = 0, \tag{3.1}$$

where C_i and F_i represent the cumulative storage and flux capacities, respectively. Furthermore, t_D, dimensionless time, is the amount of injected fluid expressed in pore volumes and x_D is the dimensionless distance normalized by the length of the aquifer.

For our specific case, the overall composition and fractional flux of CO_2 are

$$\begin{cases} C_{CO_2} = S_g C_{CO_2,g} + S_{aq.} C_{CO_2,g} \\ F_{CO_2} = f_g C_{CO_2,g} + f_{aq.} C_{CO_2,g} \end{cases} . \tag{3.2}$$

Using the method of characteristics, Noh *et al.* (2007) derived an analytical solution for 1D, two-phase, semi-miscible displacement. In their solution, CO_2 displacing water and vice versa are considered as semi-miscible displacements, because of the substantial solubility of CO_2 and water in the aqueous and gaseous phases, respectively. The solution occurs in the form of spreading or sharpening waves; for step-change boundary conditions the sharpening waves is also known as shock (Figure 3.1). The drainage part of the gas saturation profile (between regions I and J) consists of two shocks: at the leading edge between I and II and at the trailing edge between J and II; a series of spreading waves connect the two shocks. During drainage, the gaseous phase displaces the resident brine while CO_2 dissolves into the brine (semi-miscible). The specific velocity of the leading shock (fastest wave of the injected CO_2) is obtained as (Noh *et al.*, 2007):

$$\frac{x_D}{t_D} = v_{CS} = \frac{f_g^- - \overbrace{\left[\frac{C^{II}_{CO_2,aq}}{C^{II}_{CO_2,aq} - C^{II}_{CO_2,g}}\right]}^{D_{I\to II}}}{S_g^- - \left[\frac{C^{II}_{CO_2,aq}}{C^{II}_{CO_2,aq} - C^{II}_{CO_2,g}}\right]} . \tag{3.3}$$

The fractional flux of the gaseous phase is defined as

$$f_g = \frac{1 + N_g k}{1 + \frac{k_{raq.}}{k_{rg}} \frac{\mu_g}{\mu_{aq.}}}, \tag{3.4}$$

where N_g is the buoyancy number.The buoyancy number is the ratio of gravity to viscous forces defined as:

$$N_g = \frac{k_{raq.}(\rho_w - \rho_g) g \sin\alpha}{\mu_{aq} u_{inj.}} \tag{3.5}$$

In this study, we use the end-point buoyancy number; *i.e*. the end-point relative permeability value is used in Eq. (3.5). For horizontal displacements where N_g is zero, the graphical interpretation of Eq. (3.5) is a tangent line emanating from the retardation point $(D_{I\to II}, D_{I\to II})$ to the drainage fractional flow curve (Figure 3.2).

The imbibition displacement is extended between two shocks: a leading and a trailing shock. Note that we distinguish between drainage and imbibition displacements through hysteresis between the relative permeability curves. As ground water flow or post-flood injected water displaces the plume of CO_2, a leading shock separates region J from III and a trailing shock occurs between III and K (Figure 3.1). However, we discard region J as the injected gas is saturated with repect to water (assumption 9). Furthermore, we replace region II with a sharpening wave associated with the average saturation of gas behind the CO_2 front ($S^{II}_{g|Ave.}$). In other words, we assume an analogous constant-state region (Lake 1989) with saturation equal to the $S^{II}_{g|Ave}$ downstream of the imbibition displacement. Therefore, the shock between region III and the surrogate constant-state region represents the fastest sharpening wave of the imbibition. The specific velocity of

the imbibition front (v_{Cw}) is the slope of the tangent line emanating from $S^{II}_{g|Ave}$ located on the imbibition fractional flow curve (Figure 3.2).

Figure 3.3 shows the typical form of the method of characteristics (MOC) solution when CO_2 displacing water is followed by an aqueous phase. The slope of each line on the distance-time diagram is the specific velocity of the concentration attributed to that wave.

Based on the location where the fastest wave of chase water intersects the fastest wave of the injected CO_2, three possibilities exist. Figure 3.4 indicates an over-capacity condition in which the imbibition front with specific velocity of ν_{cw} intersects the drainage front with the velocity of ν_{cs} beyond the aquifer length. In other words, the imbibition front does not catch-up to the fastest drainage wave within the aquifer length; there is more CO_2 injected than the aquifer CO_2 capacity.

Figure 3.5 shows the optimal condition that takes place when the two shocks coincide at the outlet, *i.e.*, they breakthrough simultaneously. The dimensionless optimal CO_2 slug size is then calculated as

$$t_{DS} = \frac{1}{\nu_{cs}} - \frac{1}{\nu_{cw}}. \qquad (3.6)$$

The suggested CO_2 slug size is expressed as the fraction of the aquifer P.V.; it can also be interpreted as the storage efficiency defined by Bachu *et al.* (2007). When fractional flow solution of a displacement only consists of a single shock (so called piston-like displacement), the dimensionless optimal slug size will be approximately equal to the uniform gas saturation behind the front; ν_{cw} is ususally much larger than ν_{cs} implying that

imbibition shock travels fatser than the drainage front; hence, the second term in Eq. (3.6) becomes negligible compared to the first term. Furtheremore, v_{cs} can be expressed as:

$$v_{cs} = \frac{f^{upstream} - f^{downstream}}{S^{upstream} - S^{downstream}} = \frac{1-0}{S^{upstream} - 0}. \quad (3.7)$$

Substitution of Eq. (3.7) into Eq.(3.6) yields that the dimensionless optimal slug size will be approximately equal to the uniform gas saturation behind the front ($S^{upstream}$) for a piston-like displacement.

Figure 3.6 illustrates an under-capacity condition for which the imbibition front catches up with the fastest drainage shock within the aquifer length; hence, part of the aquifer remains unfilled.

In addition, the injected CO_2 has a lower density compared to the resident brine and tends to migrate upward; hence, displacement of the resident brine often occurs along a path deviated from the horizontal direction and, consequently, a non-zero buoyancy number is often required in Eq.(3.4). The graphical procedure to determine the specific velocity of the drainage front in non-horizontal displacements differs from the horizontal displacement as sufficiently large buoyancy numbers (slowly upward migration of CO_2) are characterized by gas fractional flows greater than unity (Figure 3.7). Therefore, the graphical solution may involve no tangent lines as they would lead to non-physical results. The physical explanation of gas fractional flows greater than unity is countercurrent flow that would occur under certain initial and injection conditions. For more details on modeling the gravity-dominated flow in a permeable medium, see Walsh (1991).

For sufficiently large buoyancy numbers, the gas fractional flow curve intersects the line representing $f_g = 1$ at two points with different saturations; hence, a uniform CO_2 saturation occurs behind the drainage front that represents the lower saturation. Following from Walsh (1991), the uniform saturation behind the front is determined from Eq.(3.4) for f_g=1.0:

$$1+\frac{k_{raq.}}{k_{rg}}\frac{\mu_g}{\mu_{aq.}}=1+N_g k \ . \tag{3.8}$$

Substitution of Eq. (3.5) into Eq. (3.8) gives

$$k_{rg}=\frac{u_{inj.}\mu_g}{k(\rho_w-\rho_g)g\sin\alpha}, \tag{3.9}$$

$$S_g^{upstream}=k_{rg}^{-1}\left(\frac{u_{inj.}\mu_g}{k(\rho_w-\rho_g)g\sin\alpha}\right). \tag{3.10}$$

From Eqs. (3.9) and (3.10), the gas relative permeability value and the corresponding uniform gas saturation behind the front is obtained for cases with extremely large buoyancy numbers. The specific velocity of the drainage front is equal to the slope of a line connecting the retardation point and $S_g^{upstream}$.

3.4 SIMULATION APPROACH

To verify the analytical solution, we perform a set of 1D displacement simulations and present the comparison between the results. There are 256 equal grid blocks in the *x*-direction.

Figure 3.8 shows the relative permeability functions used in the simulations. As it was mentioned earlier, local capillary effect is represented by dissimilar relative

permeability curves for drainage and imbibition displacements. Furthermore, the porosity and the permeability of all models are 0.15 and 500 md, respectively. All simulation models are initially fully saturated with brine; the outlet of the models is maintained at constant bottomhole pressure of 2300 psi representing the pressure support. However, the injection well (for both CO_2 and the post-flood displacements) is assigned a constant rate constraint.

The temperature and the salinity of the base case model are 130˚F and 5000 ppm, respectively. The PVT properties of gas and brine (density, viscosity, solubility, and the gas compressibility factor *z*) are calculated internally in the numerical simulator by the Peng-Robinson equation-of-state. The viscosity of brine and CO_2 is 0.517 and 0.052 cp, respectively.

For the base case model and a retardation factor of -1.03, a specific velocity of 0.196 is obtained through emanating a tangent line to the gas fractional flow curve. The tangent line intersects the gas fractional flow curve at S_g=0.42; however, the specific velocity of the imbibition front is obtained through extending a line from (0.52, 0.92) to (0.29, 0.06); the specific velocity of the imbibition front becomes 3.55 in this example (Figure 3.2).

The CO_2 storage capacity of the aquifer is 0.226 of the aquifer P.V. from Eq.(3.6). Under such circumstances, the drainage and the imbibition shocks collide at the outlet. In the simulations, this situation is translated into the maximal injected CO_2 slug expressed in terms of the aquifer P.V. that yields no CO_2 produced at the outlet.

Figure 3.9 illustrates the gas saturation profiles obtained by the simulations for three cases: (1) under capacity, (2) over capacity, and (3) optimum at the specified time. The injected CO_2 is spanned over the entire aquifer owing to the capillary snap-off and the dissolution trapping mechanisms while neither is produced at the optimal condition. For the under-capacity case, a relatively small amount of CO_2 is spanned over the entire length of the aquifer and is entirely trapped. Figure 3.10 confirms that the CO_2 slug size of 0.225 is the largest that yields no free gas at the outlet consistent with the value obtained from Eq.(3.6).

Tables 3.1 through 3.3 list the results of the sensitivity analysis conducted to study the effects of different water salinities, aquifer pressure, and temperatures on the CO_2 storage capacity. The storage capacity varies by changing the CO_2 solubility as observed in previous studies (Kumar *et al.*, 2005). The solubility increases by decreasing the salinity of the aqueous phase and by increasing the aquifer pressure and temperature. However, the solubility trapping is slow and time-dependent as it is a function of the amount of mixing that occurs between the free-gas and the CO_2-unsaturated aqueous phase; therefore, it contributes less in the early stage of the CO_2 sequestration (less than 10% in this study).

Next, we investigate the effect of buoyancy on the storage capacity of vertically gravity-dominated displacements. We use the base case model tilted 90 degree such that the injection well is located at the bottom and the outlet at the top. Smaller injection rates than that of the base case model is used to study gravity-dominated displacements. Figure 3.11 indicates the CO_2 storage capacity as a function of the buoyancy number. The

capacity decreases as the buoyancy number increases consistent with the simulation results obtained by Ide *et al.* (2007). The results imply that greater gas saturation during the drainage process (smaller buoyancy number) yields larger trapped gas after imbibition displacement (Figure 3.12). The simulation results confirm the storage capacities obtained from the graphical procedure.

3.5 CONCLUSIONS

The main outcome of the analytical developments presented here is a procedure that predicts the CO_2 storage capacity of aquifers owing to capillary snap-off and dissolution:

- The predicted CO_2 storage capacity of a saline formation obtained from the fractional flow theory is consistent with the simulation results.
- The simplicity of the analytical solution yields an efficient and quick method to investigate the impact of uncertainty in the parameters (such as the gas solubility and various levels of hysteresis) on the CO_2 storage capacity.
- Using the proposed graphical solution provides a dimensionless CO_2 storage capacity with respect to the size of the closed aquifers; this overcomes the scale-dependency of the previous solution as addressed by Juanes (2010).

3.6 NOMENCLATURE

N_g= buoyancy number

ppm= parts per million

$D_{I \rightarrow II}$ = retardation factor

F_i= overall flux of component *i*

f_j= fractional flow of phase *j*

C_i= overall concentration of component *i*

S_j= saturation of the phase *j*

t_D= dimensionless time; injected volume expressed in the aquifer P.V.

U_{inj}=injection volumetric rate (ft^3/d)

t_{Ds}= CO_2 slug size expressed in the aquifer P.V.

v_{Cw}= the specific velocity of the imbibition front

v_{CS}= the specific velocity of the drainage front

S_g^{II} =the gas saturation behind the gas front

μ_j= the viscosity of phase *i* (cp)

ρ_j= the mass density of phase j (lb/ft^3)

g=standard gravity constant (32.174 ft/s^2)

α=aquifer dip angle

k= permeability (md)

k_{rj}=the relative permeability of phase *j*

x_D= dimensionless distance

SUBSCRIPTS

aq= the aqueous phase

g= the gaseous phase

SUPERSCRIPTS

-= upstream

+= downstream

Table 3.1- Sensitivity analysis on the salinity of the brine

Brine salinity, ppm	Retardation factor	CO_2 storage capacity	CO_2 mole fraction in aqueous phase
1000	-1.032	0.225	0.021
5000	-1.033	0.225	0.021
10000	-1.035	0.225	0.020
20000	-1.039	0.223	0.020
30000	-1.042	0.223	0.019
40000	-1.044	0.223	0.018
50000	-1.045	0.223	0.018

Table 3.2- Sensitivity analysis on the aquifer pressure; T=130 °F

Aquifer pressure, psi	Retardation factor	CO_2 storage capacity	CO_2 mole fraction in the aqueous phase	μ_{CO2}, cp
1600	-1.028	0.21	0.019	0.040
2000	-1.032	0.223	0.021	0.046
2600	-1.033	0.225	0.021	0.051
3000	-1.042	0.23	0.022	0.063
3500	-1.048	0.235	0.023	0.069

Table 3.3- Sensitivity analysis on the aquifer temperature

Aquifer temperature, ˚F	Retardation point	Co_2 storage capacity	CO_2 mole fraction in the aqueous phase	μ_{CO2}, cp
100	-1.041	0.235	0.024	0.067
110	-1.041	0.23	0.023	0.062
120	-1.040	0.227	0.022	0.056
130	-1.033	0.225	0.021	0.051
140	-1.031	0.225	0.021	0.049
150	-1.029	0.223	0.020	0.044

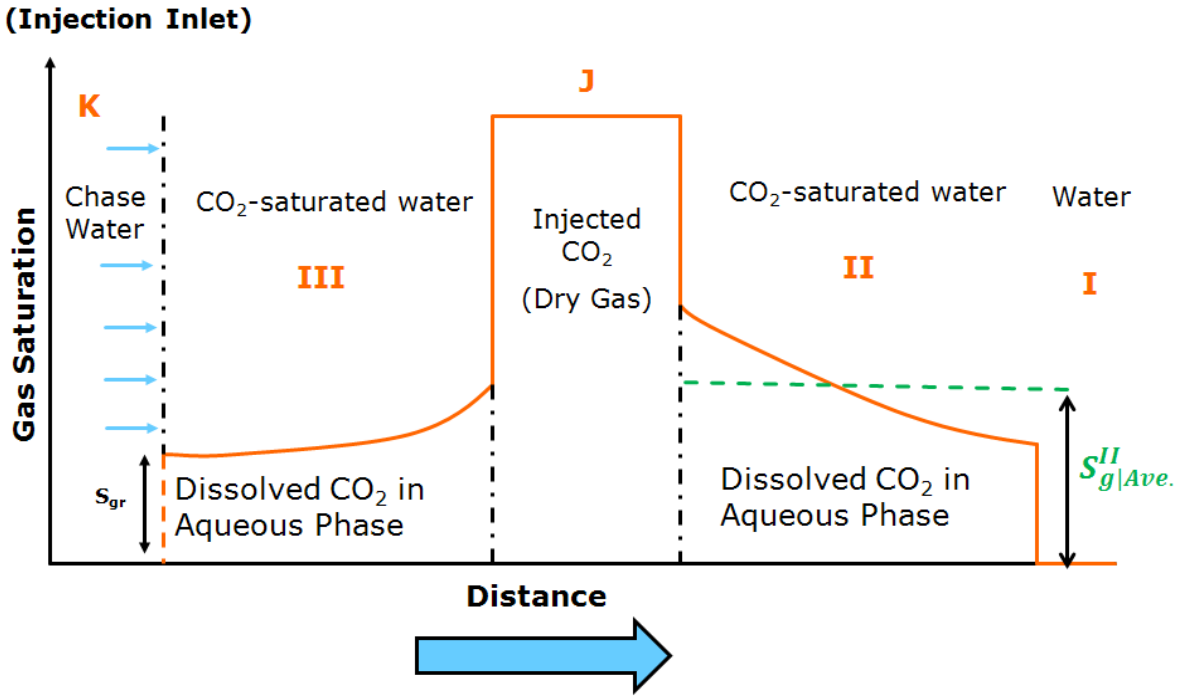

Figure 3.1: Schematic of the gas saturation profile in a set of semi-miscible displacements where injected CO_2 is followed by an aqueous phase. Five distinct regions occur at the early stage of the displacement: (1) region I is the initial condition with 100% water saturation; (2) part II is a drainage semi-miscible displacement, where a gaseous phase displaces an aqueous phase with the mutual solubility of CO_2 and water; (3) section J is the CO_2 injection condition; (4) part III is similar to region II, but is an imbibition displacement of a gaseous phase displaced by an aqueous phase; (5) K illustrates the post-CO_2 water injection that represents an imbibition displacement. The imbibition displacement occurs because of either water injection or regional ground flow that pushes the CO_2 slug further into the aquifer. $S^{II}g|_{Ave}$ represents the average gas saturation of region II.

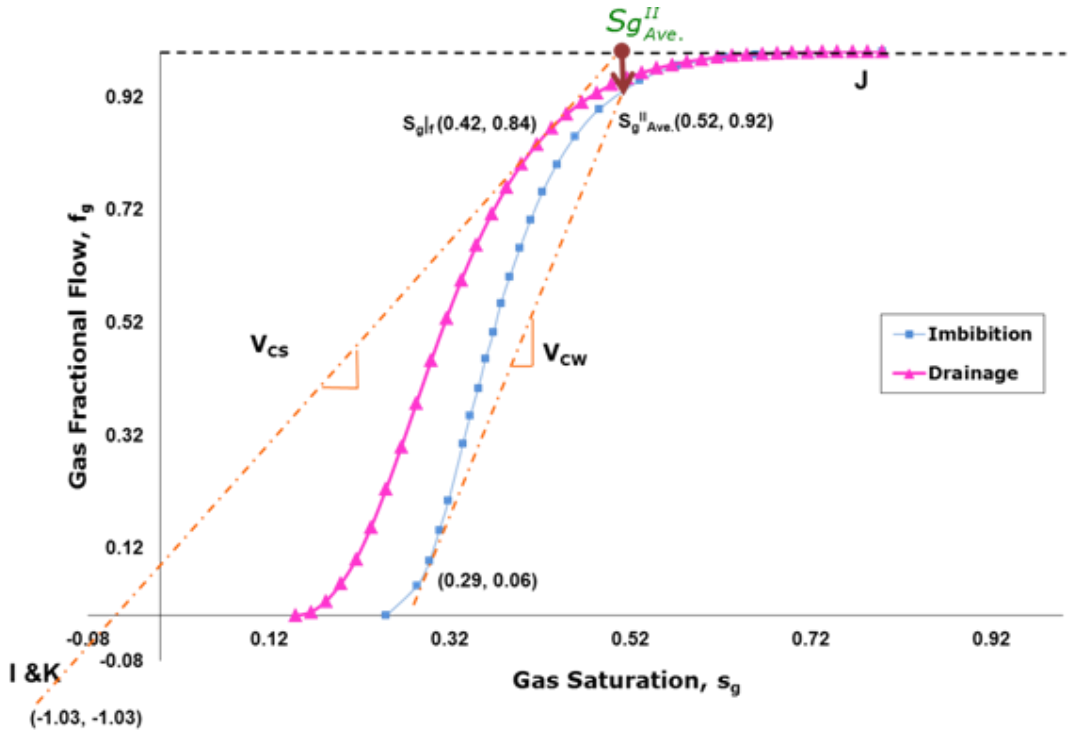

Figure 3.2: Graphical procedure to predict the CO_2 storage capacity of the aquifer. The slope of a tangent-line emanating from the retardation point (f_w, S_w)=(-1.03,-1.03) to the drainage fractional flow curve of the gaseous phase is V_{cs} and the slope of the tangent line is from $S^{II}_{g|Ave.}$ to the imbibition curve determines V_{cw}; note that the retardation point is located on the extension of the tangent line and has not been illustrated in this plot. Using Eq. (3.6), only 0.226 of the aquifer P.V. will be occupied by the trapped CO_2; trapped CO_2 occurs in the form of the capillary residual (snap-off) and dissolution trapping.

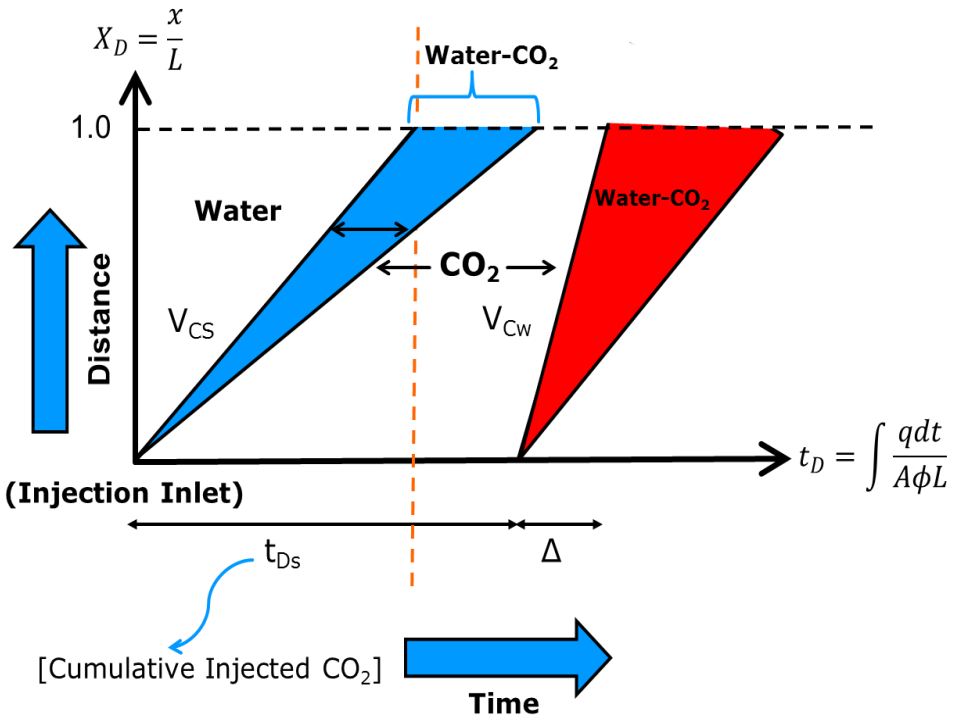

Figure 3.3: Typical form of the method of characteristics (MOC) solution when CO_2 displacing water is followed by an aqueous phase. The slope of each line on the distance-time diagram is the specific velocity of the concentration attributed to that wave.

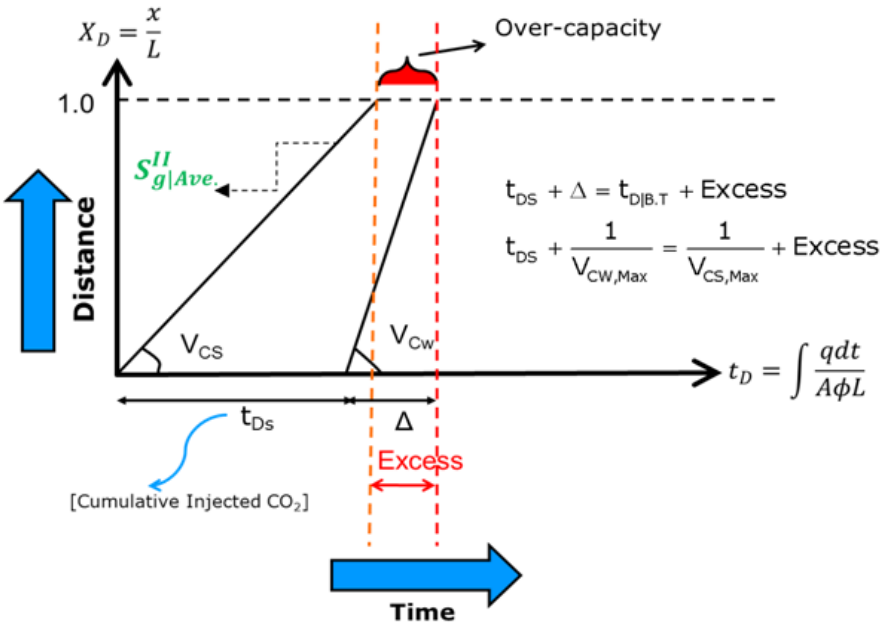

Figure 3.4: Over-capacity condition: the imbibition front with specific velocity of ν_{cw} intersects the drainage front with the velocity of ν_{cs} beyond the aquifer length. In other words, the imbibition front does not catch-up to the fastest drainage wave; there is more CO_2 injected than the aquifer capacity.

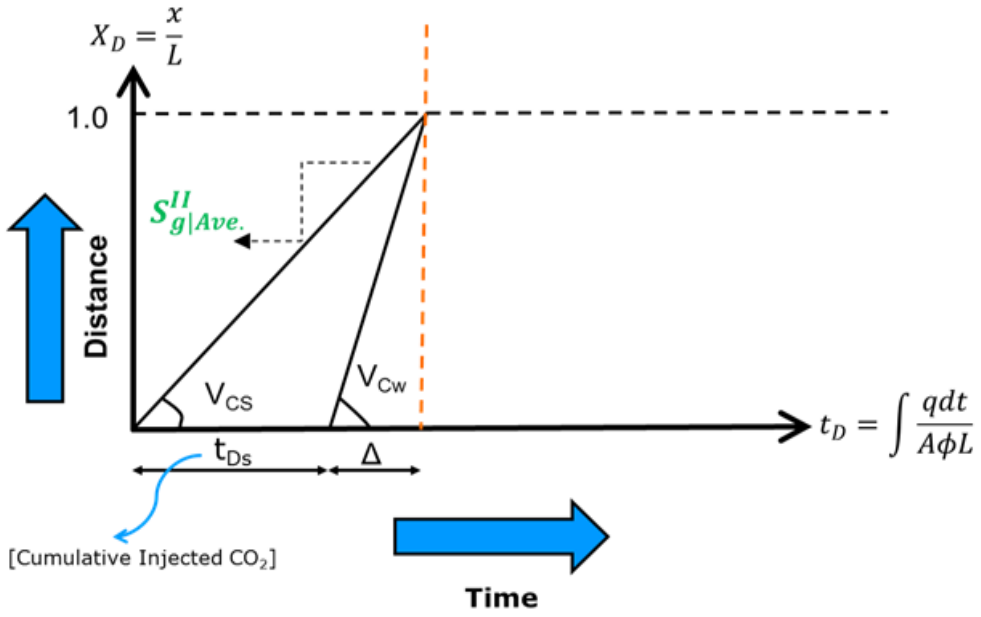

Figure 3.5: The optimal condition: the imbibition front catches-up to the fastest drainage shock at the aquifer outlet boundary and leaves behind all injected CO_2 trapped.

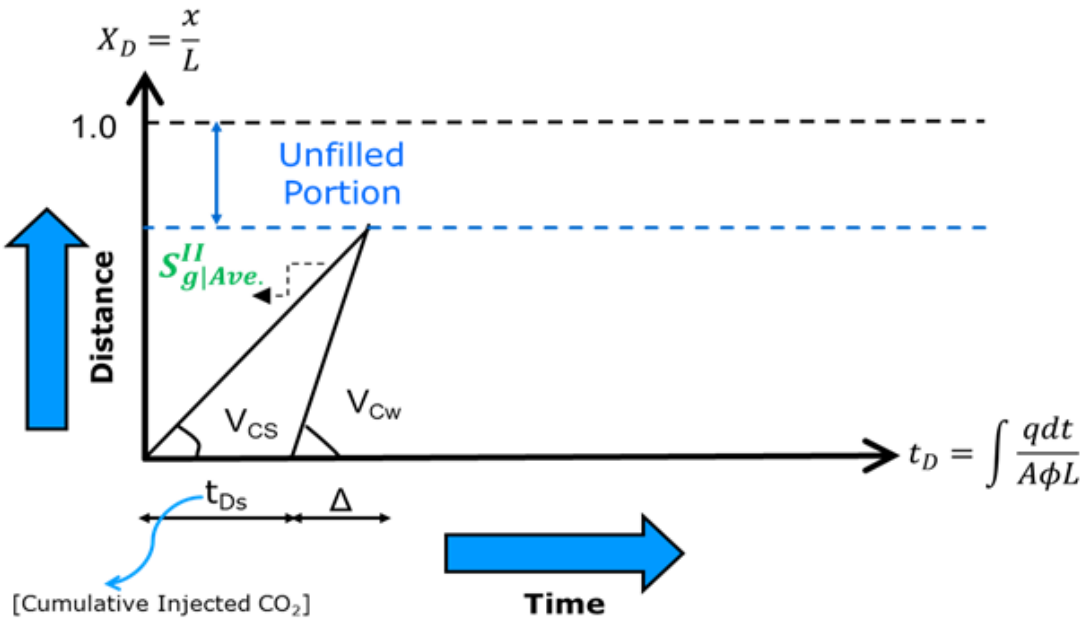

Figure 3.6: Under-capacity condition: the imbibition front catches-up to the fastest drainage shock within the aquifer length. Part of the aquifer is unfilled.

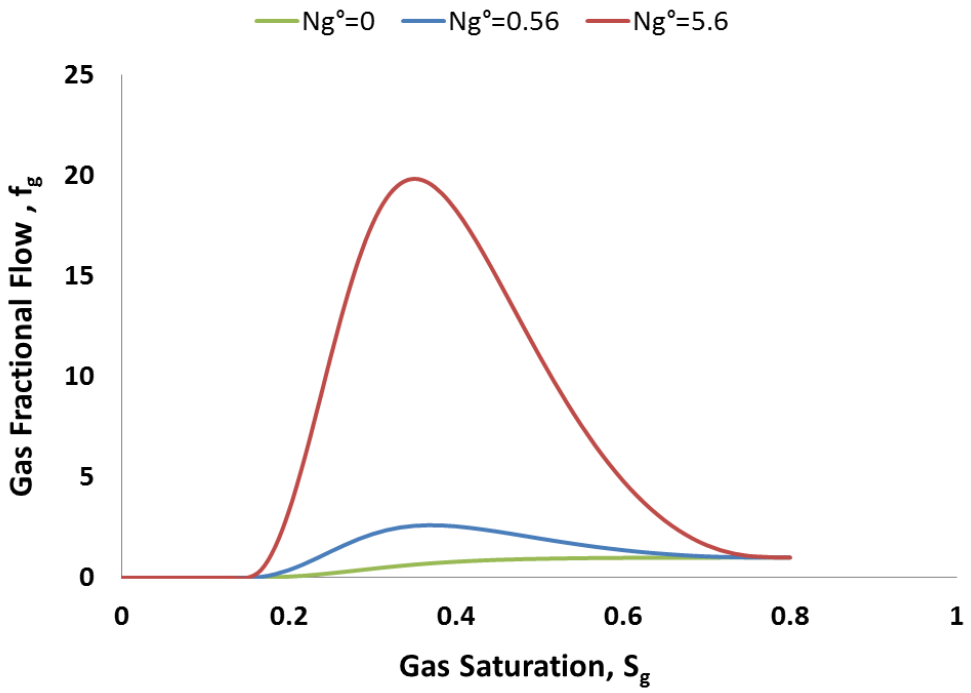

Figure 3.7: Gas fractional flow curves for different values of buoyancy number

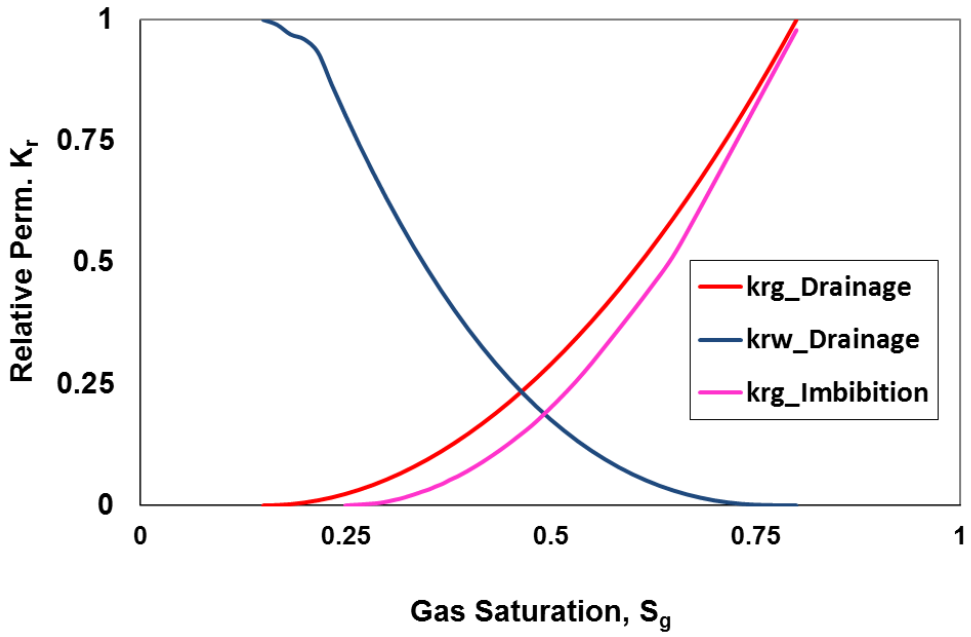

Figure 3.8: Relative permeability curves for the aqueous and gaseous phases. The pink line is the imbibition curve.

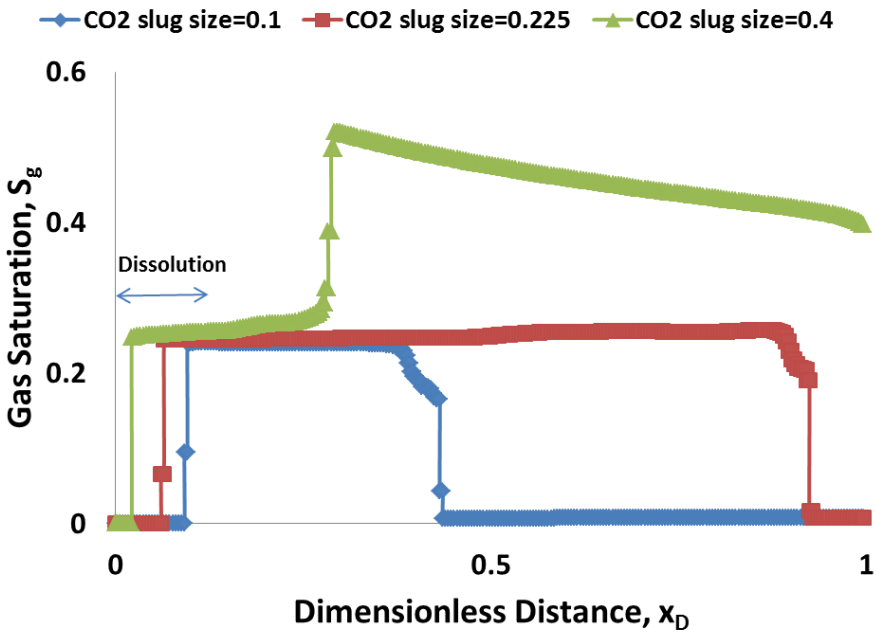

Figure 3.9: Gas saturation profile for three possible conditions at t_D=0.5. The red curve illustrates the optimal condition for which injected CO_2 is trapped evenly along the aquifer. The over capacity condition (green line) leads to gas production at the outlet; however, the drainage front never reaches the outlet, if a smaller CO_2 slug size than the optimal is injected; i.e., the aquifer will not be filled to its capacity. Therefore, simulation results suggest that the CO_2 storage capacity of the aquifer is 0.225 of the aquifer pore volume. There is a slow dissolution shock at the rear of the CO_2 plume corresponding to dissolution of the previously capillary-trapped CO_2 into the fresh injected water.

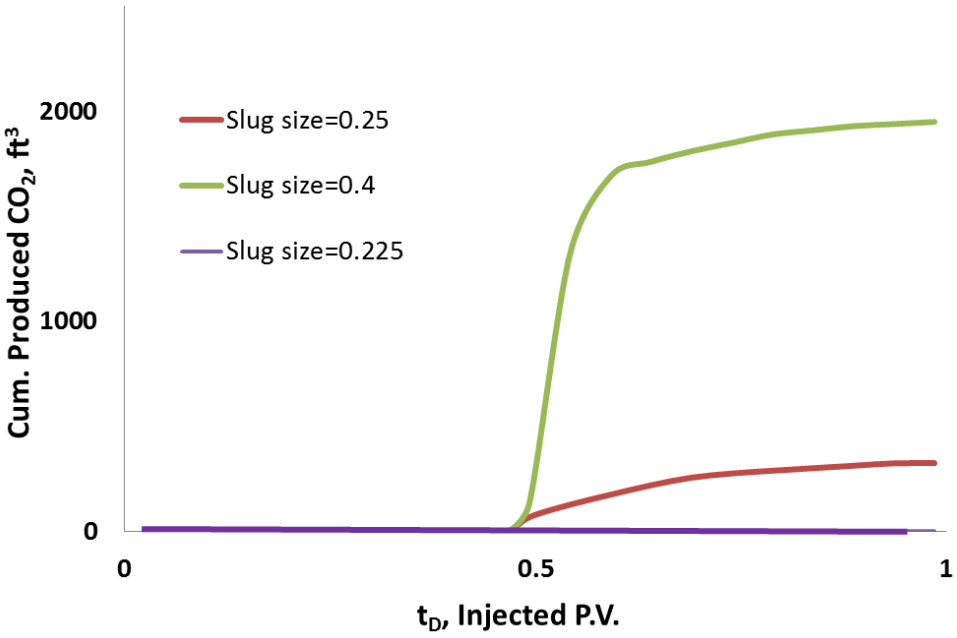

Figure 3.10: The cumulative CO_2 production for the optimal and above optimal cases. Simulation results show that the largest slug of CO_2 that yields no free gas at the outlet is equal to 0.225 of the aquifer P.V. Injecting larger slugs than the optimal (red curve) leads to the production of CO_2; in other words, the presence of CO_2 in the form of free gas at the outlet indicates that the aquifer capacity is smaller than the injected volume.

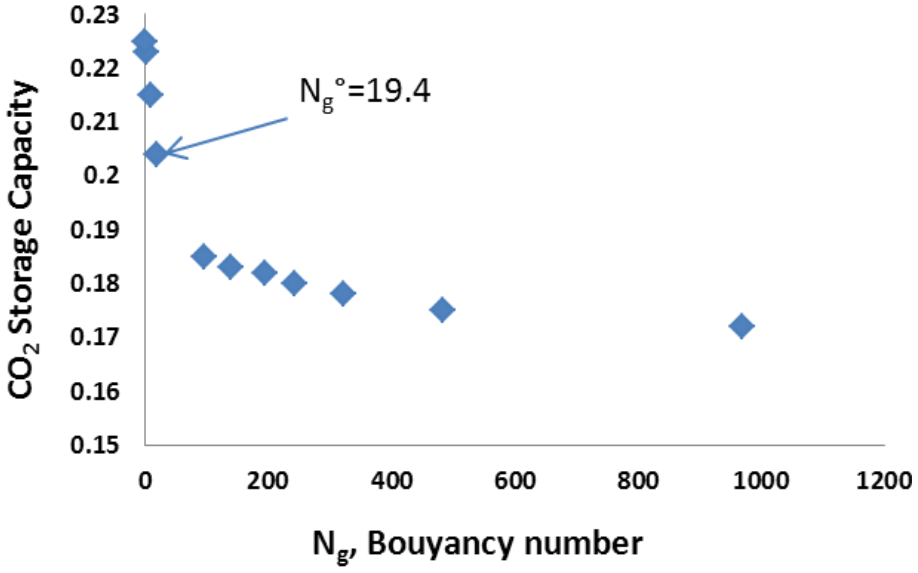

Figure 3.11: CO_2 storage capacity as a function of the buoyancy number. The storage capacity of the aquifer decreases as the displacement becomes more gravity-dominated.

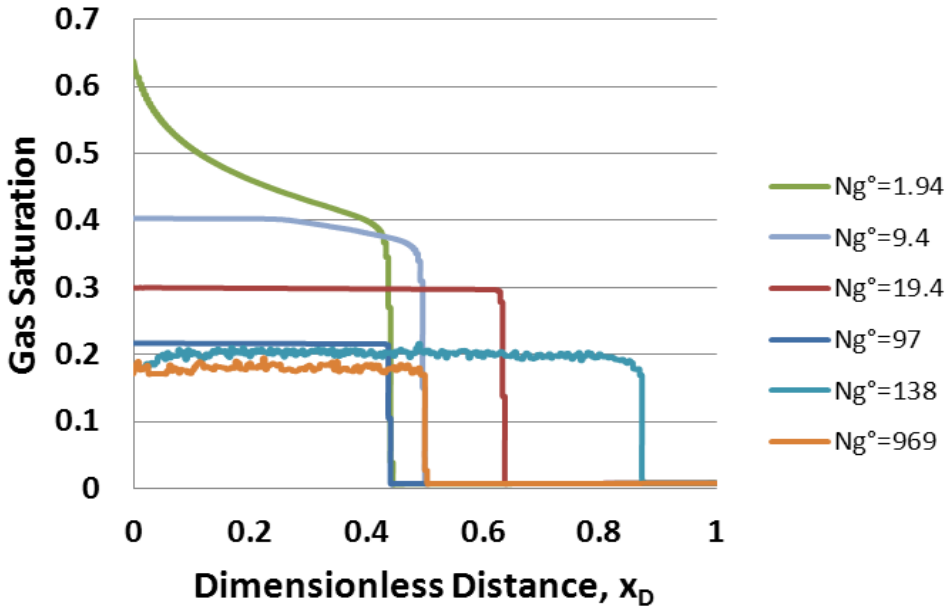

Figure 3.12: Gas saturation profiles during the drainage displacement (CO_2 displacing the brine) for different buoyancy numbers. A larger buoyancy number yields smaller gas saturation and eventually smaller residuals, because of the capillary trapping mechanism. Saturation profiles are depicted at different times.

Chapter 4: Applying Fractional Flow Theory Under the Loss of Miscibility

This chapter examines the limits of the Walsh and Lake (WL) method to predict the performance of solvent-flood when miscibility is not achieved. Despite extensive research on the applications of fractional flow theory, the prediction of flow performance under the loss of miscibility has not been investigated generically.

We introduce the idea of an analogous first-contact miscible (FCM) flood to study miscibly-degraded simultaneous water and gas (SWAG) displacements using the WL method. Furthermore, numerical simulation is used to test the WL solution on a one oil-solvent pair. In the simulations, the loss of miscibility (degradation) is attributed to either flow-associated dispersion or insufficient pressure to develop the miscibility.

One-dimensional (1D) SWAG injection simulations suggest that results of the WL method and the simulations are consistent when miscibility degradation is small. For the two-dimensional (2D) displacements, the predicted optimal SWAG ratio is accurate when the permeable medium is fairly homogeneous with a small cross-flow or heterogeneous with a large lateral correlation length (the same size or greater than the interwell spacing).

The results suggest that the accuracy of the WL solution improves as cross-flow is reduced. In addition, linear growth of the mixing zone with time is observed in cases for which the predicted optimal SWAG ratio is consistent with the simulation results. Hence, we conclude that the WL prediction is accurate when the mixing zone grows linearly with time.

4.1 INTRODUCTION

Despite large microscopic displacement efficiency, miscible gas injection has small volumetric sweep efficiency (Stalkup, 1983; Gardner *et al.*, 1981). On the other hand, injecting water in alternating slugs or simultaneously with gas forms a more stable displacement front. In principle, the co-injection of water and gas is expected to integrate the benefits of both miscible gas injection and water flooding. One of the important SWAG injection parameters is the optimal SWAG ratio (SWAG ratio is defined as the ratio of the injection rate of water to that of the solvent).

In practice, SWAG parameters are determined through numerical simulations. However, depending on the size and the complexity of the reservoir models, simulations are often time-consuming, yet there is no alternative. Therefore, the motivation of this study is to examine the accuracy of a theoretical method to reduce simulation costs.

Buckley and Leverett (1942) proposed the fractional flow theory, later used by Welge *et al.* (1961) to study miscible gas injections. SWAG injection is essentially the multicomponent and multiphase displacement of resident oil and water by a mixture of injected solvent and water. Extensive literature is available on the applications of the fractional flow theory to predict the displacement performance of multicomponent multiphase flow through a permeable medium (LaForce *et al.*, 2010). Helfferich (1981) introduced the general theory of multicomponent and multiphase flow in permeable media through incorporating the theories of multicomponent chromatography (1970) and fractional flow. Pande *et al.* (1987) showed that the 1D fractional flow solution of

immiscible displacements can be used to reproduce qualitatively the displacement performance of 2D flow with non-communicating layers.

Applying the fractional flow theory, Koval (1963), Todd and Longstaff (1972), Fayers *et al.* (1994), and Cheng *et al.* (2002) introduced empirical models to estimate the displacement performance of multidimensional miscible injections. However, fractional flow solutions of miscible floods are typically obtained using simplifying assumptions. One of the most restrictive assumptions is that the partitioning coefficients between the phases, K-values, are constant and independent of the compositions within phases. This assumption is reasonable for low pressures (*i.e.*, pressures far below minimum miscibility pressure (MMP) and pressures at which no critical locus appears in the mixture-phase-behavior diagram. However, the assumption is inaccurate for the degraded miscible displacements, considered in this study, in which the K-values are inevitably changing.

If the corresponding degraded miscible residual oil saturation, S_{orm}, is known, it is proposed that the WL method will be applicable to solvent floods, in which miscibility does not completely develop due to dispersion and/or insufficient local pressure. The objective of this work is to verify the hypothesis for 1D and 2D displacements. Furthermore, we investigate the nature of degraded 2D miscible displacements for which the predicted optimal SWAG ratio is consistent with the simulation results.

4.2 THE WALSH AND LAKE METHOD

4.2.1 The Method of Characteristics

The method of characteristics (MOC) is a mathematical technique to solve first-order strictly hyperbolic partial differential equations (PDE) such as the mass conservation equations. The goal of MOC is to convert the original PDE to a set of ordinary differential equations (ODE) along certain curves called characteristics. The mass conservation equation of component *i* in the form of fractional flow terms in 1D flow with no chemical reaction involved can be written as

$$\frac{\partial C_i}{\partial t_D} + \frac{\partial F_i}{\partial x_D} = 0 , \qquad i=1,2,..,N_{c,} \tag{4.1}$$

where C_i and F_i are the overall concentration and overall flux of component *i*, respectively. Lake (1989) discussed how Eq. (4.1) is derived from the general mass conservative equation and from the definitions of dimensionless time and position. In general, the conservation equations are nonlinear. The nonlinearity in the mass conservative equation lies in the relationship between the overall flux and the overall concentration of each component. Applying the WL assumptions (listed in Section 4.2.2), Eq. (4.1) converts to the following equation:

$$\frac{\partial s_j}{\partial t_D} + \frac{\partial f_j}{\partial x_D} = 0 , \qquad j=1,2,..,N_{P,} \tag{4.2}$$

where s_j and f_j are the saturation and fractional flow of phase *j*, respectively.

4.2.2 The WL Method

Applying the fractional flow theory, Walsh and Lake (1989) introduced a method to analyze the displacement of oil by a FCM solvent in the presence of an immiscible aqueous phase (Figure 4.1). The WL solution provides an elegant insight into the behavior of complex solvent floods. Some of the practical results of their work are: (1) the extension of the concept of optimum water-solvent ratio to arbitrary initial and injection conditions such that the optimal water-solvent ratio yields the maximum displacement efficiency while using the minimum amount of solvent. The SWAG ratio, upon which the solvent and water saturation waves move together, is the optimum for secondary displacements (Caudle and Dyes, 1959); no mobile water initially exists in the secondary displacements. (2) The development of the notion of optimum water-solvent slug size such that the optimal slug size occurs when the chase water and the solvent coincide at the producer (simultaneous breakthrough). They showed that the optimal solvent-water slug size can be expressed in reservoir pore volumes and can be approximated by the dimensionless solvent breakthrough (BT) time. Oil recovery is adversely affected by smaller slugs than by the optimum, because of the trapping of the oil by the chase water (Walsh, 1989).

Similar to all theoretical methods, the WL method rests on a set of simplifying assumptions. In this section, we itemize these assumptions. Most of these assumptions are commonly used in the fractional flow theory:

- The flow is 1D and governed by Darcy's law for multiphase flow.

- Capillary and dispersion effects (dissipation) are negligible, *i.e.*, the conservation of an individual component leads to a first-order, strictly hyperbolic PDE.
- The permeable medium is homogeneous. Fractional flow does not depend on position other than through a saturation change.
- The oil and solvent are first-contact miscible.
- There are two flowing phases (the aqueous and non-aqueous phase) and three components (water, solvent, and hydrocarbon). The aqueous and non-aqueous phases are immiscible.
- Mixing in the non-aqueous phases is ideal, *i.e.*, constant partial molar volume and no change in total volume upon mixing.
- Viscosities depend only on compositions. Relative permeabilities are monotonic and represented by differentiable curves.
- All fluids are incompressible as is the pore volume.
- The local thermodynamic equilibrium applies; *i.e.*, mass fractions of solvent are related through thermodynamic equilibrium relations.
- Step changes at the origin boundary condition ($x = 0$) apply; *i.e.*, initial saturations are uniform and the injection conditions change step-wise at the origin.

We compare the WL solution with simulation results of the same displacement while relaxing the above assumptions.

4.3 MISCIBILITY DEGRADATION

Miscibility degradation is the consequence of dispersion and insufficient local pressure to attain miscibility between the oil and gas.

The minimum pressure required to achieve multi-contact miscibility between the oil and gas at a given reservoir temperature is known as the minimum miscibility pressure (MMP). To achieve high displacement efficiency, the pressure in the reservoir should be maintained at or above MMP. In many practical situations, the gas injection is carried out at pressure slightly above MMP. However, the pressure decreases with distance traveled. Thus, at some point far from the injection well, the pressure may decline below the reservoir MMP, reducing the displacement efficiency.

On the other hand, several authors have shown that the oil recovery on the field-scale depends on the level of dispersion (Arya *et al.,* 1988; Johns *et al.,* 1993; Walsh and Orr, 1990; Haajizadeh *et al.,* 1999; Solano *et al.,* 2001). Reservoir mixing drives the composition route further away from the critical locus into the two-phase region(s) and reduces the local displacement efficiency. In addition, Lantz (1971) showed that even when the conservation equation is dispersion-free, an additional source of "superficial" dispersion (numerical dispersion) arises owing to the finite difference (FD) approximation. The numerical dispersion, which is the manifestation of inaccuracies involved in the FD approximations of spatial and temporal derivatives, can be suppressed (though not eliminated). This can be carried out using very accurate approximations of the derivatives and taking more grid blocks.

4.4 SIMULATION MODEL DESCRIPTIONS

We use the oil produced from the Welch field (Taylor *et al.*, 1998) with the API gravity of 32 and pure CO_2 as the solvent in this study. Lower mole fractions of methane (5%) and heavy components, C_{30}^{+}, compared to that of intermediate components, C_4-C_{16}, make the oil a good candidate for CO_2 flooding. Winprop, CMG's PVT analysis software package, is used to calculate fluid properties according to the Peng-Robinson equation-of-state (EOS). Furthermore, we use the PVT laboratory test data to determine the EOS parameters (Tables 4.1 through 4.3). Figure 4.2 and Table 4.3 show the relative permeability data and the fluids properties used to construct the fractional flow curves.

For heterogeneous models, the permeability heterogeneity is characterized by the Dykstra-Parsons coefficient of variation (V_{DP}) and the dimensionless correlation length in the longitudinal direction (λ_{xD}). The dimensionless correlation length in the transverse direction (λ_{zD}) is set to 0.2. The permeability fields, which are log-normally distributed, are generated using the FFTsim code (Jennings *et al.*, 2002). For all cases, porosity is uniformly distributed.

The simulations are performed using GEM, CMG's general EOS compositional reservoir simulator. The simulation models consist of two vertical wells located at the ends of a 2D cross-sectional grid with constant grid block sizes in the *x*- and *z*-directions. The tops and bottoms of the models are no flow boundaries. The injection well is assigned a constant total injection rate and the production well operates at constant pressure. However, CO_2 and water injection rates are specified to design various SWAG ratios.

The miscibility degradation at a constant level of dispersion is defined as the lowest pressure observed in the reservoir normalized by MMP; in this study, the miscibility degradation is expressed as producer's bottomhole pressure divided by MMP that consequently increases toward the producer. In the simulations, dispersion is mainly assigned through input (physical) dispersivity as the numerical dispersion is minimized by taking small grid blocks and also by adjusting the maximum time step. Equation (4.3) indicates how the Peclet number (N_{pe}), attributed to the numerical dispersion, is correlated with the number of grid blocks in the flow direction as $\left(\frac{df_j}{dS_j}\right)$, which is equal to 1, and $\left(\frac{\Delta t_D}{\Delta x_D}\right)$, which remains less than 0.01 in the simulations (Stalkup, 1983):

$$N_{pe}^{-1}\,|_{\text{Num.}} = \frac{\Delta x_D}{2}\frac{df_j}{dS_j}\left(1-\frac{\Delta t_D}{\Delta x_D}\frac{df_j}{dS_j}\right) \qquad (4.3)$$

.

4.5 One-Dimensional Simulation Results

To verify the hypothesis in 1D degraded miscible displacement, we define an analogous FCM flood such that its associated residual oil saturation is the same as the remaining oil saturation in the original degraded miscible flood. We use a fine simulation grid (512×1×1) to reduce the numerical dispersion as described in the previous section. The remaining oil saturation is taken as the saturation behind the solvent front (S_{orm}). However, S_{orm} in a degraded miscible displacement varies with time; thus, our simulation

results reveal that S_{orm} does not change significantly after 2 pore volume injections for the degradation levels considered in this study (Figure 4.3).

Figure 4.4 illustrates how the degraded miscible residual oil saturation varies as a function of the miscibility degradation for different dispersion levels. The resulting S_{orm} (the oil saturation left behind after 2 pore volume injection) is normalized by the waterflood residual oil saturation, S_{orw}. Figure 4.4 also shows that as the miscibility degradation increases (equivalently, the producer's bottomhole pressure is reduced), the corresponding S_{orm} increases. The latter is observed for all dispersion levels considered in this study. In addition, the results are in agreement with the experimental results by Lange (1998).

Figure 4.5 shows how S_{orm} changes as a function of the miscibility degradation for secondary displacements where initially there was no mobile water. Figure 4.5 illustrates the same trend as Figure 4.4, indicating that much oil remains as miscibility degradation increases. The blue shaded zone in Figure 4.4 shows the range of miscibility degradation, where the WL method is applicable as the corresponding S_{orm}, which is less than S_{orw}.

Therefore, we conclude that the residual oil saturation after a degraded miscible flood is correlated with the level of miscibility degradation. Larger miscibility degradation leads to greater residual oil saturation behind the solvent front. No excess oil will be recovered for a very large miscibility degradation level when compared to an immiscible displacement.

Next, we construct the WL solution for each example using the corresponding S_{orm}. The corresponding S_{orm} to the given miscibility degradation level is read from

Figures 4.5 and 4.6 and incorporated into the WL graphical method. The initial and injection conditions of each example is also incorporated into the WL plots. Figure 4.6 demonstrates the WL procedure for a degraded miscible SWAG displacement using an analogous FCM flood with an equivalent residual oil saturation of S_{orm}.

The WL solution is compared with the numerical results through saturation profiles (water, oil, and gas), the optimal SWAG ratio, and the optimal solvent-water slug size. Figure 4.7 and Figure 4.8 compare the oil/water/gas saturation profiles for different miscibility degradation levels. The results show that predicted profiles are consistent with the simulation results only when the peclet number (N_{pe}) exceeds 1025.

Figure 4.9 shows the recovery curves at the specified miscibility degradation for different SWAG ratios. The results indicate that the maximum oil recovery of 88% is achieved through the SWAG ratio of 0.5. Therefore, the WL optimal SWAG ratio of 0.51 is in agreement with the numerical results.

Furthermore, Figure 4.10 clearly shows that less solvent usage (larger SWAG ratios) recovers less oil. This observation points out that the success of degraded miscible displacements (even multi-contact miscibility development) depends also on the fractional flows of the injected fluids. This observation is consistent with the results of LaForce *et al.* (2009) as they pointed out that miscibility development is a function of fractional flow of water .

4.6 TWO-DIMENSIONAL SIMULATION RESULTS

In this section, we examine how the WL solution of a degraded miscible flood compares to the simulation results of a 2D displacement with the same level of miscibility degradation. The level of degradation is determined through N_{pe} and the ratio of producing pressure to MMP.

A 128 ft ×32 ft vertical cross-section model is used with128 × 32 grid blocks in the *x*- and *z*-directions, respectively. We consider the following dimensionless scaling groups that affect the displacement performance in 2D flow: the effective aspect ratio (R_L), the Dykstra-Parsons coefficient of variation (V_{DP}), the dimensionless correlation length in the *x*-direction (λ_{xD}), the buoyancy number (N_g), and N_{Pe}. The effective aspect ratio is particularly used to indicate the degree of cross-flow. For more details on the definition of permeability heterogeneity see Appendix B. A block of 46 simulation models is obtained based on the three-factorial Box-Behnken experimental design (Box and Behnken, 1960; Wood *et al.*, 2008). Table 4.5 lists the range of values (levels) used for each dimensionless group. As uncertainty inherently increases with heterogeneity, each simulation case was repeated three times with different realizations of the permeability field to reduce the associated uncertainty. Also, the conclusions made here are based on averaging the results of different realizations.

The initial water saturation map for tertiary SWAG displacements is obtained from the secondary displacement of the same simulation model. In other words, the water injection is continued until a certain producing water cut is observed at the producer

(95% in our study). Next, the most recent saturation map is used as an input saturation for the tertiary flood of the same simulation model (Figure 4.10).

Figures 4.11 through 4.13 illustrate comparisons between the vertically averaged saturation profiles predicted by the WL method and those obtained from the simulations. In fairly homogeneous cases (V_{DP} = 0.4) with a small cross-flow (small aspect ratios and buoyancy numbers), the vertically averaged saturation profile corresponds to the WL solution. However, this is not valid for heterogeneous permeable media, as the injected fluids do not move at the same velocity in all layers. Therefore, the predicted saturations profiles and the vertically averaged saturation profile obtained from simulations agree only for homogeneous cases.

In addition, the optimal solvent-water slug size in the WL method is approximated as the solvent dimensionless breakthrough time (BT). Dimensionless time is defined as the ratio of cumulative injected volume to total pore volume. The point is that total pore volume is swept by the injected fluid in 1D flow. This is not true for 2D displacements as a result of incomplete sweep efficiencies. Hence, the WL approximation of the optimal slug size cannot be applied for 2D flow.

Figure 4.14 illustrates a comparison between the predicted optimal slug size (0.61) and the recovery curves obtained from the simulation of a moderately homogenous model. The oil recoveries are expressed as a fraction of the original oil in-place. Slug sizes larger than 0.61 P.V. do not yield an improvement in the oil recovery; however, injecting smaller volumes degrades the recovery. We use two passive tracers to examine the WL notion of the optimal-solvent slug size in a fairly homogeneous medium with

weak cross-flow. Figures 4.15 through 4.17 demonstrate that the tracers simultaneously break through, but only when the injected slug size is 0.61 P.V. (optimal) and consistent with the WL prediction.

To determine the optimal SWAG ratio for each case study, we conduct a numerical simulation with at least five SWAG ratios. However, the WL definition of the optimal SWAG is not appropriate for 2D displacements, because there is no specific achievable maximum oil recovery; in fact, SWAG ratios smaller than the 1D optimum do not always yield the largest oil recovery in 2D flow as sweep efficiency becomes an issue. Therefore, we adapt the concept of optimal SWAG ratio as a SWAG ratio that yields the largest oil recovery while using the minimum solvent before the CO_2 BT occurs. In our study, gas BT is considered as the reference time to compare the oil recoveries of 2D displacements; because similarly for 1D flow, the optimal SWAG ratio is defined based on the oil recoveries achieved at gas BT in the absence of any 2D flow effect. Two-dimensional flow effects are known as viscous fingering, channeling, and gravity override that often yield small sweep efficiency. Hence, the difference between the predicted optimal SWAG ratio and a SWAG ratio with the largest oil recovery at gas BT represents the contribution of the 2D effects (Figure 4.18). A similar argument was used by Li *et al.* (1995) for immiscible floods.

However, various SWAG ratios yield different gas BTs and a unique BT does not exist for all SWAG ratios. Therefore, we consider the latest gas BT time as a reference to compare the oil recoveries of cases with different SWAG ratios. Hence, the optimal SWAG ratio in 2D displacements is expressed as the SWAG ratio that yields the largest

oil recovery. We use percent errors to compare the predicted optimal SWAG ratios with the simulation results. The percent error is defined as:

$$\text{Percent error} = \frac{(\text{predicted value}) - (\text{the optimal obtained from the simulation})}{(\text{the optimal obtained from the simulation})} \times 100 \quad . \quad (4.4)$$

Figures 4.19 through 4.20 show the percent errors of the optimal SWAG ratios obtained from the WL method and the simulations as a function of λ_{xD} for different levels of dispersion. Each simulation case is conducted with three different dispersion levels according to Table 4.5. The percent error of the optimal SWAG ratio decreases as λ_{xD} increases when R_L = 0.1. However, larger dispersion degrades the accuracy of the WL solution. In this regard, Figure 4.20 is comparable to Figure 4.19 when R_L = 1.0; nevertheless, the overall percent errors in Figure 4.20 are larger than Figure 4.19. Strictly speaking, a larger cross-flow decreases the accuracy of the WL solution.

In addition, the difference between the predicted and the optimal SWAG ratio obtained from the simulations is erratic with respect to $V_{DP,}$ except for the relatively homogeneous cases (V_{DP} = 0.4). Figure 4.21 illustrates the percent error of the optimal SWAG ratios as a function of N_g for different levels of R_L. Strong gravity cross-flow degrades the accuracy of the WL solution for all levels of R_L.

The results suggest that the percent error of the optimal SWAG ratio is less than 10% for the following:

a. fairly homogeneous ($V_{DP} \leq 0.4$) models with small cross-flow

b. a heterogeneous reservoir for which the longitudinal correlation length is of the same size or larger than the interwell spacing (equivalently expressed as strictly layered reservoirs).

4.7 DEVELOPMENT OF THE MIXING ZONE WITH TIME

We investigate the nature of miscible displacements for which the accuracy of the WL solution is examined through the optimal SWAG ratio. The WL method treats the SWAG injections as a combination of the miscible waves (gas-oil) and immiscible waves (water-oil/solvent) propagating according to the given initial and injection conditions. On the other hand, previous studies by Pande *et al.* (1987), Sorbie *et al.* (1994), and Li *et al.* (1995) showed that a linear growth of the mixing zone with time will be observed if the simulation results are consistent with the fractional flow solutions. Therefore, a similar behavior is expected for SWAG displacements when the WL solution is accurate.

We rerun four of the simulations with an added passive tracer to determine the mixing zone (see Chapter 7 for more details on the mixing zone). The predicted optimal SWAG ratios for Cases 1 and 2 are in agreement with the simulations despite Cases 3-4. The length of the mixing zone within each layer is calculated at five different time steps (at various stages of the SWAG displacement). The mixing zone is defined as the dimensionless distance between the locations where the dimensionless tracer concentration of 0.1 and 0.9 occur (Lake, 1989).

Figure 4.22 indicates that the lengths of the mixing zone for two layers in Cases 1 and 2 are strongly correlated with time. However, the problem that arises with this

procedure is that each layer should be evaluated individually, which is time-consuming. Furthermore, it never provides any general comment into the whole displacement.

To overcome this deficit, lengths of the mixing zone for all layers of a simulation model at time t_1 is stored as array x_1, at time t_2 as array x_2, and so on. Next, we adopt the notion of the correlation coefficient function as the covariance of x_1 and x_2 normalized by dividing by the variability of x_1 and x_2 (Jensen *et al.*, 2002); see Figure 4.23 for the schematic illustration. The correlation coefficient function of arrays x_1 and x_2 represents the tendency of the mixing zone to grow linearly with time (see Chapter 7 for more details).

Figure 4.24 illustrates the correlation coefficient functions as a function of elapsed time for all four cases. The correlation coefficient functions for Cases 1 and 2 stay close to unity illustrating a strong linear correlation between the lengths of mixing zones and time. This observation suggests that the previous findings regarding the accuracy of 1D fractional flow solutions for 2D flows when the mixing zone grows linearly with elapsed time, is also valid for the degraded miscible SWAG displacements. On the other hand, the correlation coefficient functions for Cases 3 and 4 are much smaller than Cases 1 and 2; overall, the mixing zones in Cases 3 and 4 do not grow linearly with time, although linear growth of the mixing zone may be observed for a few layers.

4.8 CONCLUSIONS

We successfully apply the WL method to predict the performance of degraded miscible SWAG displacements using the concept of an analogous FCM flood. In addition, the notion of the optimal SWAG ratio is modified to account for the 2D flow

effects such as viscous fingering and channeling. The WL predicted optimal SWAG ratios are accurate for either fairly homogenous permeable media or strictly layered reservoirs. Furthermore, the correlation coefficient function of lengths of the mixing zone calculated at successive time intervals is introduced as the measure to study the development of the mixing zone in 2D displacements. The main conclusions of the study are noted below:

1. The WL solution agrees most with flow in a 2D cross-section when they are strictly layered reservoirs. Therefore, previous findings that 1D miscible/immiscible fractional flow solutions are accurate for 2D displacements when the interwell correlation length of the permeability is very large, is extended to SWAG displacements.
2. The percent error of the optimal SWAG ratio decreases substantially as the permeability correlation length increases; thus, the predicted optimal SWAG ratio in a strictly layered reservoir is very close to that of a heterogeneous reservoir comprised of isolated layers.
3. The WL solution is accurate when the mixing zone grows linearly with time (*i.e.*, when the mixing zone correlation coefficient is close to unity). Therefore, less reservoir mixing improves the accuracy of the WL solution.

4.9 NOMENCLATURE

N_g = buoyancy number

N_{Pe} = Peclet number

Mmp = minimum miscibility pressure

P = injection pressure

Ppm = parts per million

R_L = effective aspect ratio

S_o = oil saturation

F_i = overall flux of component of component i

f_j = fractional flow of phase j

C_i = overall concentration of component i

K_L = dispersivity coefficient in the longitudinal direction

L = length of the reservoir

H = height of the reservoir

k_H = permeability in the horizontal direction

k_V = permeability in the vertical direction

S_j = saturation of phase j

S_w = water saturation

S_g = gas saturation

S_{orw} = residual oil saturation after waterflood

S_{orm} = residual oil saturation after degraded miscible displacement

t_D = dimensionless time

t_i = time step i

V_{DP} = the Dykstra- Parson coefficient of variation

u_T = total flow velocity

x_D = dimensionless distance

x_i =array i consists of lengths of the mixing zone for each layer of the reservoir at time t_i

λ_{xD} = dimensionless correlation length in the x-direction

λ_{zD} =dimensionless correlation length in the z-direction

ρ_h = the correlation coefficient function

Table 4.1: Oil compositions

Component	**Mole Fraction, %**
C_1	4.55
C_2	8.1
C_3	7.98
IC_4	1.69
nC_4	5.49
IC_5	2.71
nC_5	2.69
C_6	7.29
C_7^+	59.54

Table 4.3: Binary interaction coefficients

Component	CO_2	C_1	C_2	C_3	IC_4	nC_4	IC_5	nC_5	G1	G2	G3	G4
CO_2	0.000	0.089	0.130	0.125	0.116	0.116	0.115	0.115	0.115	0.161	0.055	0.087
C_1	0.089	0.000	0.002	0.014	0.015	0.015	0.016	0.016	0.017	0.062	0.027	0.041
C_2	0.130	0.002	0.000	0.000	0.000	0.000	0.062	0.062	0.050	0.050	0.050	0.050
C_3	0.125	0.014	0.000	0.000	0.000	0.000	0.000	0.000	0.000	0.000	0.000	0.000
IC_4	0.116	0.015	0.000	0.000	0.000	0.000	0.000	0.000	0.000	0.000	0.000	0.000
nC_4	0.116	0.015	0.000	0.000	0.000	0.000	0.000	0.000	0.000	0.000	0.000	0.000
IC_5	0.115	0.016	0.062	0.000	0.000	0.000	0.000	0.000	0.000	0.000	0.000	0.000
nC_5	0.115	0.016	0.062	0.000	0.000	0.000	0.000	0.000	0.000	0.000	0.000	0.000
G1*	0.115	0.017	0.050	0.000	0.000	0.000	0.000	0.000	0.000	0.000	0.000	0.000
G2*	0.161	0.062	0.050	0.000	0.000	0.000	0.000	0.000	0.000	0.000	0.000	0.000
G3*	0.055	0.027	0.050	0.000	0.000	0.000	0.000	0.000	0.000	0.000	0.000	0.000
G4*	0.087	0.041	0.050	0.000	0.000	0.000	0.000	0.000	0.000	0.000	0.000	0.000

Table 4.2: Equation-of-state parameters

Component	P_c (atm)	T_c (°K)	Accentric factor	M_w	V_c (lit/mol)	μ_c (cp)	*Omega*(A)	*Omega*(B)	Spec. gravity **
CO_2	72.8	304.2	0.225	44.01	0.094	0.094	1.045	1.177	0.81
C_1	45.4	190.6	0.008	16.043	0.099	0.099	0.957	0.957	0.30
C_2	48.2	305.4	0.098	30.07	0.148	0.148	0.503	0.503	0.35
C_3	41.9	369.8	0.152	44.09	0.203	0.203	0.653	0.653	0.50
IC_4	36	408.1	0.176	58.12	0.263	0.263	0.997	0.997	0.56
NC_4	37.5	425.2	0.193	58.12	0.255	0.255	0.997	0.997	0.58
IC_5	33.4	460.4	0.227	72.15	0.306	0.306	1.055	1.055	0.62
NC_5	33.3	469.6	0.251	72.15	0.304	0.304	1.055	1.055	0.63
Group1	32.46	507.5	0.275	86	0.344	0.344	1.055	1.055	0.69
Group2	10.6	959.0	1.165	550	1.860	1.860	1.055	1.055	0.95
Group3	26.1	618.6	0.360	127.59	0.571	0.571	1.055	0.959	0.78
Group4	16.3	791.9	0.683	262.67	1.087	1.087	1.045	1.019	0.88

*Pseudo-component

**Specific gravity is defined as the liquid density of the component at 60 °F and 1 atm divided by the density of water at 60 °F and 1 atm.

Table 4.4: Phase properties

Phase	Density, lb/ft^3	Viscosity, cp
Water	62.98	0.51
Oil	51.45	1.12
Gas	41.34	0.055

Table 4.5: Range of the dimensionless groups

	Small	Intermediate	Large
V_{DP}	0.4	0.65	0.85
λ_{xD}	0.1	1	10
R_L^*	0.1	1	10
N_{pe}^{**}	85	140	270
N_g^{***}	0.004	0.02	0.1

*The effective aspect ratio: $R_L = \frac{L}{H}\sqrt{\frac{k_V}{k_H}}$

**Peclet number: $N_{Pe} = \frac{u_T}{\phi L K_L}$

***Buoyancy number: $N_g|_{oil-gas} = \frac{k\Delta\rho_{o-g}g}{\mu_o u_T}$

(For more information on the dimensionless scaling groups see Appendix C)

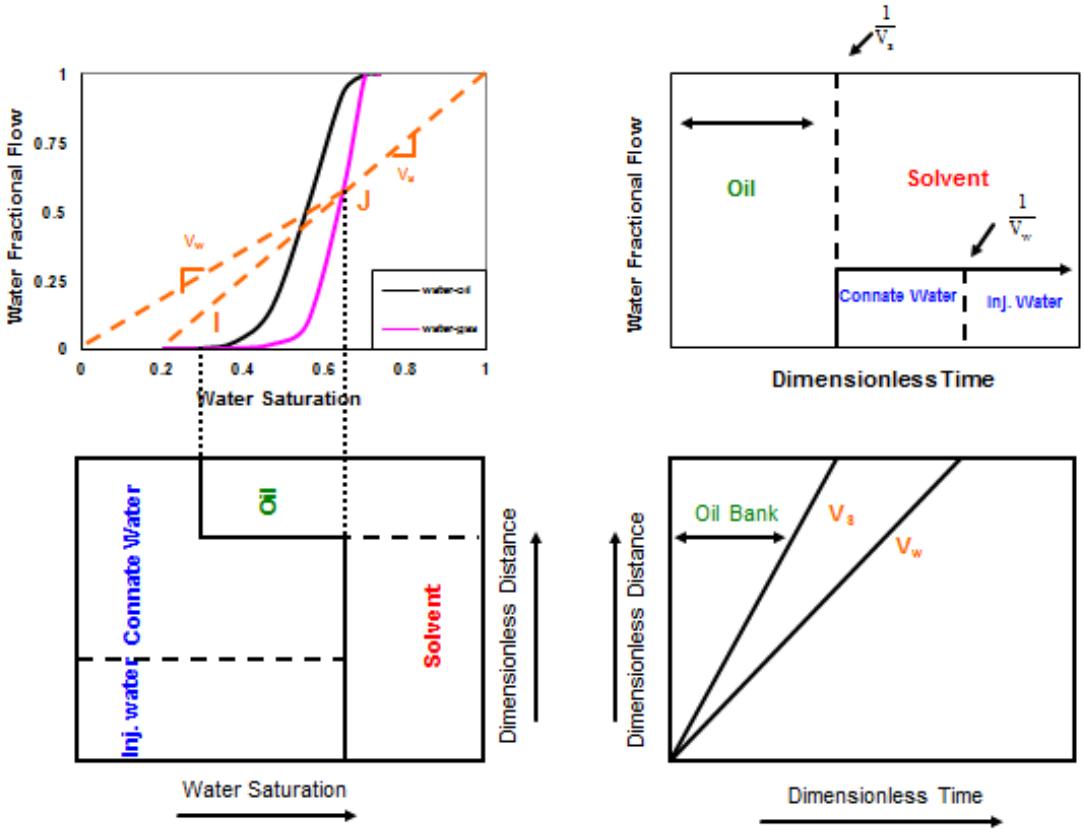

Figure 4.1: The WL plots: (1) the upper left plot illustrates the solvent-water and water-oil fractional flow curves. The points representing the initial and injection conditions are shown in this plot by I and J; (2) the bottom left is a profile plot: the overall concentration of component *i* versus dimensionless distance at a fixed time; (3) the upper right shows a history plot: the overall fractional flow of component *i* at the effluent end of the permeable medium versus dimensionless time; (4) The lower right plot demonstrates a time-distance diagram. The slope of each line on the latter plot, which is called a characteristic, represents the specific velocity. The overall concentration is constant along each characteristic line. The viscosities in the WL method are evaluated at the average reservoir pressure. Dimensionless time is defined as the cumulative volume of the injected fluids (solvent and water) in reservoir volumes divided by the total cross-sectional pore volume.

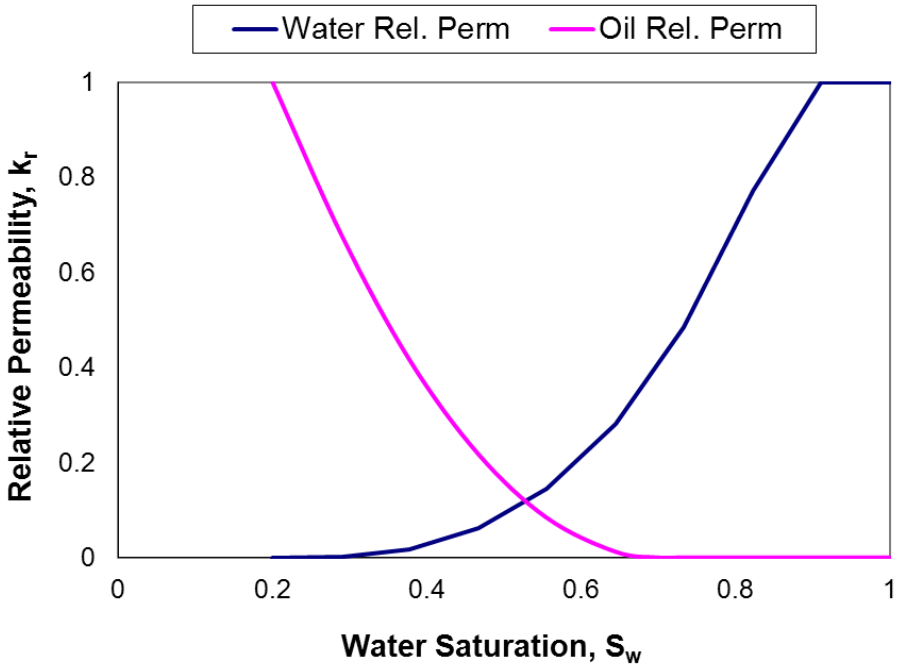

Figure 4.2: Relative permeability curves used to construct the WL plots. In the simulations, Stone II is used to compute the three-phase relative permeabilities.

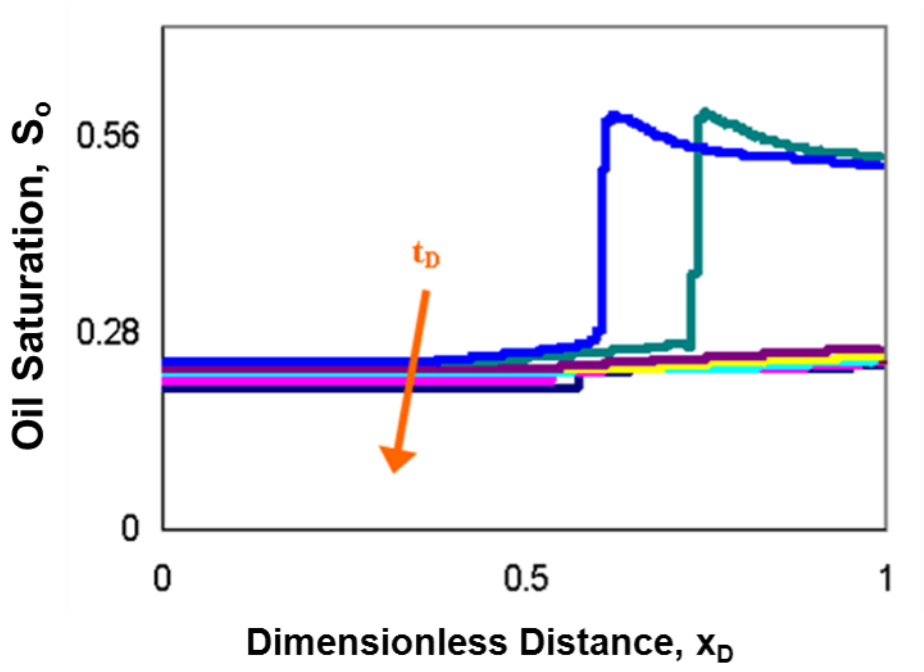

Figure 4.3: Variation of the oil saturation with distance (normalized by the interwell spacing) at various stages of the displacement.

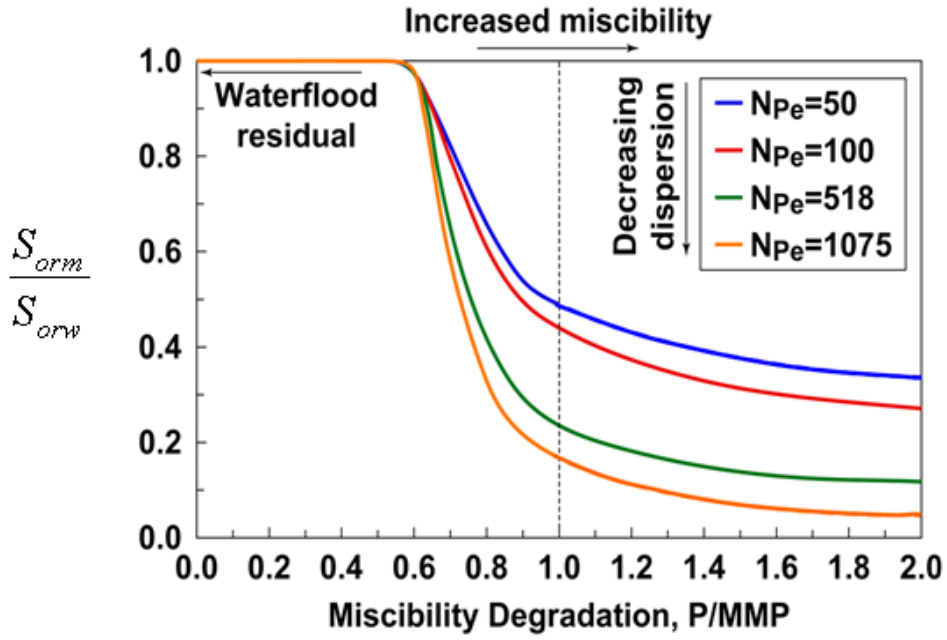

Figure 4.4: S_{orm}/S_{orw} as a function of the miscibility degradation for tertiary displacements. For miscibility degradation below 0.5, no advantage is obtained from the solvent injection as no reduction in the residual oil saturation is observed. The horizontal axis represents the ratio of the producer's bottomhole pressure to MMP.

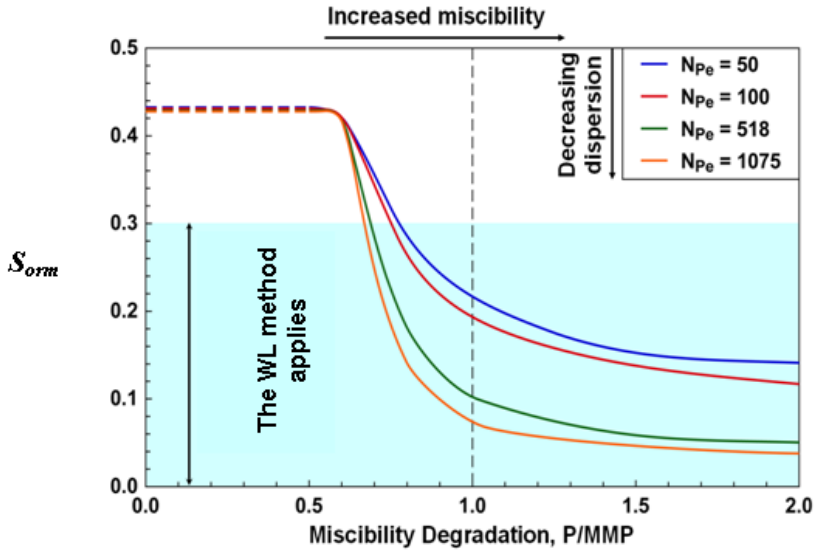

Figure 4.5: S_{orm} as a function of the miscibility degradation for secondary displacements. The blue zone illustrates the degraded miscible displacements, for which S_{orm} are smaller than S_{orw}. The horizontal axis represents the ratio of producer's bottomhole pressure to MMP.

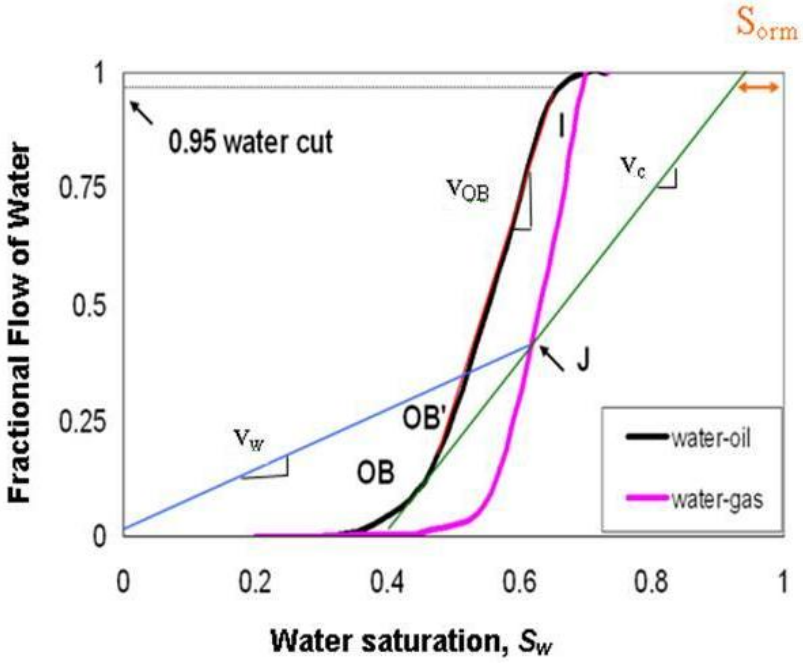

Figure 4.6: The WL procedure to determine the optimal SWAG ratio for a degraded miscible flood. For this tertiary displacement, the predicted optimal ratio is equal to 0.51 (Walsh and Lake, 1989).

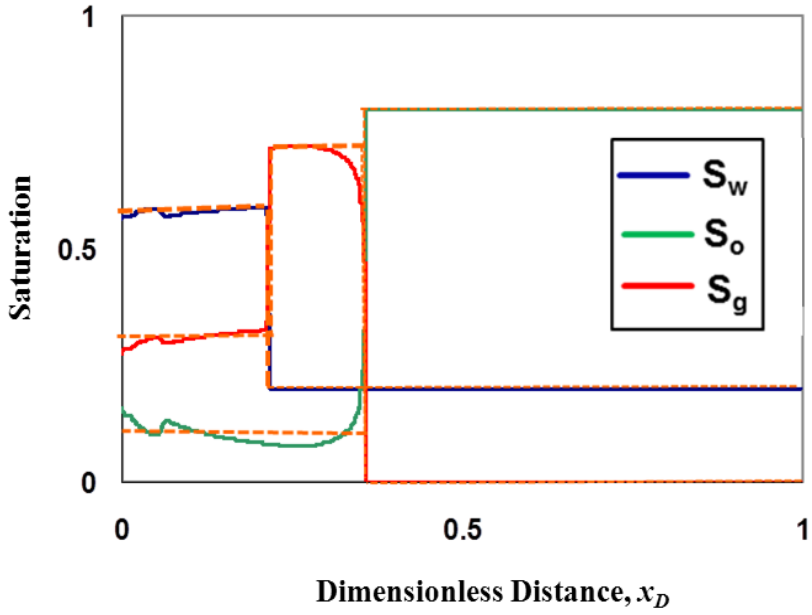

Figure 4.7: Saturation profiles (distance is normalized by the interwell spacing) for a SWAG displacement with the SWAG ratio of 0.5 at t_D = 0.25. P/MMP and NPe are set to 0.95 and 1025, respectively. The blue curve represents water saturation, the green curve is oil saturation, and the red curve is gas saturation. The dashed orange curves show the WL solution.

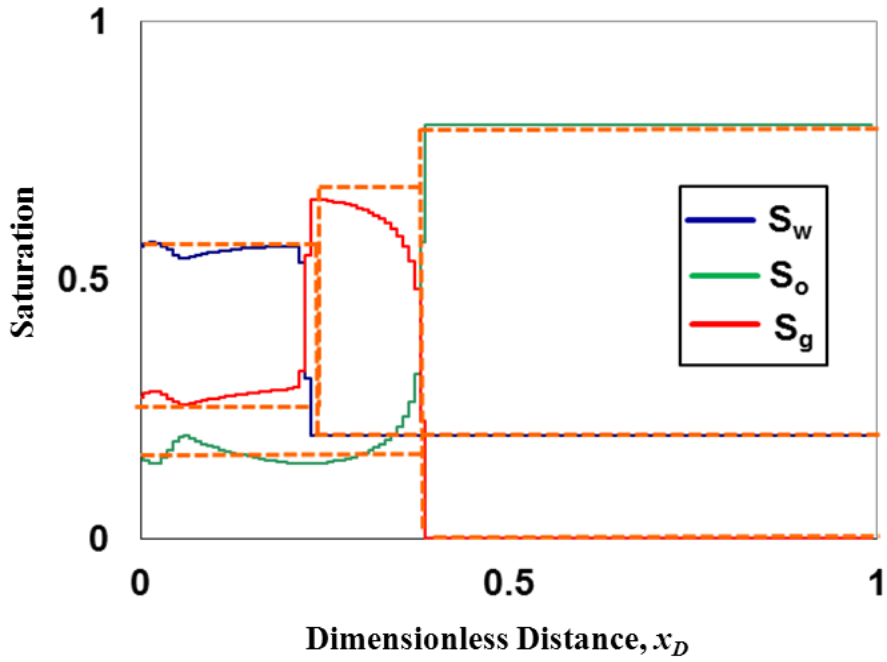

Figure 4.8: Saturation profiles (distance normalized by the interwell spacing) for a SWAG displacement with the SWAG ratio of 0.5 depicted at $t_D = 0.25$. P/MMP and N_{Pe} are set to 0.95 and 240, respectively. The blue curve represents water saturation, the green curve is oil saturation, and the red curve indicates gas saturation. The dashed orange curves are the WL solution.

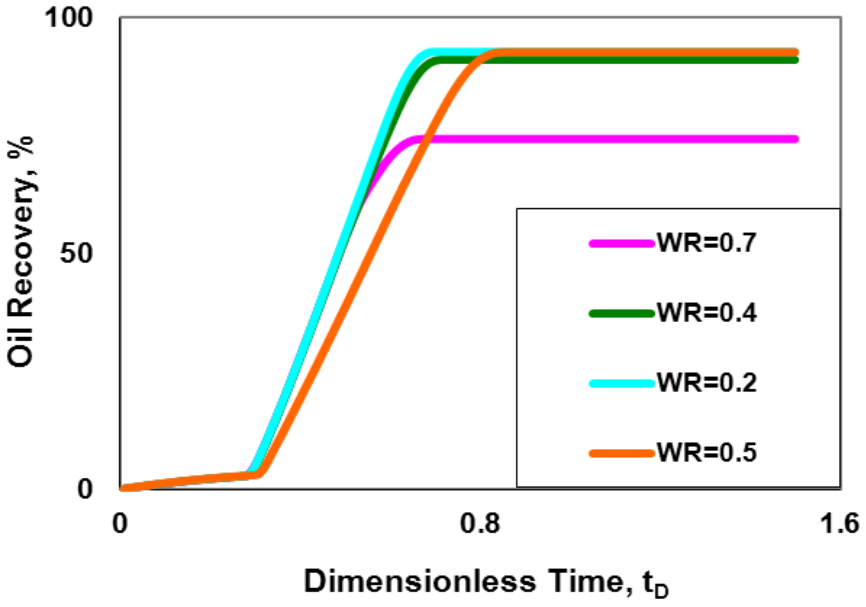

Figure 4.9: Oil recovery curves for 1D degraded miscible displacements with five different SWAG ratios. Because of the miscibility degradation (N_{Pe} = 512 and P/MMP = 0.95), the maximum oil recovery never reaches 100%. The SWAG ratio of 0.5 gives the largest recovery. The WL optimal SWAG ratio for the same displacement is 0.51 consistent with the simulation.

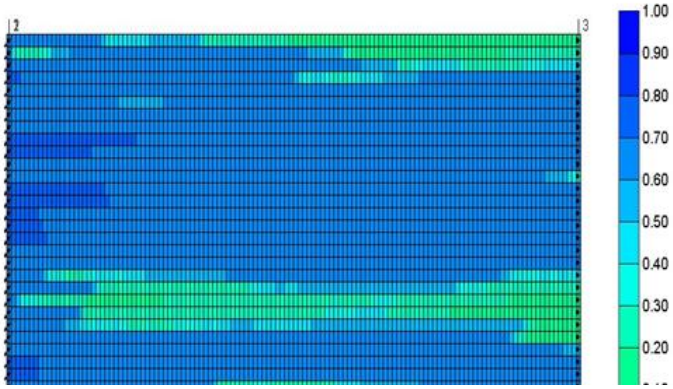

Figure 4.10 a: Water saturation distribution for VDP=0.85 and λ_{XD}=0.5 during water flooding. The other dimensionless groups are set to their intermediate level according to Table 4.5.

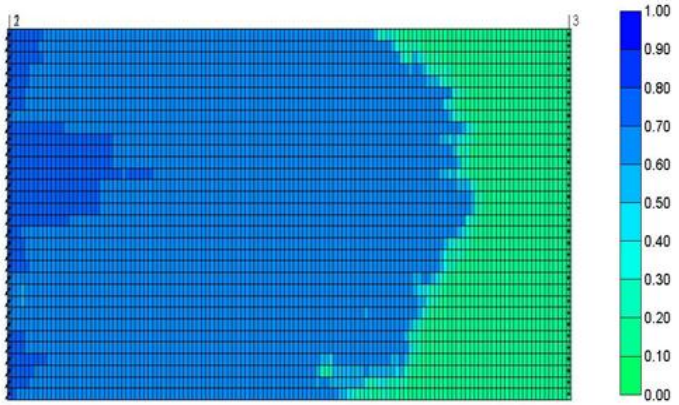

Figure 4.10b: Water saturation distribution for V_{DP}=0.85 and λ_{XD}=0.05 during water flooding. The other dimensionless groups are set to their intermediate level according to Table 4.5.

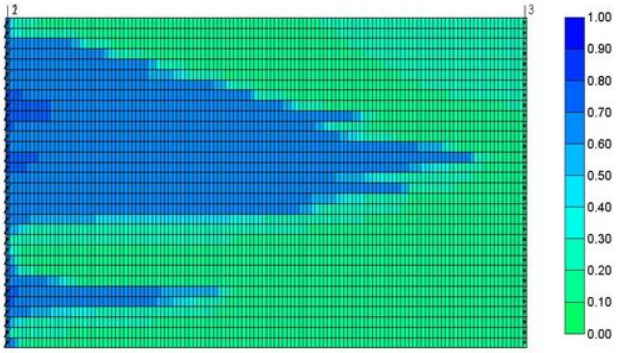

Figure 4.10c: Water saturation distribution for V_{DP}=0.85 and λ_{XD}=10 during water flooding. The other dimensionless groups are set to their intermediate level according to Table 4.5.

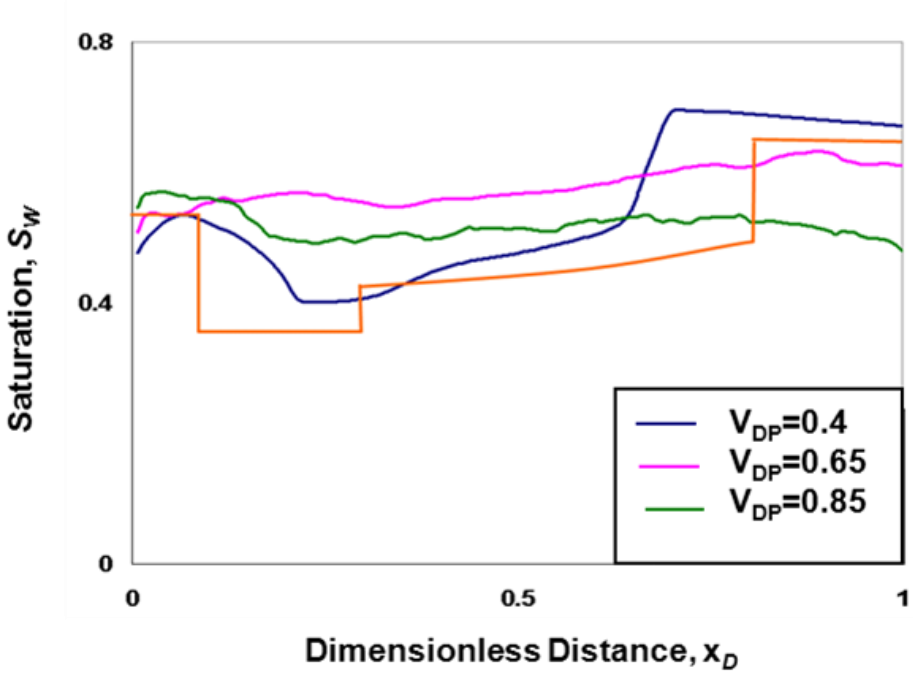

Figure 4.11: A comparison of the WL-predicted (orange curve) and the simulated water saturation profiles (distance is normalized by the interwell spacing) for different levels of heterogeneity depicted at t_D = 0.25. P/MMP and N_{Pe} are set to 0.95 and 1025, respectively. V_{DP}, N_g, λ_{xD}, and R_L are at their lowest level according to Table 4.5.

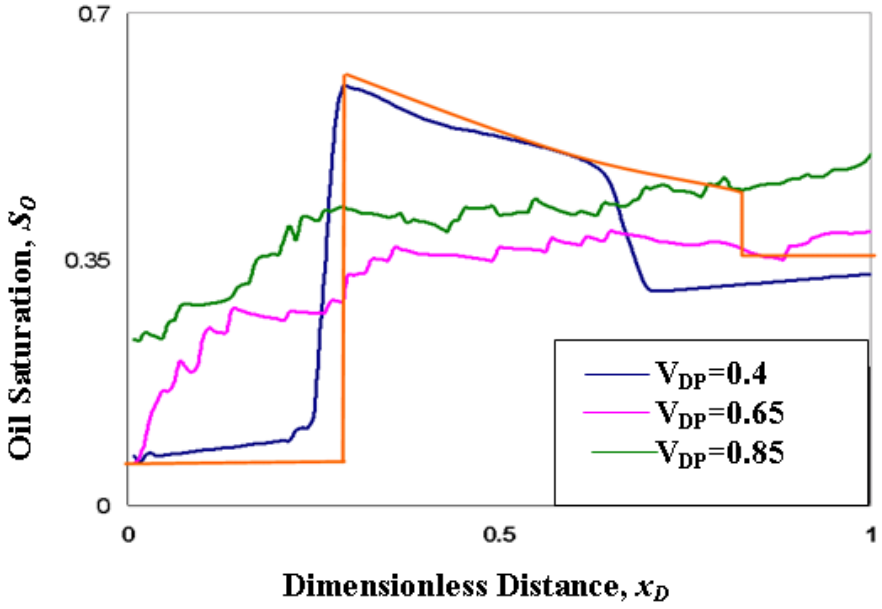

Figure 4.12: A comparison of the WL-predicted (orange curve) and the simulated oil saturation profiles (distance is normalized by the interwell spacing) for different levels of heterogeneity depicted at t_D = 0.25. P/MMP and N_{Pe} are set to 0.95 and 1025, respectively. V_{DP}, N_g, λ_{xD}, and R_L are at their lowest level according to Table 4.5.

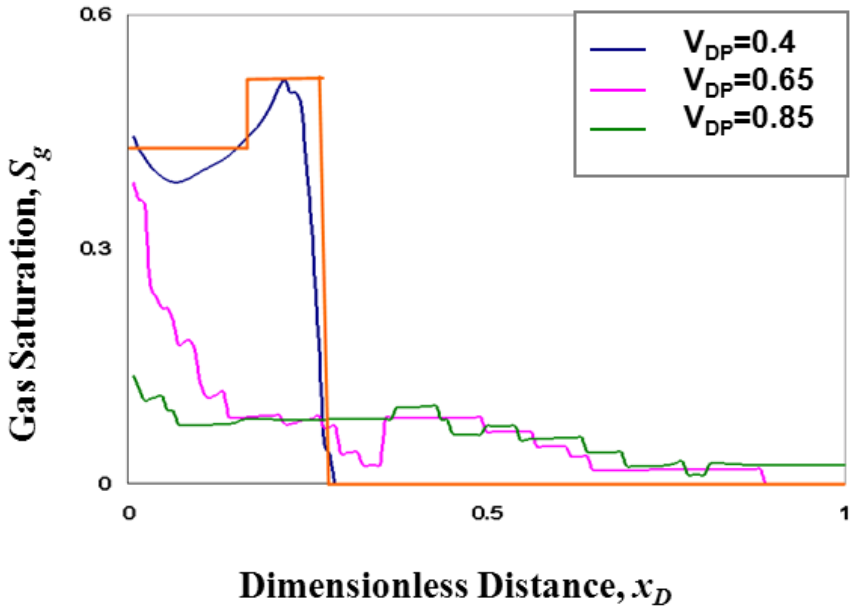

Figure 4.13: A comparison of the WL-predicted (orange curve) and the simulated gas saturation profiles (distance is normalized by the interwell spacing) for different levels of heterogeneity at t_D = 0.25. P/MMP and N_{Pe} are set to 0.95 and 1025, respectively. V_{DP}, N_g, λ_{xD}, and R_L are at their lowest level according to Table 4.5.

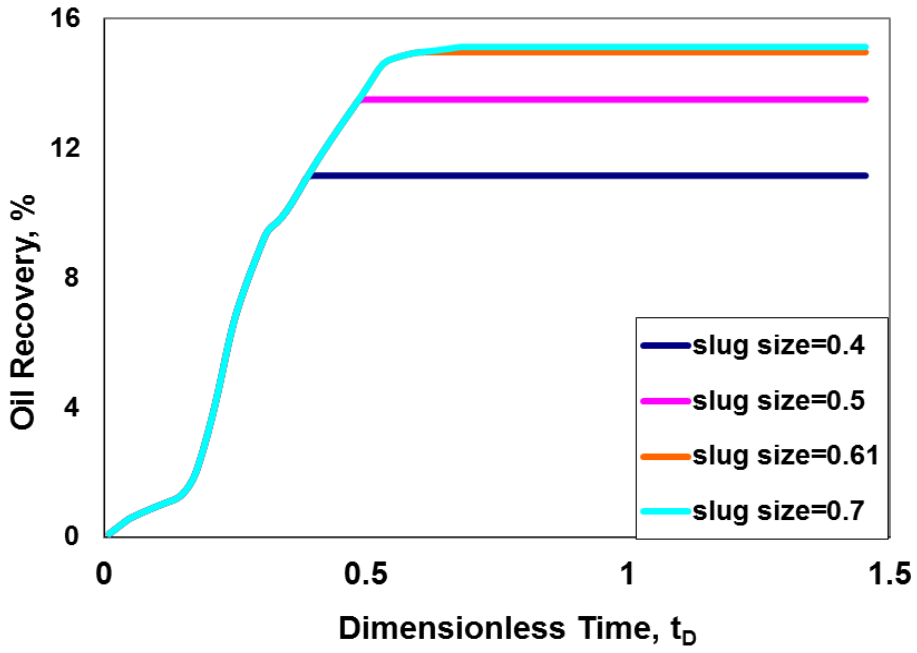

Figure 4.14: Oil recovery curves for four different slug sizes; slug sizes larger than 0.61 P.V. do not affect the oil recovery. For all four cases, P/MMP and N_{Pe} are set to 0.95 and 1025, respectively; V_{DP}, λ_{xD}, N_g and R_L are at their lowest level according to Table 4.5.

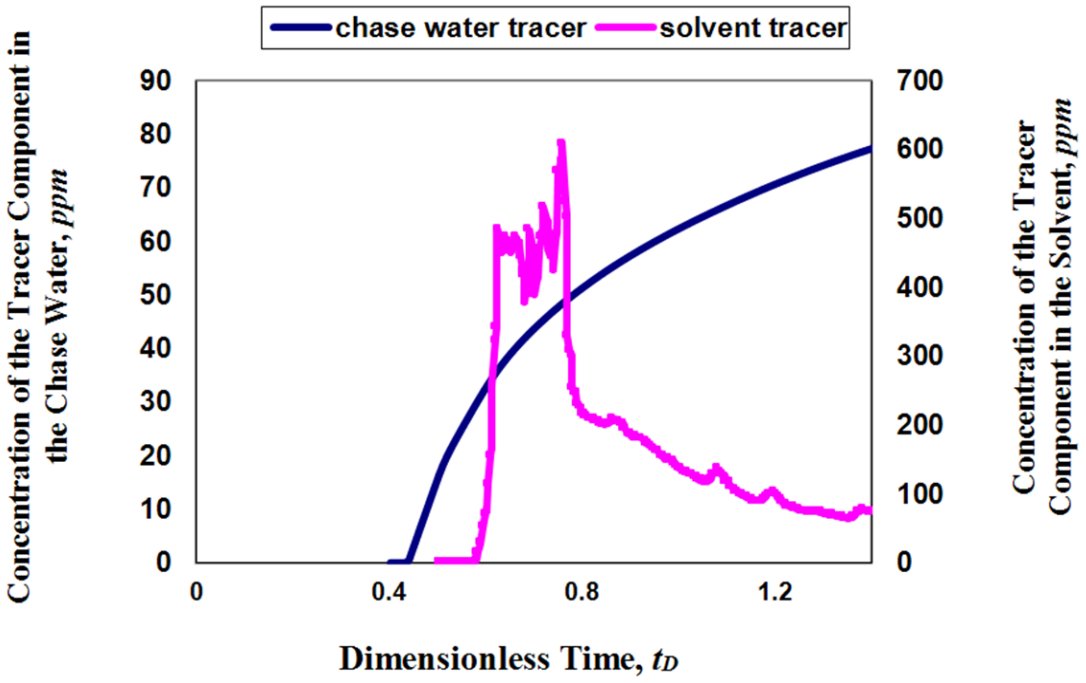

Figure 4.15: Concentration history plots for the tracer component in the chase water and solvent. The plot shows that injecting a smaller solvent-water slug size (0.4) than the optimal (the WL prediction is 0.61) yields an ear;ier chase water breakthrough than the solvent. P/MMP and N_{Pe} are set to 0.95 and 1025, respectively; V_{DP}, N_g, λ_{xD}, and R_L are at their lowest level according to Table 4.5.

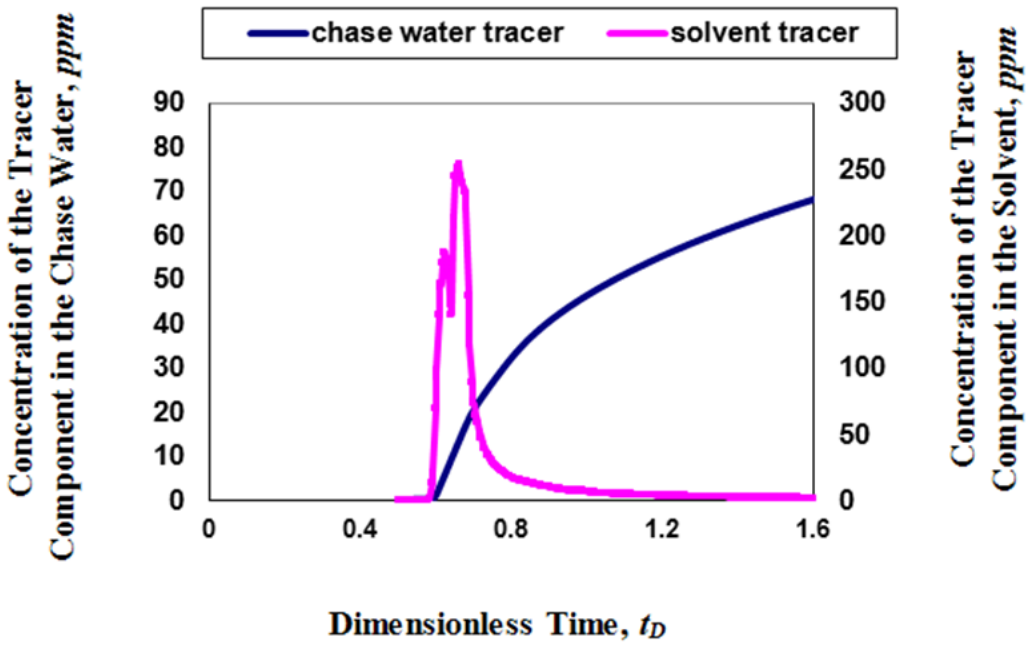

Figure 4.16: Concentration history plots for the tracer component in chase water and solvent. The plot shows that the optimal water-solvent slug size (0.61) yields simultaneous breakthroughs of the solvent and chase water. P/MMP and N_{Pe} are set to 0.95 and 1025, respectively; V_{DP}, N_g, λ_{xD}, and R_L are at their lowest level according to Table 4.5.

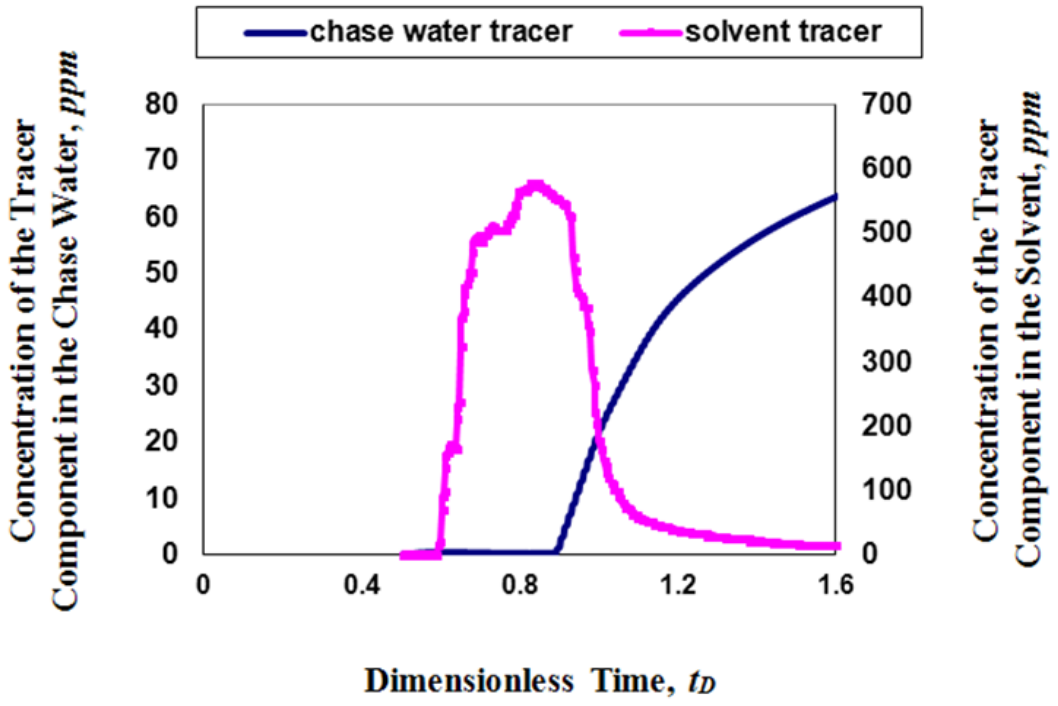

Figure 4.17: Concentration history plots for the tracer component in chase water and solvent. The plot shows that injecting a larger solvent-water slug size (0.8) than the optimal size (0.61) yields a delayed breakthrough for the chase water tracer. P/MMP and N_{Pe} are set to 0.95 and 1025, respectively; V_{DP}, N_g, λ_{xD}, and R_L are at their lowest level according to Table 4.5.

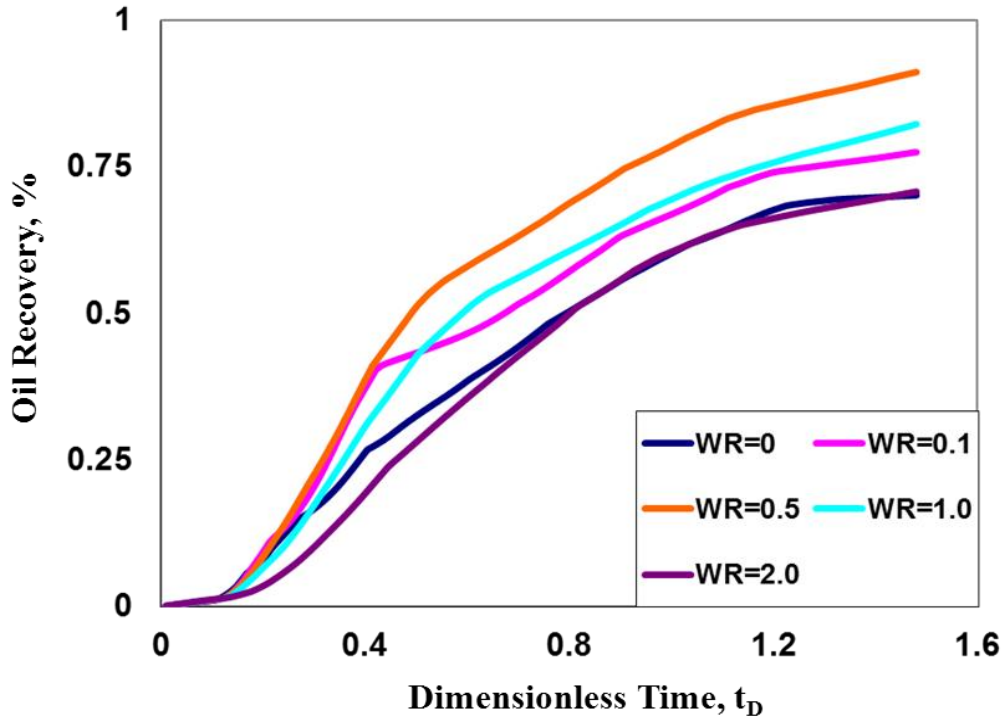

Figure 4.18: Oil recovery curves for a 2D displacement with five different SWAG ratios. The plot illustrates that the SWAG ratio=0.5 (the WL optimal SWAG ratio=0.51) yields the largest recovery. Before the earliest gas BT, the recovery curves are almost identical. P/MMP and N_{Pe} are set to 0.95 and 1025, respectively; V_{DP}, N_g, λ_{xD}, and R_L are at their intermediate level according to Table 4.5.

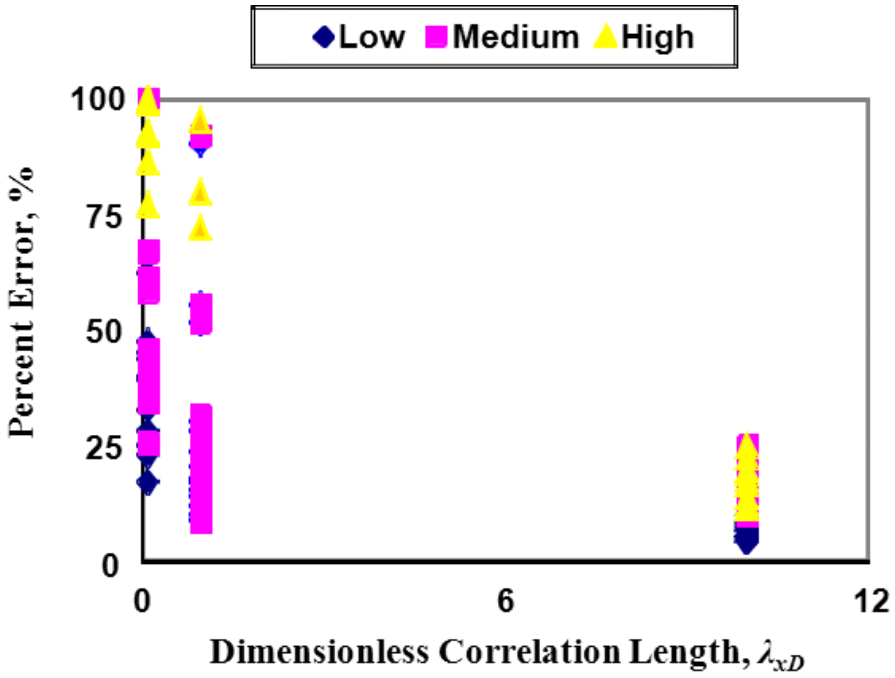

Figure 4.19: Percent errors of the optimal SWAG ratios for all 2D cases as a function of the dimensionless correlation length of the permeability at three different levels of dispersion when R_L=0.1.

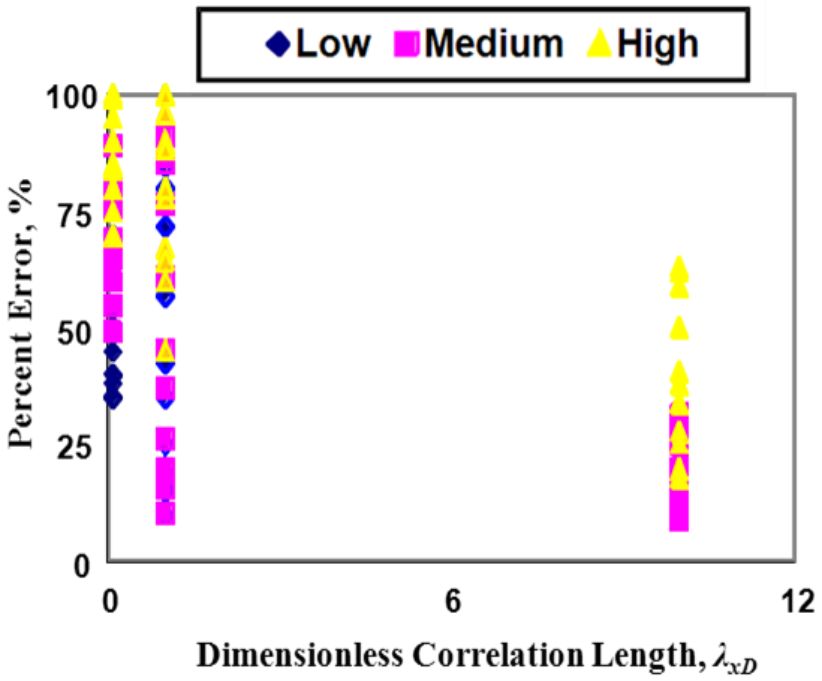

Figure 4.20: Percent errors of the optimal SWAG ratios for all 2D cases as a function of the dimensionless correlation length of the permeability at three different levels of dispersion when R_L=1.0.

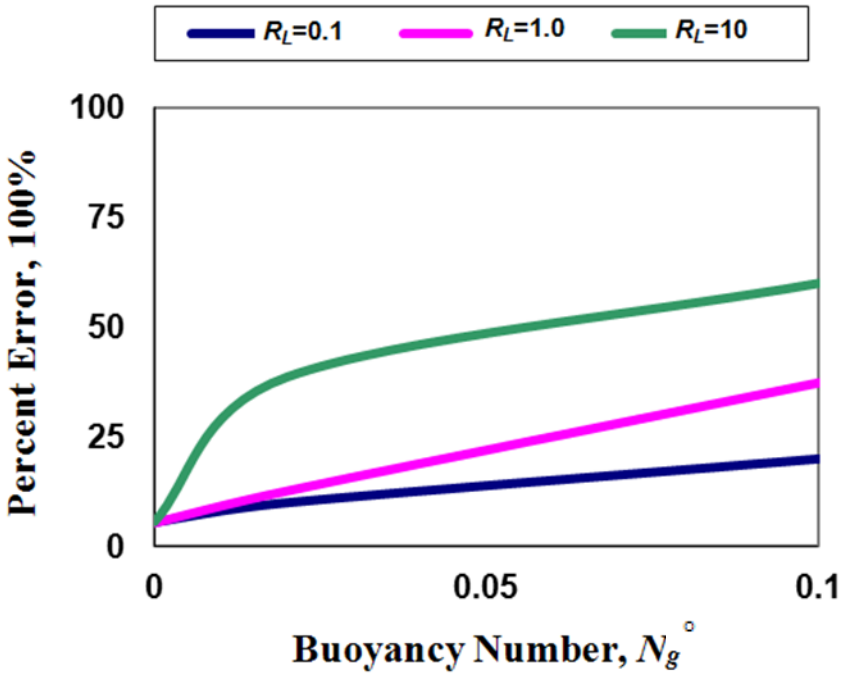

Figure 4.21: Percent error of the optimal SWAG ratios as a function of the end-point buoyancy number(the end-point relative permeability values are used) for fairly homogenous cases (V_{DP} =0.4) at different levels of R_L. As N_g° increases, the percent error increases. The Peclet number is 270.

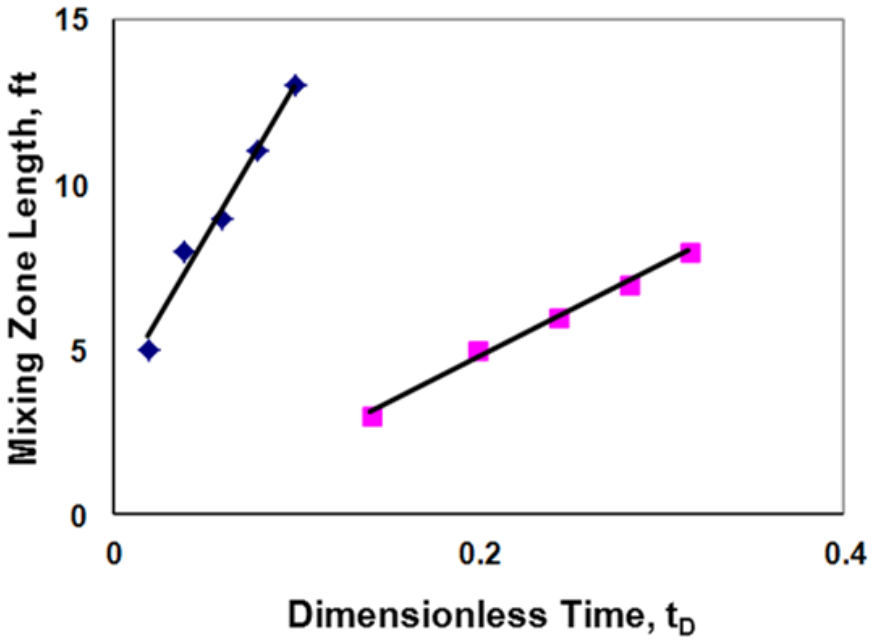

Figure 4.22: Lengths of the mixing zone as a function of the dimensionless time. The plot illustrates the linear growth of the mixing zone for two layers of the case study 1, for which the predicted optimal SWAG ratio agrees with the numerical results. The lengths of the mixing zone are linearly correlated with elapsed time.

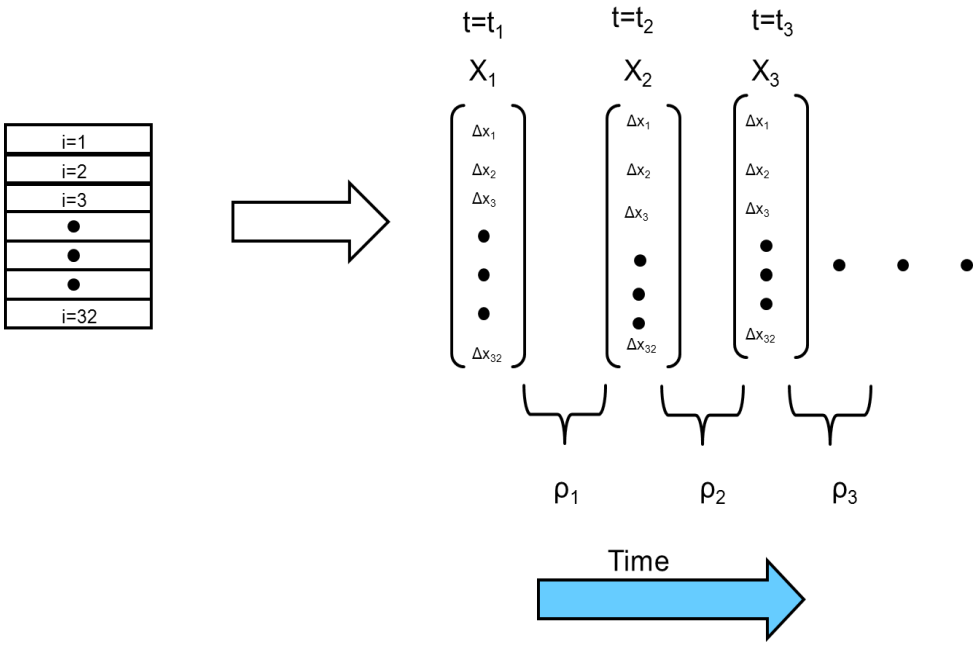

Figure 4. 23: The schematic demonstrates the arrays of the lengths of the mixing zone for a reservoir with 32 layers and the correlation coefficient function, ρ_h, between the arrays.

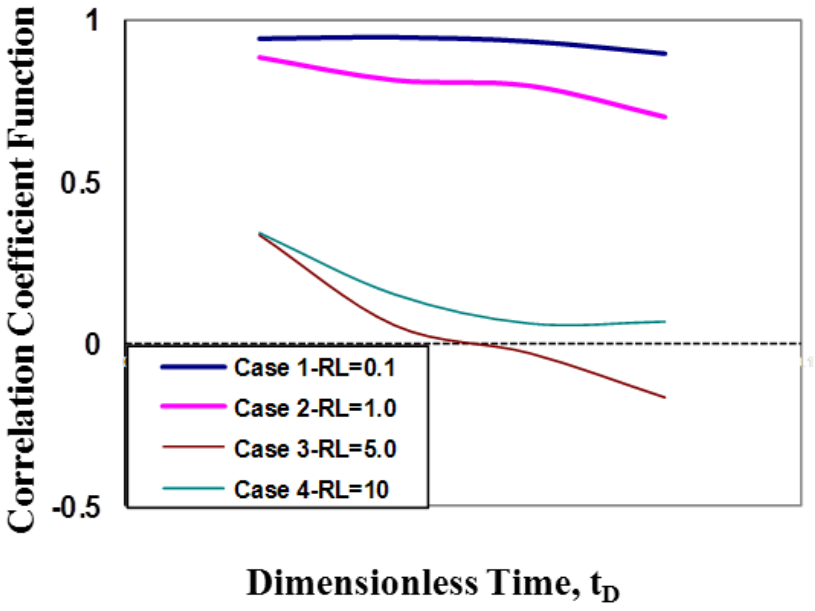

Figure 4.24: Correlation coefficient function of the length of the mixing zone as a function of time. The overall trend shows the linear growth of the mixing zone with time for Cases 1 and 2 as the corresponding correlation coefficient functions stay close to unity; in addition, a non-linear correlation between the lengths of the mixing zone and time is observed for Cases 3 and 4.

Chapter 5: Decoupling of Large- and Small-Scale Heterogeneities in Multi-Layered Reservoirs with No Cross-Flow

This section examines the decoupling of the local heterogeneity and permeability variation in multi-layered reservoirs in the absence of cross-flow between layers. Dispersion caused by local velocity gradients, locally heterogeneous streamline lengths, mechanical dispersion, and diffusion in permeable media, degrades displacement efficiency (as detailed in Chapter 4). Dispersivity, as the measure of dispersion, represents how far tracer particles stray from the path of the fluid carrying them. In other words, tracer particles are gradually spread in all directions around the mean path of flow.

Dispersivity is often obtained from matching the concentration history of tracer tests with a linear one-dimensional (1D) solution of the convection-diffusion (CD) equation. However, convective spreading caused by permeability variations seems to dominate when the 1D solution of the CD equation is used to interpret the tracer test results in heterogeneous permeable media (John, 2008). The impact of convective spreading, which is caused by widely varying breakthrough times of tracer in different layers, is similar to dispersive mixing (dilution) as they both cause dissipation. However, convective spreading is a reversible phenomenon whereas diffusive transport is not (John, 2008).

In this study, the growth of vertically averaged concentrations is formulated through incorporating dispersivity and the permeability variation. This approach uses the Koval heterogeneity factor to replace the need for scale-dependent transmission dispersivities; hence, the vertically averaged concentration in layered media is obtained using dispersivities no larger than input values in this Chapter.

We use a simulation approach to verify the analytical solution derived in this study. The simulation models consist of a vertical injection well and a producer located at

the ends of 2D heterogeneous reservoirs. The injection and production wells are assigned a constant rate and a constant bottomhole pressure constraint, respectively. Numerical dispersion is minimized through simulations and a constant physical (input) dispersivity is used for all grid blocks. The tracer concentrations at grid blocks located at specific distances from the injection well are used from the simulation results to calculate the corresponding vertically averaged concentration. The vertically averaged concentration from simulation is compared with the average concentration obtained from an analytical solution. Moreover, the simulation results match the analytical solution.

We conclude that scale-dependent dispersivity at the field-scale represents the lack of knowledge about the heterogeneity involved in the system we are simulating. Details that are averaged when using a macroscopic approach manifest themselves as an apparent scale-dependent dispersivity caused by velocity variations at the local-scale. In fact, scale-dependent dispersivity in heterogeneous permeable media represents a naive treatment of multi-dimensional displacements with the 1D solution of the CD equation. In this study, dispersivity becomes scale-independent when all involved heterogeneities are modeled explicitly.

The results suggest that the analytical solution accurately predicts the vertically averaged tracer concentration in heterogeneous reservoirs in the absence of cross-flow. Furthermore, the impact of heterogeneity and dispersivity on the length of the mixing zone within each layer of reservoir is evaluated. From that, we determine the fraction of layers in which the mixing zone grows faster than that of the dispersive flow regime as a function of the Koval factor and input dispersivity. The transition between channeling and dispersive flow regimes is clearly shown in the examples. For more details about definition of flow regimes, see Chapter 7.

5.1 INTRODUCTION

The impact of mixing on miscible displacements has been studied in reservoir engineering for decades. However, dispersive transport in heterogeneous permeable media has not yet been understood thoroughly; this issue is severe for layered reservoirs as the flow becomes pre-asymptotic regime (non-Fickian/non-Gaussian; see Chapter 6 for the definition of Fickian regime). As long as the asymptotic behavior is not reached in a heterogeneous permeable medium, the convection-diffusion (CD) equation does not hold. The Fickian model for dispersion assumes a dispersive flux proportional to the concentration gradient with a constant proportionality (dispersivity) independent of time and space.

Despite the vast amount of literature on dispersion, the current practice of using a 1D solution of the CD equation to determine dispersivity is not appropriate for heterogeneous reservoirs especially when considerable autocorrelation is present for permeability. In other words, changes in the dispersivity with distance indicate an inevitable consequence of using a 1D solution of the CD equation to treat multi-dimensional flow. For instance, convective spreading caused by local-scale variations of velocity plays an important role when the 1D solution of the CD equation is used to interpret the tracer test in heterogeneous permeable media.

The convective spreading is incorporated into dispersive mixing to yield very large values of dispersivity obtained in the field-scale. We can distinguish between the convective spreading and dispersive mixing mechanisms as the convective spreading is a reversible phenomenon whereas diffusive transport is not. For more detail about spreading and mixing and how mixing in the small-scale can lead to significant dilution at the large-scale, see John (2008).

Gelhar and Axness (1981) used spectral methods to generate permeability fields and studied the interplay between dispersion and the permeability variability in stratified permeable media. They found that dispersive transport exhibits non-Fickian behavior for a stratified medium in early time and asymptomatically approaches Fickian dispersive transport at late time if there is cross-flow between layers. Matheron and DeMarsily (1980) show that cross-flow between layers would restore Fickian transport, asymptomatically, at late time. Furthermore, Lake and Hirasaki (1981) studied dispersion in stratified formations and concluded that transverse dispersion between layers yields an average longitudinal dispersion coefficient asymptotically.

Several review papers present measured dispersivities over a wide range of length scales (Schulze-Makuch, 2005; Vandeborght and Vereecken, 2007; Zhou *et al.*, 2007). In all of these datasets, the longitudinal dispersivity increases with distance traveled. Furthermore, Su *et al.* (2005) used a dispersivity coefficient that varies with time to match concentration history plots; however, this lacks a clear physical explanation. Greenkorn *et al.* (1983) discussed the scaling of mixing during miscible displacement in heterogeneous permeable media.

In addition, Coats *et al.* (2009) used a constant physical scale-independent dispersivity to account for pore-scale heterogeneity and additional scale-dependent dispersivity reflecting permeability heterogeneity. The latter is used as a fitting parameter to match concentration history plots.

In this section, an analytical solution for the averaged tracer concentration in layered permeable media is presented. We restrict our analysis to tracer flow with a mobility ratio of one and no cross-flow between layers. We assume horizontal permeability to be a random variable with a log-normal distribution. Furthermore, we evaluate the impact of heterogeneity and dispersivity on the growth of the mixing zone

within each. Also, the fraction of layers in which the mixing zone grows faster than that of the dispersive flow regime, is determined as a function of the Koval factor and input dispersivity.

5.2 PROBLEM STATEMENT

Figure 4.1 indicates a stratified permeable medium that consists of an ensemble of *n* layers with different properties: permeability, thickness, and porosity separated by thin barriers that yield no vertical permeability. The cumulative flow capacity *F* and cumulative storage capacity *C* at a given vertical cross-section is defined as (Lake, 1989)

$$F = \sum_{l=1}^{n} \frac{k_l h_l}{H_t \bar{k}} \quad , \qquad l = 1,2,\ldots \text{n (number of layers)} \tag{5.1}$$

where $\bar{k}$ and H_t are the arithmetic average permeability and total thickness of the given cross-section. Therefore,

$$C = \sum_{l=1}^{n} \frac{\phi_l h_l}{H_t \bar{\phi}} \quad , \tag{5.2}$$

where $\bar{\phi}$ is the arithmetic average porosity for that cross-section. From Darcy's law, the interstitial velocity of a passive tracer through each layer is represented by the ratio of permeability to porosity of the same layer $\left(r_l = \frac{k_l}{\phi_l} \right)$. If we rearrange the interstitial velocity of flow in all layers in decreasing order of r_l, F_l represents the fraction of flow at a velocity greater or equal to r_l. Similarly, C_l indicates the associated pore volume with the fraction of flow that travels at the velocity of r_l or faster. From the definition, the derivative of a continuous *F* with respect to *C* at any given C_l is the interstitial velocity

within the corresponding layer divided by the arithmetic average of interstitial velocity of the whole ensemble.

The approximate solution of the CD equation in 1D flow that describes the conservation of the injected component (tracer) through an isothermal miscible displacement has the form of (Lake, 1989)

$$c_D = \frac{1}{2}\left[1 - erf\left(\frac{x_D - t_D}{2\sqrt{\alpha_D t_D}}\right)\right], \tag{5.3}$$

where α_D is the dimensionless dispersivity normalized by the length of the permeable medium; equivalently, we can use the inverse of the Peclet number (N_{Pe}^{-1}) instead of α_D. The above solution is derived considering the following premises: incompressible fluid and pore space, ideal mixing, single phase flow, the same dispersivity (α) for all layers, and semi-infinite medium assumptions.

The arithmetic average of the tracer concentration over a vertical cross-section at the distance of x_D from the injector and at the given time t_D is determined as

$$c_D = \frac{\sum_{l=1}^{n} c_{D,l} h_l}{H_t}, \tag{5.4}$$

where $c_{D,l}$, the dimensionless concentration at each layer, is defined as

$$
\begin{cases}
c_{D,1} = \dfrac{1}{2}\left[1 - erf\left(\dfrac{x_D - \beta_1 t_D}{2\sqrt{\alpha_{D,1} t_D}}\right)\right] \\
c_{D,2} = \dfrac{1}{2}\left[1 - erf\left(\dfrac{x_D - \beta_2 t_D}{2\sqrt{\alpha_{D,2} t_D}}\right)\right] \\
c_{D,3} = \dfrac{1}{2}\left[1 - erf\left(\dfrac{x_D - \beta_3 t_D}{2\sqrt{\alpha_{D,3} t_D}}\right)\right] \\
, \\
\ldots \\
c_{D,n} = \dfrac{1}{2}\left[1 - erf\left(\dfrac{x_D - \beta_n t_D}{2\sqrt{\alpha_{D,n} t_D}}\right)\right],
\end{cases}
$$

where β_l is the fraction of injected volume that enters into layer l. Furthermore, $\alpha_{D,l}$ is the inverse Peclet number of layer l. However, we assume that the Peclet number is the same for all layers in the remainder of this chapter. There is no viscous cross-flow between layers and, thus, the fluid injected in any layer stays within the same layer. Traditionally, the above system of equations should be solved numerically to obtain the c_D for a given t_D and x_D. However, we incorporate the notion of cumulative flow and storage capacities into Eq. (5.4) to find an analytical solution for c_D.

Considering the tracer flow assumptions (mobility ratio of unity and matched density), in addition to no vertical communication, β_l can be interpreted as the fraction of injected volume entering the layer l at the inlet face. The volume injected in each layer remains in the same layer throughout flow as there is no convective cross-flow between layers. Therefore, F can be translated as the cumulative distribution function of β when F

is a continuous function of C. Hence, the derivative of F with respect to C calculated at C_l will be equal to β_l (Jensen *et al*., 2002).

We propose the following analytical solution for the tracer concentration at a layer with cumulative storage capacity of C:

$$c_D\,|_C = \frac{1}{2}\left[1 - erf\left(\frac{x_D - \frac{dF}{dC}|_C\; t_D}{2\sqrt{\alpha_D \frac{dF}{dC}|_C\; t_D}}\right)\right] \tag{5.5}$$

Equation (5.5) is obtained from substitution of $\left(\beta_l t_D\right)$ by $\left(\frac{dF}{dC}|_C\; t_D\right)$ in the 1D solution of the CD equation.

The dimensionless mixing zone within each layer is defined as the distance between locations where the dimensionless concentrations of 0.1 and 0.9 occur. Following Lake (1989),

$$\Delta x_D\,|_C = \left(x_D\,|_C\right)_{c_D=0.1} - \left(x_D\,|_C\right)_{c_D=0.9}\ , \tag{5.6}$$

where $x_D\,|_C$ is distance in the layer with the cumulative storage capacity of C. Also, $\Delta x_D\,|_C$ represents length of the mixing zone normalized by the length of permeable medium.

To calculate the mixing zone, we invert Eq. (5.3) for $\left(x_D\,|_C\right)_{c_D=0.1}$ to yield

$$\left(x_D\,|_C\right)_{c_D=0.1} = 2erfc^{-1}\left((0.2)\sqrt{\alpha_D \frac{\partial F}{\partial C}|_C\; t_D}\right) + \frac{\partial F}{\partial C}|_C\; t_D\,. \tag{5.7}$$

Similarly, we determine $\left(x_D\,|_C\right)_{c_D=0.9}$ and substitute into Eq.(5.6); hence,

$$\Delta x_D\,|_C = 3.625\sqrt{\alpha_D \frac{\partial F}{\partial C}|_C\, t_D}\,. \tag{5.8}$$

5.3 DERIVATION

In this section, we determine the vertically averaged dimensionless concentration of traced as a function of x_D, t_D, H_K, and α_D. The integration of $c_D\,|_C$ over an interval [C_1, C_2] yields the vertically averaged concentration (according to the integral mean value theorem):

$$c_D = \frac{\int_{C_1}^{C_2} c_D\,|_C\, dC}{C_2 - C_1}. \tag{5.9}$$

Thus, the first step to solve Eq. (5.9) is to determine the derivative of F with respect to C, $\frac{dF}{dC}$. Using the Koval (1963) heterogeneity factor, the following relationship between F and C holds true:

$$\frac{F}{1-F} = \frac{C}{1-C} H_K. \tag{5.10}$$

where H_k is the Koval heterogeneity factor. Inverting Eq. (5.10) gives

$$\frac{1-F}{F} == \frac{1-C}{C} H_K\,.$$

Hence, F can be expressed as

$$F = \frac{C}{1 - C + CH_K} H_K \qquad . \tag{5.11}$$

Differentiation of F with respect to C yields an expression for $\frac{dF}{dC}$ as

$$\frac{dF}{dC} = \frac{H_K}{\left[1+(H_K-1)C\right]^2} \quad . \tag{5.12}$$

All terms on the right side of Eq. (5.12) are positive; hence, the square root of $\frac{dF}{dC}$ can be expressed as

$$\sqrt{\frac{dF}{dC}} = \frac{\sqrt{H_K}}{\left[1+(H_K-1)C\right]} \quad . \tag{5.13}$$

The next step is to insert Eq. (5.13) into Eq. (5.5) to determine the integration of the numerator of Eq.(5.9). However, there is no analytical solution for Eq. (5.9) in the standard integral tables. Therefore, we use the method of variable transformation (the substitution rule) and consider the argument of the error function as interim variable *z*:

$$z = \frac{x_D}{2\sqrt{\alpha_D \frac{dF}{dC} t_D}} - \frac{\sqrt{\frac{dF}{dC} t_D}}{2\sqrt{\alpha_D}} \quad . \tag{5.14}$$

Rearranging Eq. (5.14) gives

$$t_D\left(\sqrt{\frac{dF}{dC}}\right)^2 + 2\sqrt{\alpha_D t_D}\, z \sqrt{\frac{dF}{dC}} - x_D = 0 \quad . \tag{5.15}$$

However, there are two roots (described below) and the non-negative solution of the quadratic equation (because $\sqrt{\frac{dF}{dC}}$ is always positive) that represent a proper relation between the newly defined variable *z* and $\frac{dF}{dC}$. The general form of the solution of Eq. (5.15) is defined as

$$\sqrt{\frac{dF}{dC}} = \frac{-b \pm \sqrt{b^2 - 4ac}}{2a} \quad , \tag{5.16}$$

where

$$a = t_D$$

$$b = 2\sqrt{\alpha_D t_D}\, z$$

$$c = -x_D \quad .$$

Further investigation shows that the root with a positive square root of the discriminant always leads to the non-negative solution. Therefore,

$$\sqrt{\frac{dF}{dC}} = \frac{-\sqrt{\alpha_D t_D}\, z + \sqrt{\left(\sqrt{\alpha_D t_D}\, z\right)^2 + t_D x_D}}{t_D} \tag{5.17}$$

.

Next, we insert Eq. (5.17) into Eq. (5.13) to determine the relation between cumulative storage capacity *C* and *z*:

$$\frac{\sqrt{H_K}}{\left[1 + (H_K - 1)C\right]} = \frac{-\sqrt{\alpha_D t_D}\, z + \sqrt{\left(\sqrt{\alpha_D t_D}\, z\right)^2 + t_D x_D}}{t_D} \tag{5.18}$$

.

Rearranging Eq. (5.18) yields an expression for the cumulative storage capacity as a function of x_D and t_D:

$$C = \frac{1}{(H_K - 1)} \left(\frac{t_D \sqrt{H_K}}{\left(-\sqrt{\alpha_D t_D}\, z + \sqrt{\left(\sqrt{\alpha_D t_D}\, z\right)^2 + t_D x_D} \right)} - 1 \right) \quad . \tag{5.19}$$

Also, we recast the integral in the numerator of Eq. (5.9) using the variable transformation. To determine the derivative with respect to the newly defined variable, we use the chain rule as

$$c_D = \frac{\int_{C_1}^{C_2} c_D\,|_C \, dC}{C_2 - C_1} = \frac{\int_{z_1}^{z_2} c_D\,|_z \, \frac{dC}{dz} dz}{z_2 - z_1} \quad . \tag{5.20}$$

To evaluate the above equation, we must determine the derivative of C with respect to $z, \left(\frac{dC}{dz} \right)$, which can be expressed as

$$\frac{dC}{dz} = \frac{t_D \sqrt{H_K}}{(H_K - 1)} \left(\frac{\sqrt{\alpha_D t_D} - \frac{z \alpha_D t_D}{\sqrt{\left(\sqrt{\alpha_D t_D}\, z \right)^2 + t_D x_D}}}{\left(-\sqrt{\alpha_D t_D}\, z + \sqrt{\left(\sqrt{\alpha_D t_D}\, z \right)^2 + t_D x_D} \right)^2} \right) \quad . \tag{5.21}$$

Still, there is no general equation for the integral in the numerator of Eq.(5.20):

$$\int_{z_1}^{z_2} c_D\,|_z \, \frac{dC}{dz} dz = 0.5 \int_{z_1}^{z2^2} \left(1 - Erf\,(z)\right) \frac{t_D \sqrt{H_K}}{(H_K - 1)} \left(\frac{\sqrt{\alpha_D t_D} - \frac{z \alpha_D t_D}{\sqrt{\left(\sqrt{\alpha_D t_D}\, z \right)^2 + t_D x_D}}}{\left(-\sqrt{\alpha_D t_D}\, z + \sqrt{\left(\sqrt{\alpha_D t_D}\, z \right)^2 + t_D x_D} \right)^2} \right) dz \,. \tag{5.22}$$

Using integration by parts, which is based upon the product rule for differentiation, we rearrange the right side of Eq. (5.22) as

$$\int \mathrm{Erfc}(z)\frac{t_D\sqrt{H_K}}{(H_K-1)}\left(\frac{\sqrt{\alpha_D t_D}-\frac{z\alpha_D t_D}{\sqrt{\left(\sqrt{\alpha_D t_D}\,z\right)^2+t_D x_D}}}{\left(-\sqrt{\alpha_D t_D}z+\sqrt{\left(\sqrt{\alpha_D t_D}\,z\right)^2+t_D x_D}\right)^2}\right)dz$$

$$= \mathrm{Erfc}(z)\overbrace{\left[\int \frac{\sqrt{\alpha_D t_D}-\frac{z\alpha_D t_D}{\sqrt{\left(\sqrt{\alpha_D t_D}\,z\right)^2+t_D x_D}}}{\left(-\sqrt{\alpha_D t_D}\,z+\sqrt{\left(\sqrt{\alpha_D t_D}\,z\right)^2+t_D x_D}\right)^2}dz\right]}^{A} - \int \mathrm{d}(\mathrm{Erfc}(z))\overbrace{\left[\int \frac{\sqrt{\alpha_D t_D}-\frac{z\alpha_D t_D}{\sqrt{\left(\sqrt{\alpha_D t_D}\,z\right)^2+t_D x_D}}}{\left(-\sqrt{\alpha_D t_D}z+\sqrt{\left(\sqrt{\alpha_D t_D}\,z\right)^2+t_D x_D}\right)^2}dz\right]}^{A} dz \quad .$$

(5.23)

Furthermore, the solution for the integral A on the right side of Eq. (5.23) can be expressed as

$$\int \left(\frac{\sqrt{\alpha_D t_D}-\frac{z\alpha_D t_D}{\sqrt{\left(\sqrt{\alpha_D t_D}\,z\right)^2+t_D x_D}}}{\left(-\sqrt{\alpha_D t_D}\,z+\sqrt{\left(\sqrt{\alpha_D t_D}\,z\right)^2+t_D x_D}\right)^2}\right)dz = \frac{\sqrt{\alpha_D t_D z^2+t_D x_D}+\sqrt{\alpha_D t_D}z}{t_D x_D}.$$

. (5.24)

Also, the derivative of the complementary error function is determined as

$$\frac{d(Erfc(z))}{dz} = -\frac{2}{\sqrt{\pi}} e^{-z^2} \quad . \tag{5.25}$$

Therefore, Eq. (5.23) is written as

$$\int Erfc(z) \frac{t_D \sqrt{H_K}}{(H_K - 1)} \left(\frac{\sqrt{\alpha_D t_D} - \frac{z \alpha_D t_D}{\sqrt{\left(\sqrt{\alpha_D t_D}\, z\right)^2 + t_D x_D}}}{\left(-\sqrt{\alpha_D t_D}\, z + \sqrt{\left(\sqrt{\alpha_D t_D}\, z\right)^2 + t_D x_D} \right)^2} \right) dz$$

$$= \frac{\sqrt{H_K}}{(H_K - 1) x_D} \left(\begin{array}{l} Erfc(z)\left(\sqrt{\alpha_D t_D z^2 + t_D x_D} + \sqrt{\alpha_D t_D}\, z \right) \\ + \frac{1}{\sqrt{\pi}} \sum_{n=1}^{\infty} \frac{(-1)^{n+1}}{(n-1)!} z^{2n} \left(\frac{\sqrt{\alpha_D t_D}}{n} - \frac{2 t_D x_D \sqrt{\frac{\alpha_D}{x_D} z^2 + 1}\; {}_2F_1\left[-\frac{1}{2}, n - \frac{1}{2}; n + \frac{1}{2}; -\frac{\alpha_D}{x_D} z^2 \right]}{(z - 2nz) \sqrt{\alpha_D t_D z^2 + t_D x_D}} \right) \end{array} \right) .$$

(5.26)

Finally, we insert Eq. (5.26) back into Eq.(5.20):

$$c_D = \frac{0.5}{z_2 - z_1} \left(\frac{\sqrt{H_K}}{(H_K - 1) x_D} \left(\begin{array}{l} Erfc(z)\left(\sqrt{\alpha_D t_D z^2 + t_D x_D} + \sqrt{\alpha_D t_D}\, z \right) \\ - \frac{1}{\sqrt{\pi}} \sum_{n=1}^{\infty} \frac{(-1)^{n+1}}{(n-1)!} z^{2n} \left(\frac{\sqrt{\alpha_D t_D}}{n} - \frac{2 t_D x_D \sqrt{\frac{\alpha_D}{x_D} z^2 + 1}\; {}_2F_1\left[-\frac{1}{2}, n - \frac{1}{2}; n + \frac{1}{2}; -\frac{\alpha_D}{x_D} z^2 \right]}{(z - 2nz) \sqrt{\alpha_D t_D z^2 + t_D x_D}} \right) \end{array} \right) \right) \Bigg|_{z_1}^{z_2},$$

(5.27)

where, ${}_2F_1$ is the first hypergeometric function (Gauss's hypergeometric function) that arises in physical problems (Barnes, 1908). In general form, the first hypergeometric function for arbitrary parameters a, b, and c and variable *z* is expressed as

$$ {}_2F_1(a,b;c;z) = 1 + \frac{ab}{1!c}z + \frac{a(a+1)b(b+1)}{2!c(c+1)}z^2 + \ldots = \sum_{n=0}^{\infty} \frac{(a)_n (b)_n}{(c)_n} \frac{z^n}{n!}. \tag{5.28} $$

Furthermore, z_1 and z_2 (interim variables) are determined through Eq. (5.13) and Eq. (5.14) as

$$ \begin{cases} \text{If } C_1 = 0 \xrightarrow{\text{Eq.5.13}} \sqrt{\dfrac{dF}{dC}} = \sqrt{H_K} \xrightarrow{\text{Eq.5.14}} z_1 = \dfrac{x_D - \dfrac{dF}{dC} t_D}{2\sqrt{\alpha_D \dfrac{dF}{dC} t_D}} = \dfrac{x_D - H_K t_D}{2\sqrt{\alpha_D H_K t_D}} \\ \text{If } C_2 = 1 \xrightarrow{\text{Eq.5.13}} \sqrt{\dfrac{dF}{dC}} = \dfrac{1}{\sqrt{H_K}} \xrightarrow{\text{Eq.5.14}} z_2 = \dfrac{x_D - \dfrac{dF}{dC} t_D}{2\sqrt{\alpha_D \dfrac{dF}{dC} t_D}} = \dfrac{x_D - \dfrac{1}{H_K} t_D}{2\sqrt{\alpha_D \dfrac{1}{H_K} t_D}} \end{cases}. \tag{5.29} $$

Basically the flow becomes 1D when the Koval heterogeneity factor tends to unity. we can show analytically that the proposed analytical solution reduces to 1D solution of CD equation when the Koval factor becomes unity. Inserting H_K=1.0 into Eq. (5.13) yields

$$ \sqrt{\frac{dF}{dC}} = \frac{\sqrt{H_K}}{[1 + (H_K - 1)C]} \xrightarrow{H_K = 1} \sqrt{\frac{dF}{dC}} = 1.0 . \tag{5.30} $$

Inserting Eq. (5.30) into Eq.(5.5) yields Eq.(5.3), which is 1D solution of CD equation. Furtheremore, the length of the mixing zone becomes zero as α_D tends to zero in Eq. (5.8) and the displacement within each layer turns into piston-like displacement.

In addition, we compare concentrations obtained from Eq. (5.27) with those obtained from the 1D solution of CD equation for H_K=1.001. We compare the concentrations as a function of dimensionless distance at the fixed t_D=0.5 for two values of α_D: 0.01 and 1E-10. Figure 5.2 compares the concentrations obtained from Eq. (5.27) and those of the 1D solution of CD equation when H_K=1.001 and α_D =1E-2. Both curves coincide illustrating that Eq. (5.27) produces the same result as the 1D solution of CD equation when H_K tends toward unity.

Figure 5.3 compares the concentrations obtained from Eq. (5.27) and those of the 1D solution of CD equation when H_K=1.001 and α_D =1E-10. Both curves coincide showing that Eq. (5.27) produces the same result as the 1D solution of CD equation when H_K tends toward unity.

Similarly,

5.4 MIXING ZONE ANALYSIS

In this section, we evaluate the growth of mixing zone within layers of a heterogeneous reservoir without cross-flow. Figure 5.4 shows the map of tracer concentrations of 0.1 and 0.9 depicted at t_D=0.5 for each layer (which is represented by C) as a function of distance from the injector. In these examples α_D = 0.0001. The distance is normalized by the length of the permeable medium. The flow occurs basically in 1D when H_k is one. These curves are obtained from Eq. (5.5) for various values of H_K. A comparison between the lengths of the mixing zone, which is the distance between c_D = 0.1 and c_D = 0.9, for different cases reveals that the mixing zone shrinks as H_k increases; however, the length of the mixing zone does not decrease uniformly within all layers.

Note that each layer of the permeable medium is represented by the corresponding cumulative storage capacity.

The length of the mixing zone reaches a maximum at $C = 0.3$ when H_k is 100. This is an interesting observation as it illustrates a distinct transition of flow patterns over the range of $0.2 < C < 0.4$. A small fraction of injected volume enters into layers with a larger cumulative storage capacity ($C > 0.4$) and, hence, small dimensionless length of the mixing zone is expected from Eq. (5.8). Furthermore, most of the injected fluid gets into layers with a smaller cumulative storage capacity ($C < 0.2$); hence, the flow pattern within these layers is no longer dispersive; instead, channeling occurs as will be discussed in the next section. Note that a larger cumulative storage capacity represents smaller conductivity and vice versa. For more information regarding the flow patterns, see Chapter 7.

Figure 4.5 compares the lengths of the mixing zone at $t_D = 0.5$ for two cases: H_k =1 and $H_k = 10$ when α_D is equal to 0.0001. The length of the mixing zone is obtained from Eq. (5.8). The length of the mixing zone is constant for $H_k = 1$ as it represents 1D flow. However, the mixing zone grows differently within layers when $H_k = 10$. It grows faster than $H_k = 1$ within layers represented by a cumulative storage capacity smaller than 0.25. Larger flow velocity in those layers yields the channeling flow regime as will be discussed in the next section. Less injected fluid permeates into layers, which is represented by larger cumulative storage capacity values; thus, the dispersive transport dominates over the convective flow.

Figure 4.6 compares the lengths of the mixing zone at $t_D = 0.5$ for two cases: H_k = 1 and H_k =100 when α_D is equal to 0.0001. The length of the mixing zone is obtained from Eq. (5.8). The mixing zone grows differently within layers when H_k = 100. It grows faster than H_k = 1 within layers represented by a cumulative storage capacity smaller than 0.10. Larger flow velocity in those layers indicates the channeling flow regime as discussed in the next section. Less injected fluid flows into layers represented by a larger cumulative storage capacity, and, consequently, dispersive transport dominates over the convective flow.

Figure 5.7 illustrates the cumulative flow capacity as a function of dimensionless lengths of the mixing zone depicted at t_D=0.5 for two cases: H_k =1 and H_k =100 when α_D = 0.0001. The length of the mixing zone is obtained from Eq. (5.8). For the case of H_K = 100, the mixing zone grows faster than H_K=1.0 (in large fraction of bulk flow~0.92) because the flow is convection-dominated. Analyzing Figures 5.7 and 5.8 reveals that 92% of flow passes through only 10 % of the whole reservoir thickness when H_K=100 and α_D = 0.0001.

Figure 4.8 shows the map of tracer concentrations of 0.1 and 0.9 depicted at t_D=0.5 for each layer (which is represented by C) as a function of distance from the injector. In these examples α_D = 0.01. The distance is normalized by the length of the permeable medium. These curves are obtained from Eq. (5.5)for various values of H_K. The lengths of the mixing zone are an order of magnitude larger than those depicted at Figure 4.4, consistent with Eq. (5.8). Similar to Figure 4.4, the mixing zone shrinks as H_k increases; however, the length of the mixing zone does not decrease uniformly within all

layers. Across layers that are represented by a cumulative storage capacity greater than 0.4, the concentration of 0.9 does not occur except at $x_D = 0.0$ when $H_k = 100$ (*i.e.*, small fraction of injected volume enters into the corresponding layers). However, a sufficient amount of the injected volume flows into layers represented by a smaller cumulative storage capacity ($C < 0.4$); thus, different flow patterns occur within layers as discussed in the next section.

Figure 4.9 compares the lengths of the mixing zone at t_D=0.5 for two cases: H_k = 1 and H_k = 10 when α_D is equal to 0.01. The length of the mixing zone is obtained from Eq. (5.8). The mixing zone grows differently within layers when H_k = 10. Similar to Figure 4.5, it grows faster than H_k = 1 within layers represented by a cumulative storage capacity smaller than 0.25. Larger flow velocity in those layers indicates the channeling flow regime as discussed in the next section. Less injected fluid gets into the layers, represented by larger cumulative storage capacity values; consequently, the dispersive transport dominates over the convective flow.

Figure 4.10 compares the lengths of the mixing zone at t_D=0.5 for two cases: H_k = 1 and H_k =100 when α_D is equal to 0.01. The length of the mixing zone is obtained from Eq. (5.8). The mixing zone grows differently within layers when H_k =100. Similar to Figure 4.6, it grows faster than H_k =1 within layers represented by a cumulative storage capacity smaller than 0.10. Larger flow velocity in those layers indicates the channeling flow regime as discussed in the next section. Less injected fluid gets into the layers, represented by a larger cumulative storage capacity; thus, the dispersive transport dominates over the convective flow.

5.5 CONCENTRATION HISTORY PLOTS

In this section, we evaluate the change in concentration with time at a fixed location within different layers of a heterogeneous reservoir without cross-flow. Figure 5.11 shows the concentration history plots (concentrations as a function of time) when H_k =1 for three different values of α_D, depicted at x_D = 0.5. Larger spreading occurs as α_D increases, consistent with Eq. (5.3).

Figure 4.12 shows the concentration history plots for selected layers (represented by various cumulative storage capacities) depicted at x_D = 0.5 when H_k = 10 and α_D = 0.01. Furthermore, a comparison between the curves reveals that less spreading occurs for C = 0.1; however, Figure 4.9 indicates that the mixing zone grows faster for small cumulative storage capacity than for 1D dispersive flow. Therefore, the flow regime must have changed to channeling in which the mixing zone develops faster (proportional to time) rather than the square root of time as is in the dispersive flow pattern.

Figure 4.13 shows the concentration history plots for selected layers (represented by various cumulative storage capacity values) depicted at x_D=0.5 when H_k = 100 and α_D = 0.01. Less conductivity occurs the larger the cumulative storage capacity is and, thus, the concentration curve starts at a later time. For C = 0.8, the tracer has not arrived at x_D = 0.5 even after 10 pore volume (P.V.) injection. Furthermore, a comparison between the curves reveals that less spreading occurs for C = 0.1; however, Figure 4.10 indicates that the mixing zone grows faster within layers represented by a small cumulative storage capacity rather than 1D dispersive flow if compared at the same time. Therefore, the channeling flow regime occurs within those layers because the mixing zone develops

faster (proportional to time) rather than the square root of time as in the dispersive flow pattern. Despite the case in which H_k = 10, the injected fluid does not breakthrough within all layers when H_k = 100 at the specified time and location. This is explained by the greater level of the permeability heterogeneity when H_k = 100. Furthermore, if we use Eq. (5.3) to determine the apparent dispersivity for each layer of this example, different values will be obtained despite the fact that all layers are assigned the same dispersivity value; this clearly demonstrates how the treatment of 2D displacement with the 1D solution of the CD equation can be misinterpreted.

Figure 4.14 shows concentration history plots for selected layers (represented by cumulative storage capacities of 0.1, 0.3, and 0.5) depicted at values depicted at x_D = 0.5 when H_k = 10 and α_D = 0.0001. In general, less spreading occurs compared to Figure 4.12. Less conductivity is present the larger the cumulative storage capacity is and, thus, the concentration curve starts at a later time.

Figure 4.15 shows concentration history plots for selected layers (represented by cumulative storage capacities of 0.1, 0.3, and 0.5) values depicted at x_D = 0.5 when H_k = 100 and α_D = 0.0001. In general, less spreading occurs compared to Figure 4.13. Less conductivity is present the larger the cumulative storage capacity is; therefore, the concentration curve starts at a later time. For C = 0.8, the tracer has not arrived at x_D = 0.5 even after 10 P.V. injection. Furthermore, a comparison between the curves reveals that less spreading occurs for C = 0.1; however, Figure 4.6 indicates that the mixing zone grows faster for a small cumulative storage capacity rather than for 1D dispersive flow. Therefore, the flow regime must have changed to channeling, in which the mixing zone

develops faster (proportional to time) compared to the square root of time as in the dispersive flow pattern. Despite the case in which H_k = 10, the injected fluid does not breakthrough within all layers when H_k = 100 at the specified time and location. This is explained by the greater level of permeability heterogeneity in the latter case.

5.6 VERTICALLY AVERAGED CONCENTRATIONS AS A FUNCTION OF DISTANCE

In this section, we evaluate the change in the vertically averaged concentration with distance at a fixed time in a heterogeneous reservoir without cross-flow. Figure 4.16 shows the vertically averaged concentration as a function of dimensionless distance (normalized by the length of the permeable medium) using Eq. (5.27); the concentration profile is depicted at t_D = 0.5 and the Koval heterogeneity as a factor of one. As α_D decreases, less dispersion and less spreading occurs. The results are consistent with the 1D solution of Eq. (5.3), as H_K = 1 represents the no-flow channeling effect.

Figure 4.17 indicates the vertically averaged concentration as a function of dimensionless distance (normalized by the length of the permeable medium) using Eq. (5.27); the concentration profile is depicted at t_D = 0.5 and the Koval heterogeneity factor of 10. As α_D decreases less dispersion and less spreading occurs. As a result of the flow channeling that occurs (because of a large Koval factor), less sweep efficiency is realized (for more details, see Chapter 7).

Figure 4.18 shows the vertically averaged concentration as a function of dimensionless distance (normalized by the length of the permeable medium) using Eq. (5.27); the concentration profile is depicted at t_D = 0.5 and the Koval heterogeneity as a factor of 100. Similar to Figure 4.17, less sweep efficiency is realized. Furthermore, in the presence of large permeability heterogeneity, the impact of dispersivity becomes insignificant.

5.7 VERIFICATION

A simulation approach is used to verify the hypothesis for stratified heterogeneous permeable media with no cross-flow between layers. The simulations are performed using GEM, CMG's general equation-of-state compositional reservoir simulator. The simulation models consist of vertical injectors and producers located at the ends of a 2D grid with constant grid block sizes in the *x*- and *z*-directions. The permeable medium is initially filled with water and a passive tracer (tagged water) is injected to measure local mixing (Lake, 1989). The top and bottom of the models are no-flow boundaries. The injection and production wells are assigned a constant rate and a constant bottomhole pressure constraint, respectively. The bottomhole pressure for the producer is set to the initial pressure and the injection rate is 0.27 P.V. per day. Table 5.1 details the other properties of the models. In addition, simulations are continued until t_D = 3. Heterogeneous permeability fields with the log-normal distribution are generated using the FFTsim code (Jennings *et al.*, 2002). Furthermore, a uniform porosity of 0.14 is considered.

Simulation models consist of 1024 x 32 grid-blocks in the *x*- and *z*-directions. The length and width of the models are 128 and 3.2 feet, respectively. Furthermore, the effective aspect ratio, a measure of viscous cross-flow between layers (R_L), set to zero to represent no convective cross-flow between layers (see Appendix C for more details on the dimensionless scaling groups).

Equation (5.31) shows the Peclet number attributed to numerical dispersion for two-phase flow (Orr, 2007). Considering no input physical dispersivity, the Peclet

number attributed to the longitudinal numerical dispersivity is 2847, (α_L^{Num} =0.045 ft), as $\left(\frac{df_j}{dS_j}\right)$ is equal to one (tracer flow) and Δt_D is 0.001 in the simulations.

$$N_{pe}^{-1}|_{Num.} = \frac{\Delta x_D}{2}\frac{df_j}{dS_j}\left(1-\frac{\Delta t_D}{\Delta x_D}\frac{df_j}{dS_j}\right) \quad . \tag{5.31}$$

An input longitudinal physical dispersivity of 1.45 ft is added to each grid block so that the total dispersivity increases to 1.495 ($\alpha_L^{Num}+\alpha_L^{Phys}$ =1.495 ft); therefore, the Peclet number is now reduced to 86.

Figure 4.19 indicates the flow velocity for selected grid blocks located at different layers as a function of time. Following from the continuity equation for incompressible fluid, the velocity at which fluids pass through each grid block (at any time) is the same as the velocity that occurs across the layer. Furthermore, flow velocities though different layers of the permeable medium are constant values with time as a constant rate is injected and no convective cross-flow occurs between layers.

The tracer concentrations at grid blocks located at equally spaced vertical cross-sections are used to determine the vertically averaged concentration. Next, the vertically averaged concentrations obtained from the simulations are compared with the values obtained from Eq. (5.27) at different times. Dimensionless time used in Eq. (5.27) corresponds to the injected pore volume as the injected volume divided by the formation's pore volume. Solver, Microsoft® Excel's optimization tool, is used to match the average concentrations at each distance from the injector. The objective function is to minimize the squared differences between the simulation results and the analytical

solution; this can be performed by changing the Koval heterogeneity factor (H_K) and dispersivity value (α_D) in Eq. (5.27) (Figure 4.20 through Figure 4.25).

Using Eq.(5.27) with input dispersivity values, we could match simulation results when the permeability fields has small correlation length; however, as Figure 4.26 indicates, scale-dependent dispersivities are needed to match the simulation results with Eq.(5.3). In other words, scale-dependent dispersivity is not required to describe the displacement performance if large- and small-scale heterogeneities are properly incorporated as in Eq.(5.27).

Figure 4.27 shows the optimized Koval factor values obtained separately at each distance while dispersivities are limited to the input value. An average constant value of 5.3 for the Koval factor is proper to describe the displacement using Eq.(5.27).

Figure 4.28 compares the dispersivity required to match the simulation results using Eq. (5.27) with those obtained from Eq. (5.3) when the permeability distribution has a large correlation length. A similar observation to the previous example is obtained as the average concentration is well-matched with input dispersivity.

Figure 4.29 illustrates the Koval factors used to match the simulation concentrations at each distance. A comparison between Figure 4.28 and Figure 4.29 indicate that a larger H_K is needed to match the simulation results using Eq.(5.27); this is expected because of a larger permeability dimensionless correlation length and more channeling in the second example. However, the Koval factor used to match the concentrations varies with distance in this example; it initially increases then decreases afterward. This observation can be explained as flow becomes more dispersive further

from the injection well when the permeability is highly correlated with distance (See Chapter 6 for more details).

5.8 DISCUSSION

In this study, we decouple the convective spreading from local-scale heterogeneity for heterogeneous reservoirs with no cross-flow between layers. In other words, the need for scale-dependent dispersivity is replaced by the Koval factor to match the vertically averaged concentration over a cross section. Our results are consistent with Coats *et al.* (2009) as they used scale-independent dispersivity and a fitting parameter to match concentration history plots using a 1D solution of the CD equation. However, we incorporate the Koval factor (large-scale heterogeneity measure) into the commonly used solution of the CD equation instead of a fitting parameter. In the present study, transverse dispersivity is ignored; however, transverse dispersion in layered systems may play an important role as described by Lake and Hirasaki (1981).

5.9 CONCLUSIONS

We conclude that details averaged when using a macroscopic approach manifest themselves as an apparent convective spreading dispersivity. This section illustrates that scale-dependent (transmission) dispersivity caused by permeability variation, which are observed in the field-scale, can be replaced by the Koval factor. Hence, the impact of convective spreading can be eliminated by incorporating the Koval factor into the commonly used solution of the CD equation. In other words, if all heterogeneities are

modeled explicitly there would be no need for scale-dependent dispersivity. Below is a summary of this chapter:

- An analytical solution is developed and examined to characterize the dispersive transport in layered heterogeneous reservoirs with weakly/significantly correlated permeability. The analytical solution is constructed assuming no cross-flow between layers.
- The vertically averaged concentrations obtained from the derived analytical solution greatly match the simulation results while using scale-independent dispersivity.
- The fraction of layers in which the mixing grows faster than the dispersive flow regime is determined as a function of the Koval factor and input dispersivity. Fewer layers are invaded by the injected fluid for reservoirs with large Koval factor as more channeling occurs.

5.10 NOMENCLATURE

α_L = dispersivity in the longitudinal direction

α_D = dimensionless dispersivity equivalent to the inverse of the Peclet number

α_{HK}= input dispersivity required to match Eq. (5.27) with the simulation results

α_{Input}= simulation input dispersivity

N_{Pe}^{-1}=inverse of the Peclet number

D_L =the longitudinal dispersion coefficient

α_T = dispersivity in the transverse direction

N_{Pe} = Peclet number

β = fraction of the injected fluid entering each layer

R_L = effective aspect ratio

c_D = dimensionless concentration of component i

C = cumulative storage capacity

$t_{D=}$ = dimensionless time (injected pore volume)

V_{DP} = the Dykstra-Parson coefficient of permeability variation

x_D = dimensionless distance

λ_{xD} = dimensionless autocorrelation length in the x-direction

λ_{zD} =dimensionless autocorrelation length in the z-direction

Δt_D = the maximum dimensionless time step in the simulation

$f_{j=}$ fractional flow of phase j

H_t=total thickness

h_l = thickness of layer l

H_K = Koval factor

$S_{j=}$ saturation of phase j

ϕ = porosity

F = cumulative flow capacity

z = interim variable

t = time

Table 4.1: Simulation model properties

Dimensionless Scaling Group	**First Example**	**Second Example**
V_{DP}	0.8	0.8
λ_{xD}	0.05	10
R_L^*	0.0	0.0
N_{Pe}^{**}	86	86

*The effective aspect ratio: $R_L = \frac{L}{H}\sqrt{\frac{k_z}{k_x}}$

**Input Peclet number: $N_{Pe} = \frac{u_T}{\phi L K_x}$

(See Appendix C for more details on dimensionless scaling groups)

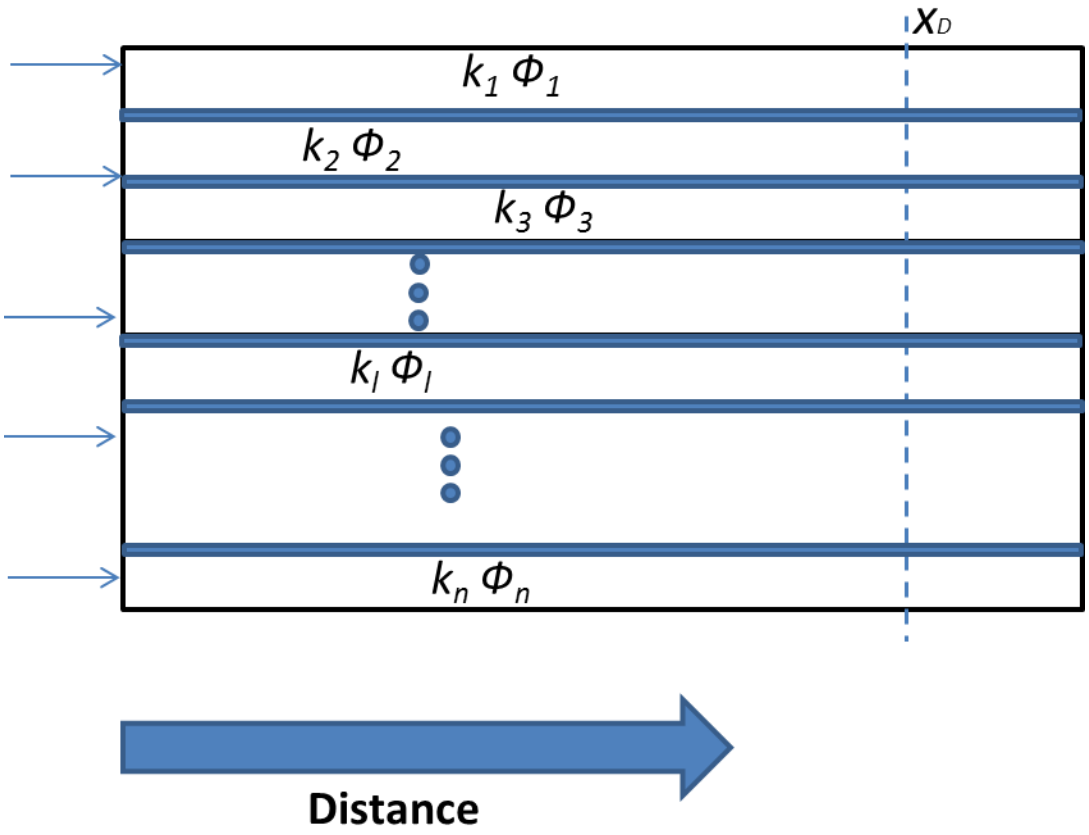

Figure 4.1: Schematic of a 2D heterogeneous reservoir with no convective cross-flow between layers. The reservoir layers are separated by thin impermeable layers (blue strata).

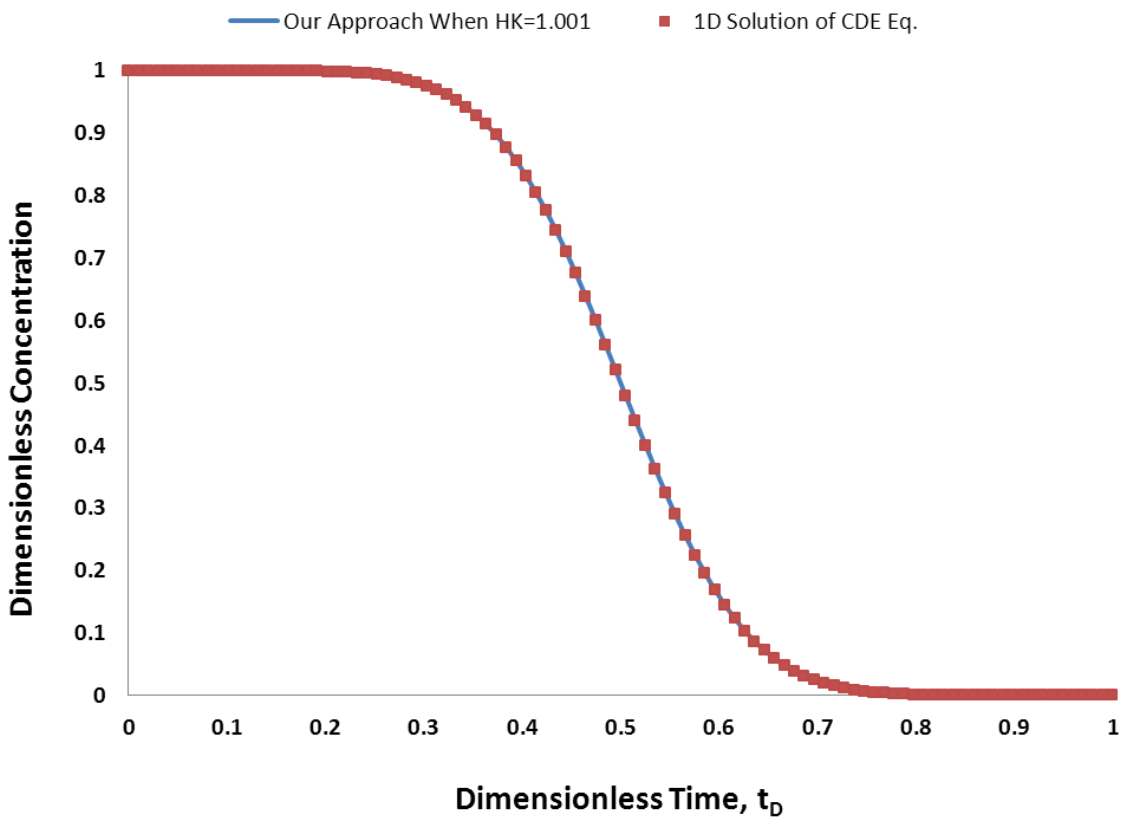

Figure 4.2: A comparison between the concentrations obtained from Eq. (5.27) and the 1D solution of CD equation when H_K=1.001 and α_D =1E-2.

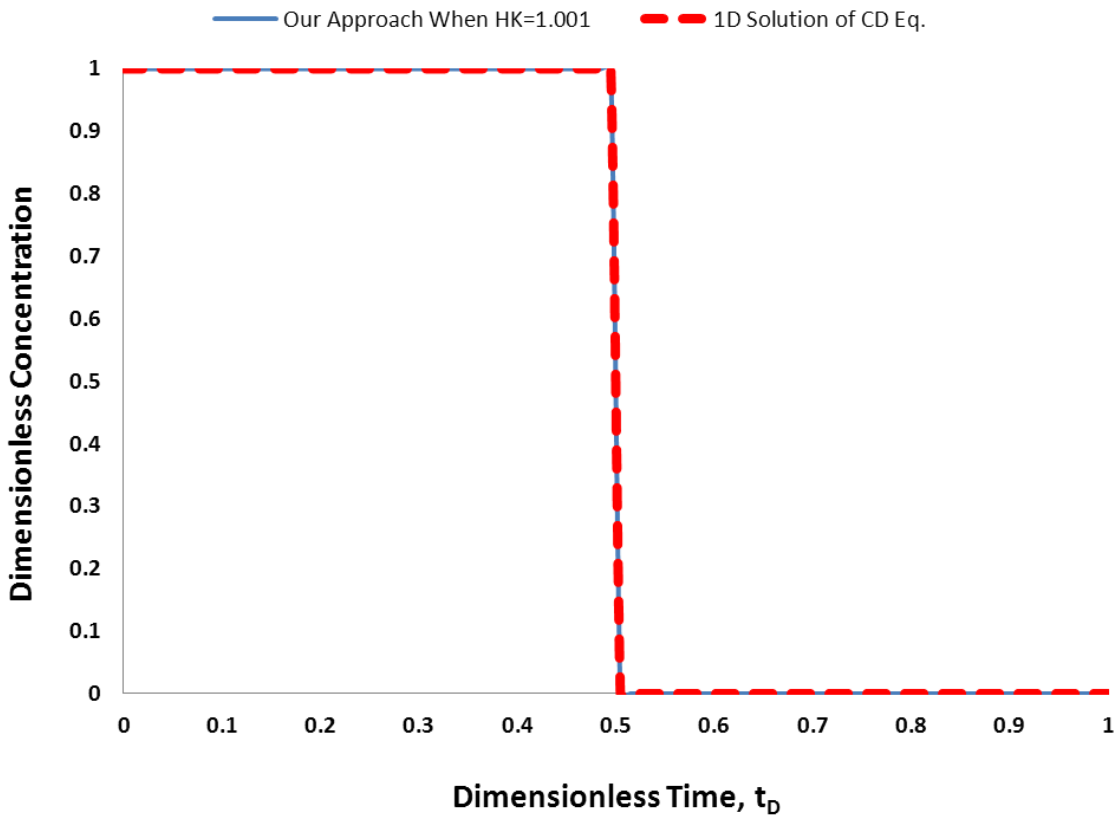

Figure 4.3: A comparison between the concentrations obtained from Eq. (5.27) and the 1D solution of CD equation when H_K=1.001 and α_D =1E-10.

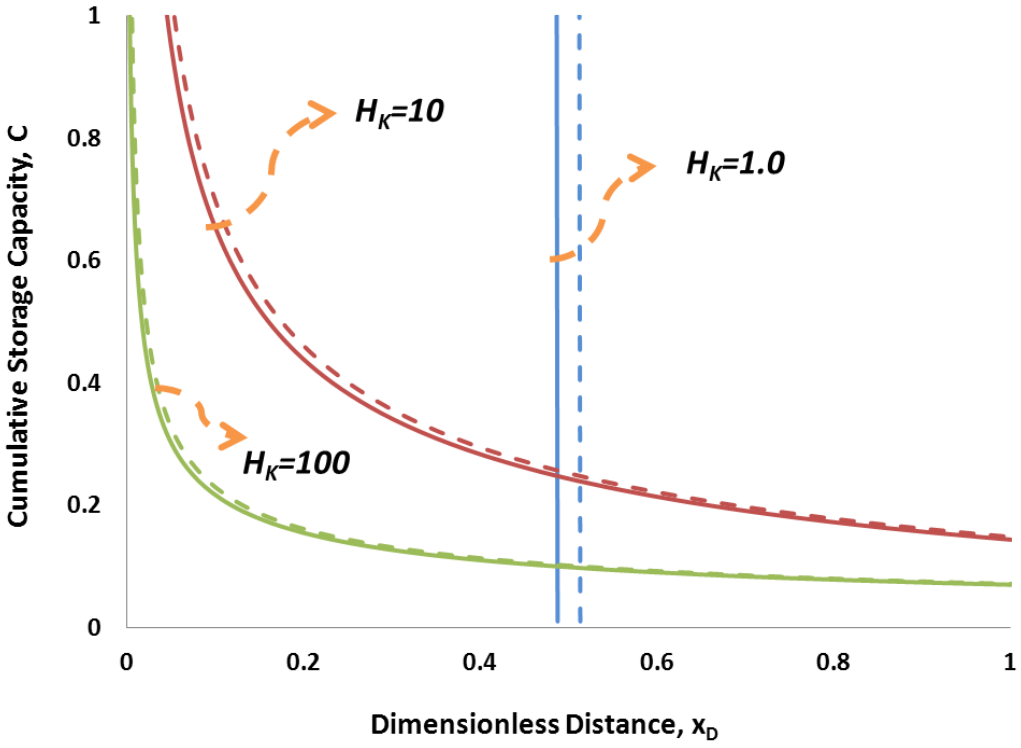

Figure 4.4: The map of tracer concentrations of 0.1 and 0.9 within each layer (obtained from Eq. (5.5) depicted at t_D=0.5 as a function of distance from the injector. Solid and dashed lines represent concentrations of 0.9 and 0.1, respectively. In these examples α_D = 0.0001. The distance is normalized by the length of the permeable medium.

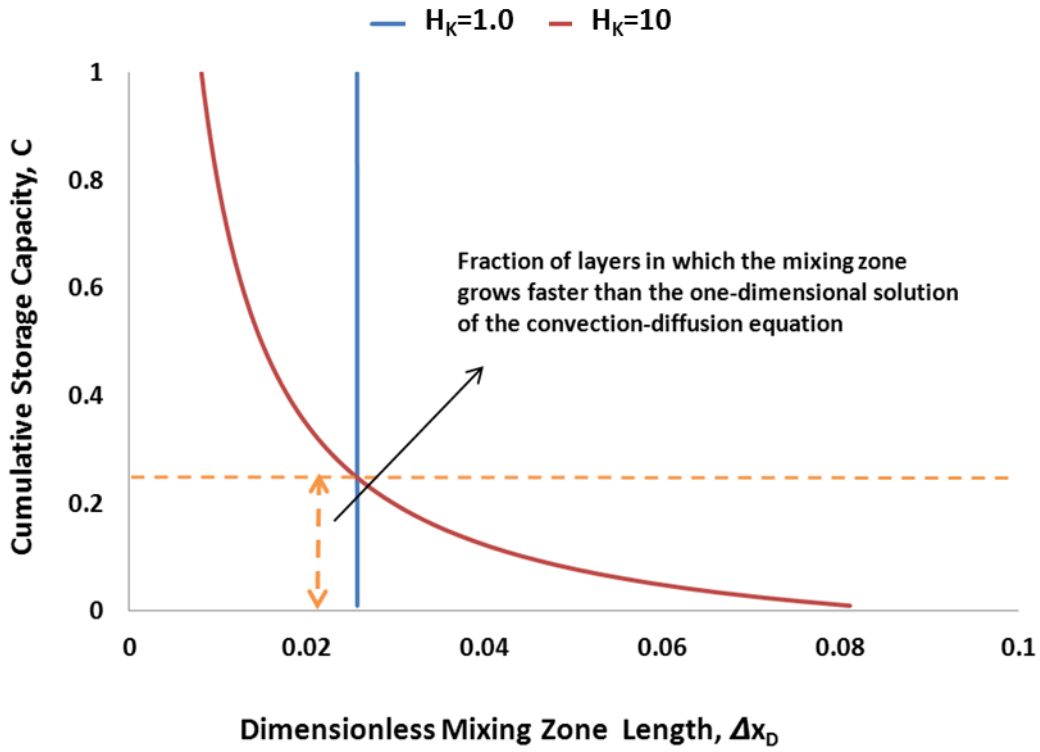

Figure 4.5: A comparison of the lengths of the mixing zone (normalized by the length of the reservoir) for all layers depicted at t_D=0.5 when α_D is equal to 0.0001. Two examples are considered: H_k =1 and H_k =10. The length of the mixing zone is obtained from Eq. (5.8). The larger the H_K, the more convection-dominated the flow is and, consequently, the mixing zone grows faster (with time) rather than the squared root of time

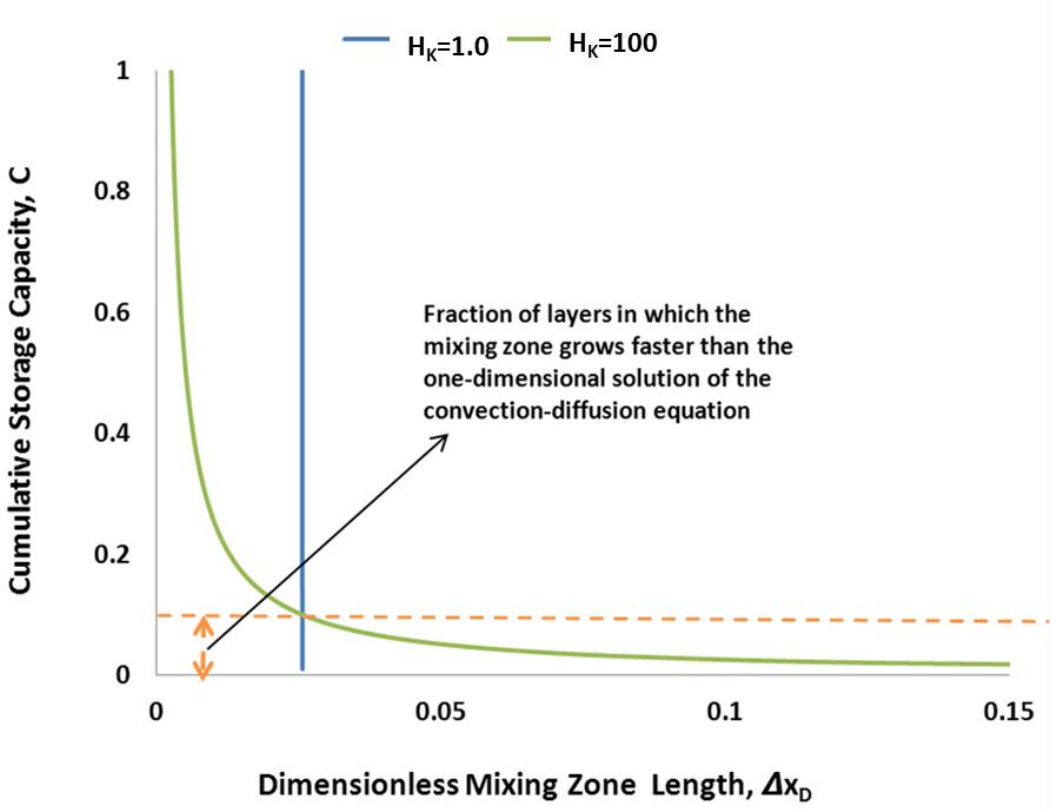

Figure 4.6: A comparison of the lengths of the mixing zone (normalized by the length of the reservoir) for all layers depicted at t_D=0.5 when α_D is equal to 0.0001. Two examples are considered: H_k =1 and H_k =100. The length of the mixing zone is obtained from Eq. (5.8). The larger the H_K, the more convection-dominated the flow is and, consequently, the mixing zone grows faster (with time) rather than the squared root of time

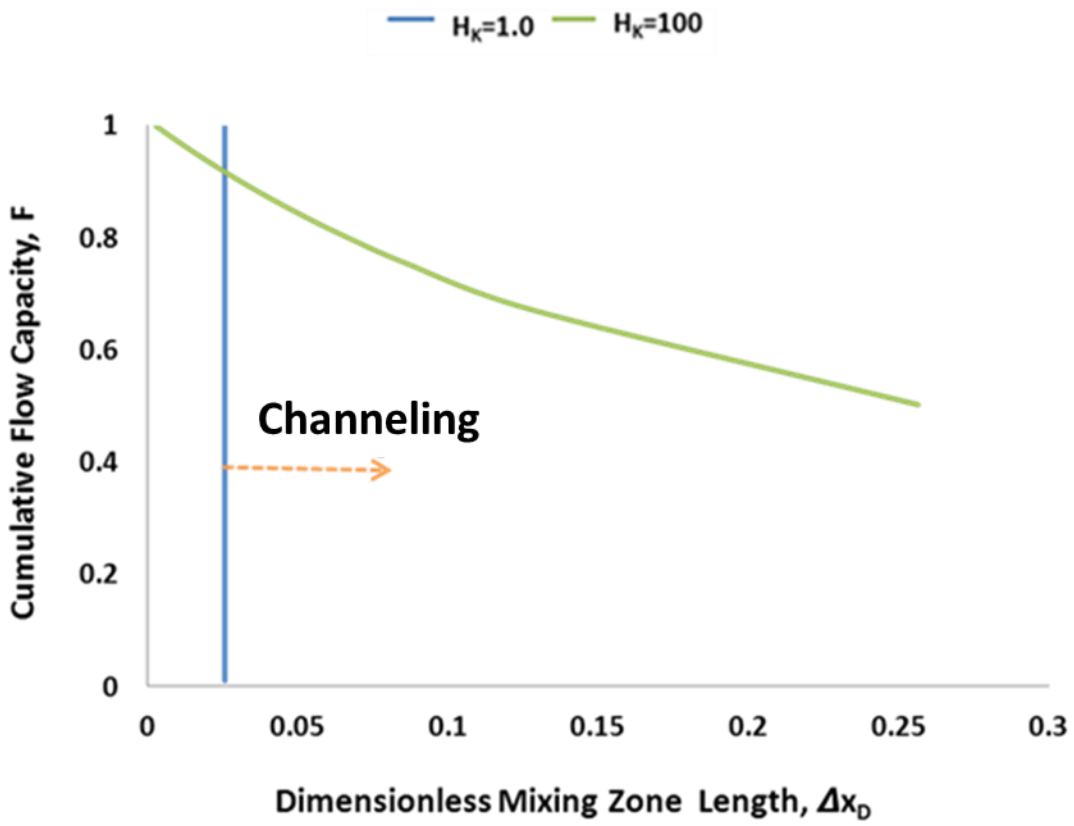

Figure 4.7: Cumulative flow capacity as a function of dimensionless lengths of the mixing zone (normalized by the length of the reservoir) at t_D=0.5 for two cases: H_k =1 and H_k =100 when α_D is equal to 0.0001. The length of the mixing zone is obtained from Eq. (5.8).For the case of H_K=100, the mixing zone grows faster than H_K=1.0 (in large fraction of bulk flow~0.92) because the flow is convection-dominated.

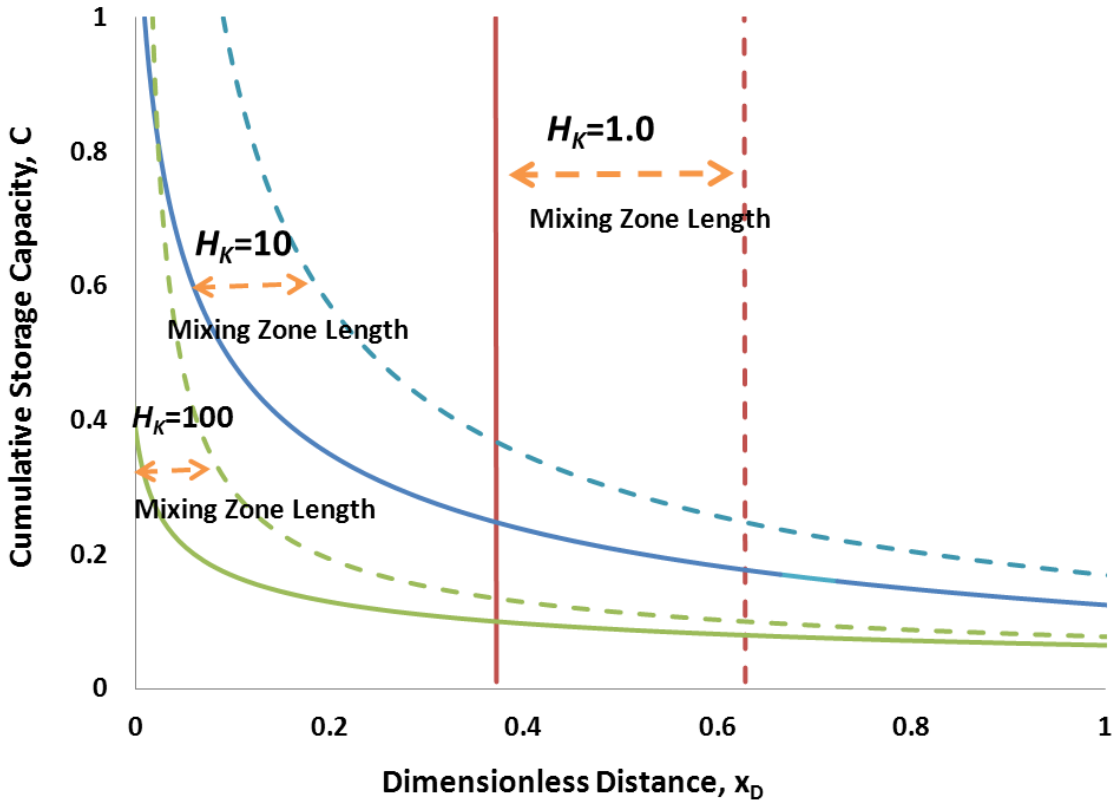

Figure 4.8: The map of tracer concentrations of 0.1 and 0.9 within each layer (obtained from Eq. (5.5) depicted at t_D=0.5 as a function of distance from the injector. Solid and dashed lines represent concentrations of 0.9 and 0.1, respectively. In these examples α_D = 0.01. The distance is normalized by the length of the permeable medium.

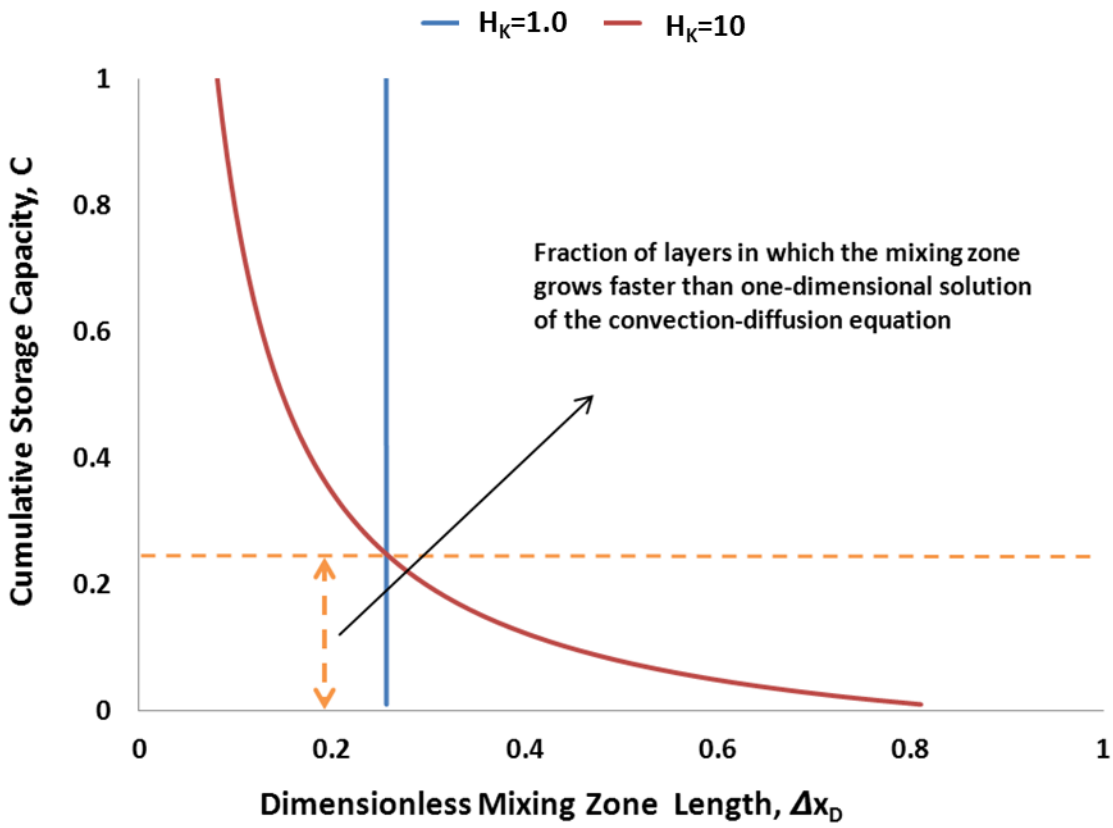

Figure 4.9: A comparison of the lengths of the mixing zone (normalized by the length of the reservoir) for all layers depicted at t_D=0.5 when α_D is equal to 0.01. Two examples are considered: H_k =1 and H_k =10. The length of the mixing zone is obtained from Eq.(5.8). The larger the H_K, the more convection-dominated the flow is and, consequently, the mixing zone grows faster (with time) rather than the squared root of time.

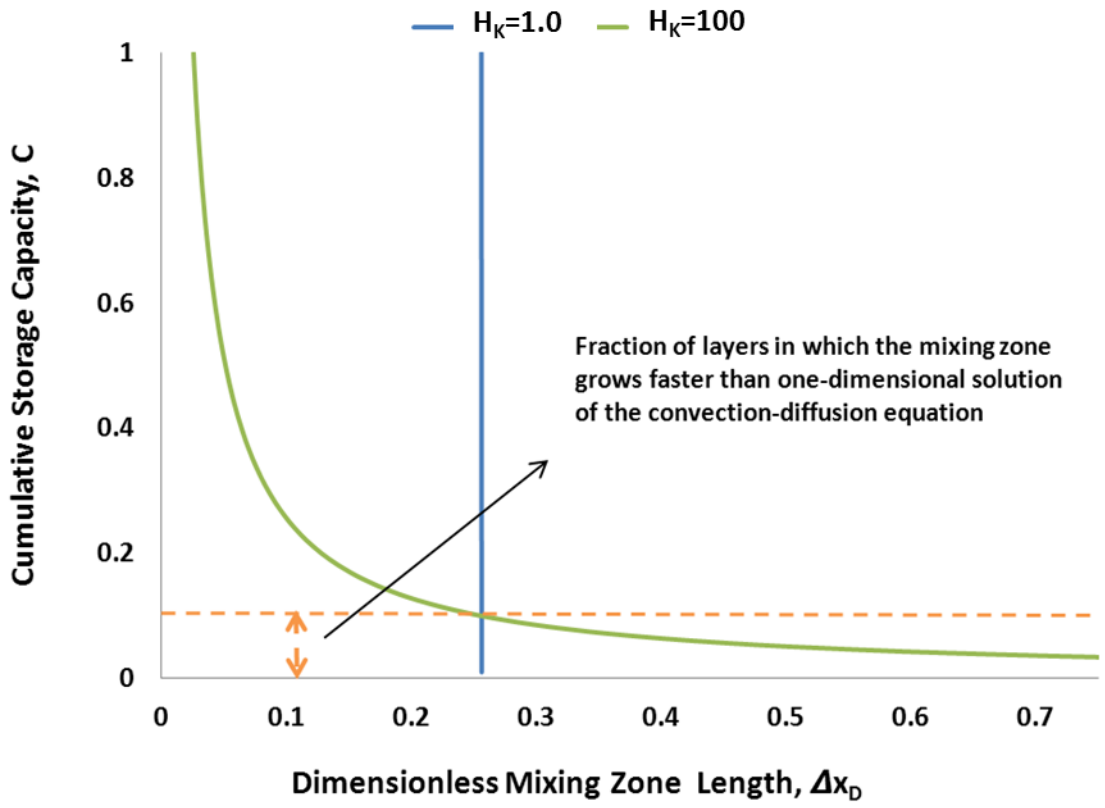

Figure 4.10: A comparison of the lengths of the mixing zone (normalized by the length of the reservoir) for all layers depicted at t_D=0.5 when α_D is equal to 0.01. Two examples are considered: H_k =1 and H_k =100. The length of the mixing zone is obtained from Eq. (5.8). The larger the H_K, the more convection-dominated flow is and, consequently, the mixing zone grows faster (with time) rather than the squared root of time

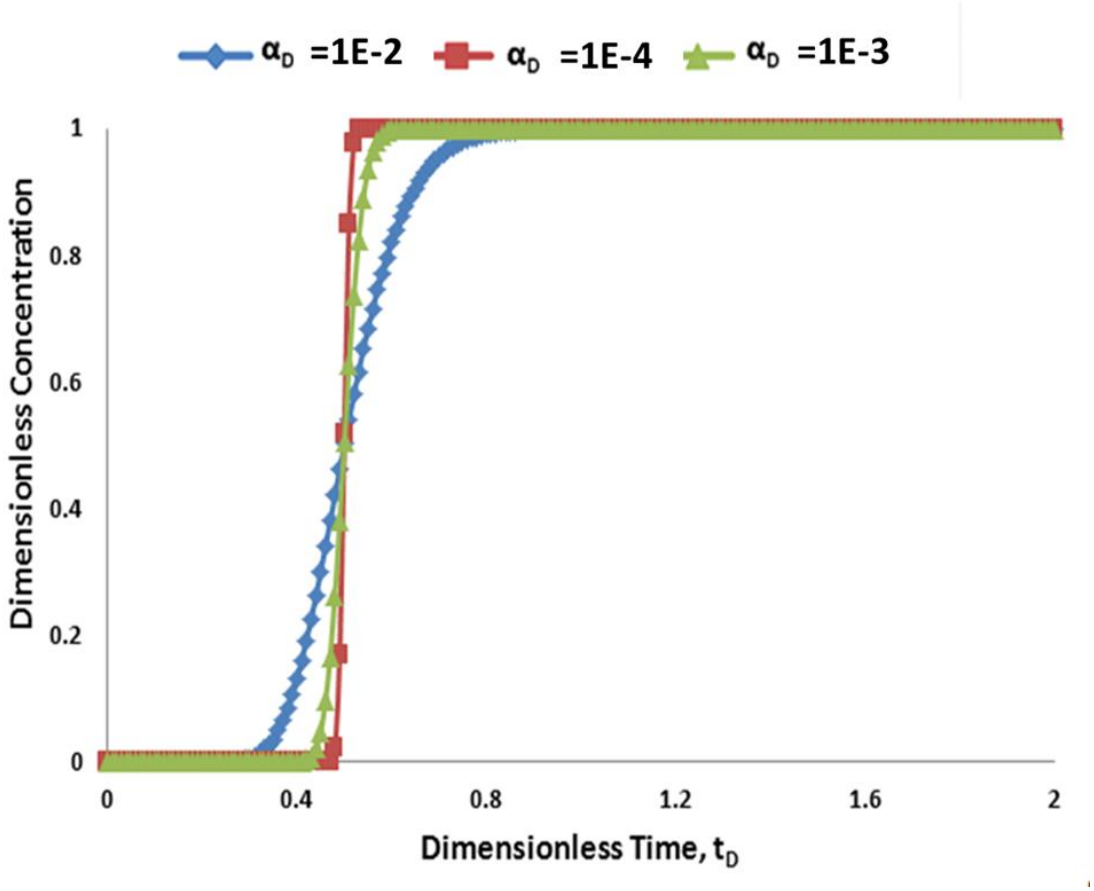

Figure 4.11: Concentration history plots when H_k =1 for three different values of α_D depicted at x_D=0.5. Larger spreading occurs as α_D increases, consistent with the 1D solution of the CD equation.

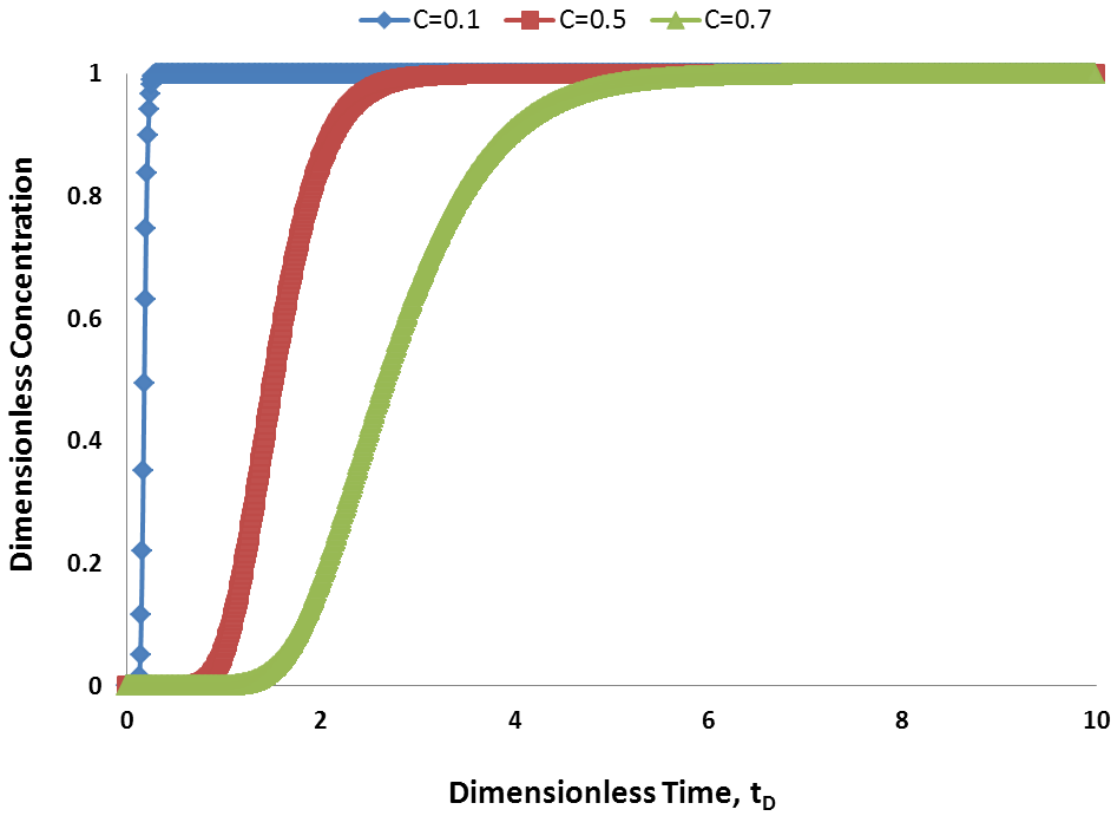

Figure 4.12: Concentration history plots for selected layers (represented by cumulative storage capacities of 0.1, 0.5, and 0.7) depicted at x_D=0.5 when H_k = 10 and α_D = 0.01.

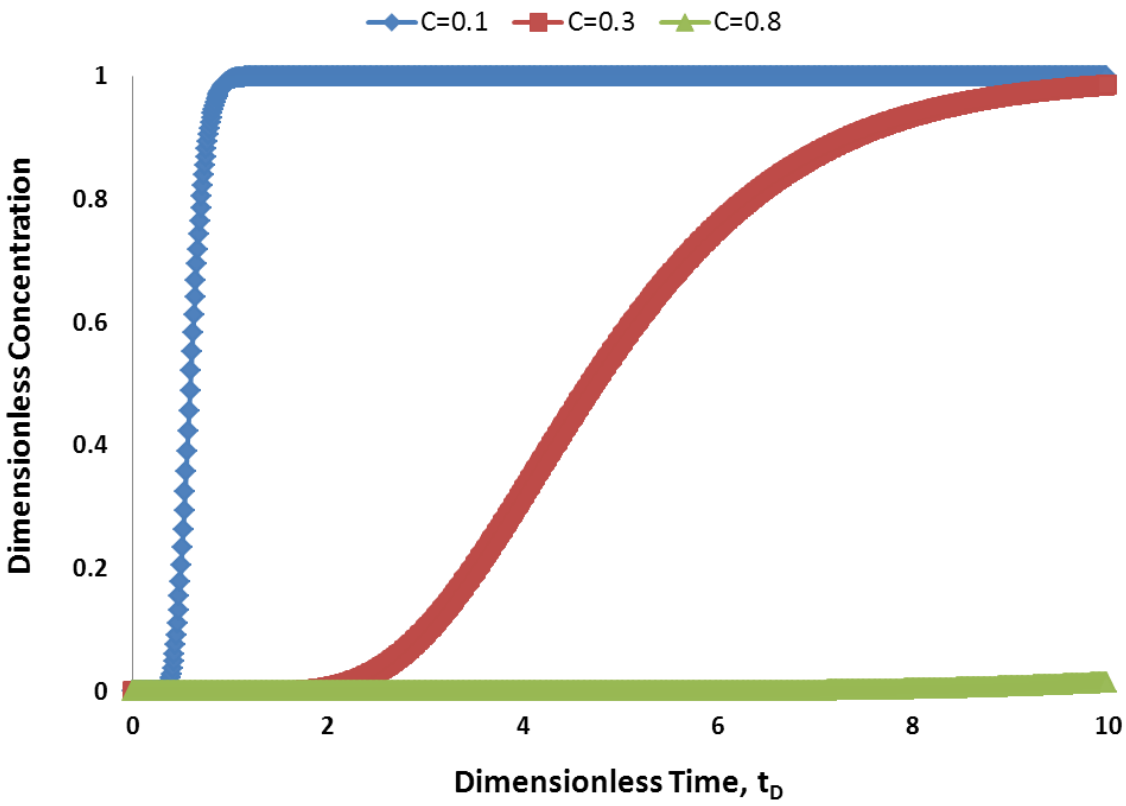

Figure 4.13: Concentration history plots for selected layers (represented by cumulative storage capacities of 0.1, 0.3, and 0.8) depicted at x_D=0.5 when H_k = 100 and α_D = 0.01.

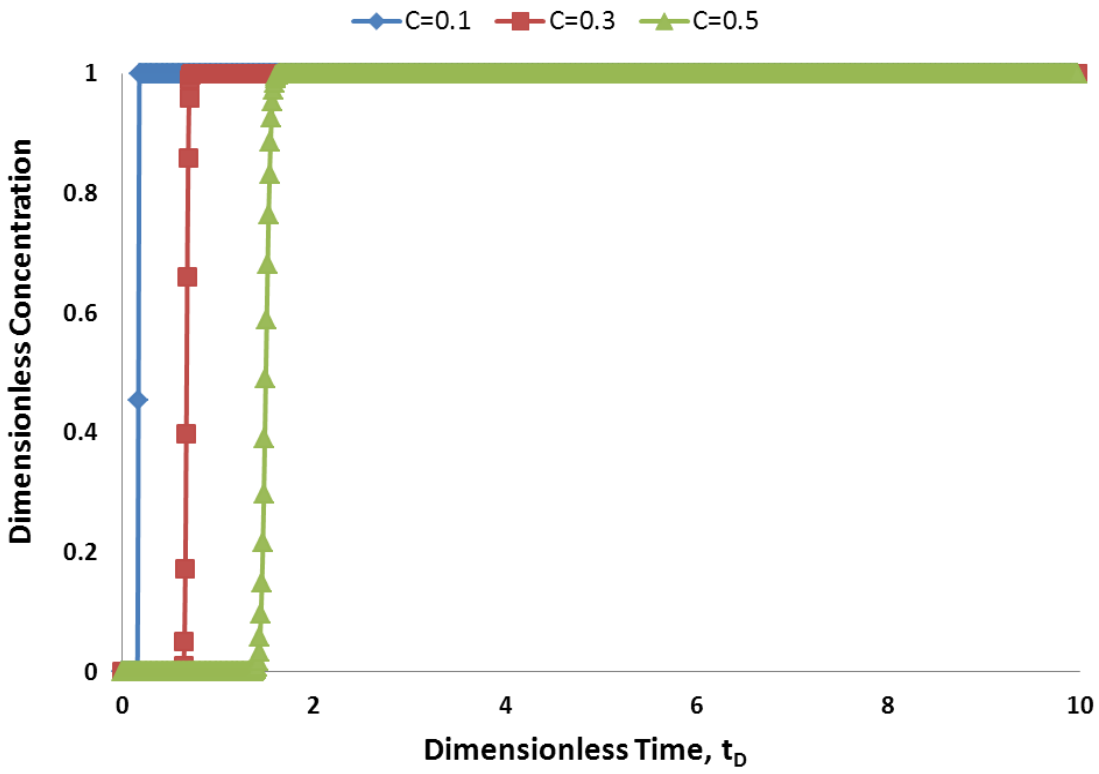

Figure 4.14: Concentration history plots for selected layers (represented by cumulative storage capacities of 0.1, 0.3, and 0.5) depicted at x_D=0.5 when H_k = 10 and α_D = 0.0001.

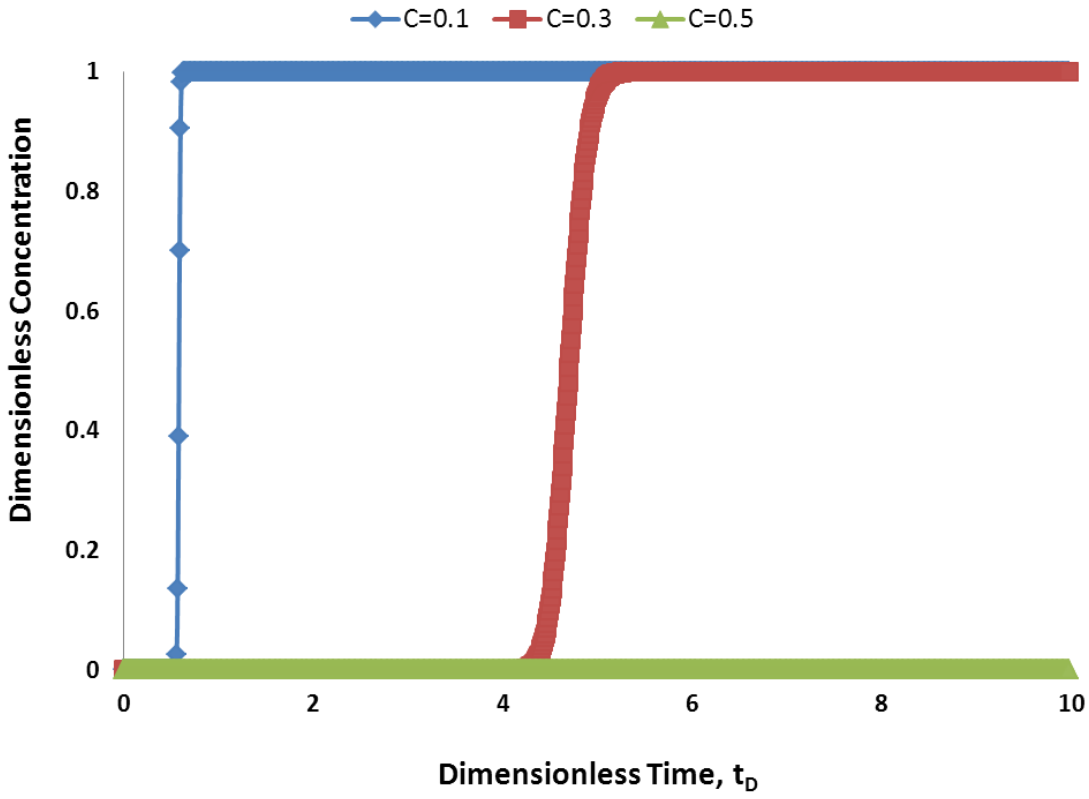

Figure 4.15: Concentration history plots for selected layers (represented by cumulative storage capacities of 0.1, 0.3, and 0.5) depicted at at x_D=0.5 when H_k = 100 and α_D = 0.0001.

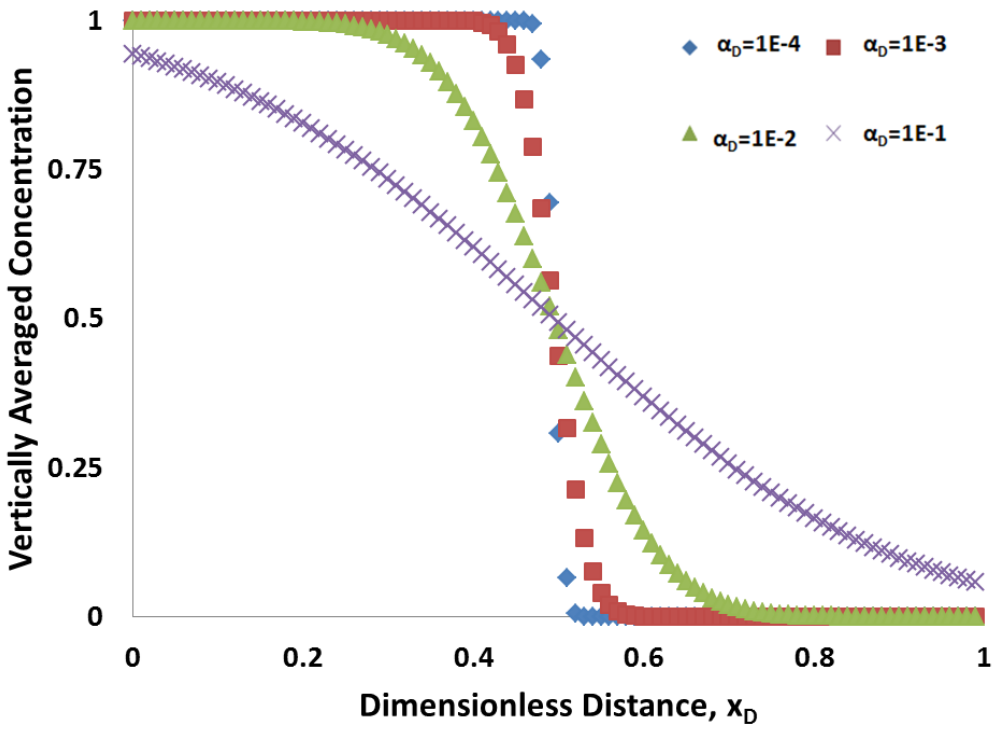

Figure 4.16: Vertically averaged concentration as a function of dimensionless distance (normalized by the length of the permeable medium) obtained from Eq.(5.27); the concentration profile is depicted at t_D=0.5 and the Koval heterogeneity of one. As α_D decreases, less spreading occurs.

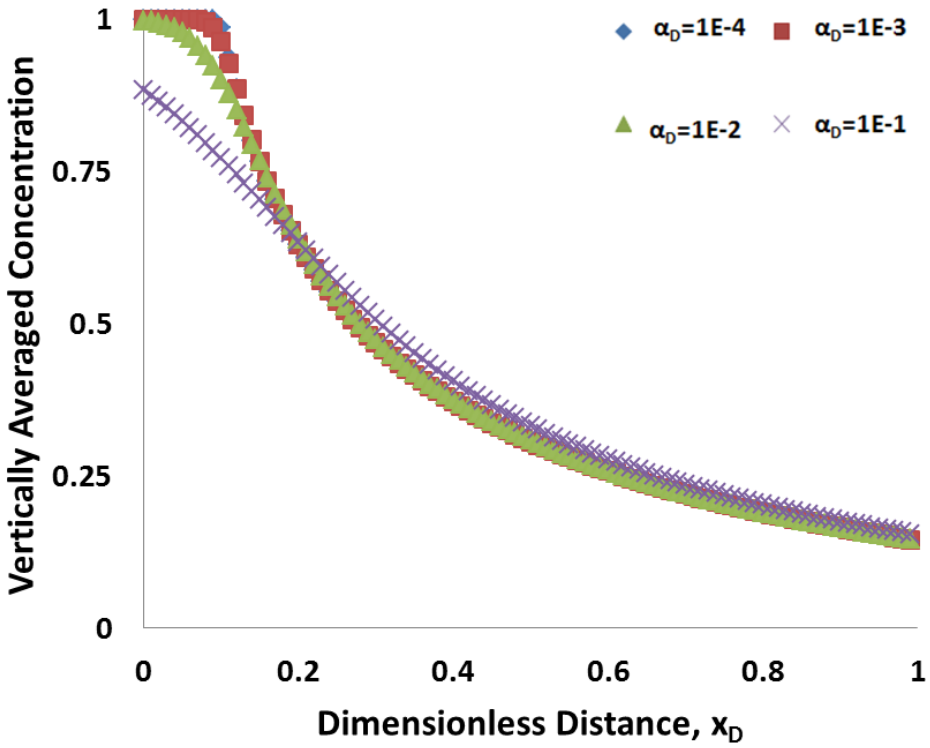

Figure 4.17: Vertically averaged concentration as a function of dimensionless distance (normalized by the length of the permeable medium) obtained from Eq.(5.27); the concentration profile is depicted at t_D=0.5 and the Koval heterogeneity is H_K=10. As α_D decreases, less spreading occurs.

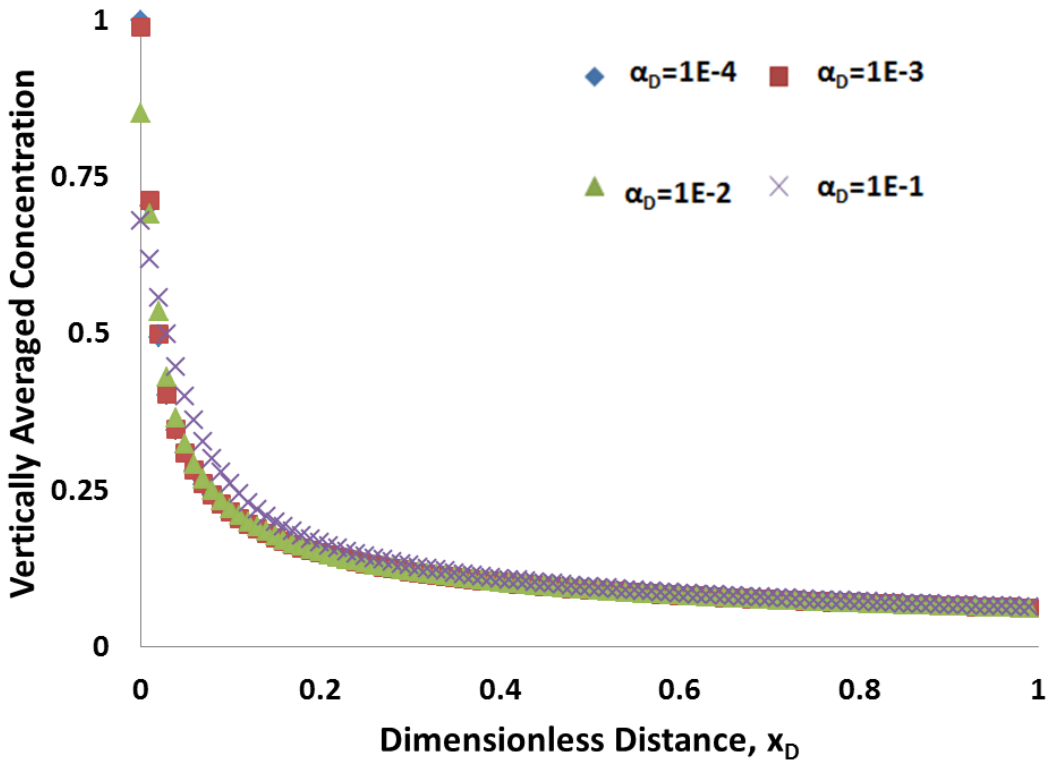

Figure 4.18: Vertically averaged concentration as a function of dimensionless distance, (normalized by the length of the permeable medium) obtained from Eq.(5.27); the concentration profile is depicted at t_D=0.5 and H_K=100. In the presence of large permeability heterogeneity (H_K =100), the impact of dispersivity becomes insignificant.

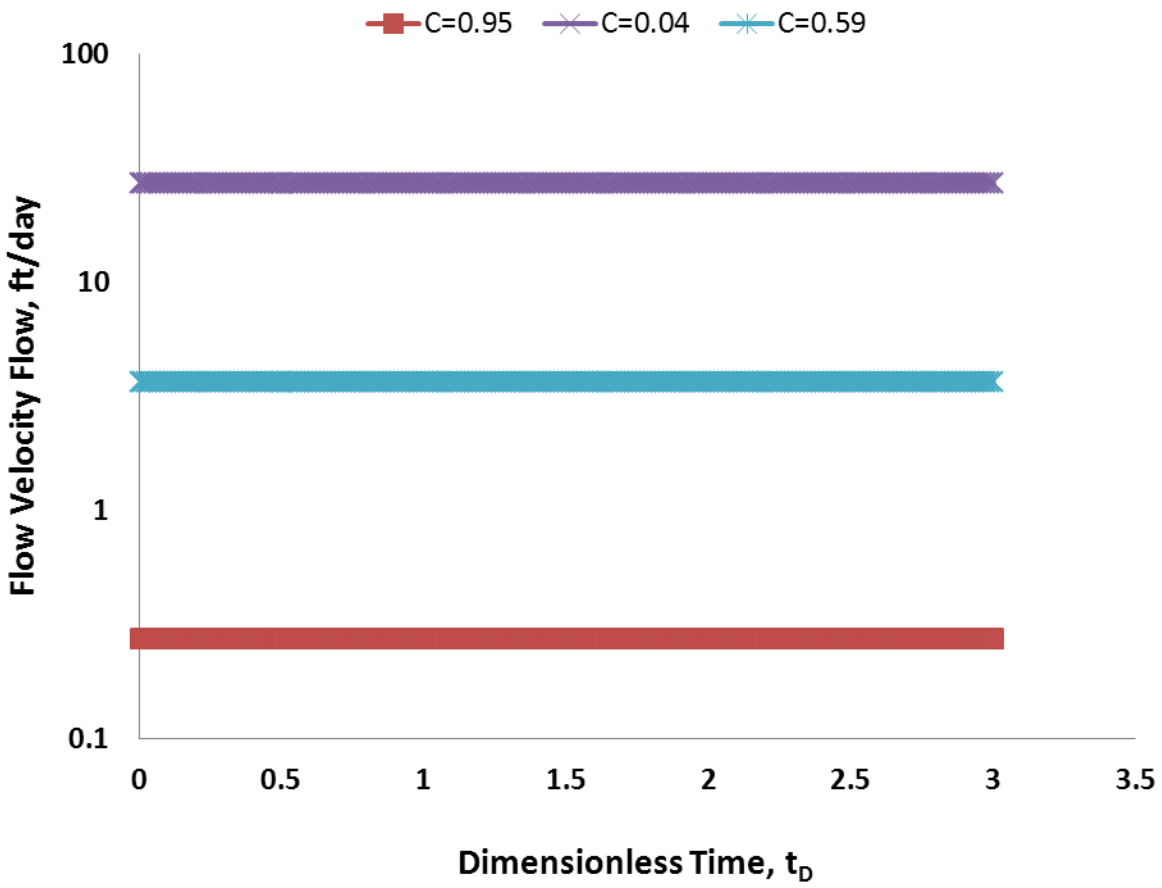

Figure 4.19: Flow velocity for selected grid layers as a function of time. There are 32 layers in this example; flow velocities though different layers of the permeable medium stay constant with time as in individual grid blocks, because of the incompressible displacement without cross-flow.

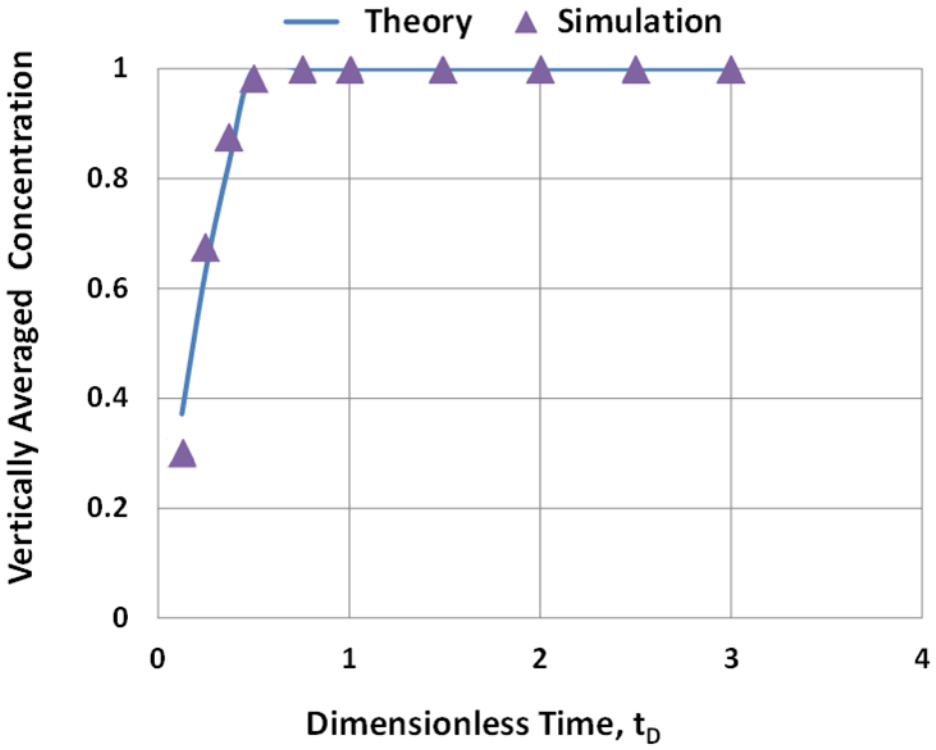

Figure 4.20: Comparison of theoretical and simulation results for vertically averaged concentrations along a cross-section located at x_D=0.1 at different times. V_{DP}=0.8 and λ_{xD}=0.05 for this example. The Koval factor used to match concentrations is 5.1.

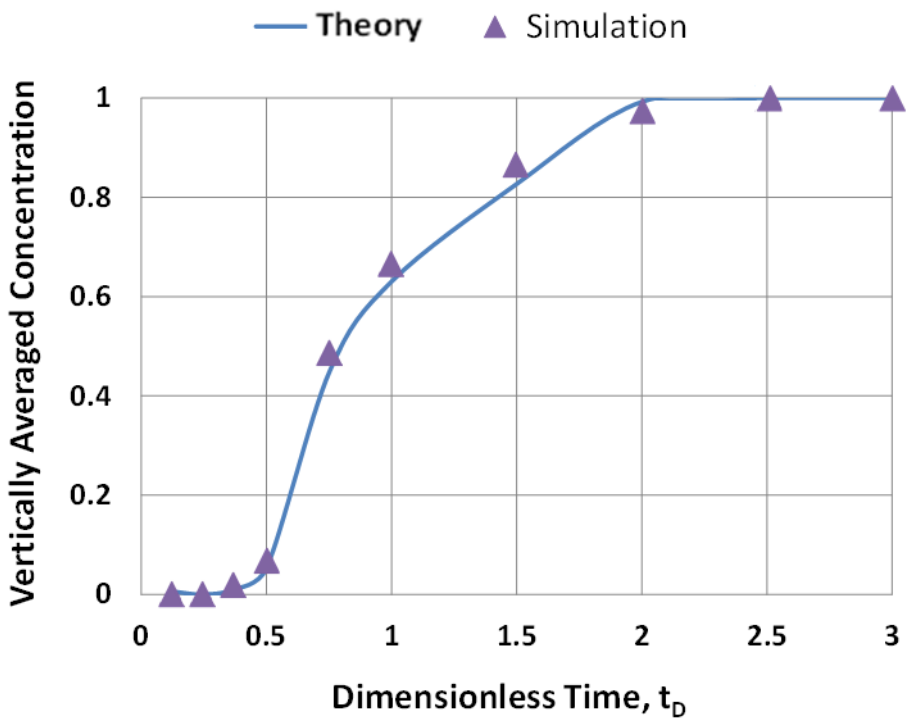

Figure 4.21: Comparison of theoretical and simulation results for vertically averaged concentrations along a cross-section located at x_D=0.4 at different times. V_{DP}=0.8 and λ_{xD}=0.05 for this example. The Koval factor used to match concentrations is 5.4.

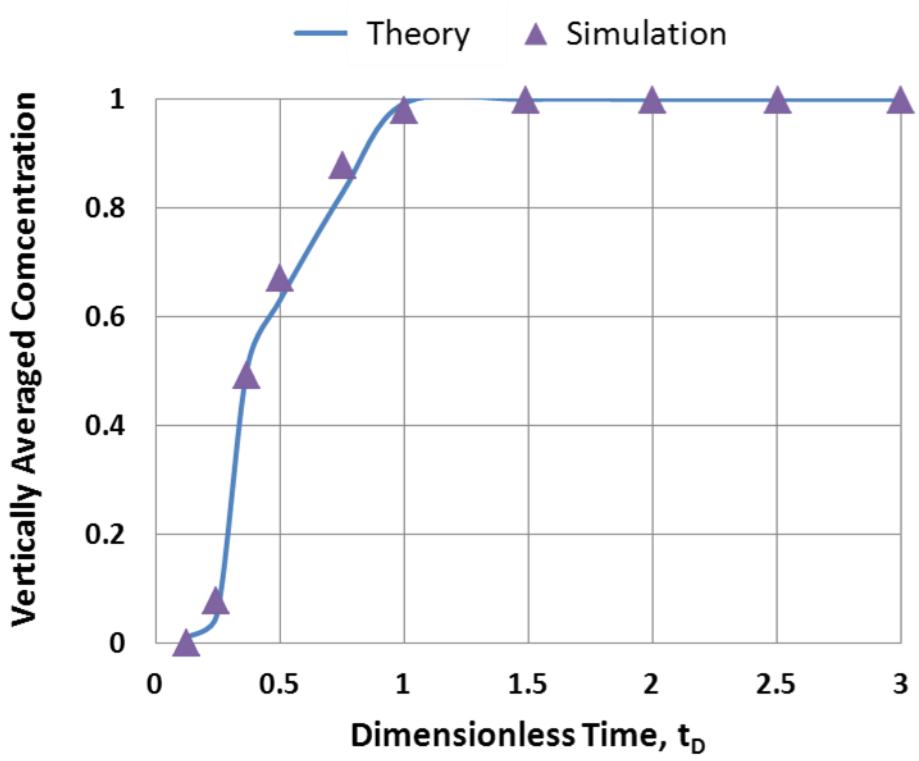

Figure 4.22: Comparison of theoretical and simulation results for vertically averaged concentrations along a cross-section located at x_D=0.9 at different times. V_{DP} = 0.8 and λ_{xD} = 0.05 for this example. The Koval factor used to match concentrations is 5.4.

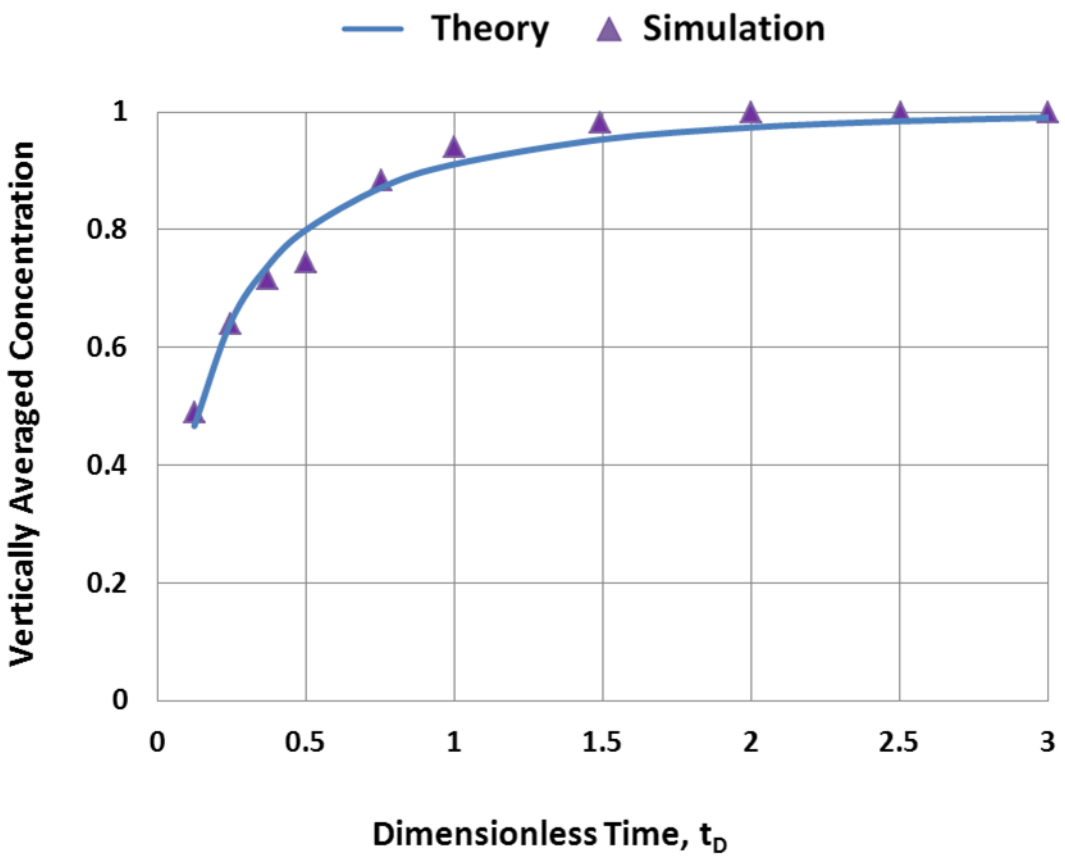

Figure 4.23: Comparison of theoretical and simulation results for vertically averaged concentrations along a cross-section located at x_D=0.1 at different times. V_{DP}=0.8 and λ_{xD}=10 for this example. The Koval factor used to match concentrations is 6.3.

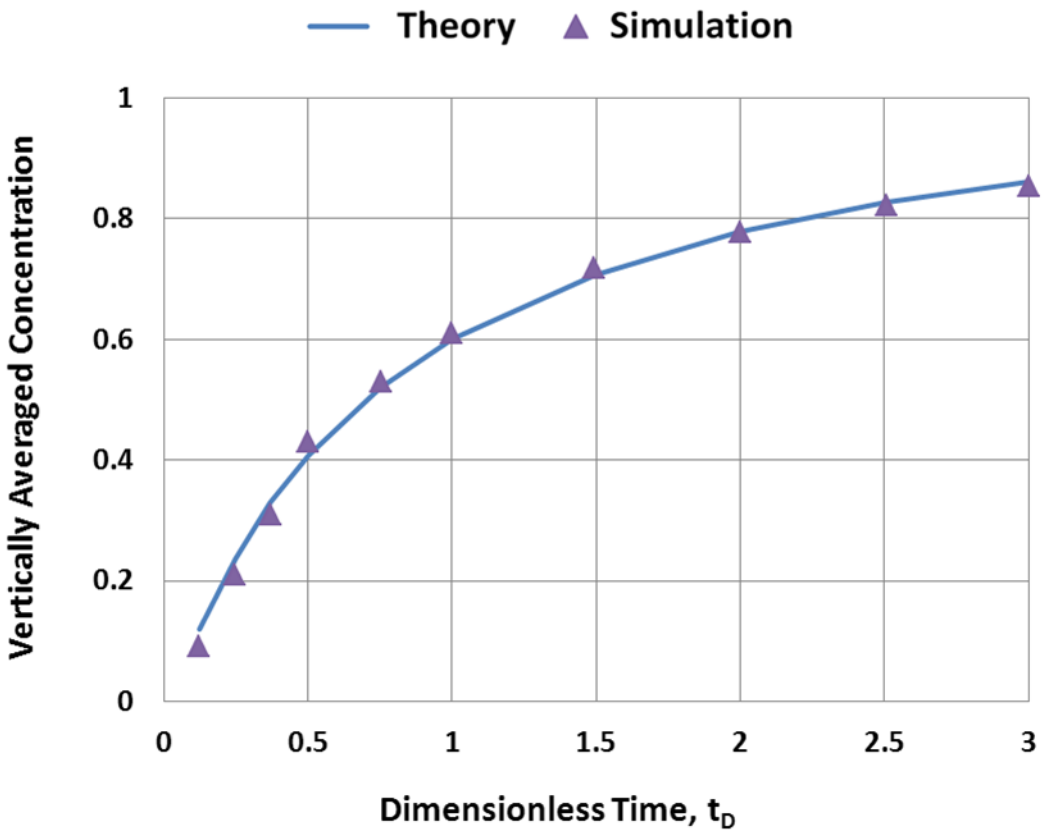

Figure 4.24: Comparison of theoretical and simulation results for vertically averaged concentrations along a cross-section located at x_D=0.4 at different times. V_{DP}=0.8 and λ_{xD}=10 for this example. The Koval factor used to match the concentrations is 7.3.

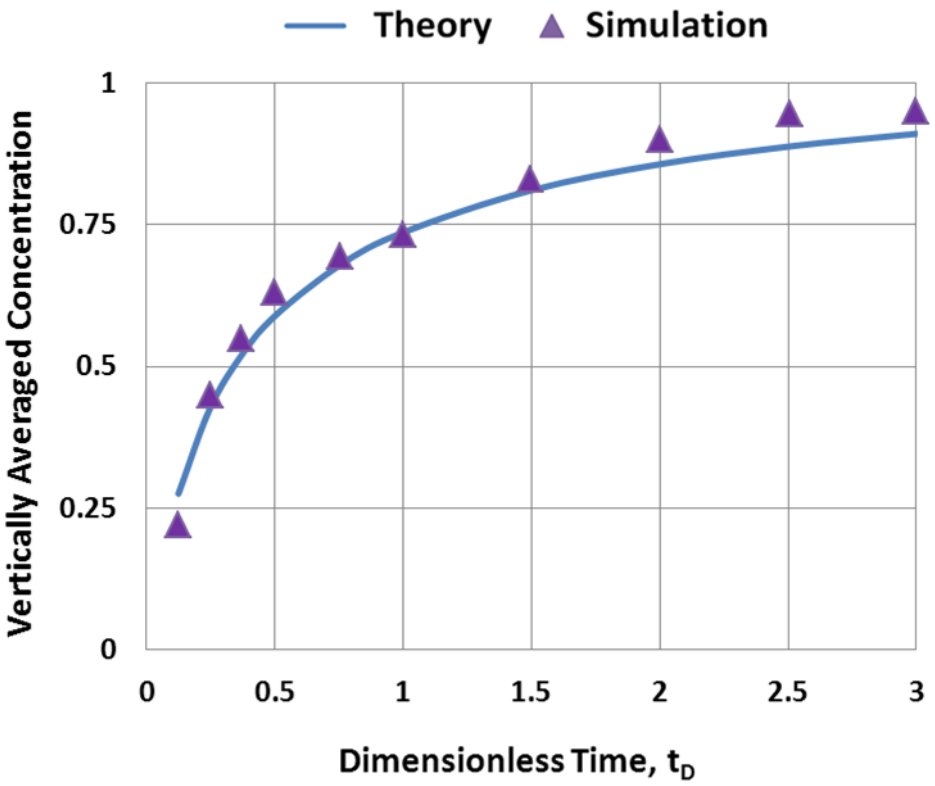

Figure 4.25: Comparison of theoretical and simulation results for vertically averaged concentrations along a cross-section located at x_D=0.9 at different times. V_{DP}=0.8 and λ_{xD}=10 for this example. The Koval factor used to match concentrations is 5.4.

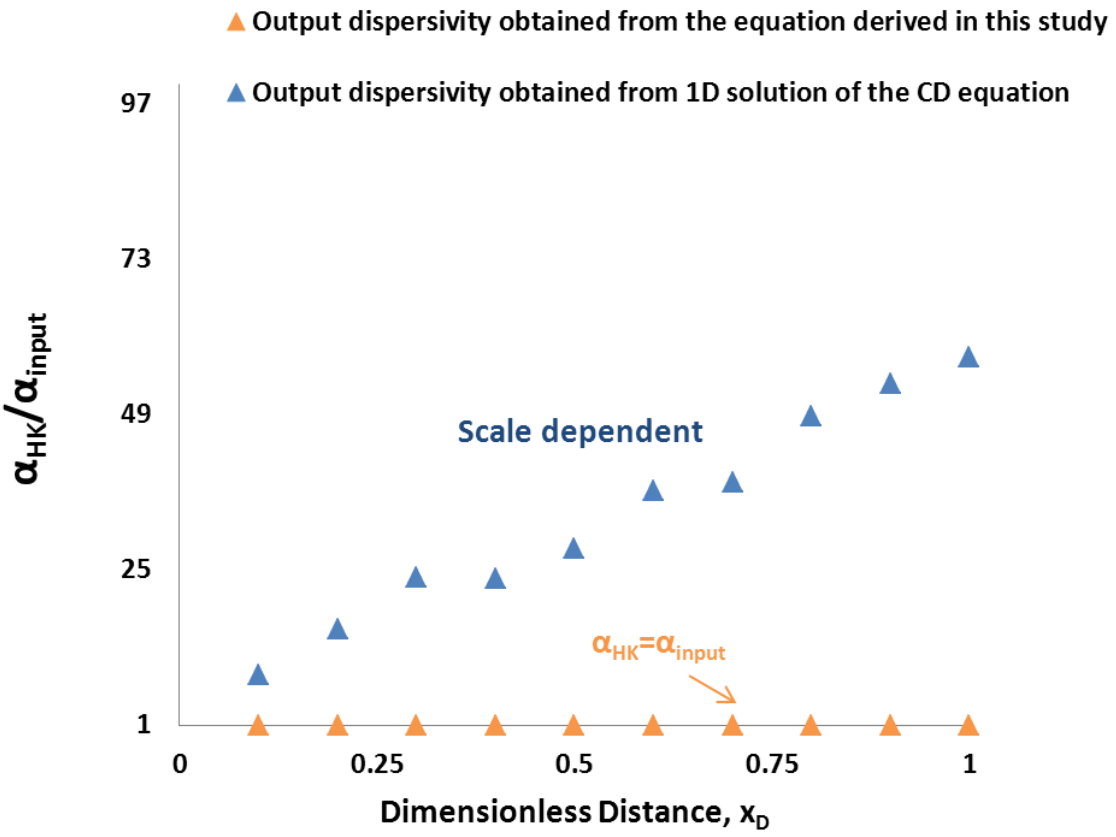

Figure 4.26: The ratio of dispersivity values, which are used in Eq. (5.27) and Eq. (5.3) to match the simulation results, to the input dispersivity as a function of x_D. The graph clearly shows that dispersivity is not scale-dependent when Eq. (5.27) is used. V_{DP}=0.8 and λ_{xD}=0.05 for this example.

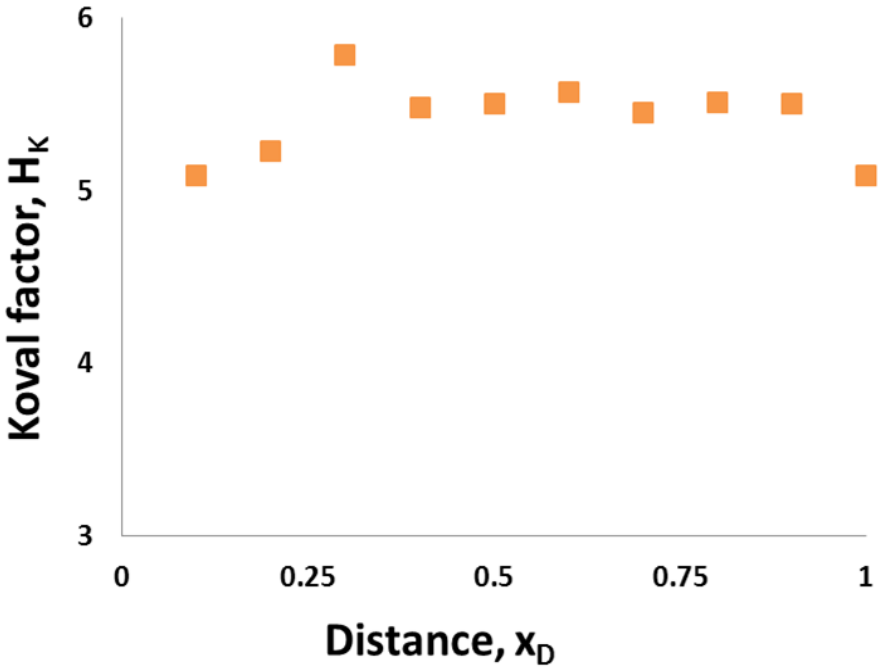

Figure 4.27: The Koval factor values used in Eq. (5.27) to match the simulation results. V_{DP}=0.8 and λ_{xD}=0.05 for this example. Each point in this figure corresponds to a point in Figure 4.26.

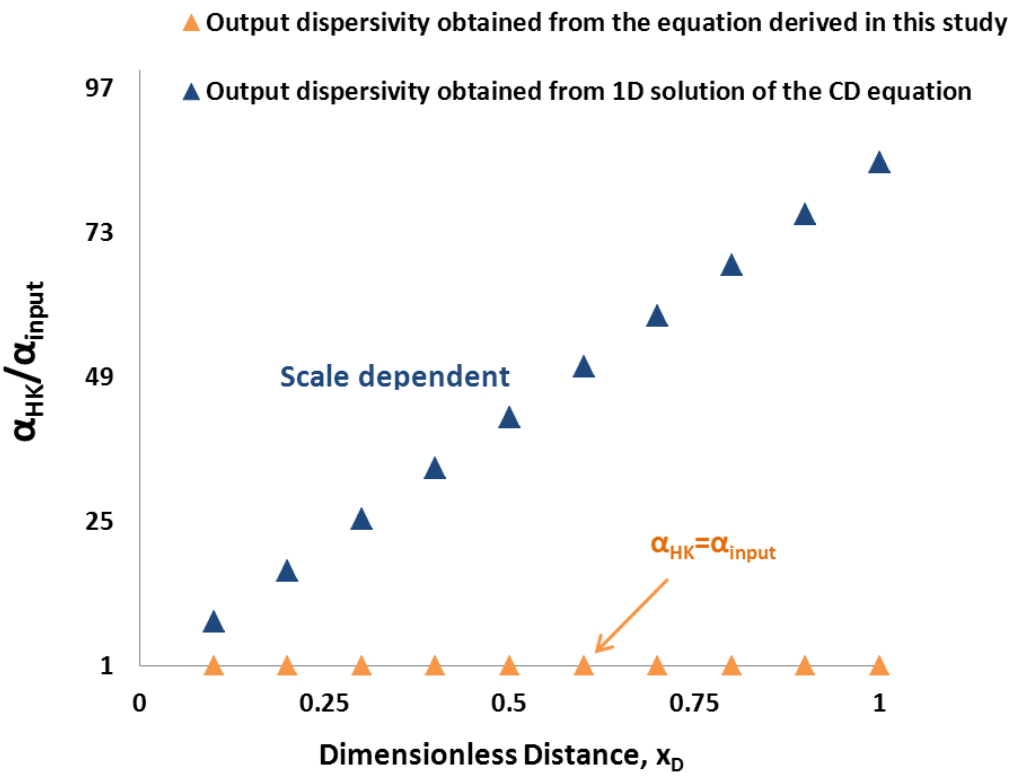

Figure 4.28: The ratio of dispersivity values ,which are used in Eq. (5.27) and Eq. (5.3) to match the simulation results, as a function of x_D. The graph clearly indicates that dispersivity is not scale-dependent when Eq. (5.27) is used. V_{DP}=0.8 and λ_{xD}=10 for this example.

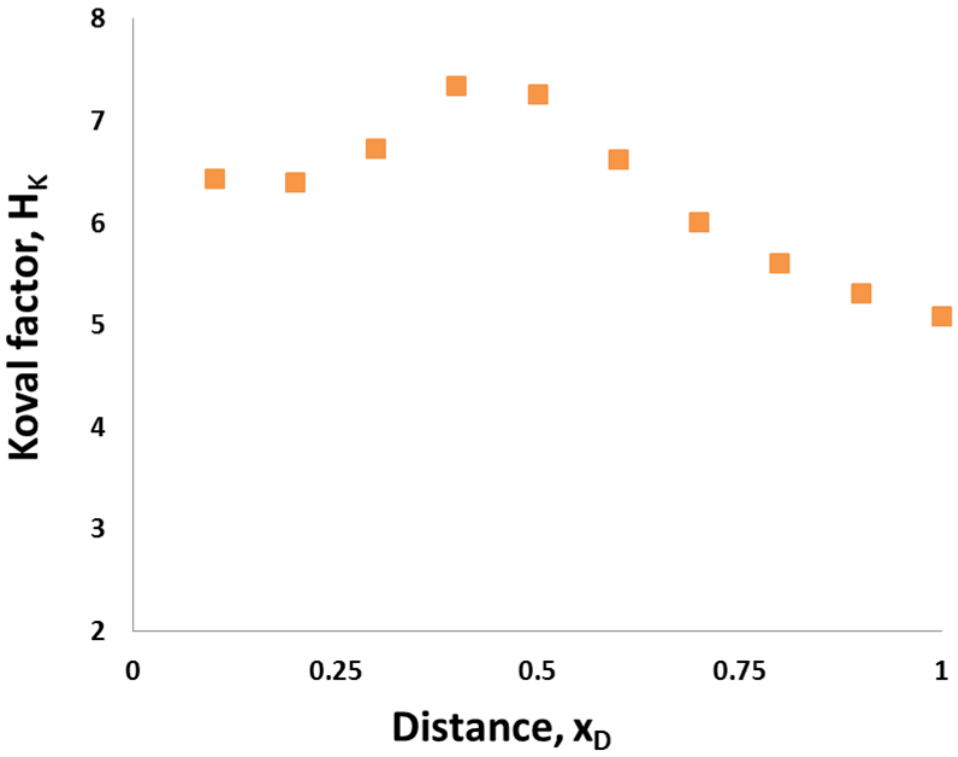

Figure 4.29: The Koval factor values used in Eq. (5.27) to match the simulation results. V_{DP} =0.8 and λ_{xD} =10 for this example. Each point in this figure corresponds to a point in Figure 4.28.

Chapter 6: Evaluation of Local Mixing in Heterogeneous Reservoirs

Dispersive mixing degrades field-scale miscible displacements through the dilution of the injected solvent. In this chapter, we derive and verify the numerical dispersion coefficients when flow velocity varies along the distance travelled. Numerical dispersion is associated with the truncation error inevitably introduced into the finite difference approximations of the conservation equations.

We derive the finite difference form of the convection-dispersion equation to determine the numerical dispersion coefficients when flow velocity varies with travelled distance. The off-diagonal elements of the numerical dispersion tensor double when the flow velocity changes with distance. In addition, a specific simulation configuration is presented to verify the derived coefficients.

The second part of this chapter examines how local mixing changes as the convective cross-flow increases. We apply two methods to determine the local mixing: the method developed in Chapter 5 and the conventional method of matching the concentration history of a grid block to the 1D solution of the convection-dispersion equation. The two-dimensional (2D) simulation models, used in this study, consist of an injector and a producer. Our simulation results indicate that the magnitude of the local mixing increases as cross-flow increases. Hence, flow manifests more dispersive behavior as cross-flow increases.

6.1 INTRODUCTION

The inaccurate modeling of dispersion in miscible displacements yields an inaccurate prediction of oil recoveries (Garmeh *et al.*, 2010). Dispersion in permeable media is a dilution process caused by molecular diffusion, velocity gradients at the pore-scale level, locally heterogeneous streamline lengths, and mechanical mixing in pore bodies. Also, dispersive mixing degrades the displacement performance in field-scale miscible floods (Haajizadeh and Fayers, 2000; Walsh and Orr, 1990; Johns *et al.*, 2002; Jessen *et al.*, 2002, and Chapter 4 of this dissertation).

Taylor (1922, 1953, and 1954) explains the fundamentals of dispersion; an extension of his dispersion theory to permeable media is described in detail by Perkins and Johnston (1963), Greenkorn and Kessler (1969), Bear (1972), and Lake and Hirasaki (1981).

The dispersive flux is defined as the flux of component *i* in phase *j* with respect to volume-averaged velocity (Darcy velocity) because of dispersion. Dispersion flux is often represented by the Fickian form:

$$\vec{j}_{Dij} = -\phi S_j \overline{\overline{K}}_{ij} . \vec{\nabla}\left(\rho_j \omega_{ij}\right), \tag{6.1}$$

where ω_{ij} is the mass fraction of component *i* in phase *j* and, consequently, $\rho_j \omega_{ij}$ is the mass concentration of component *i* expressed per pore volume. Hence, the overall dispersive flux of component *i* becomes

$$\vec{j}_{D_i} = -\sum_{j=1}^{N_P} \phi S_j \overline{\overline{K}}_{ij} . \vec{\nabla}\left(\rho_j \omega_{ij}\right). \qquad j=1,2, ..N_P \tag{6.2}$$

The dispersion coefficient includes both molecular diffusion and mechanical spreading (Aronofsky and Heller, 1957). If *x* and *y* represent a 2D coordinate system, the dispersion tensor of component *i* in phase *j*, $\overline{\overline{K}}_{ij}$, may be expressed as

$$\overline{\overline{K}}_{ij} = \begin{vmatrix} K_{xx} & K_{xy} \\ K_{yx} & K_{yy} \end{vmatrix} . \tag{6.3}$$

Following Bear (1972), the elements of the dispersion tensor for a homogeneous, isotropic permeable medium are defined as

$$K_{xx} = \frac{D_{ij}}{\tau} + \frac{\alpha_l u_{xj}^2 + \alpha_t u_{yj}^2}{\phi S_j \left|\vec{u}_j\right|} , \tag{6.4}$$

$$K_{yy} = \frac{D_{ij}}{\tau} + \frac{\alpha_l u_{yj}^2 + \alpha_t u_{xj}^2}{\phi S_j \left|\vec{u}_j\right|} , \tag{6.5}$$

$$K_{xy} = K_{yx} = \frac{\left(\alpha_l - \alpha_t\right) u_{yj} u_{xj}}{\phi S_j \left|\vec{u}_j\right|} , \tag{6.6}$$

where α_l is called the longitudinal (parallel to bulk flow) dispersivity and α_t is known as the transverse (perpendicular to bulk flow) dispersivity; both α_l and α_t are often

assumed to be phase-independent, *i.e.*, dispersivity is considered the same for all phases. D_{ij} is the effective binary diffusion coefficient of component *i* in phase *j*. Also, τ is the tortuosity factor that accounts for the reduction in diffusive flux caused by the tortuous paths traced by particles of component *i*.

If interstitial velocity is greater than 3 cm/day, the longitudinal dispersion coefficient, K_{xx}, can be written as (Lake, 1989)

$$K_{xx} \approx \alpha_L \frac{|\vec{u}|}{\phi} . \tag{6.7}$$

Numerical solutions to the conservation equations are usually obtained through finite difference methods. Hence, the numerical solutions are always affected by the truncation error associated with the differencing schemes. Lantz (1971), Fanchi (1983), and Yang (1990) showed that the truncation error introduces additional second-order (in some cases even first-order) terms in finite difference representations of the mass conservation equation; in practice, as Yang (1990) pointed out, the flow velocity rarely remains constant with distance because of the cross-flow between layers or the compressibility of fluids. Hence, we determine and verify the numerical dispersion coefficients when the flow velocity varies with distance.

The main objectives of this chapter are: (1) to derive numerical dispersion coefficients when the flow velocity changes with distance and verify them and (2) evaluate the local mixing when the convective cross-flow varies.

6.2. PART I:

6.2.1 The Convection-Diffusion Equation

The 2D convection-diffusion (CD) equation describes the mass conservation of the tracer component. Assuming constant porosity (incompressible pore space), the two-dimensional CD equation becomes

$$\frac{\partial \omega}{\partial t} + \frac{1}{\phi}\frac{\partial \left(\omega u_x\right)}{\partial x} + \frac{1}{\phi}\frac{\partial \left(\omega u_y\right)}{\partial y} = K_{xx}\frac{\partial^2 \omega}{\partial x^2} + K_{yy}\frac{\partial^2 \omega}{\partial y^2}, \tag{6.8}$$

where ω is the mass of the displacing component expressed per unit pore volume. In addition, we assume that the principal axes of dispersion and permeability tensors coincide. The cross-derivatives are not included in Eq. (6.8) and, hence, we assume that the corresponding coefficients are zero (*i.e.*, the off-diagonal elements of the physical (input) dispersion tensor are zero).

The variation of the flow velocity with distance caused by cross-flow between layers is considered in the present work. It is customary to inject a conservative (passive) tracer into the permeable medium and match the concentration history with a one-dimensional (1D) solution of the CD equation to determine dispersivity as a matching parameter to fit the concentration history plots.

6.2.2 Finite Difference Form of the CD Equation

Most partial differential equations (PDE) cannot be solved analytically. Hence, numerical solutions are often used to convert PDEs to algebraic equations. The algebraic equations can then be solved by direct or iterative methods. The essence of numerical

methods for PDEs lies in converting the derivative terms to "finite differences." An explicit difference form of Eq. (6.8) can be written as

$$\Delta_t \omega = K_{xx}\Delta_x^2\omega + K_{yy}\Delta_y^2\omega - \frac{1}{\phi}\left(\omega\Delta_x u_x + u_x\Delta_x\omega\right) - \frac{1}{\phi}\left(\omega\Delta_y u_y + u_y\Delta_y\omega\right). \tag{6.9}$$

Finite difference schemes commonly used to approximate the derivatives are forward, backward, and central differences. A forward difference uses the function values at x and $(x+h)$:

$$\Delta_h f = f\left(x+h\right) - f\left(x\right), \tag{6.10}$$

where h is the spacing. Thus, the gradient of function in the x direction at $(x+h)$ can be linearly approximated by

$$\left.\frac{\partial f}{\partial x}\right|_{x+h} \cong \frac{f|_{x+h} - f|_x}{\left(x+h\right)-x} = \frac{f|_{x+h} - f|_x}{h}. \tag{6.11}$$

This is a reasonable approximation when h is small. Similarly, a backward difference uses the function values at x and $(x-h)$:

$$\nabla_h f = f\left(x\right) - f\left(x-h\right). \tag{6.12}$$

Thus,

$$\left.\frac{\partial f}{\partial x}\right|_{x-h} \cong \frac{f|_{x-h} - f|_x}{\left(x-h\right)-x} = \frac{f|_x - f|_{x-h}}{h}. \tag{6.13}$$

Finally, the central difference is given by

$$\delta_h f = f\left(x+\frac{h}{2}\right) - f\left(x-\frac{h}{2}\right), \tag{6.14}$$

and, hence, the gradient of function in the x-direction at $(x+h/2)$ becomes

$$\left.\frac{\partial f}{\partial x}\right|_{x+\frac{h}{2}} \cong \frac{f\big|_{x+\frac{h}{2}} - f\big|_{x-\frac{h}{2}}}{\left(x+\frac{h}{2}\right)-\left(x-\frac{h}{2}\right)} = \frac{f\big|_{x+\frac{h}{2}} - f\big|_{x-\frac{h}{2}}}{h} \quad . \tag{6.15}$$

Using Taylor's series of expansion, the forward difference form of the time derivative in Eq. (6.9) becomes

$$\Delta_t \omega = \frac{\partial \omega}{\partial t} + \frac{\Delta t}{2!}\frac{\partial^2 \omega}{\partial t^2} + \frac{(\Delta t)^2}{3!}\frac{\partial^3 \omega}{\partial t^3} + \ldots \quad . \tag{6.16}$$

In addition, the first-order distance derivatives in Eq. (6.9) are approximated as

$$\Delta_x \omega = \frac{\partial \omega}{\partial x} + \frac{\Delta x}{2!}\frac{\partial^2 \omega}{\partial x^2} + \frac{(\Delta x)^2}{3!}\frac{\partial^3 \omega}{\partial x^3} + \ldots \quad , \tag{6.17}$$

$$\Delta_y \omega = \frac{\partial \omega}{\partial y} + \frac{\Delta y}{2!}\frac{\partial^2 \omega}{\partial y^2} + \frac{(\Delta y)^2}{3!}\frac{\partial^3 \omega}{\partial y^3} + \ldots \quad , \tag{6.18}$$

$$\Delta_x u_x = \frac{\partial u_x}{\partial x} + \frac{\Delta x}{2!}\frac{\partial^2 u_x}{\partial x^2} + \frac{(\Delta x)^2}{3!}\frac{\partial^3 u_x}{\partial x^3} + \ldots \quad , \tag{6.19}$$

$$\Delta_y u_y = \frac{\partial u_y}{\partial y} + \frac{\Delta y}{2!}\frac{\partial^2 u_y}{\partial y^2} + \frac{(\Delta y)^2}{3!}\frac{\partial^3 u_y}{\partial y^3} + \ldots \quad . \tag{6.20}$$

Similarly, the second-order distance derivatives are approximated as

$$\Delta_x^2 \omega = \frac{\partial^2 \omega}{\partial x^2} + \frac{(\Delta x)^4}{12}\frac{\partial^4 \omega}{\partial x^4} + \ldots \quad , \tag{6.21}$$

$$\Delta_y^2 \omega = \frac{\partial^2 \omega}{\partial y^2} + \frac{(\Delta y)^4}{12}\frac{\partial^4 \omega}{\partial y^4} + \ldots \quad . \tag{6.22}$$

The substitution of Eqs. (6.16) through (6.22) into Eq.(6.9), while retaining terms only through the second-order differentials, yields

$$\left(\frac{\partial\omega}{\partial t}+\frac{\Delta t}{2!}\frac{\partial^2\omega}{\partial t^2}\right)=K_{xx}\frac{\partial^2\omega}{\partial x^2}+K_{yy}\frac{\partial^2\omega}{\partial y^2}-\frac{u_x}{\phi}\left(\frac{\partial\omega}{\partial x}+\frac{\Delta x}{2!}\frac{\partial^2\omega}{\partial x^2}\right)-\frac{u_y}{\phi}\left(\frac{\partial\omega}{\partial y}+\frac{\Delta y}{2!}\frac{\partial^2\omega}{\partial y^2}\right)$$
$$-\frac{\omega}{\phi}\left(\frac{\partial u_x}{\partial x}+\frac{\Delta x}{2!}\frac{\partial^2 u_x}{\partial x^2}\right)-\frac{\omega}{\phi}\left(\frac{\partial u_y}{\partial y}+\frac{\Delta y}{2!}\frac{\partial^2 u_y}{\partial y^2}\right) \quad (6.23)$$

Next, the second-order time derivative term on the left side of Eq. (6.23) is substituted by equivalent terms to determine the numerical dispersion coefficients. The equivalent terms of the second-order time derivative is determined by taking the derivative of Eq. (6.8) with respect to time:

$$\frac{\partial^2\omega}{\partial t^2}+\frac{u_x}{\phi}\frac{\partial^2\omega}{\partial t\partial x}+\frac{\partial u_x}{\partial t}\frac{\partial\omega}{\partial x}+\frac{1}{\phi}\frac{\partial\omega}{\partial t}\frac{\partial u_x}{\partial x}+\frac{1}{\phi}\omega\frac{\partial^2 u_x}{\partial t\partial x}+$$
$$\frac{u_y}{\phi}\frac{\partial^2\omega}{\partial t\partial y}+\frac{\partial u_y}{\partial t}\frac{\partial\omega}{\partial y}+\frac{1}{\phi}\frac{\partial\omega}{\partial t}\frac{\partial u_y}{\partial y}+\frac{1}{\phi}\omega\frac{\partial^2 u_y}{\partial t\partial y}= \quad (6.24)$$
$$K_{xx}\frac{\partial^3\omega}{\partial t\partial x^2}+K_{yy}\frac{\partial^3\omega}{\partial t\partial y^2}$$

Next, the differentiation of Eq. (6.8) with respect to *x* gives

$$\frac{\partial^2\omega}{\partial x\partial t}+\frac{1}{\phi}\frac{\partial u_x}{\partial x}\frac{\partial\omega}{\partial x}+\frac{u_x}{\phi}\frac{\partial^2\omega}{\partial x^2}+\frac{\omega}{\phi}\frac{\partial^2 u_x}{\partial x^2}+\frac{1}{\phi}\frac{\partial u_x}{\partial x}\frac{\partial\omega}{\partial x}+$$
$$\frac{1}{\phi}\frac{\partial u_y}{\partial x}\frac{\partial\omega}{\partial y}+\frac{u_y}{\phi}\frac{\partial^2\omega}{\partial x\partial y}+\frac{\omega}{\phi}\frac{\partial^2 u_y}{\partial x\partial y}+\frac{1}{\phi}\frac{\partial\omega}{\partial x}\frac{\partial u_y}{\partial y}= \quad (6.25)$$
$$K_{xx}\frac{\partial^3\omega}{\partial x^3}+K_{yy}\frac{\partial^3\omega}{\partial x\partial y^2}$$

Also, the differentiation of Eq. (6.8) with respect to *y* gives

$$\frac{\partial^2\omega}{\partial y\partial t}+\frac{1}{\phi}\frac{\partial u_x}{\partial y}\frac{\partial\omega}{\partial x}+\frac{u_x}{\phi}\frac{\partial^2\omega}{\partial y\partial x}+\frac{\omega}{\phi}\frac{\partial^2 u_x}{\partial y\partial x}+\frac{1}{\phi}\frac{\partial\omega}{\partial y}\frac{\partial u_x}{\partial x}+$$
$$\frac{1}{\phi}\frac{\partial u_y}{\partial y}\frac{\partial\omega}{\partial y}+\frac{u_y}{\phi}\frac{\partial^2\omega}{\partial y^2}+\frac{1}{\phi}\frac{\partial\omega}{\partial y}\frac{\partial u_y}{\partial y}+\frac{\omega}{\phi}\frac{\partial^2 u_y}{\partial y^2}= \quad (6.26)$$
$$K_{xx}\frac{\partial^3\omega}{\partial y\partial x^2}+K_{yy}\frac{\partial^3\omega}{\partial y^3}$$

After eliminating $\frac{\partial^2\omega}{\partial t\partial x}$ and $\frac{\partial^2\omega}{\partial t\partial y}$ between Eqs. (6.24) through (6.26), the second-order time derivative term is expressed as

$$\begin{aligned}\frac{\partial^2\omega}{\partial t^2} = &-\frac{\partial\omega}{\partial x}\left(\frac{\partial u_x}{\partial t}-\frac{2u_x}{\phi^2}\frac{\partial u_x}{\partial x}-\frac{u_y}{\phi^2}\frac{\partial u_x}{\partial y}-\frac{u_x}{\phi^2}\frac{\partial u_y}{\partial y}\right)\\ &-\frac{\partial\omega}{\partial y}\left(-\frac{u_x}{\phi^2}\frac{\partial u_y}{\partial x}-2\frac{u_y}{\phi^2}\frac{\partial u_y}{\partial y}-\frac{u_y}{\phi^2}\frac{\partial u_x}{\partial x}+\frac{\partial u_y}{\partial t}\right)-\frac{\partial\omega}{\partial t}\left(\frac{1}{\phi}\frac{\partial u_x}{\partial x}+\frac{1}{\phi}\frac{\partial u_y}{\partial y}\right)\\ &+\overbrace{\left(2\frac{u_y u_x}{\phi^2}\right)}^{K_{Cross}^{Num}}\frac{\partial^2\omega}{\partial x\partial y}+\overbrace{\left(\frac{u_y}{\phi}\right)}^{K_{yy}^{Num}}\frac{\partial^2\omega}{\partial y^2}+\overbrace{\left(\frac{u_x}{\phi}\right)}^{K_{xx}^{Num}}\frac{\partial^2\omega}{\partial x^2}\\ &-\frac{1}{\phi}\omega\frac{\partial^2 u_x}{\partial t\partial x}-\frac{1}{\phi}\omega\frac{\partial^2 u_y}{\partial t\partial y}+\frac{\omega u_x}{\phi^2}\frac{\partial^2 u_x}{\partial x^2}+\frac{\omega u_x}{\phi^2}\frac{\partial^2 u_y}{\partial x\partial y}+\frac{u_y\omega}{\phi^2}\frac{\partial^2 u_x}{\partial y\partial x}+\frac{\omega u_y}{\phi^2}\frac{\partial^2 u_y}{\partial y^2}\\ &K_{xx}\frac{\partial^3\omega}{\partial t\partial x^2}+K_{yy}\frac{\partial^3\omega}{\partial t\partial y^2}-\frac{u_x}{\phi}K_{xx}\frac{\partial^3\omega}{\partial x^3}-\frac{u_x}{\phi}K_{yy}\frac{\partial^3\omega}{\partial x\partial y^2}-\frac{u_y}{\phi}k_{xx}\frac{\partial^3\omega}{\partial y\partial x^2}-\frac{u_y}{\phi}K_{yy}\frac{\partial^3\omega}{\partial y^3}.\end{aligned} \tag{6.27}$$

Finally, the substitution of Eq. (6.27) into Eq. (6.23) yields the expressions for the longitudinal, transverse, and the off-diagonal elements (cross-term dispersion coefficients) as

$$K_{xx}^{Num} = \left(\frac{u_x}{\phi}\right)^2\frac{\Delta t}{2!}+\frac{u_x}{\phi}\frac{\Delta x}{2!}, \tag{6.28}$$

$$K_{yy}^{Num} = \left(\frac{u_y}{\phi}\right)^2\frac{\Delta t}{2!}+\frac{u_y}{\phi}\frac{\Delta y}{2!}, \tag{6.29}$$

$$K_{Cross}^{Num} = \left(\frac{u_y u_x}{\phi^2}\right)\Delta t. \tag{6.30}$$

These elements are coefficients of the second-order derivatives of ω with respect to distance in Eq. (6.27). Two principal axes (longitudinal and transverse directions) and two off-diagonal directions are considered for dispersive transport through a 2D permeable medium. Following Fanchi (1983), equations (6.28) through (6.30) indicate numerical dispersion coefficients along the principal (longitudinal and transverse) and the cross-term axes, where the concentration gradient and the mass transfer direction are not collinear. A comparison of the numerical dispersion terms defined by Fanchi (1983), $\left(\frac{u_y u_x}{\phi^2}\right)\frac{\Delta t}{2}$, and Eq. (6.30) suggests a larger cross-term coefficient (multiplied by a factor of two in this study). Thus, the numerical cross-term elements of the numerical dispersion tensor double when velocity varies along principal axes (as in this study).

To verify the derived off-diagonal elements of the numerical dispersion tensor, a simulation model with a specific configuration is required to prevent the interference of the longitudinal dispersion. Convective flow in the diagonal and transverse directions should be suppressed; otherwise, the longitudinal dispersion will interfere the length of mixing zone in any direction that flow occurs. However, the convective flow cannot be prevented when the coordinate system of the simulation model coincides with the principal axes of the permeability.

Figure 6.1 shows a schematic of a composite simulation model consisting of a thin 2D model (flow strip) attached to another permeable medium (base). The simulations are performed using GEM, CMG's general equation-of-state compositional reservoir simulator. The objective is to evaluate dispersivity in the diagonal direction of a thin permeable medium (the flow strip) under two conditions: (1) when flow velocity changes with distance and (2) when flow velocity is constant along the flow strip.

We make the simulation models such that flow takes place only along the diagonal direction (45° with respect to the *x*-direction). Elementary geometry then suggests that cross-term dispersion will be collinear with the coordinate system. However, we must assure that the direction of flow is fixed during the displacement; therefore, the permeability in the *x*-direction of grid blocks in the base is assigned three orders of magnitude smaller than those in the flow strip (Figure 6.1). Hence, the cross-term dispersion can be assessed through monitoring the growth of the mixing zone along the *y*-direction.

Two simulation models (Model 1 and Model 2) are used to evaluate the cross-term dispersivities. All parameters are the same for both models except that the thickness of grid blocks in the flow strip changes in Model 2 while it is fixed in Model 1. The change in the thickness of grid blocks yields the variation of local velocity with distance. Figure 6.2 shows the variation of the grid thickness in Model 2. Thus, total pore volume of the flow strip is kept the same for both models. Note that the grid thickness in the *z*-direction is uniform for Model 1.

The permeable medium is homogenous and initially filled with water and a tracer component is injected to measure local mixing. The simulation models consist of an injector and a producer that are operating under the constant bottomhole pressure constraint. Therefore, the pressure drop across the flow strip always remains constant. However, the grid thickness and, consequently, the flow velocity vary with distance in Model 2. Figure 6.3 shows how the velocity changes with distance in Model 2, because of the variation in the thickness of grid blocks in the flow strip. As inferred from Figure 6.3Figure , no significant flow occurs in the base permeable medium.

Figure 6.4 compares the injection and production rates for both models. Injection and production rates are the same and remain constant with time for each model; however, the rates are larger (by a factor of 1.17) in Model 1 compared to Model 2.

Figure 6.5 illustrates the tracer concentration in Model 1 after 1465 days. The length of the mixing zone in the *y*-direction represents the magnitude of dispersion in the cross-direction. Furthermore, the transverse dispersion is lessened by reducing the permeability in the *x*-direction of the base by three orders of magnitude compared to that of the flow strip. Note that for our geometry, the transverse dispersion coincides with line $x = y$ (the bisector of the angle between *x*- and *y*-axes).

Figure 6.6 shows the tracer concentration in Model 2 after 1715 days; note that the concentration profiles are depicted at the same dimensionless time (injected P.V.). A visual comparison of Figures 6.5 and 6.6 suggests that a larger mixing zone occurs in the diagonal direction of Model 2 compared to Model 1 (see Appendix A for more details on the mixing zone). This can be explained only through a larger dispersivity in the diagonal

direction of Model 2 compared to Model 1 as both Figures are depicted at the same dimensionless time.

In addition, Figure 6.7 compares the cumulative distribution function of the lengths of the mixing zone obtained in the *y*-direction for both models at the same dimensionless time. As inferred from the plot, the mode of distribution for Model 1 corresponds to the mixing zone length of 82 ft compared to that of 115 ft for Model 2; hence, the ratio of the lengths of the mixing zone in Model 2 to that of Model 1 is 1.40 ($\sim\sqrt{2}$). As the mixing zone is proportional to $\sqrt{K}$ (see appendix A), the dispersivity of Model 2 should be twice as large as in Model 1, consistent with Eq.(6.30).

The remainder of this chapter evaluates the change in local mixing caused by the convective cross-flow.

6.3. PART II:

A simulation approach is used to evaluate local mixing in heterogeneous permeable media when cross-flow between layers varies. The simulations are performed using GEM. Two-dimensional simulation models consist of an injector and a producer and have constant grid block sizes in the *x*- and *y*-directions. The permeable medium is initially filled with water and a passive tracer is injected to measure local mixing. The top and bottom of the models are no flow boundaries. The injector is assigned a constant rate whereas the producer is operating under a constant bottomhole pressure. Figure 6.8 shows the log-normally-distributed permeability field generated using the FFTsim code (Jennings *et al.*, 2002). Furthermore, a uniform porosity of 0.14 is considered.

Three simulation models are used to evaluate local mixing caused by cross-flow. They consist of 128 × 32 grid-blocks in the *x*- and *y*-directions. The length and width of the models are 1280 and 320 feet, respectively. All other parameters of the simulation models (as described in Table 6.1) are the same except for the effective aspect ratio (R_L); the effective aspect ratio is the ratio of the transverse to longitudinal velocity. Three values of R_L are examined for the purpose of this Chapter: 0, 0.126, and 10 and the ratio of permeability in y- to x-direction was adjusted, accordingly.

Equation (6.30) shows the Peclet number attributed to the numerical dispersion for two-phase flow (Orr, 2007). The Peclet number attributed to numerical dispersivity becomes 250, (α_L^{Num} =5.086 ft), as $\left(\frac{df_j}{dS_j}\right)$ is equal to one (tracer flow), and Δt_D is 0.001 in the simulations.

$$N_{Pe}^{-1}\big|_{\mathbf{Num.}} = \frac{\Delta x_D}{2}\frac{df_j}{dS_j}\left(1-\frac{\Delta t_D}{\Delta x_D}\frac{df_j}{dS_j}\right) \quad . \tag{6.30}$$

In addition, an input longitudinal dispersivity of 5.0 ft is added so that total dispersivity (numerical + physical) of each grid block becomes equal ($\alpha_L^{Num} + \alpha_L^{Phys}$ = 10.086 ft); consequently, the corresponding Peclet number is now reduced to 125.

In addition, the simulation continued long enough (10 P.V.) to provide enough data to construct the concentration history plots. The local mixing is determined either through matching the concentration history of the tracer to the solution of a 1D convection-dispersion equation (Eq. A-7) or based on the method developed in Chapter 5.

The level of mixing that occurs in a heterogeneous reservoir is widely debated; however, it is well understood that reservoir mixing is sensitive to permeability heterogeneity. Considering a set of ten equally-spaced cross-sections along the permeable medium, we calculate the local mixing for grid blocks located on them (Figure 6.9). Note that the principal axes of dispersivity and the permeability coincide in this study.

Figures 6.10 shows the concentration history plots obtained from grid blocks located on the third cross-section (as shown in Figure 6.9) when R_L=0.126.

Using Eq. (A-11) to match the concentration history plots, we get the longitudinal dispersivity for each grid block (output dispersivity) from Eq. (A-11). The slope of lines in Figure 6.11 is used to calculate the Peclet number and, consequently, the dispersivity for each grid block located on the third cross-section. Note that the x_D term, which is used in Eq. (A-11) to determine the output dispersivity of a grid block, is the dimensionless distance from the injector; hence, x_D is equal to 0.5 for grid blocks located on the third cross-section, etc. Furthermore, dimensionless time used in Eq. (A-11) corresponds to the ratio of the cumulative amount of fluid injected at any time to the fraction of total pore volume constrained between the injector and that cross-section; hence, the dimensionless time used in Eq. A-11 for grid blocks located on the third cross-section, is equal to (t_D / 0.3), etc. Similarly, Figures 6.12 through 6.25 illustrated the concentration history curves and the corresponding calculated dispersivity values for different R_L's.

Figure 6.26 shows the calculated dispersivity as a function of distance, normalized by the length of the reservoir, when R_L = 0.126. The black circles represents the dispersivity values calculated as if there is only one large grid block covering the

whole cross-section. Note that the local mixing at each grid block is much smaller than the averaged value represented by the black circles. Furthermore, the results suggest that the dispersivity increases with distance travelled.

Figure 6.27 shows the calculated dispersivity as a function of distance, normalized by the length of the reservoir, when $R_L = 10$. The averaged dispersivity (black circles) in this case is in the same order as the local mixing calculated at each grid block indicating that larger local mixing is realized with greater convective cross-flow between layers. Furthermore, the results suggest that the dispersivity increases with distance travelled.

Figure 6.28 shows ddispersivity values used in Eq. (5.27) to match the concentration history plots. The graph clearly indicates that larger dispersivity is needed when the cross-flow increases and the concentration history curves are easily matched with the dispersivity equal to the input value.

Figure 6.29 shows the koval heterogeneity values used in Eq. (5.27) to match the concentration history plots. The graph clearly indicates that smaller koval factor is needed when the cross-flow increases indicating that flow becomes more dispersive with distance travelled if there is convective cross-flow. Furthermore, the results suggest that the dispersivity increases with distance travelled.

6.4 DISCUSSION AND CONCLUSIONS

The expressions for the numerical dispersion coefficients associated with the finite- difference form of the CD equation is presented and tested when velocity varies with distance. Oscillatory velocity may occur because of the cross-flow between layers in heterogeneous permeable media or the compressibility of fluids (Yang, 1990). The latter was not discussed in this study; however, the off-diagonal elements of the numerical dispersion tensor were shown to double when the flow velocity changes with distance. A specifically designed simulation model confirms the greater off-diagonal numerical dispersion coefficient when the flow velocity varies.

Furthermore, the simulation results in Part II indicate that the flow becomes more dispersive with distance travelled if there is convective cross-flow. In addition, local mixing increases with the convective cross-flow between layers. In the examples shown in this Chapter, no significant transverse dispersion is present.

6.5 NOMENCLATURE

α_L = dispersivity in the longitudinal direction

K_{xx} = longitudinal dispersion coefficient

α_T = dispersivity in the transverse direction

K_{yy} = transverse dispersion coefficient

D_{cross} = off-diagonal element of numerical dispersivity tensor

t_D = dimensionless time defined as the ratio of cumulative amount of fluid injected at any time to total pore volume

x_D = dimensionless distance

$s_{j=}$ saturation of phase j

ϕ = porosity

v = interstitial velocity

u_x = Darcy velocity in the x-direction

u_y = Darcy velocity in the y-direction

τ = tortuosity factor

var = variance

t = time

J_{Di} = overall dispersive flux of component i

J_{Dij} = dispersive flux of component i in phase j

Δt_D = maximum time step in the simulation

$f_{j=}$ fractional flow of phase j

$s_{j=}$ saturation of phase j

N_{Pe} = Peclet number

λ_{yD} = dimensionless correlation length in the y-direction

R_L = effective aspect ratio

V_{DP} = Dykstra-Parson coefficient of variation

Table 6.1: The properties of the simulation model in Part II

Dimensionless Scaling Group	**Value**
V_{DP}	0.8
λ_{xD}	0.15
λ_{yD}	0.1
N_{Pe}^{*}	125

*Peclet number caused by total dispersivity: $N_{Pe} = \frac{u_T}{\phi L K_{xx}}$

(For more details on the dimensionless scaling groups see Appendix C)

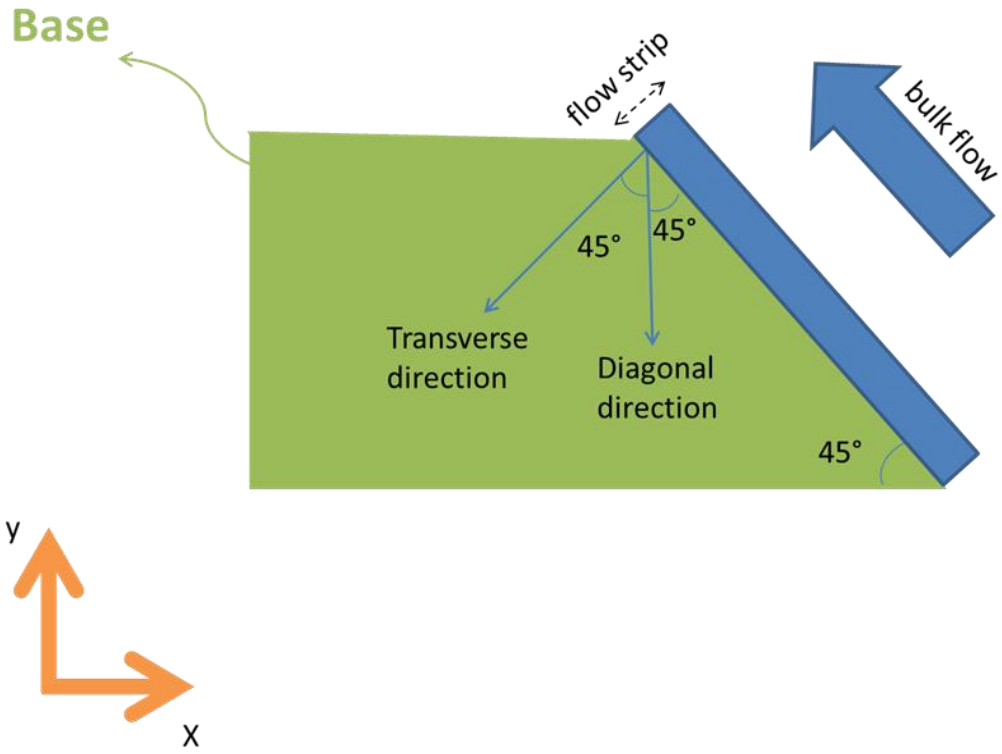

Figure 6.1: Schematic of a composite simulation model used in Part I to investigate the dispersivity term in the cross-direction of a thin 2D model (flow strip) attached to another permeable medium (base). Bulk flow occurs only across the flow strip as the permeability in the *x*-direction of the base is three-order of magnitude smaller than that of the flow strip. The flow strip consists of at least two grid blocks in the transverse direction.

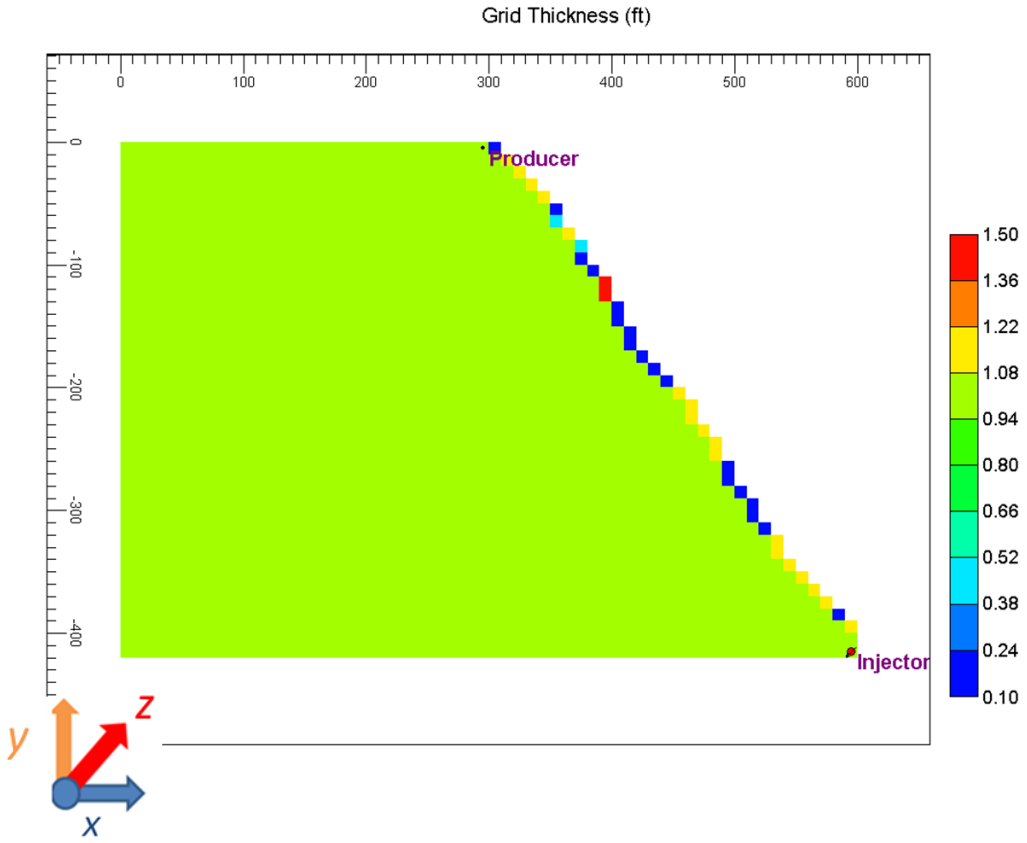

Figure 6.2: The map of grid block thickness (ft) in Model 2. The thickness of grid blocks in the flow strip changes along the z-direction.

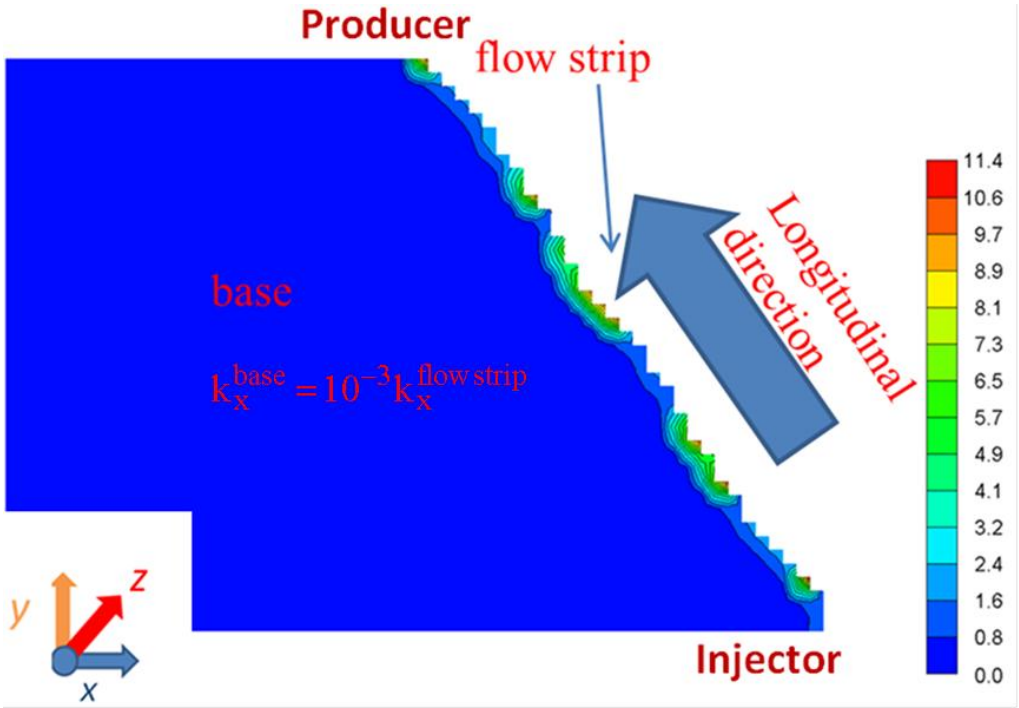

Figure 6.3: Map of flow velocity (ft/d) in Model 2. The flow velocity changes with distance because of the variation in the thickness of the grid block located in the flow strip. Note that the permeability in the *x*-direction is reduced by a factor of 0.001 for the grid blocks located in the base permeable medium.

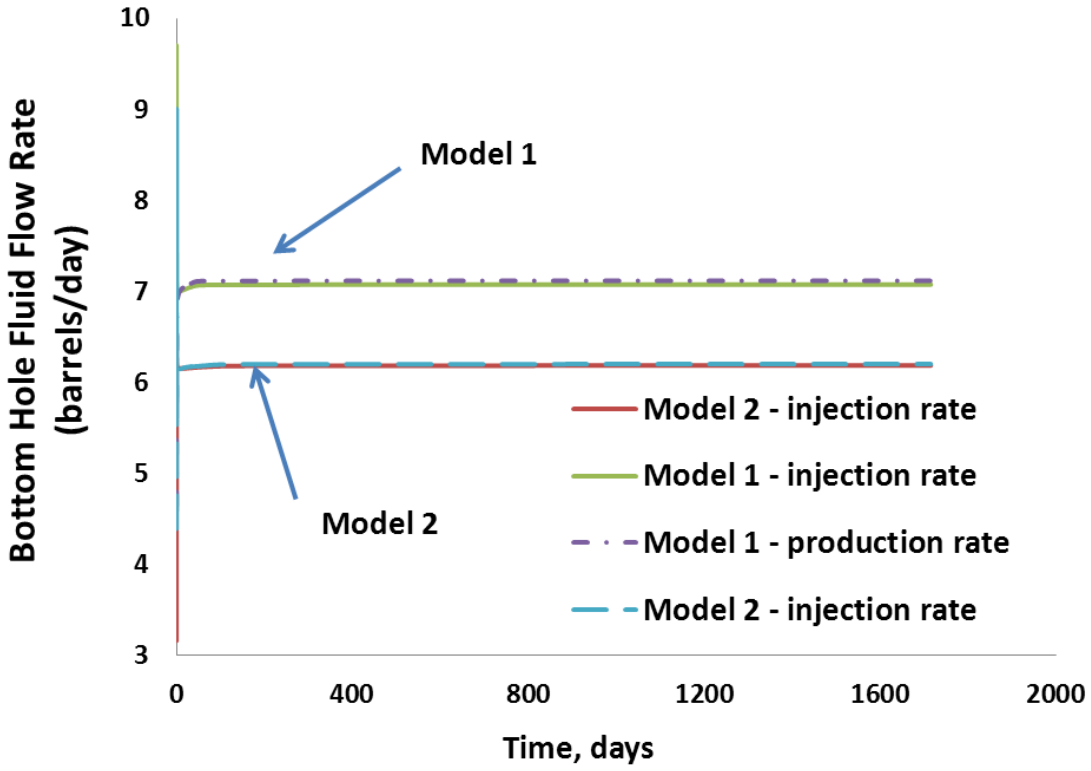

Figure 6.4: Injection and production rates expressed in reservoir volumes per day for Model 1 and Model 2. The injection and production rates are equal and constant with time for each model.

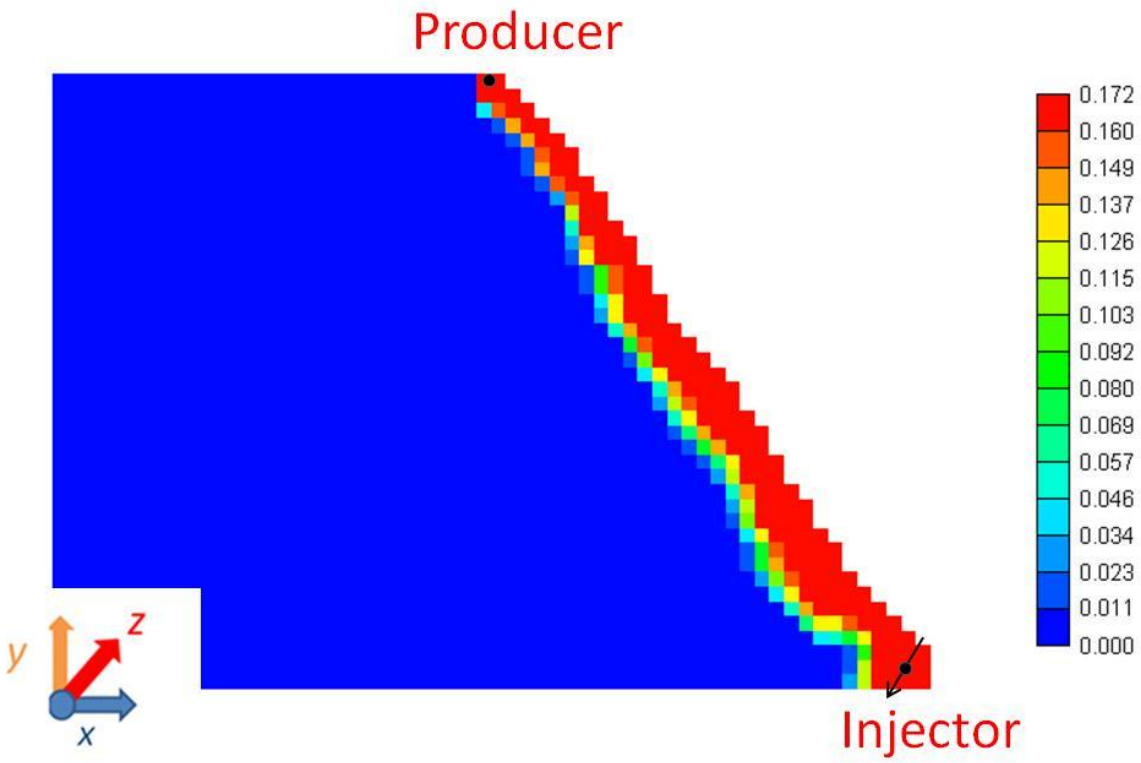

Figure 6.5: Dimensionless tracer concentration in Model 1 after 1465 days.

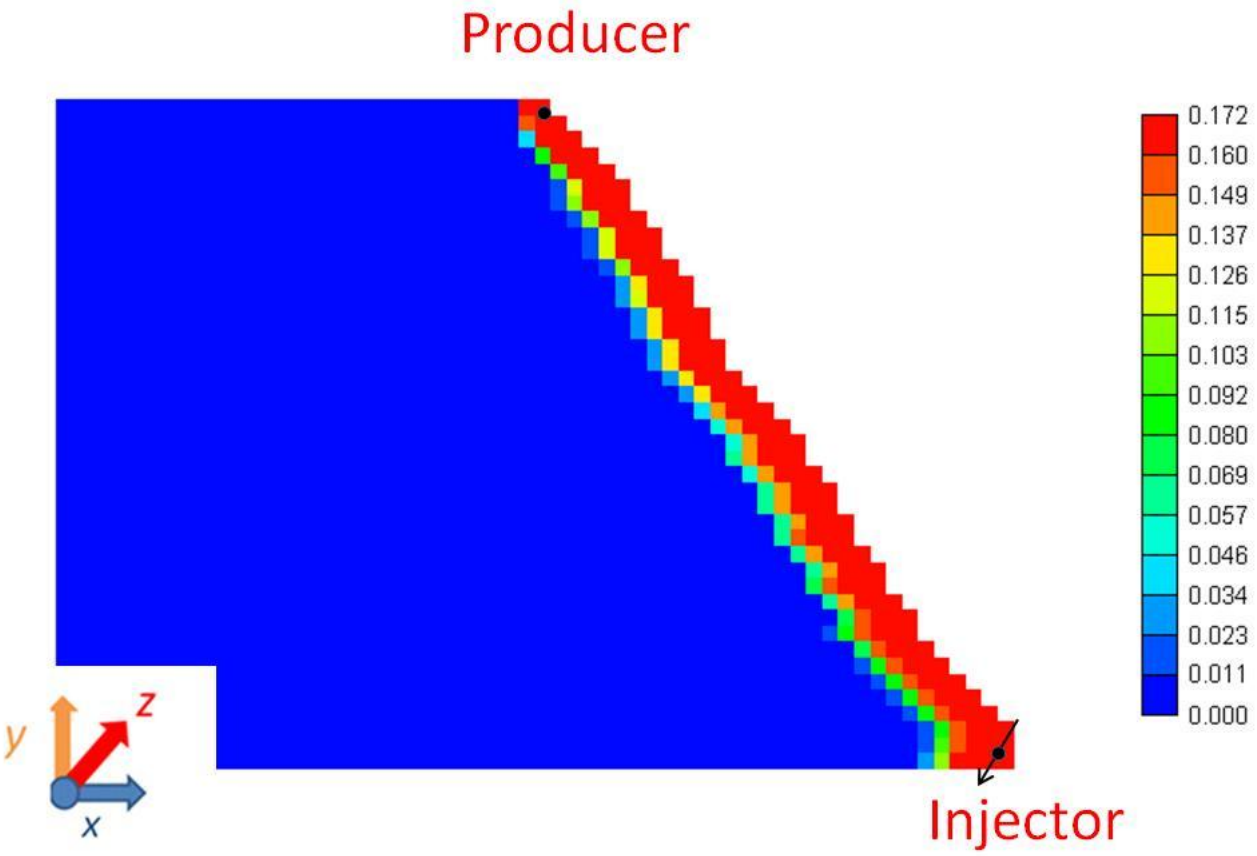

Figure 6.6: Dimensionless tracer concentration in Model 2 after 1715 days.

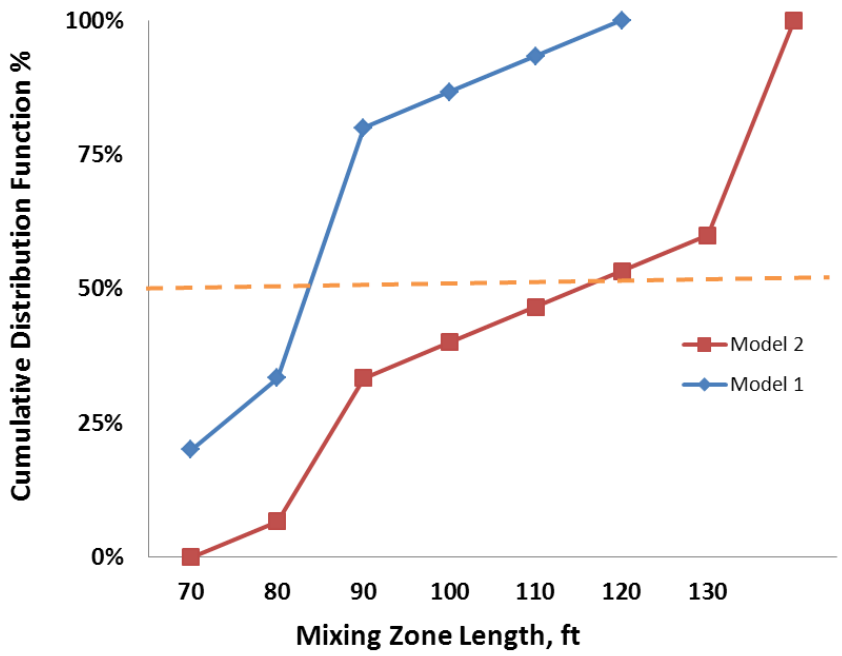

Figure 6.7: Cumulative distribution functions of the mixing zone length obtained in the *y*-direction at the same dimensionless time. As inferred from the plot, the mode of the distribution for Model 1 corresponds to the mixing zone length of 82 ft compared to that of 115 ft for Model 2.

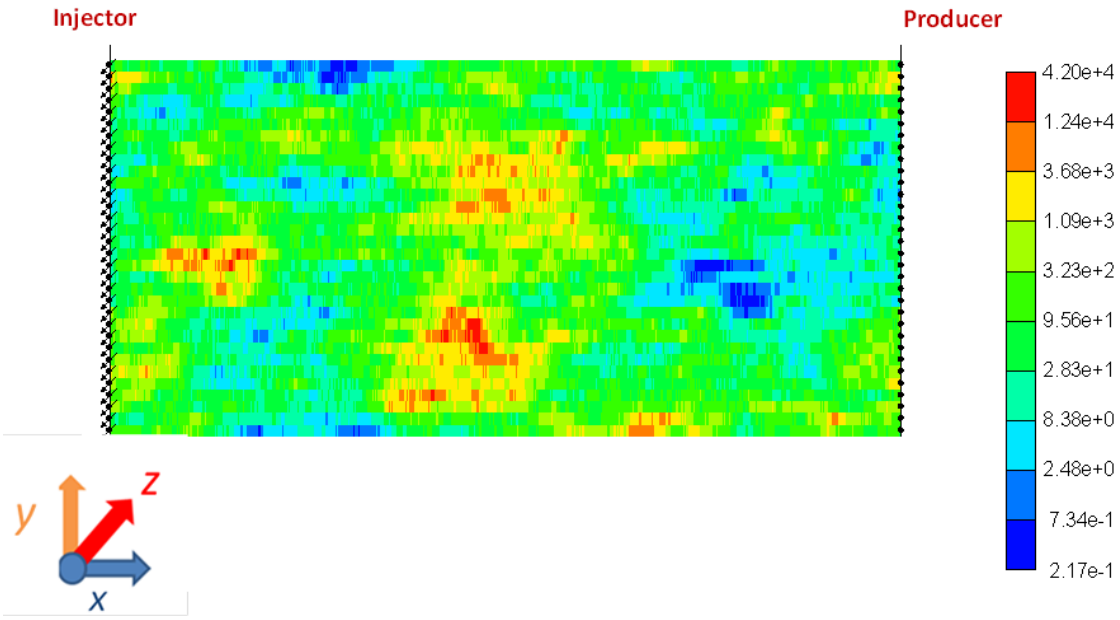

Figure 6.8: Permeability field (md) used in Part II. V_{DP} and λ_{xD} are 0.8 and 0.15, respectively.

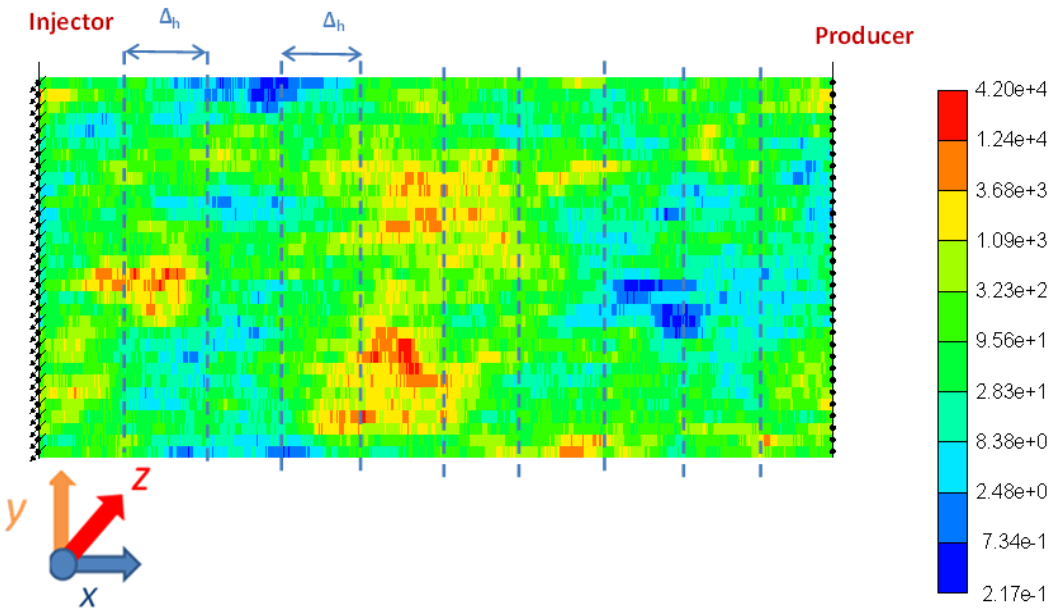

Figure 6.9: Permeability field (md) used in Part II. V_{DP} and λ_{xD} are 0.8 and 0.15, respectively.

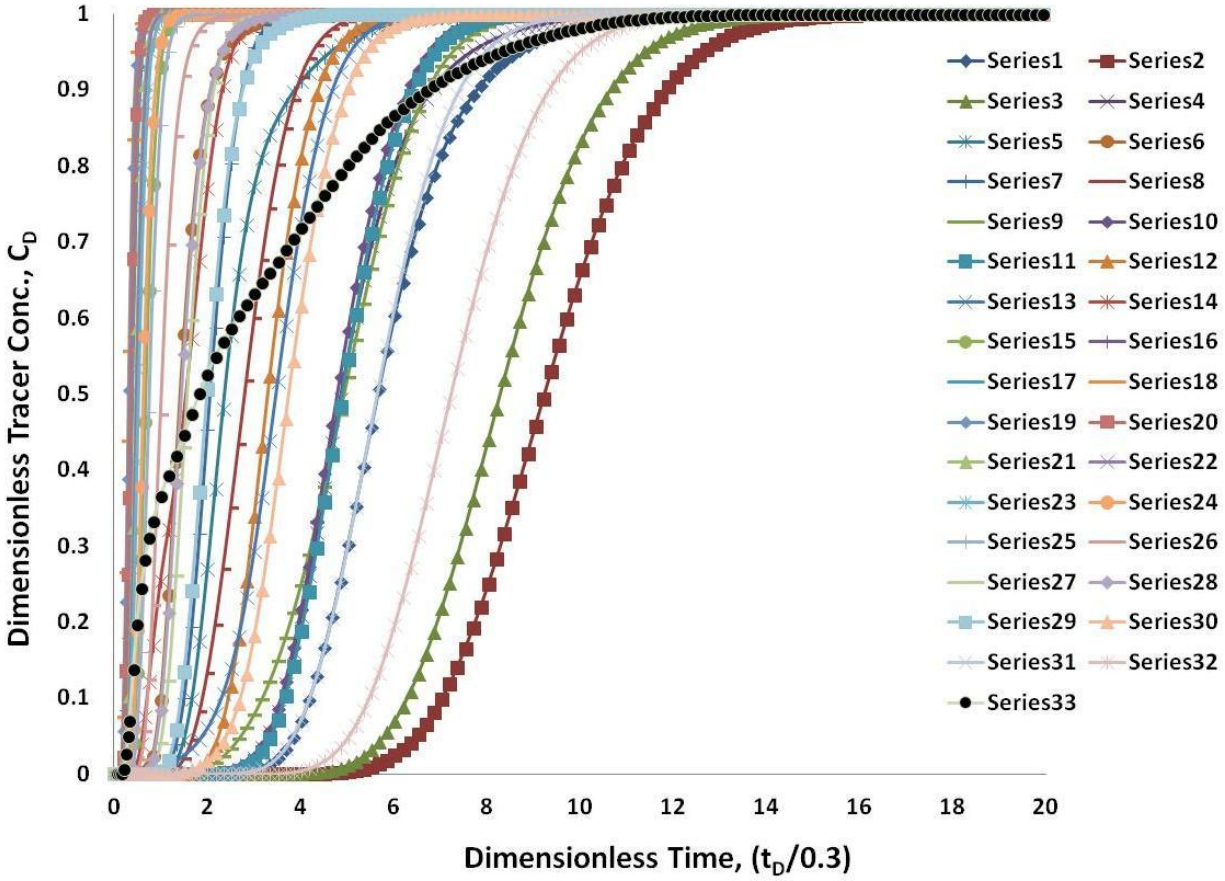

Figure 6.10: Concentration history plots for all grid blocks located at x_D = 0.3 when R_L=0.126. The dimensionless time represents the fraction of total pore volume constrained between the injector and the third cross-section.

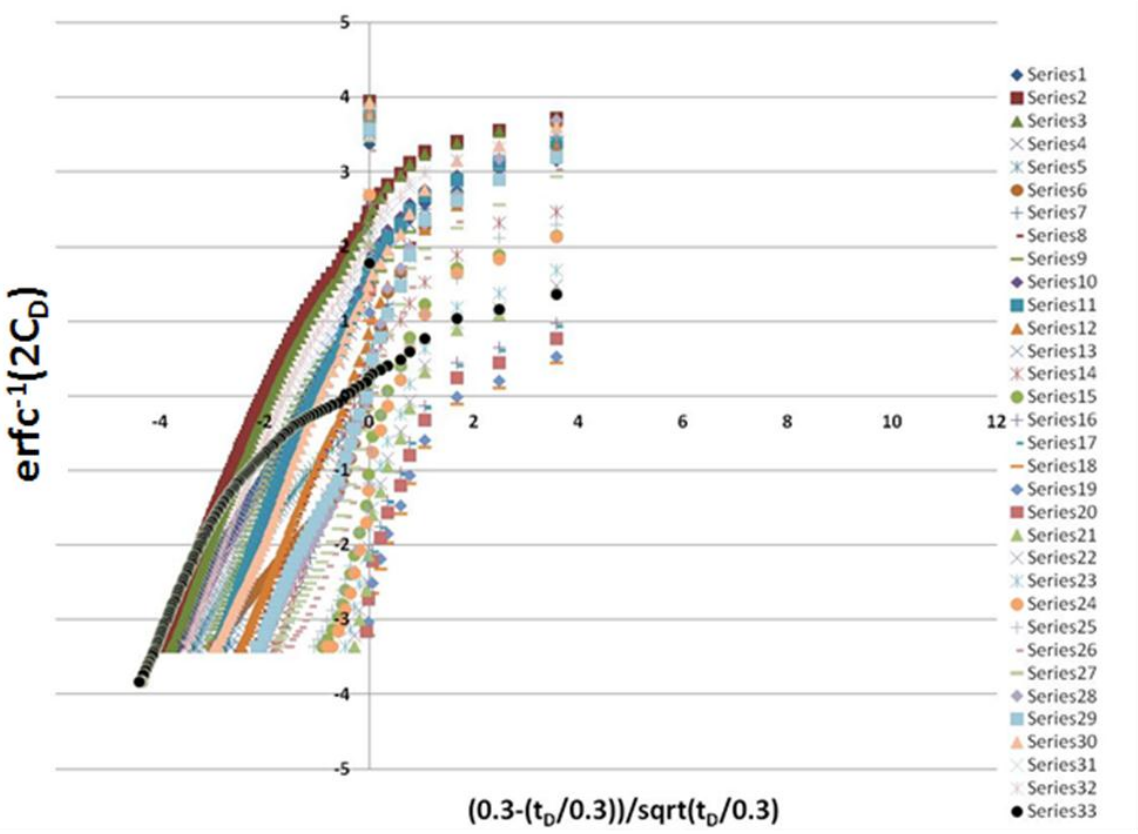

Figure 6.11: $\text{Erfc}^{-1}(2c_D)$ as a function of $\frac{(x_D - t_D)}{\sqrt{t_D}}$ obtained from Figure 6.10. The longitudinal dispersion coefficient for each grid block is obtained from the slope of the corresponding line constructed on this plot; for this plot, x_D =0.3 and $t_D|\text{cross-section} = (t_D/0.3)$ are used in Eq. (A-11).

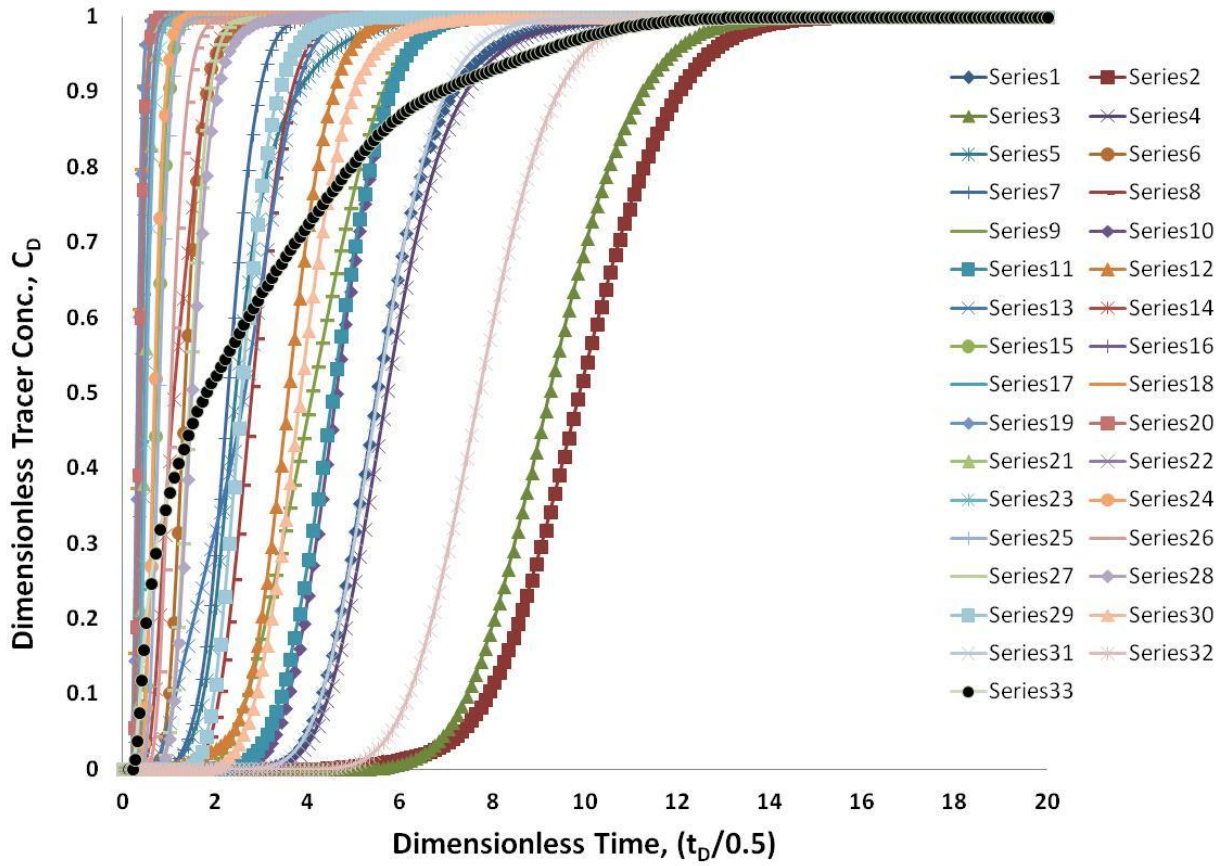

Figure 6.12: Concentration history plots for all grid blocks located at $x_D = 0.5$ when R_L=0.126. The dimensionless time represents the fraction of total pore volume constrained between the injector and the fifth cross-section.

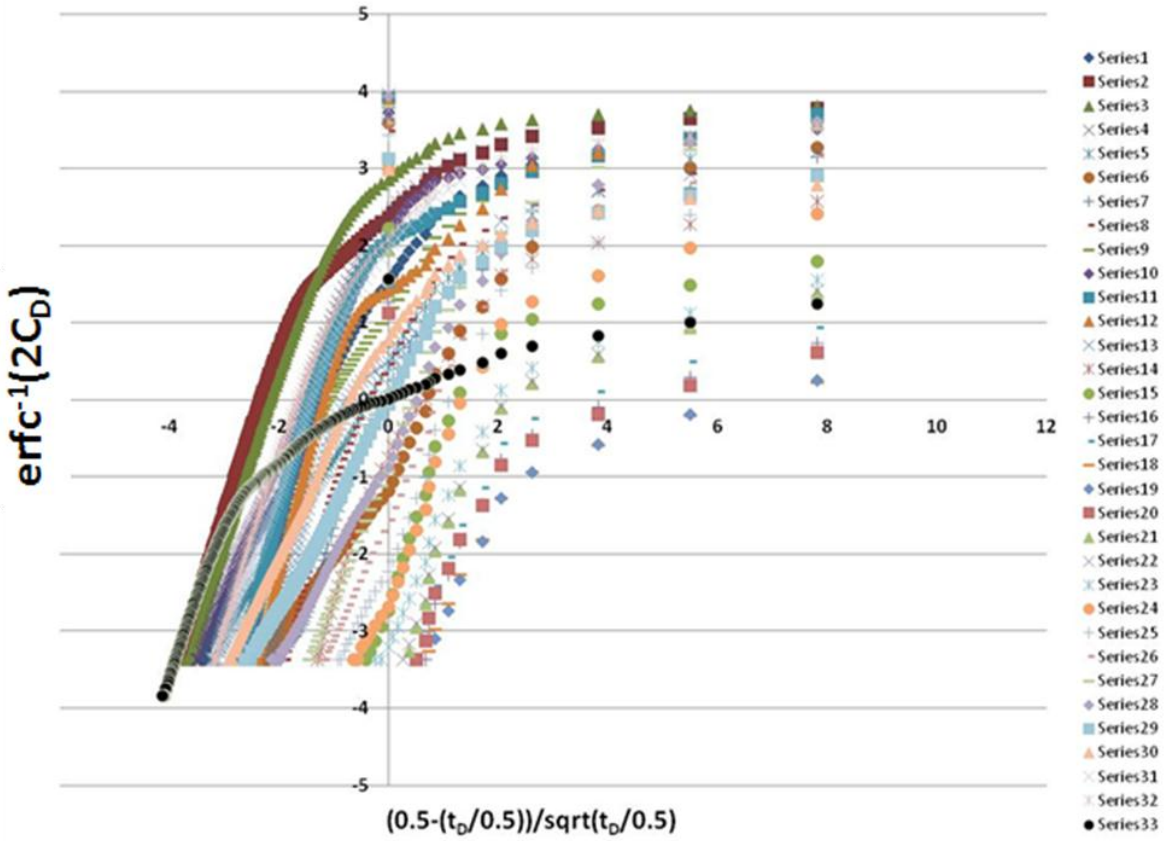

Figure 6.13: $\mathrm{Erfc}^{-1}(2c_D)$ as a function of $\frac{(x_D - t_D)}{\sqrt{t_D}}$ obtained from Figure 6.12. The longitudinal dispersion coefficient for each grid block is obtained from the slope of the corresponding line constructed on this plot; for this plot, x_D =0.5 and $t_D|$cross-section = (t_D/0.5) are used in Eq. (A-11).

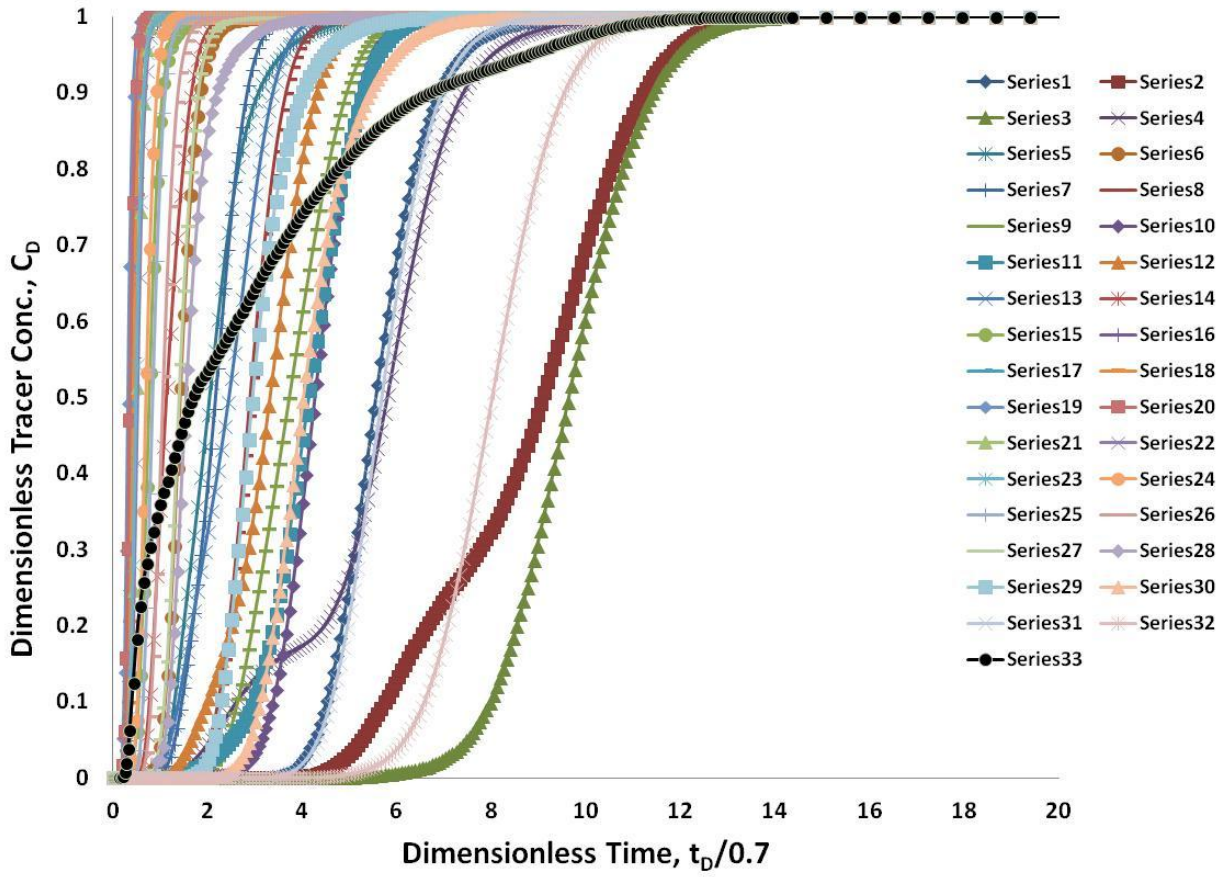

Figure 6.14: Concentration history plots for all grid blocks located at $x_D = 0.7$ when R_L=0.126. The dimensionless time represents the fraction of total pore volume constrained between the injector and the seventh cross-section.

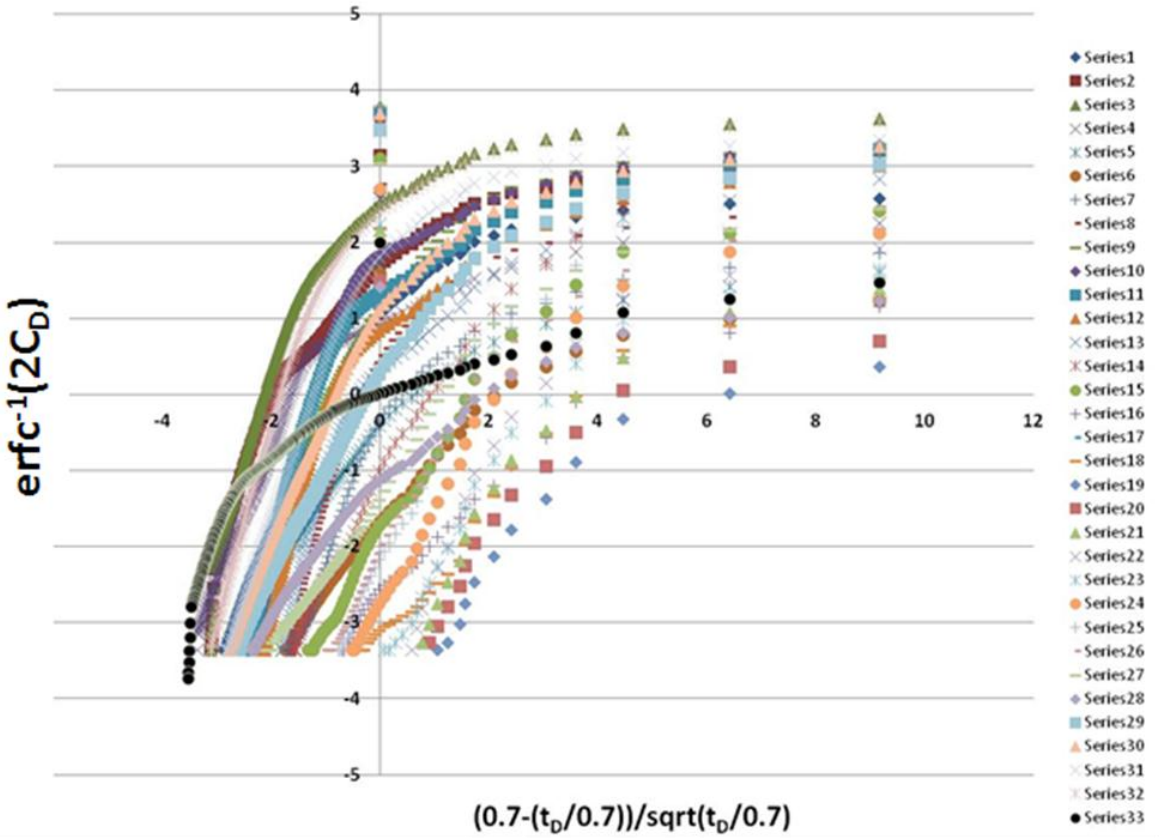

Figure 6.15: $\text{Erfc}^{-1}(2c_D)$ as a function of $\frac{(x_D - t_D)}{\sqrt{t_D}}$ obtained from Figure 6.14. The longitudinal dispersion coefficient for each grid block is obtained from the slope of the corresponding line constructed on this plot; for this plot, x_D =0.7 and $t_D|\text{cross-section} = (t_D/0.7)$ are used in Eq. (A-11).

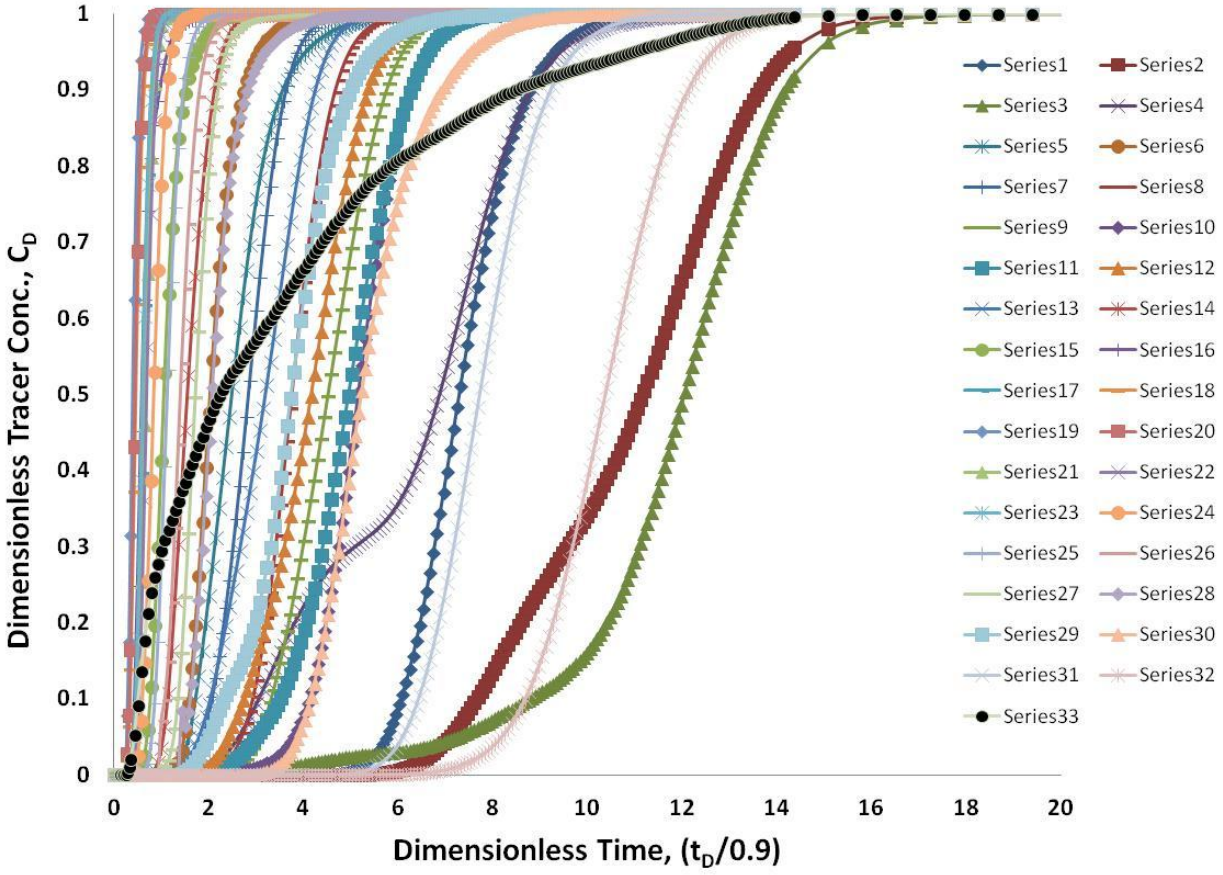

Figure 6.16: Concentration history plots for all grid blocks located at $x_D = 0.9$ when R_L=0.126. The dimensionless time represents the fraction of total pore volume constrained between the injector and the ninth cross-section.

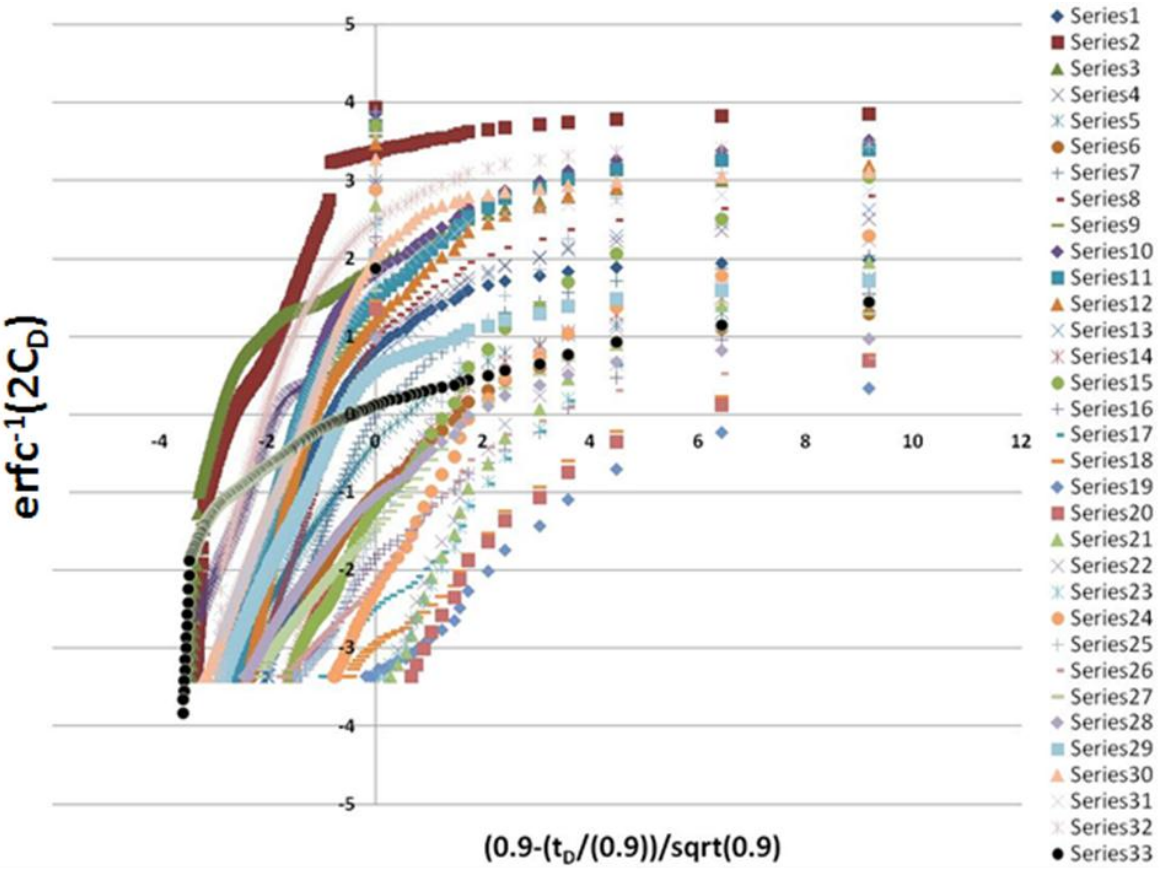

Figure 6.17: $\text{Erfc}^{-1}(2c_D)$ as a function of $\frac{(x_D - t_D)}{\sqrt{t_D}}$ obtained from Figure 6.16. The longitudinal dispersion coefficient for each grid block is obtained from the slope of the corresponding line constructed on this plot; for this plot, x_D =0.9 and $t_D|\text{cross-section} = (t_D/0.9)$ are used in Eq. (A-11).

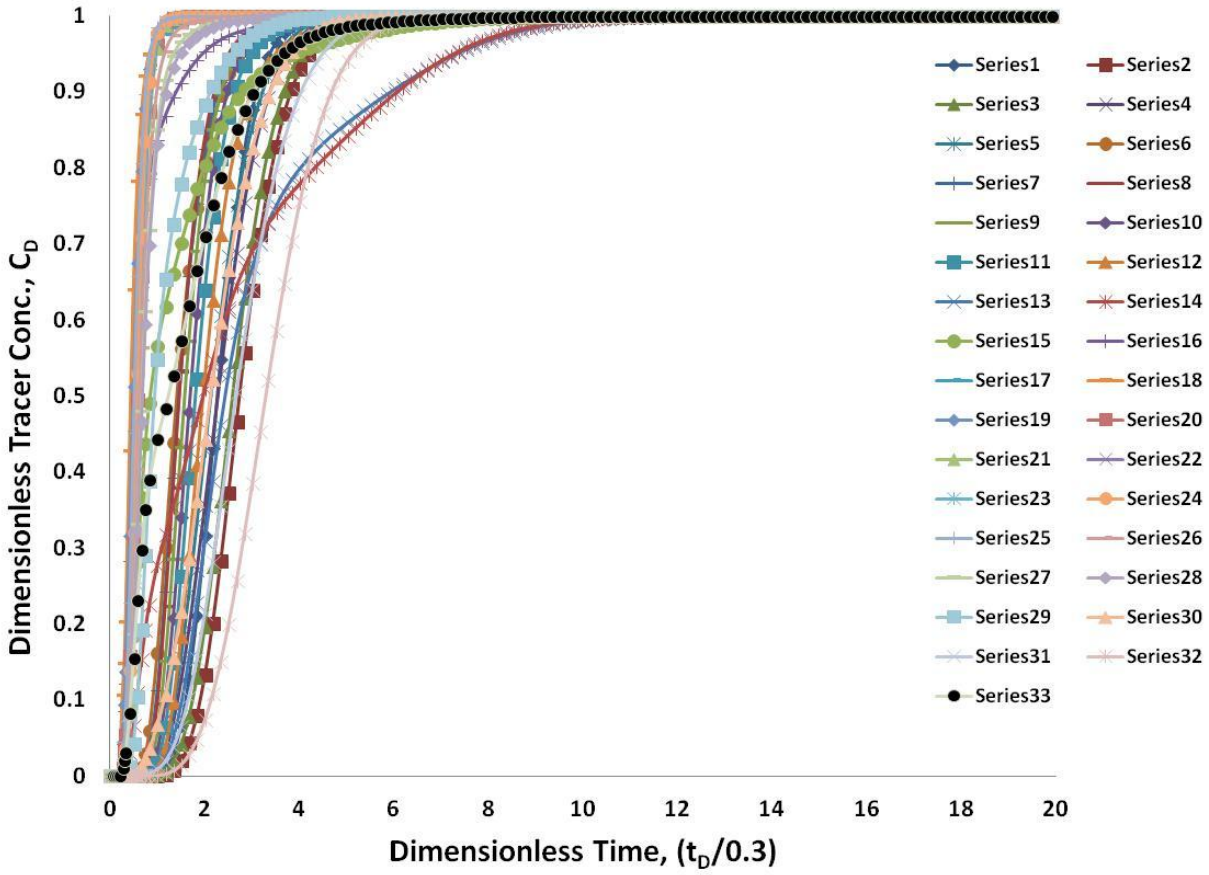

Figure 6.18: Concentration history plots for all grid blocks located at $x_D = 0.3$ when R_L=10. The dimensionless time represents the fraction of total pore volume constrained between the injector and the third cross-section.

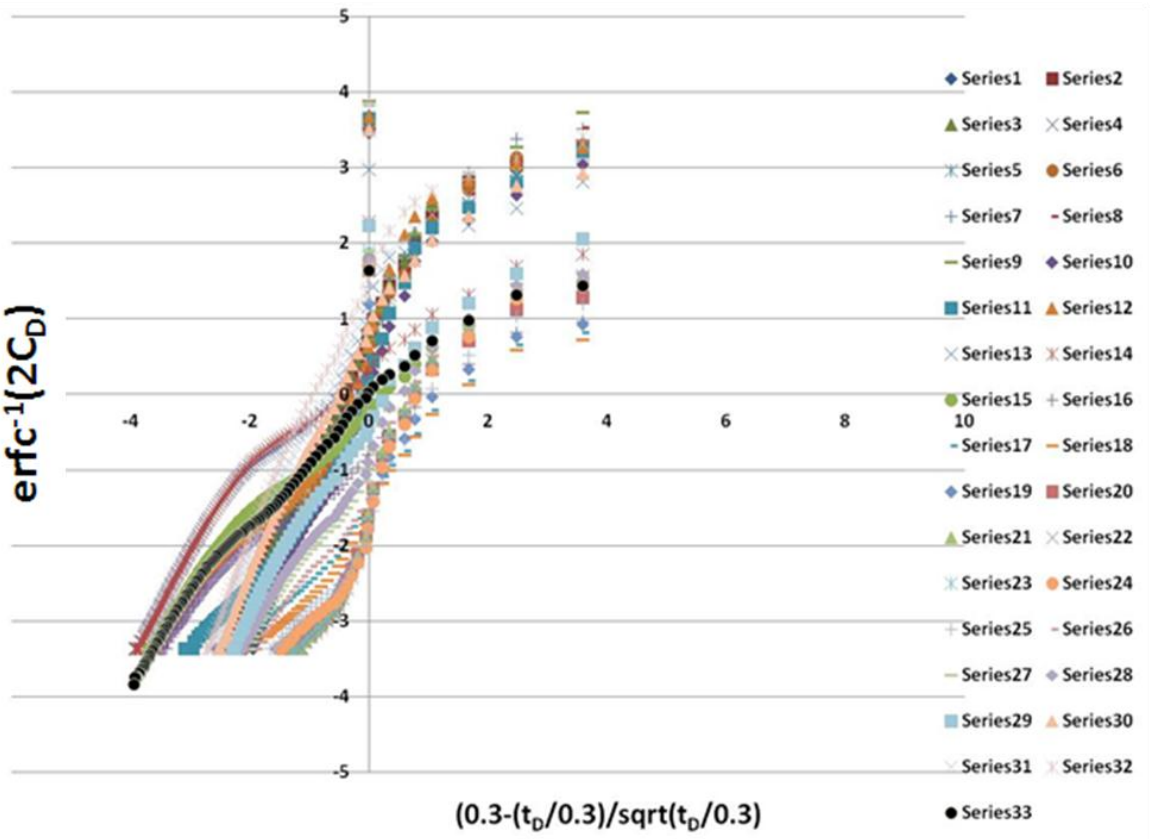

Figure 6.19: $\mathrm{Erfc}^{-1}(2c_D)$ as a function of $\frac{(x_D - t_D)}{\sqrt{t_D}}$ obtained from Figure 6.18. The longitudinal dispersion coefficient for each grid block is obtained from the slope of the corresponding line constructed on this plot; for this plot, x_D =0.3 and $t_D|$cross-section = (t_D/0.3) are used in Eq. (A-11).

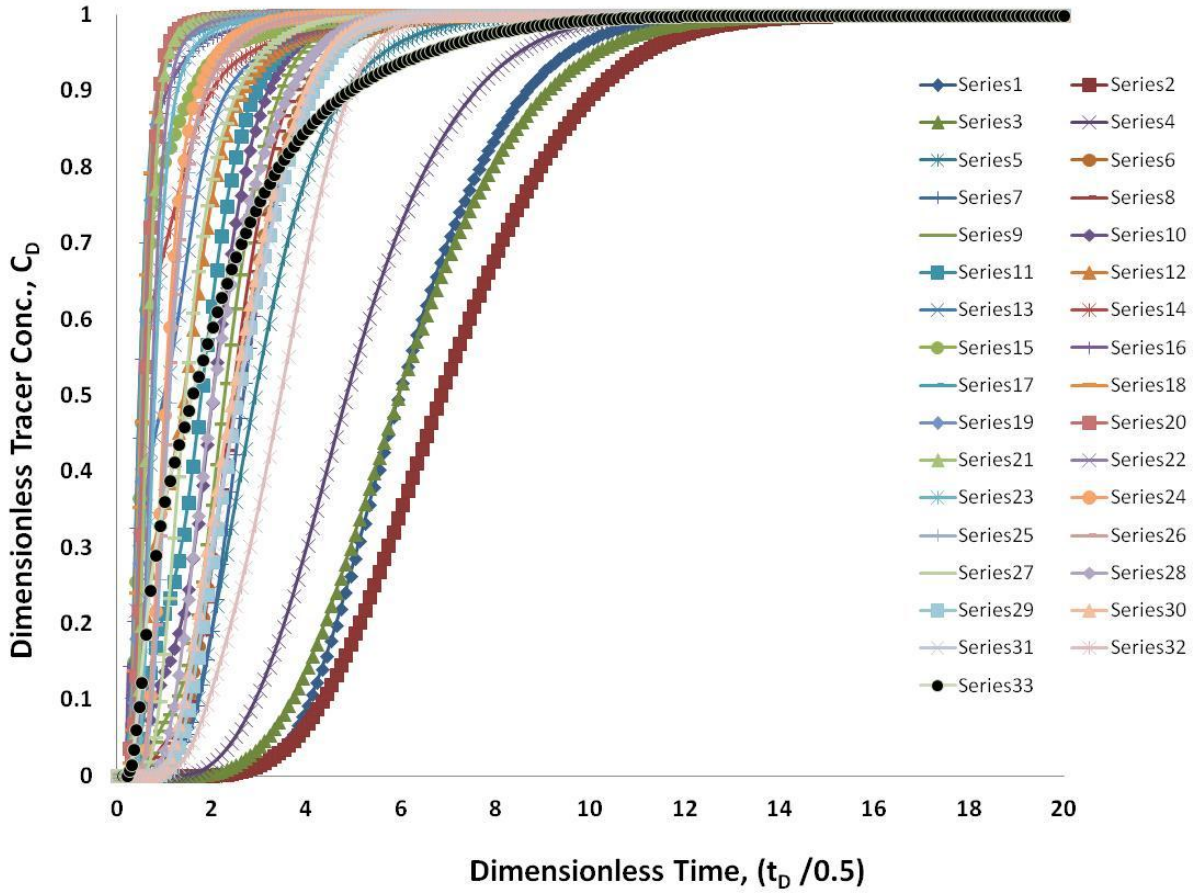

Figure 6.20: Concentration history plots for all grid blocks located at $x_D = 0.5$ when R_L=10. The dimensionless time represents the fraction of total pore volume constrained between the injector and the fifth cross-section.

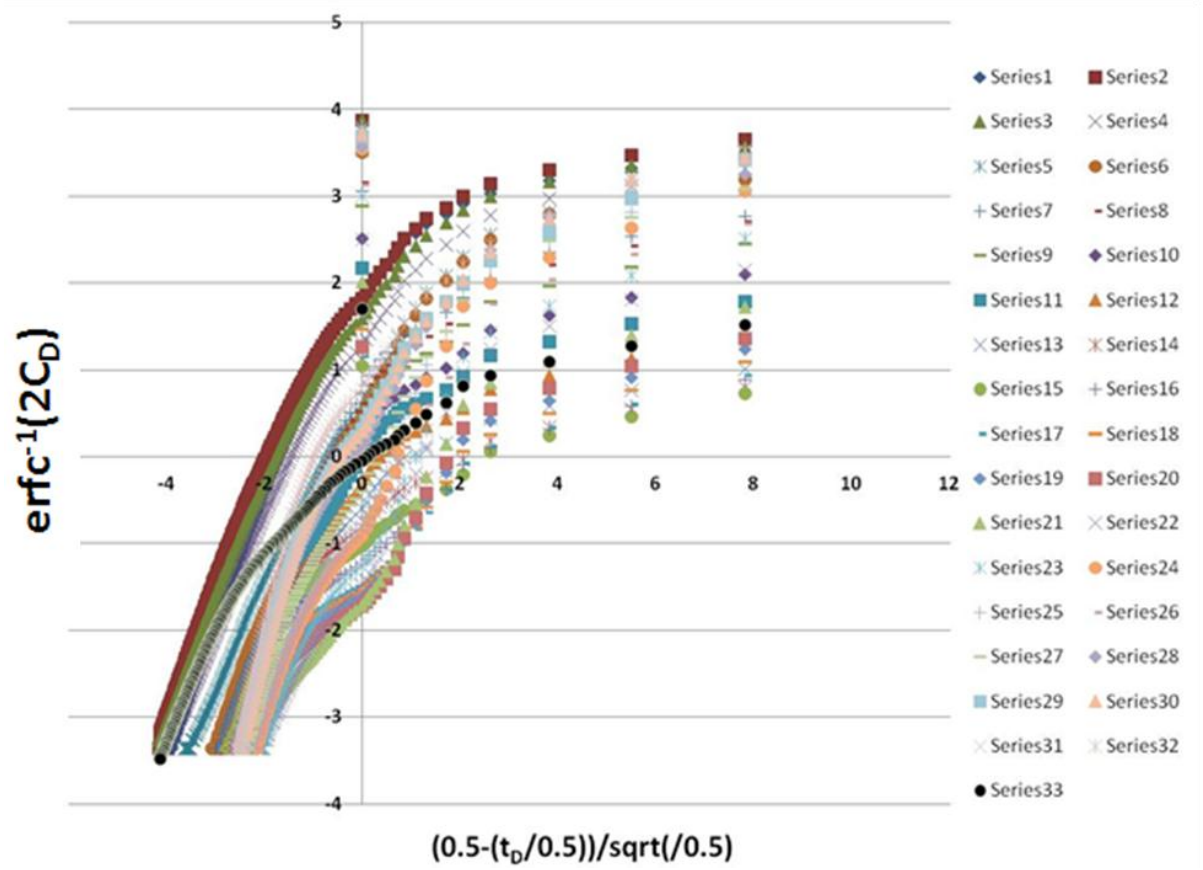

Figure 6.21: $\text{Erfc}^{-1}(2c_D)$ as a function of $\frac{(x_D - t_D)}{\sqrt{t_D}}$ obtained from Figure 6.20. The longitudinal dispersion coefficient for each grid block is obtained from the slope of the corresponding line constructed on this plot; for this plot, x_D =0.5 and $t_D|\text{cross-section} = (t_D/0.5)$ are used in Eq. (A-11).

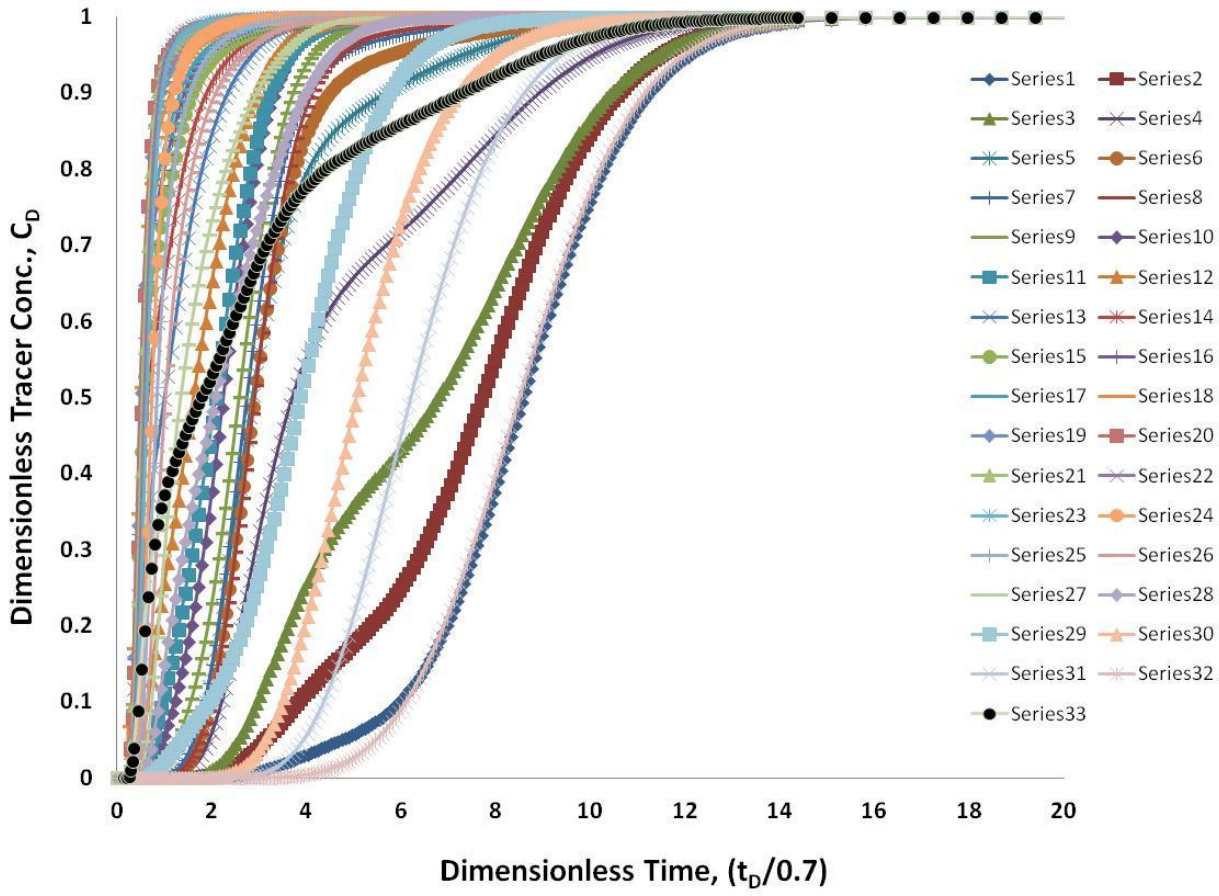

Figure 6.22: Concentration history plots for all grid blocks located at $x_D = 0.7$ when R_L=10. The dimensionless time represents the fraction of total pore volume constrained between the injector and the seventh cross-section.

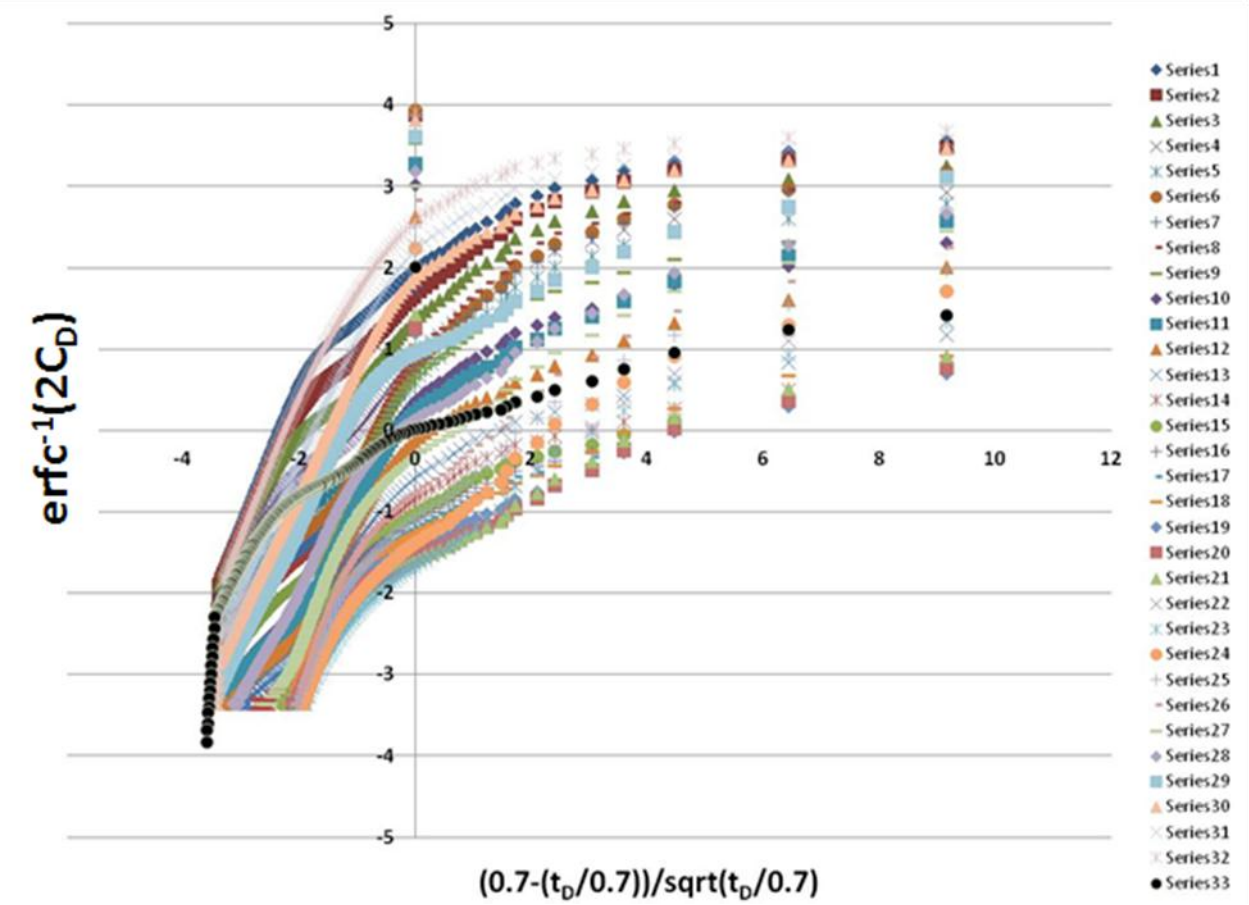

Figure 6.23: $\text{Erfc}^{-1}(2c_D)$ as a function of $\frac{(x_D - t_D)}{\sqrt{t_D}}$ obtained from Figure 6.22. The longitudinal dispersion coefficient for each grid block is obtained from the slope of the corresponding line constructed on this plot; for this plot, x_D =0.7 and $t_D|\text{cross-section} = (t_D/0.7)$ are used in Eq. (A-11).

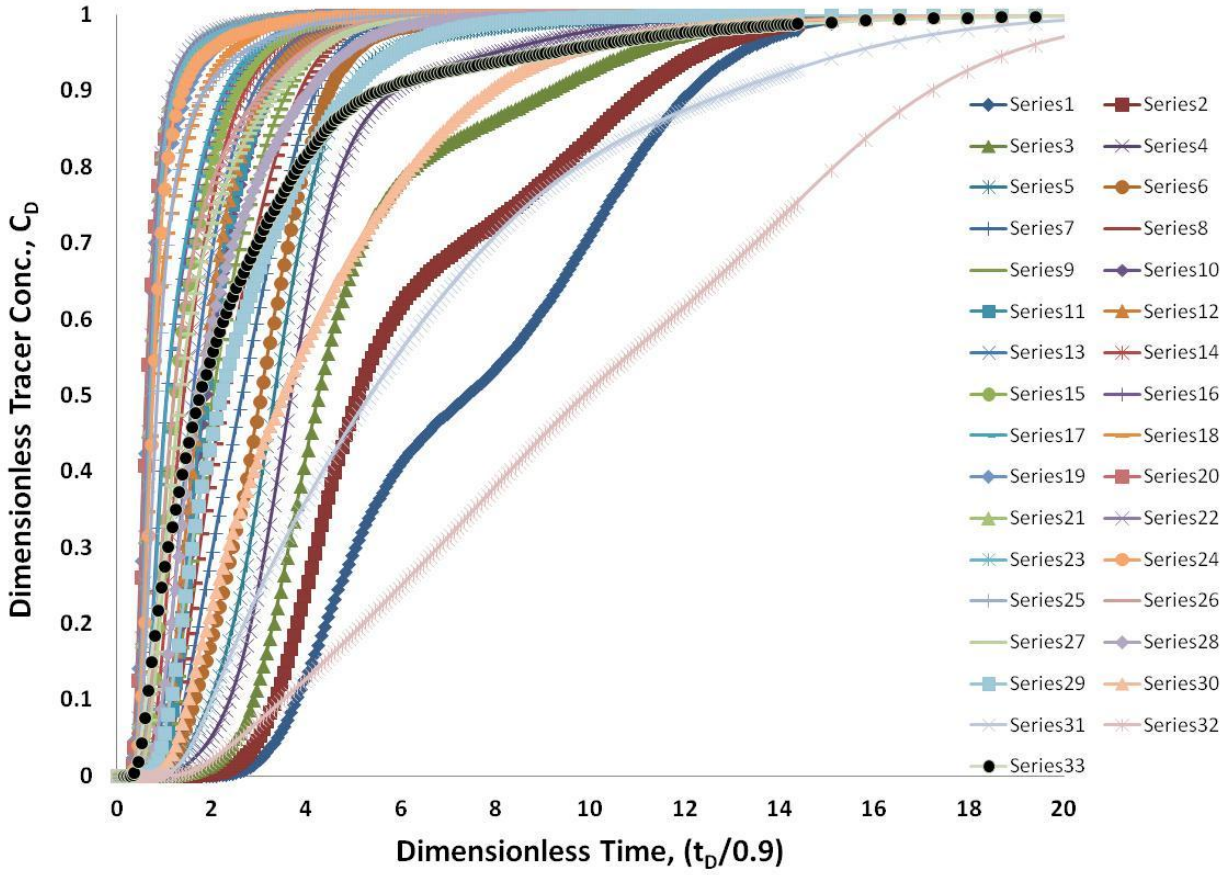

Figure 6.24: Concentration history plots for all grid blocks located at $x_D = 0.9$ when R_L=10. The dimensionless time represents the fraction of total pore volume constrained between the injector and the ninth cross-section.

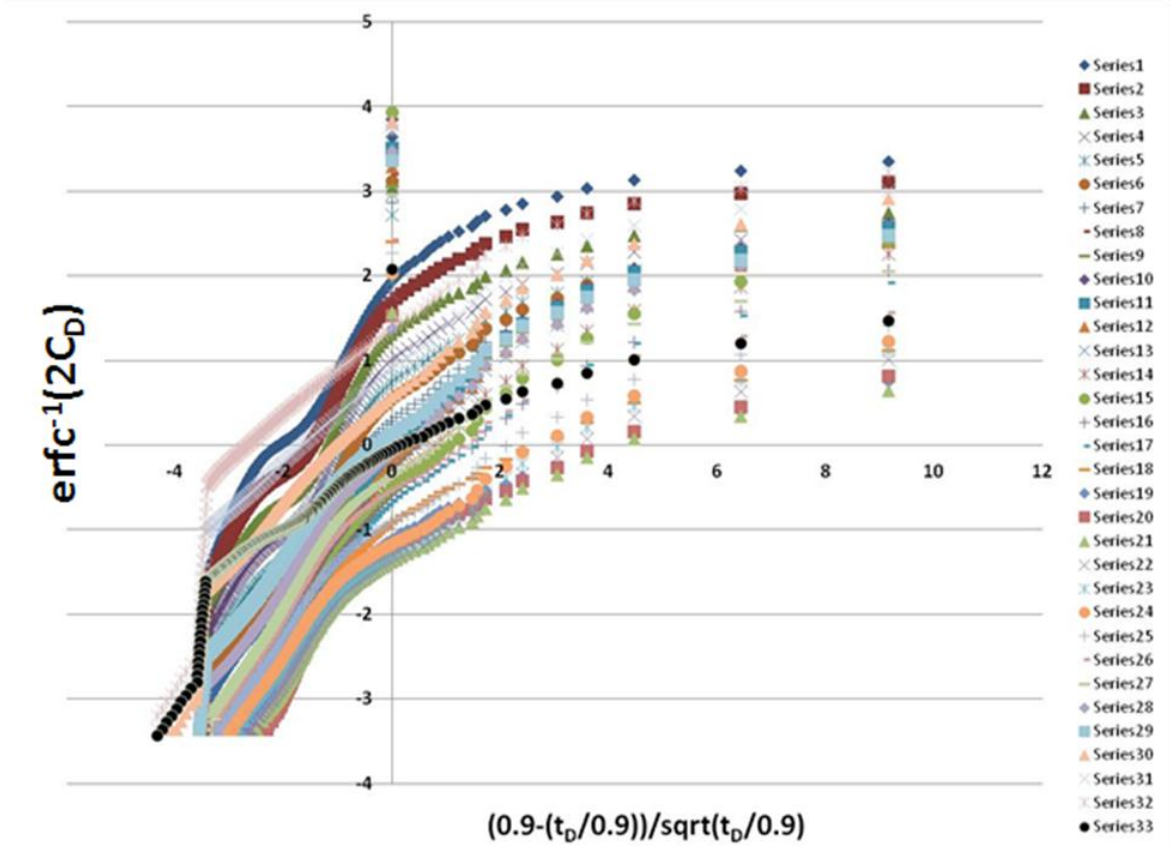

Figure 6.25: $\mathrm{Erfc}^{-1}(2c_D)$ as a function of $\frac{(x_D - t_D)}{\sqrt{t_D}}$ obtained from Figure 6.24. The longitudinal dispersion coefficient for each grid block is obtained from the slope of the corresponding line constructed on this plot; for this plot, x_D =0.9 and $t_D|$cross-section = (t_D/0.9) are used in Eq. (A-11).

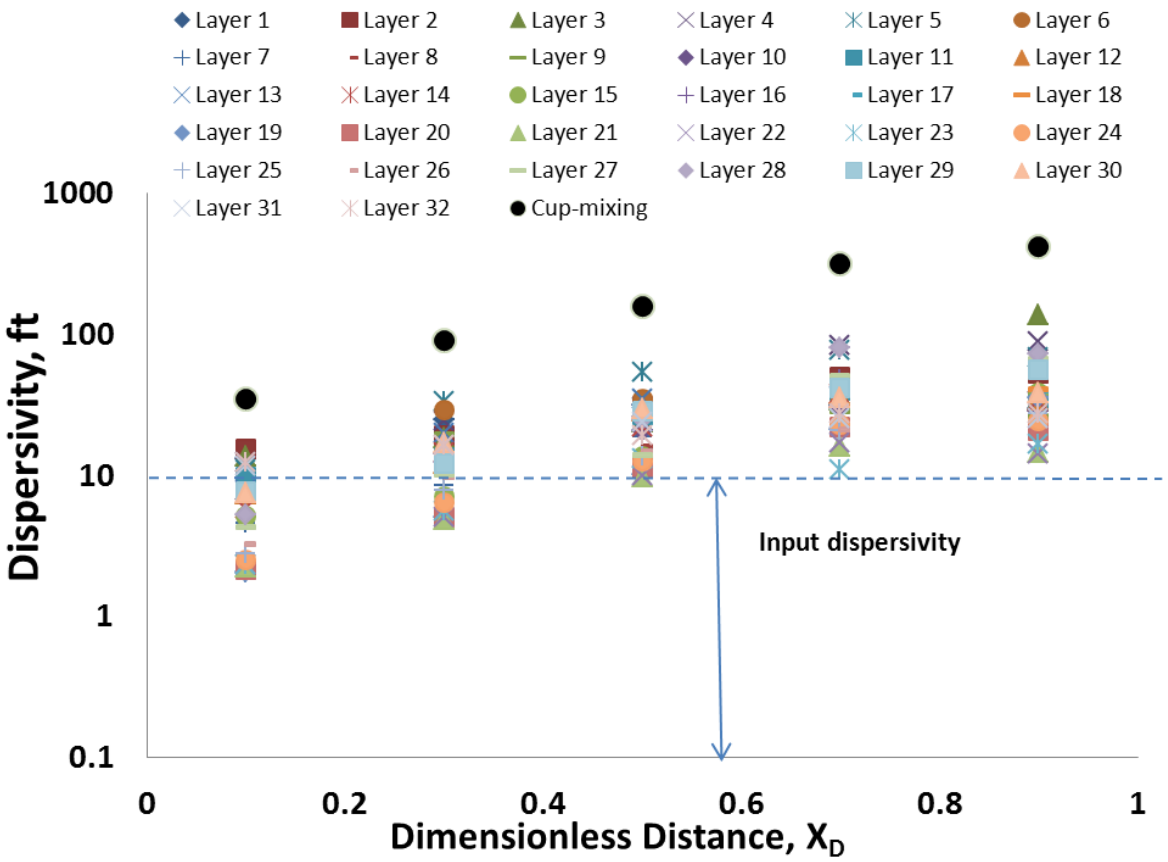

Figure 6.26: Calculated output dispersivity as a function of distance when R_L=0.126. The black solid points represent the corresponding dispersivity obtained from the cup- mixing concentrations as a function of x_D.

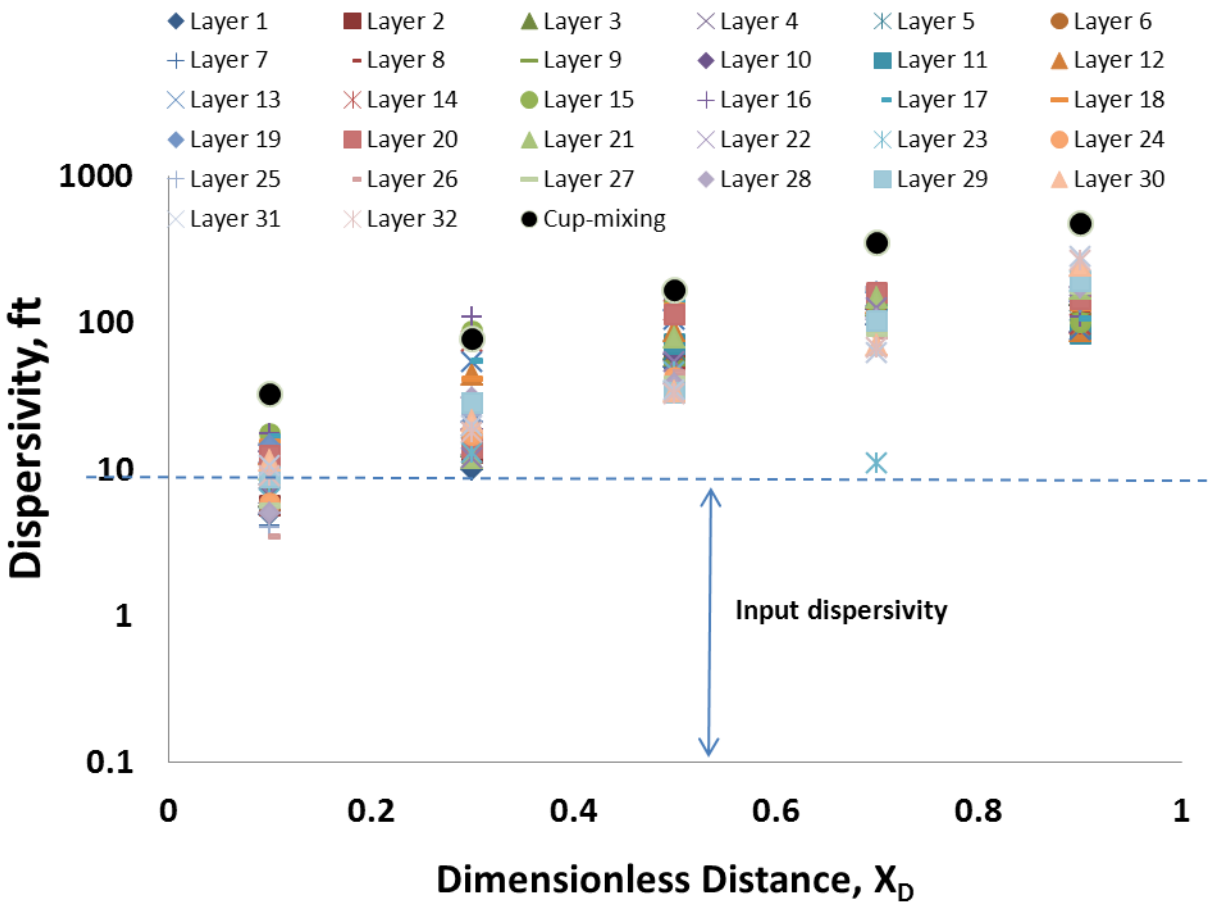

Figure 6.27: Calculated output dispersivity as a function of distance when R_L=10. The black solid points represent the corresponding dispersivity obtained from the cup- mixing concentrations as a function of x_D.

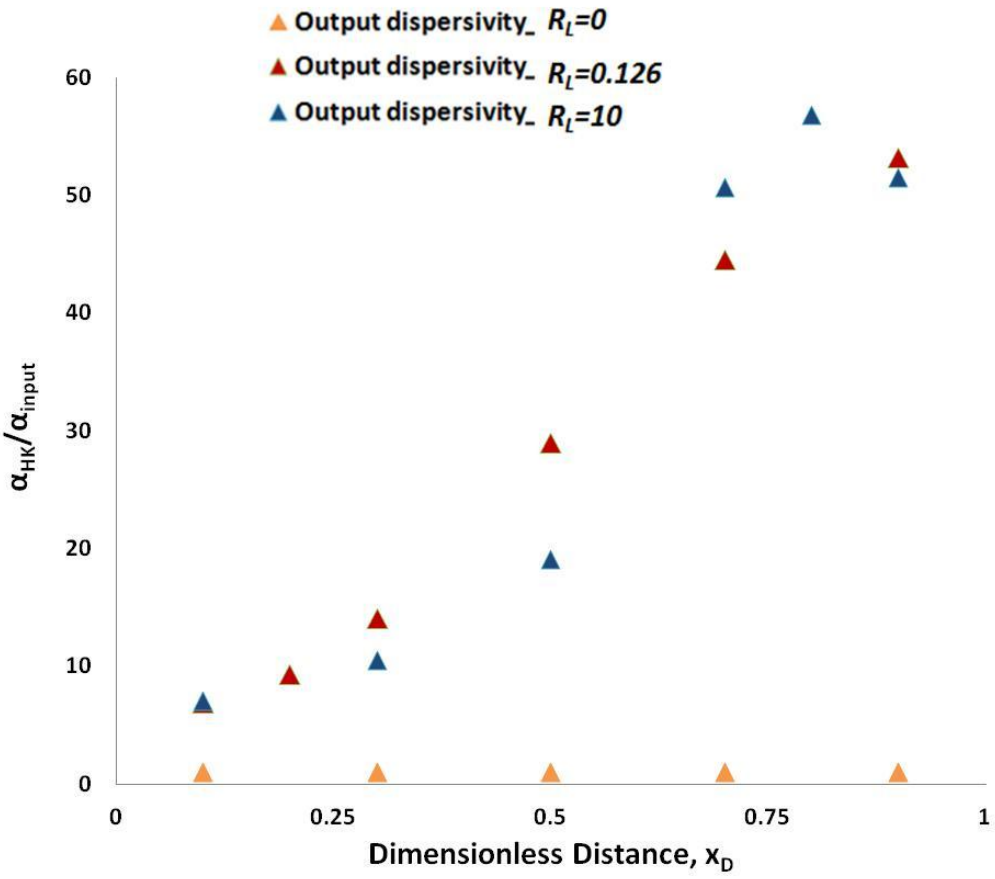

Figure 6.28: The ratio of dispersivity values, which are used in Eq. (5.27) to match the concentration history plots, to the input dispersivity as a function of x_D. The graph clearly indicates that larger dispersivity is needed when the cross-flow increases.

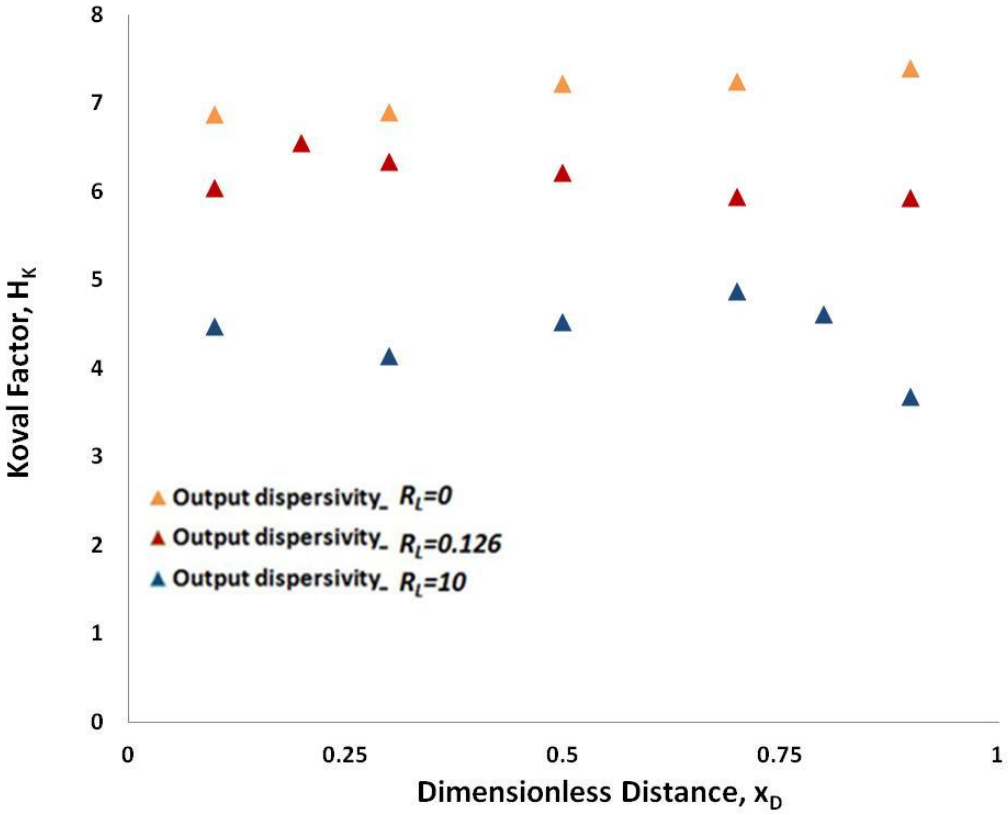

Figure 6.29: The Koval heterogeneity factor values used in Eq. (5.27) to match the concentration history plots. The graph clearly indicates that smaller Koval factor is needed when the cross-flow increases. This observation is expected based on the Taylor's theory.

Chapter 7: Numerical Indicator for Flow through Heterogeneous Permeable Media

This chapter details a numerical indicator to examine the nature of miscible displacements in heterogeneous permeable media. We evaluate miscible displacements using assigned numerical values to their governing flow regimes. Previous studies state that the competition between effects is the cause of developing various types of flow regimes (dispersive, fingering, gravity override, and channeling). However, the distinction between the flow patterns is only possible qualitatively (visually) so far; hence, the current identification method fails to properly characterize displacements with a similar flow pattern. Furthermore, we cannot use visual identification to evaluate the displacement performance of miscible floods, quantitatively.

We adopt the correlation coefficient function and use the progression of the mixing zone to assign a numerical value to the flow pattern. The correlation coefficient function of the lengths of the mixing zone calculated between two different times represents the tendency of the mixing zone to propagate linearly with time. Also, we demonstrate that the correlation coefficient function of the squared length of the mixing zone corresponds to the linear growth with the square root of time. Using the arithmetic average of the correlation coefficient functions over successive time intervals, we introduce a flow regime value to study the nature of miscible floods. We use a simulation approach to verify it and find that the numerical values assigned to the flow patterns are consistent with the visual identification.

We conclude that flow pattern value is an effective measure of mixing zone development in heterogeneous permeable media. Furthermore, we demonstrate that the development pattern of the mixing zone can be monitored quantitatively. This is especially important in the prediction of displacement performance when cross-flow is small. In this study, we investigate the relation between flow pattern values and the displacement performance of miscible floods.

7.1 INTRODUCTION

Miscible gas flooding has proven to be one of the few cost-effective enhanced oil recovery techniques in the last decade. However, the success of miscible floods is often limited by poor volumetric sweep efficiency owing to the adverse viscosity ratio, the density difference between the solvent and the oil, and reservoir heterogeneity. The volumetric sweep efficiency is defined as the fraction of oil contacted by the displacing fluid (Lake, 1989). On the contrary, the fraction of oil not contacted by the displacing agent is called the missing oil; the latter notation is used mostly in this study. The interplay of effects (heterogeneity, unmatched density/viscosity, and effective aspect ratio, R_L,) often reduces the volumetric sweep efficiency and yields specific types of flow regimes such as viscous fingering, channeling, and gravity override. Field observations indicate that varying the well spacing (between an injector and a producer) often changes flow patterns and, consequently, affects the amount of missing oil.

The first study of viscous fingering is attributed to Hill (1952). Waggoner *et al.* (1992) studied the miscible flow regimes through permeable media under the vertical equilibrium (VE) condition and introduced the channeling flow regime. They

summarized that the competition between various effects is why different types of flow regime occur. Chang *et al.* (1994) and Sorbie *et al.* (1994) extended the work of Waggoner *et al.* to unmatched density and non-VE displacements, respectively. Li *et al.* (1994) introduced a Buckley-Leverett flow pattern for immiscible displacements when R_L becomes negligible. However, these classifications are of little use (limited solely to the definition) without a way to quantify them.

Despite different terminology, all flow patterns that reduce the volumetric sweep efficiency exhibit a similar propagation characteristic: the solvent front travels linearly with time. However, dispersive flow prevails under certain circumstances and results in the growth of the mixing zone with $\sqrt{\text{Time}}$. This delays the solvent breakthrough time (BT) and increases the vertical sweep efficiency. The mixing zone is defined as the dimensionless distance between the locations where the dimensionless solvent concentrations of 0.1 and 0.9 occur (Lake, 1989). The objective of this work is to assign numerical values to the flow patterns of miscible displacements in heterogeneous permeable media.

7.2 DESCRIPTION

In general, the following flow patterns are known for miscible displacements:

1. Fingering that is caused by an adverse mobility ratio, yields oil bypassing and, consequently, is considered an unfavorable flow regime.
2. Gravity override that represents oil bypassing due to the density difference between the oil and the injected gas and is considered an unfavorable flow pattern.

3. Channeling because of the permeability heterogeneity that yields oil bypassing and is considered an unfavorable flow pattern.
4. Dispersive that is in favor as it reduces the oil bypassing caused by the above patterns.

The first three categories manifest inefficient recovery and early solvent breakthrough; conversely, the dispersive flow yields late solvent breakthrough. The principal distinction between channeling and the two other unfavorable flow patterns is that gravity overrides and fingering becomes dispersive when the oil and gas properties (density and viscosity) match; this is not true for channeling as it is caused by the inherent permeability variation of the system. The unfavorable flow patterns represent linear propagation of the gas front with time despite the dispersive regime for which the mixing zone grows with $\sqrt{\text{Time}}$ (favorable). The growth of the mixing zone with the square root of time also may be interpreted as the growth of the squared length of the mixing zone with time. Thus, regardless of the causes, the unfavorable flow regimes represent the same flow pattern for the mixing zone growth.

Suppose x_1 is the length of the mixing zone at time t_1 and x_2 is the length of the mixing zone at time t_2. The the correlation coefficient function (Appendix B) of x_1 and x_2 over the time domain represents how strongly x_1 and x_2 are correlated with respect to time.

As the first step is to assign a numerical value to a flow pattern, we store lengths of the mixing zone in all layers of a two-dimensional (2D) model at time t_1 (after solvent

injection) as array x_1, at time t_2 as array x_2, and so on. See Figure 7.1and Figure 7.2 for the schematic illustration of the approach.

The correlation coefficient function of arrays x_1 and x_2 represents the tendency of the mixing zone to grow linearly with time (unfavorable). Similarly, the correlation coefficient function of arrays x'_1 and x'_2 represents the tendency of the mixing zone to grow linearly with $\sqrt{\text{Time}}$ (favorable). Next, we take the average of the correlation coefficients calculated over equal time intervals. The average correlation coefficient functions of arrays x_1 and x_2 imply the tendency of the mixing zone to linearly grow with time. Similarly, the average correlation coefficient functions of arrays x'_1 and x'_2 imply the tendency of the mixing zone to linearly grow with $\sqrt{\text{Time}}$. The ratio of the average correlation coefficient functions is defined as the flow pattern value. The flow pattern value falls in three possible ranges:

$$\begin{cases} \dfrac{\text{Average}\left(\rho_{[\Delta x|\text{mix zone}]}\right)}{\text{Average}\left(\rho_{[\Delta x|\text{mix zone}]}^{\,2}\right)} = \dfrac{\text{Average}(\rho)}{\text{Average}(\rho')} > 1 \\ \dfrac{\text{Average}\left(\rho_{[\Delta x|\text{mix zone}]}\right)}{\text{Average}\left(\rho_{[\Delta x|\text{mix zone}]}^{\,2}\right)} = \dfrac{\text{Average}(\rho)}{\text{Average}(\rho')} = 1 \\ \dfrac{\text{Average}\left(\rho_{[\Delta x|\text{mix zone}]}\right)}{\text{Average}\left(\rho_{[\Delta x|\text{mix zone}]}^{\,2}\right)} = \dfrac{\text{Average}(\rho)}{\text{Average}(\rho')} < 1 \end{cases} . \quad (7.1)$$

The unfavorable type of flow will be dominant if the ratio is greater than unity; conversely, the miscible displacement yields a better sweep efficiency when the ratio is smaller than one. Both favorable and unfavorable flow patterns occur and neither is

dominant. However, the logarithm of the above ratio is used to represent the flow pattern in this study.

7.3 VERIFICATION

We use a simulation approach to compare the flow pattern values and visual identification. To be consistent with the literature, the simulation cases presented in Sorbie *et al.* (1992) are used to evaluate the proposed flow pattern values. Table 7.1 shows the properties of the simulation models. The FFTsim code (Jennings *et al.*, 2002) is used to generate heterogeneous permeability filed for each example. Furthermore, for all case studies, porosity is uniformly distributed.

The simulations are performed using GEM, CMG's general equation-of-state compositional reservoir simulator. The simulation models consist of two vertical wells located at the ends of 2D cross-sectional grid with constant grid block sizes in the *x*- and *z*-directions. The top and bottom of the models are no flow boundaries. Both wells operate under a constant rate constraint. Furthermore, single component oil and a first contact miscible solvent are used. The solvent viscosity, the transverse permeability, and the physical dispersivity are adjusted to maintain the specified values for the mobility ratio, the effective aspect ratio (R_L), and the Peclet number (N_{pe}) in each example.

In addition, the dispersion levels are mainly determined based on the input physical dispersivities in the simulations as the numerical dispersion is reduced by choosing small grid blocks and adjusting the maximum time step. Equation (7.2) shows the Peclet number attributed to the numerical dispersion for two-phase flow. The

numerical dispersion is inversely correlated with the number of grid blocks in the flow direction as $\left(\frac{df_j}{dS_j}\right)$ is equal to one and $\left(\frac{\Delta t_D}{\Delta x_D}\right)$ is kept less than 0.01 in this study:

$$N_{pe}^{-1}\,|_{\mathbf{Num.}} = \frac{\Delta x_D}{2}\frac{df_j}{dS_j}\left(1-\frac{\Delta t_D}{\Delta x_D}\frac{df_j}{dS_j}\right) . \qquad (7.2)$$

Table 7.2 compares the visual identification with the calculated pattern values. As the governing flow pattern becomes more dispersive, the corresponding numerical value increases, and vice versa. Figure 7.3 illustrates the solvent breakthrough time (BT) (expressed in reservoir pore volumes) as a function of the assigned numerical values. Overall, the trend implies that larger numerical values tend to have more unfavorable flows and premature BT; in contrast, smaller numerical values have more favorable flows that lead to negative values and, consequently, late BT.

Overall, the results do not strongly support a one-to-one functionality between BT and the flow regime. This non-unique relation is because of the evolution of the mixing zone that occurs during displacements. Cross-flow between the layers explains why the flow pattern varies with time. Figure 7.4 and Figure indicate different stages of the miscible displacement for two cases with small ($R_L=1.0$) and large cross-flows, respectively; large cross-flows imply the vertical equilibrium (VE) condition (Lake, 1989). Under the VE condition in a heterogeneous permeable medium, the injected fluid instantaneously communicates between the layers (to reach an equilibrium condition with respect to the pressure drop); this affects the pace at which the mixing zone grows within each layer and eventually leads to erratic flow patterns.

In contrast, if we limit the analysis to the blue points on Figure 7.3 that represent displacements with weak cross-flow between layers, a strong co-relation between the flow pattern and the corresponding BT exists; in other words, the flow pattern in which the mixing zone develops does not change when R_L is small.

Figure 7.5 shows the missing oil as a function of flow regime. The similar discussion as the BT applies where a strong co-relation exists only when R_L becomes small. Thus, larger flow regime values correspond to more missing oil when a weak communication is present between the layers.

In addition, we can predict the displacement performance of miscible displacements when R_L becomes negligible if the governing flow pattern is known. To determine the flow pattern value, the simulation should be conducted to identify the mixing zone development pattern; however, the simulation needs to be conducted only for a few time steps as the flow regime will not change when cross-flow between layers is not present.

7.4 CONCLUSIONS

We successfully implement numerical values to present flow patterns that occur during miscible displacements in heterogeneous permeable media. The main conclusions of the study are:

1. The numerical value assigned to the flow patterns is the most succinct form of describing miscible displacements in heterogeneous permeable media. It accounts for the interplay of effects by capturing all of them into a single

parameter and facilitates the development of the co-relations for the missing oil/breakthrough time.

2. The numerical values attributed to the flow patterns provide a better understanding of flow than the visual method by evaluating various stages of the miscible displacements; Furthermore, it enables us investigate the evolution of the mixing zone during the displacements.
3. Strong co-relations are observed between the flow pattern values and the missing oil/ breakthrough time when the reservoir layers exhibit poor vertical communications.

7.5 NOMENCLATURE

f_j= fractional flow of phase j

S_j= saturation of phase j

R_L= effective aspect ratio :$k_v/k_h\sqrt{L/h}$ where L and h are the length and the width of the cross-section and K_v and k_h are vertical and the longitudinal permeability, respectively

N_{Pe}= Peclet number:v/LK_l , where v and K_l are interstitial velocity and the longitudinal dispersion coefficient, respectively.

$t_{D=}$= dimensionless time

t_i= time step i , where $i=1,2,3,...$

V_{DP}= the Dykstra- Parson coefficient of variation

x_D= dimensionless distance

x_i=array i consists of lengths of the mixing zone for each grid layer of the model at t_i

λ_{xD}= dimensionless correlation length in the *x*-direction

λ_{zD}= dimensionless correlation length in the *z*-direction

ρ_h= the correlation coefficient function

$M°$= mobility ratio

Table 7.1: Specifications of the simulation models (Sorbie *et al.*, 1994)

Run	V_{DP}	λ_{XD}	λ_{ZD}	M°	R_L	N_{Pe}
1	0.5	0.024	0.024	1	1	80
2	0.5	0.024	0.024	10	1	80
3	0.5	0	0	1	6	240
4	0.85	0	0	1	6	240
5	0.5	0	0	10	6	240
6	0.85	0	0	10	6	240
7	0.85	0	0	10	19	240
8	0.85	0	0	10	30	240
9	0.85	0	0	10	60	240
10	0.833	0.025	0.025	1	1	160
11	0.833	0.025	0.025	1	60	160
12	0.941	0.025	0.025	1	1	160
13	0.941	0.025	0.025	1	60	160
14	0.833	0.025	0.025	3	1	160
15	0.833	0.025	0.025	3	60	160
16	0.941	0.025	0.025	3	1	160
17	0.941	0.025	0.025	3	60	160
18	0.718	0.05	0.05	3	1	160
19	0.718	0.05	0.05	3	60	160
20	0.865	0.05	0.05	3	1	160
21	0.865	0.05	0.05	3	60	160
22	0.757	0.1	0.1	3	1	160
23	0.4	0.025	0.025	10	1	160
24	0.4	0.025	0.025	10	60	160
25	0.6	0.025	0.025	10	1	160
26	0.6	0.025	0.025	10	60	160

Table 7.2: A comparison between visual identification and the flow pattern-assigned values. F, C, and D represent fingering, channeling, and dispersive flow regimes, respectively (Sorbie et al., 1994)

Run	Numerical value	Visual identification
11	-0.0948	D
21	-0.0823	D
10	-0.0589	D?
4	-0.0570	D
26	-0.0430	D
13	-0.0413	D
24	-0.0292	D
3	-0.0276	D
18	-0.0200	D
1	-0.0171	D
15	-0.0118	D
9	-0.0043	D
5	0.0019	F
14	0.0100	F/D?
25	0.0120	F
2	0.0237	F
6	0.0271	F
17	0.0439	D?
7	0.0514	F/D
23	0.0758	F
19	0.0828	D/C?
16	0.0841	C?
8	0.0903	F-D
12	0.1243	C?
20	0.2197	C
22	0.392441974	C

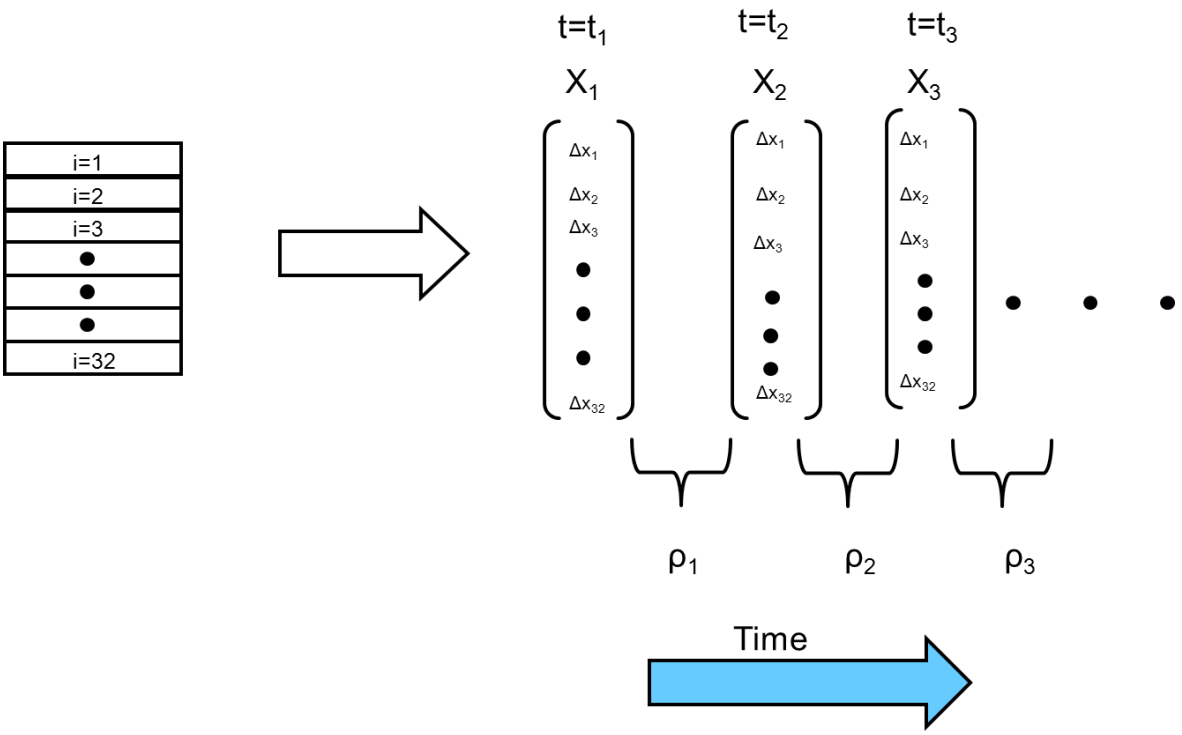

Figure 7.1: The correlation coefficient function, ρ_h, of the lengths of the mixing zone for a reservoir with 32 layers

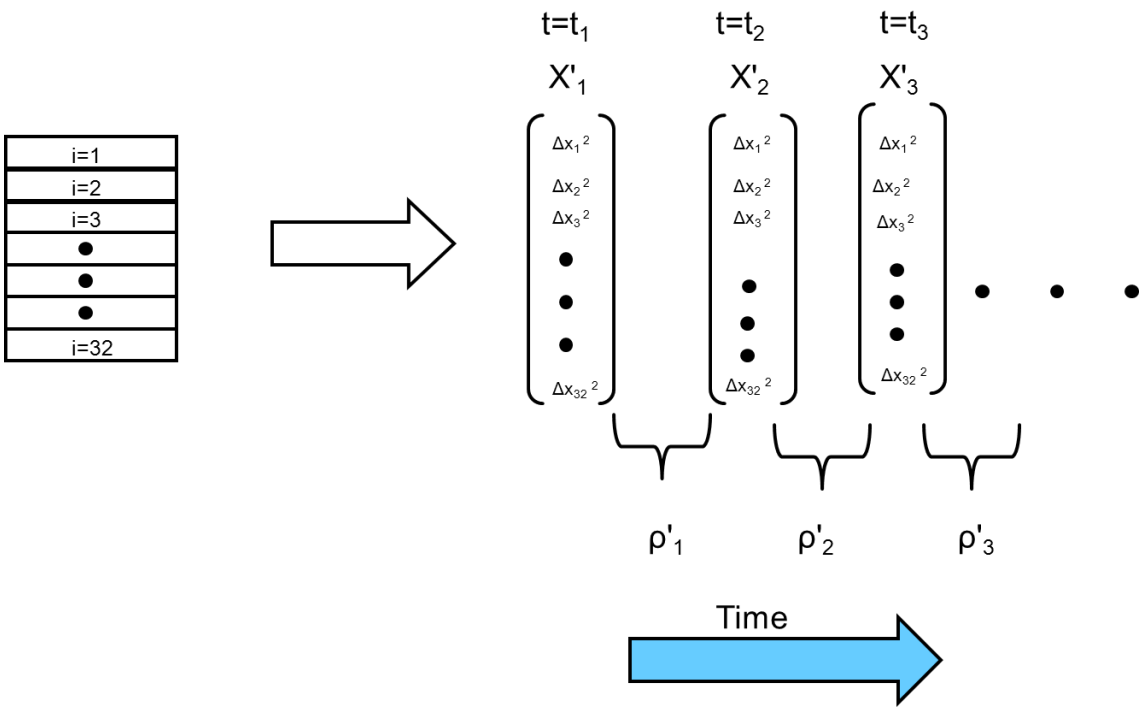

Figure 7.2: The correlation coefficient function, ρ_h, of the squared lengths of the mixing zone for a reservoir with 32 layers

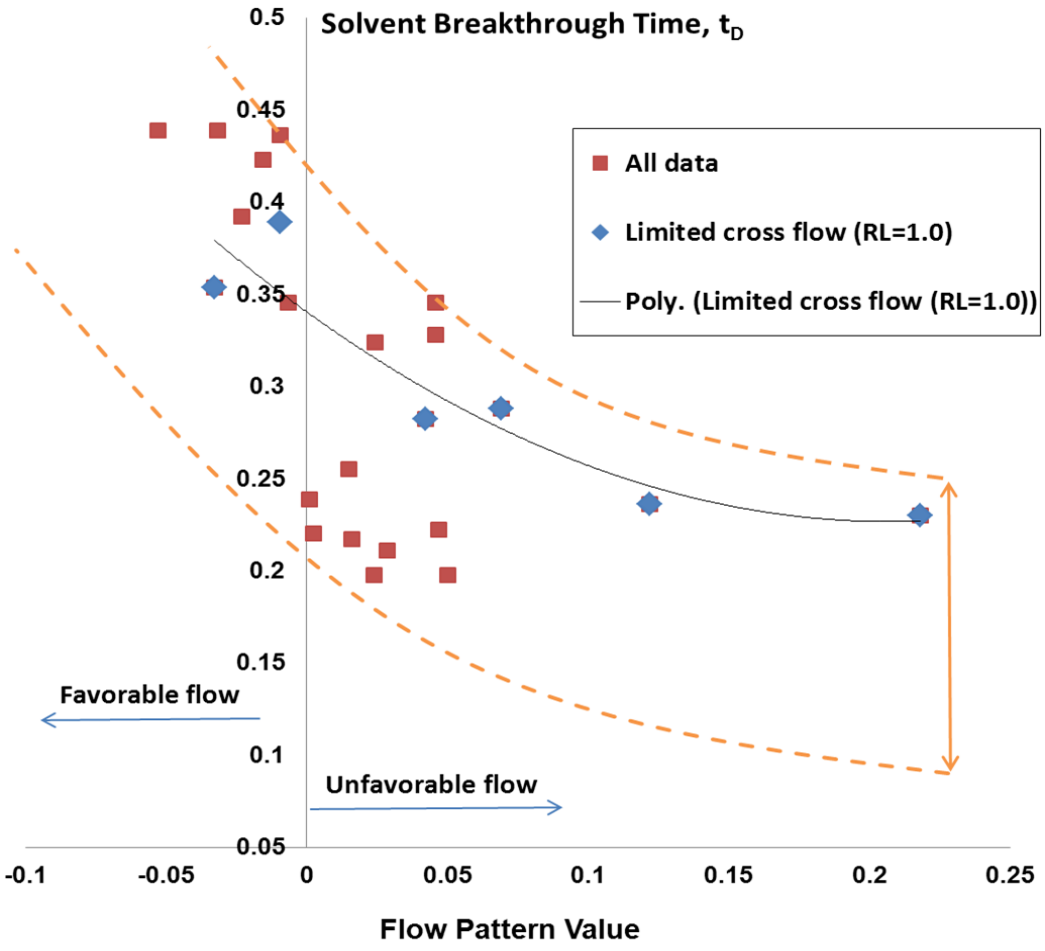

Figure 7.3: The plot illustrates the solvent dimensionless BT expressed in the reservoir pore volumes as a function of flow pattern values. The results are erratic except for small cross-flow where a strong correlation exists. As the pattern value increases, an earlier breakthrough occurs and, consequently, a poor displacement performance is realized (unfavorable)

Figure 7.4: Evolution of the mixing zone in Run 17 under the VE condition; the rate at which the mixing zone grows varies during the displacement

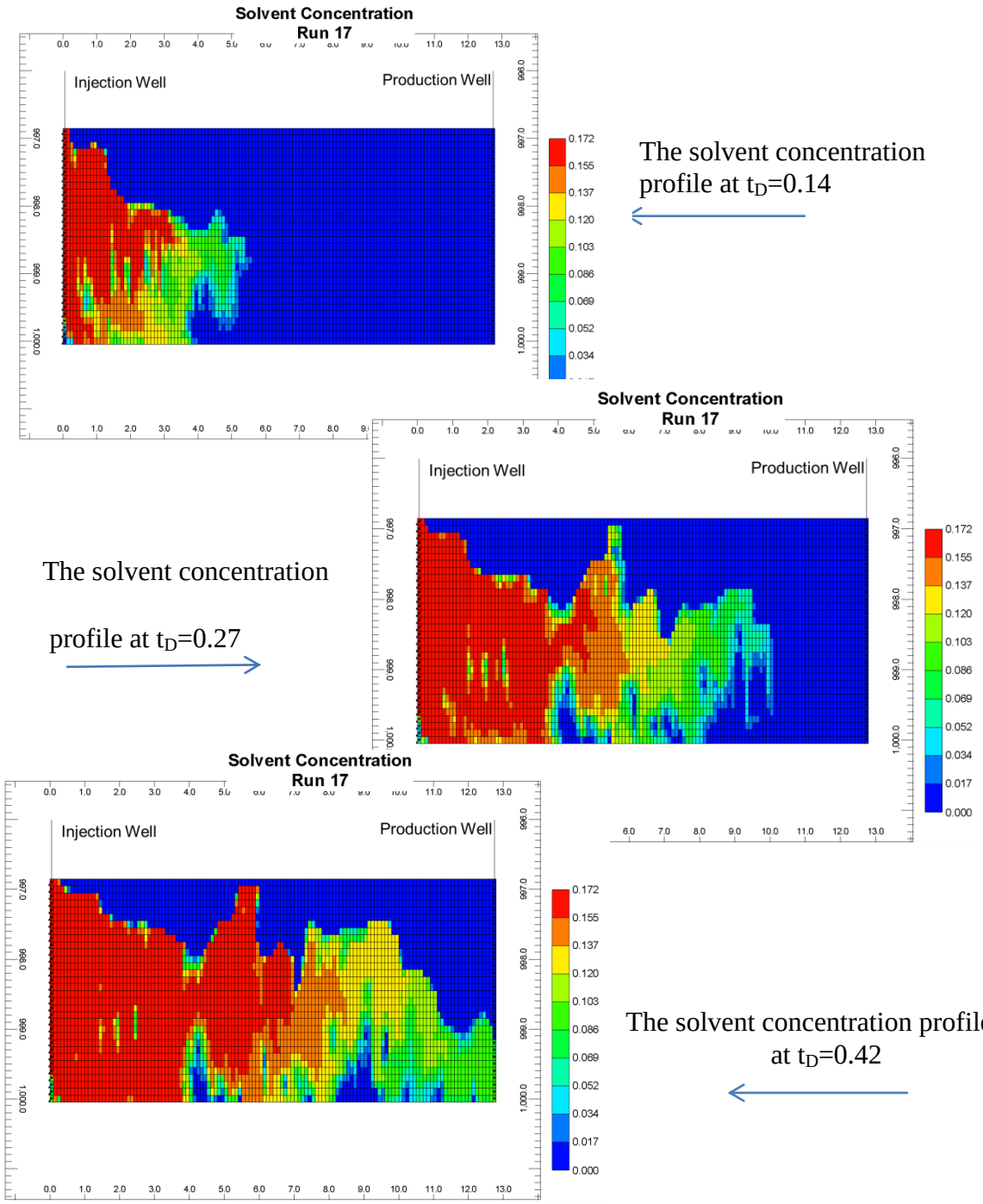

Figure 7.5: The development of the mixing zone in Run 22 with small cross-flow for the pace at which the mixing zone's growth stays almost constant during the displacement

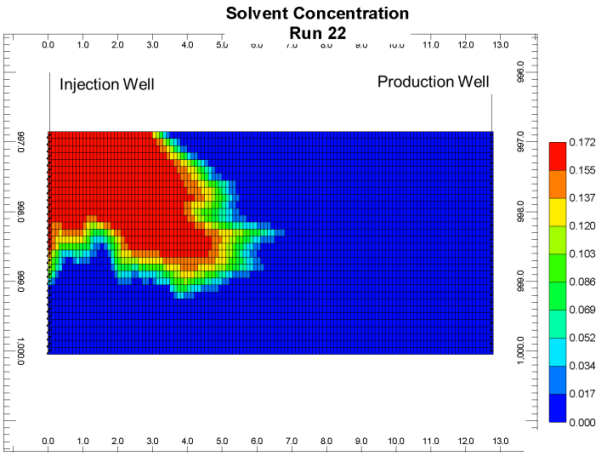

The solvent concentration profile at t_D=0.14

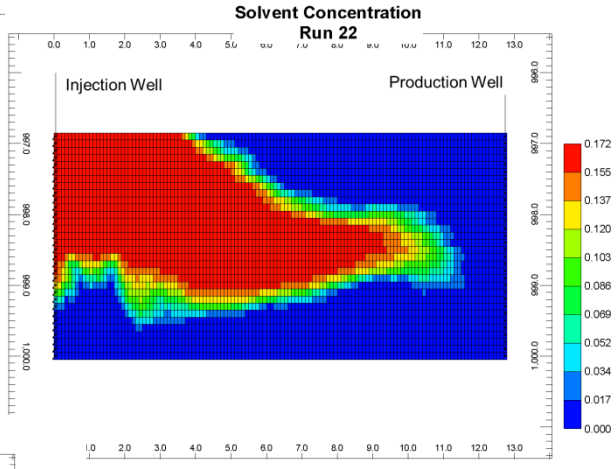

The solvent concentration profile at t_D=0.27

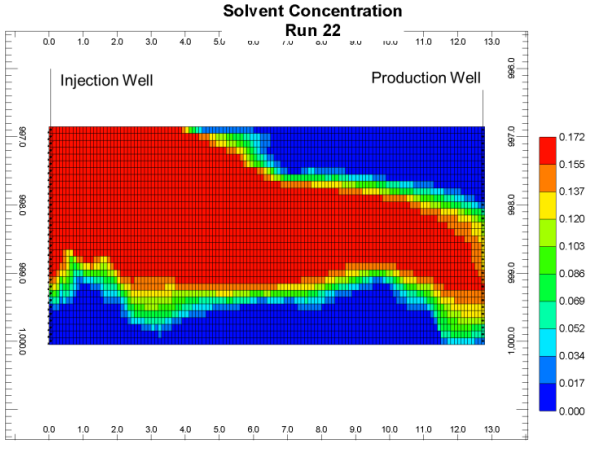

The solvent concentration profile at t_D=0.42

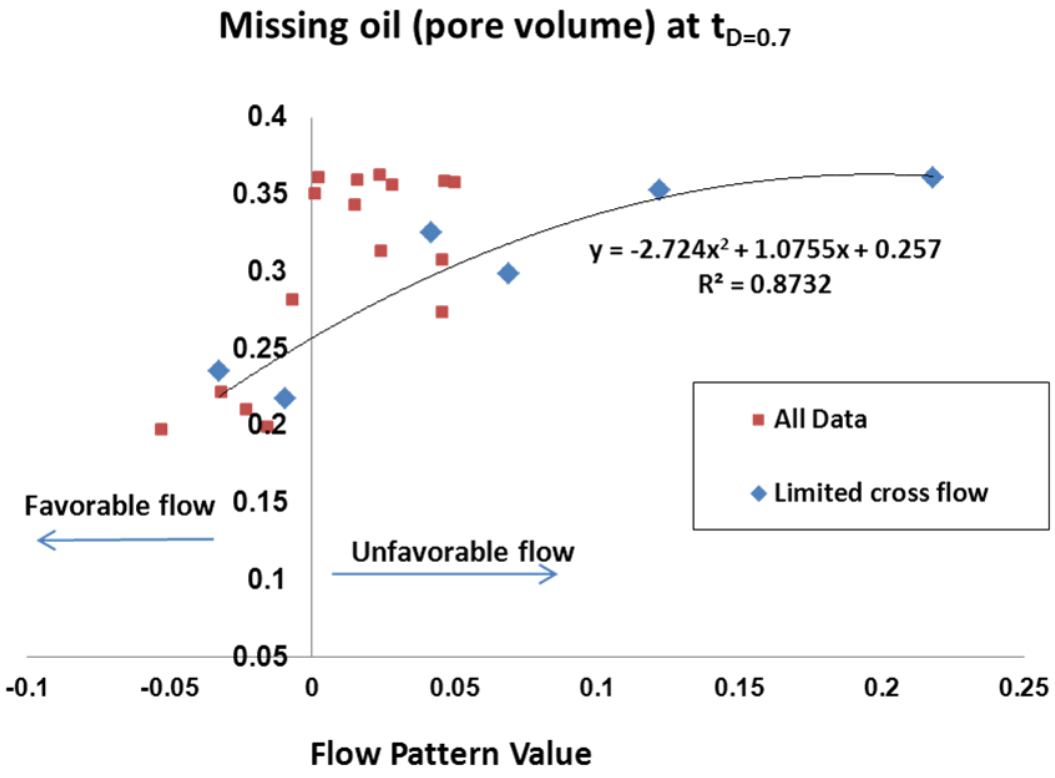

Figure 7.5: The missing oil (the remaining oil after 0.7 pore volume solvent injection) as a function of flow pattern values; a strong correlation exists only when the cross-flow becomes small.

Chapter 8: Contributions and Recommendations

This chapter lists the main contributions of research described in this dissertation and offers recommendations for future research.

8.1 MAJOR CONTRIBUTIONS

- The method of characteristics (MOC) solution of the mass conservation equation of a component in two-phase flow through permeable media is derived in the presence of compressibility (Chapter 2).

- A graphical procedure is proposed to evaluate the CO_2 storage capacity of a one-dimensional (1D) saline aquifer because of the capillary and dissolution trapping mechanisms (Chapter 3).
- The Walsh and Lake (WL) method is extended to predict the displacement performance of degraded miscible floods in the presence of weak cross-flow (Chapter 4).
- We decouple the convective spreading from local-scale heterogeneity for heterogeneous reservoirs with no cross-flow between layers. In addition, an analytical solution is derived to determine the averaged concentration as a function of the problem parameters. Furthermore, the fraction of layers in which the mixing grows faster than the dispersive flow regime is determined analytically as a function of the Koval factor and input dispersivity (Chapter 5).

- The numerical dispersion coefficients are determined when flow velocity varies with distance. The off-diagonal elements of the numerical dispersion tensor double when the flow velocity changes with distance. A specific simulation configuration is examined successfully to verify the off-diagonal coefficients (Chapter 6).

- The flow becomes more dispersive with distance travelled if there is convective cross-flow. In addition, local mixing increases with the convective cross-flow between layers (Chapter 6).
- A numerical indicator is presented to examine the nature of miscible displacements in heterogeneous permeable media (Chapter 7).

8.2 RECOMMENDATIONS FOR FUTURE WORK

The following is a list of topics for future research to expand the technical work presented in this dissertation:

- Extension of the derived MOC solution in Chapter 2 to
    - multicomponent multiphase flow
    - reactive flow
- Extension of the graphical method presented in Chapter 3 in the presence of compressibility
- Extension of the WL method in the presence of compressibility
- Decoupling of large- and small-scale heterogeneity in the presence of cross-flow using a similar treatment as in Chapter 5.

Appendix A: Convection-Diffusion equation

A dimensionless form of the one-dimensional CD equation can be written as (Lake, 1989)

$$\frac{\partial c_D}{\partial t_D} + \frac{\partial c_D}{\partial x_D} = \overbrace{\left[\frac{1}{N_{pe}}\right]}^{\alpha_D} \frac{\partial^2 c_D}{\partial x_D^2}, \tag{A-1}$$

where dimensionless parameters for the equation are defined as

$$c_D = \frac{c - c_I}{c_J - c_I}, \tag{A-2}$$

$$t_D = \frac{ut}{\phi L}, \tag{A-3}$$

$$x_D = \frac{x}{L}, \tag{A-4}$$

$$\frac{1}{N_{Pe}} = \alpha_D = \frac{\phi K_{xx}}{uL}, \tag{A-5}$$

where c_D is the dimensionless concentration normalized to the initial-injection concentration difference, t_D is the dimensionless time (P.V. injected), x_D is the dimensionless distance (normalized by the length of the reservoir), K_{xx} is the longitudinal dispersion coefficient, and N_{Pe} is the Peclet number. The Peclet number is the ratio of convective to dispersive transport. Thus, for large Peclet numbers, convective transport dominates over dispersive mixing, and for small Peclet numbers, dispersive mixing prevails.

As discussed in Chapter 6, from Eq. (6.7) for larger interstitial velocity than 3 cm/day, Eq. (A-5) can be written as

$$\frac{1}{N_{Pe}} = \alpha_D = \frac{\alpha}{L}. \tag{A-6}$$

Furthermore, the exact solution of Eq. (A-1) under the following boundary and initial conditions becomes

$$\begin{cases} c_D(x_D, 0) = 0 & @ \quad x_D \geq 0 \\ c_D(\infty, t_D) = 0 & @ \quad t_D \geq 0 \\ c_D(0, t_D) = 1 & @ \quad t_D \geq 0 \end{cases} \quad \Rightarrow \tag{A-7}$$

$$c_D(x_D, t_D) = \frac{1}{2} erfc\left(\frac{x_D - t_D}{2\sqrt{\frac{t_D}{N_{Pe}}}} \right) + \frac{e^{x_D N_{Pe}}}{2} erfc\left(\frac{x_D + t_D}{2\sqrt{\frac{t_D}{N_{Pe}}}} \right), \tag{A-8}$$

where *erfc* is the complementary error function given by

$erfc(x) = 1 - erf(x)$,

and

$erf(x) = \frac{2}{\sqrt{\pi}} \int_0^x e^{-x^2} dx$.

However, an approximate commonly-used solution of Eq. (A-1) is expressed as

$$c_D(x_D, t_D) = \frac{1}{2} \text{erfc}\left(\frac{x_D - t_D}{2\sqrt{\alpha_D t_D}} \right) . \tag{A-9}$$

Equation (A-9) can be used to determine local mixing (dispersivity) from the concentration history plots. Knowing the dimensionless concentrations as a function of

dimensionless time and distance, we determine α_D from Eq. (A-9). To do so, we rearrange Eq. (A-9) as

$$\operatorname{erfc}^{-1}\left(2c_D\right)=\overbrace{\left(\frac{1}{2\sqrt{\alpha_D}}\right)}^{\text{slope}}\frac{x_D-t_D}{\sqrt{t_D}} \quad . \qquad (A-10)$$

Furthermore, incorporating Eq. (A-6) into Eq. (A-10) yields

$$\operatorname{erfc}^{-1}\left(2c_D\right)=\overbrace{\left(\frac{1}{2\sqrt{\frac{\alpha}{L}}}\right)}^{\text{slope}}\frac{x_D-t_D}{\sqrt{t_D}} \quad . \qquad (A-11)$$

Hence, the longitudinal dispersion coefficient can be obtained from the slope of lines constructed on the plot of $\operatorname{erfc}^{-1}\left(2c_D\right)$ as a function of $\frac{x_D-t_D}{\sqrt{t_D}}$.

In addition, the solution of 2D convection-diffusion equation (Eq. (6.8)) subject to the instantaneous point source for a homogenous permeable medium is given as

$$c(x,y,t)=\frac{c_0 A}{4\pi t\sqrt{K_L K_T}}\exp\left[-\frac{(x-vt)^2}{4K_L t}-\frac{y^2}{4K_T t}\right], \qquad (A-12)$$

where c_0 is the tracer concentration at the source point and A is the volume per length of the source. Furthermore, v is the magnitude of total velocity.

The mixing zone length at any direction is determined through finding the distance between the locations where $c_D=\frac{c}{c_0}=0.1$ and $c_D=\frac{c}{c_0}=0.9$ occur. Hence, we evaluate

the mixing zone along the line $x = y$ (the bisector of the angle between x- and y-axes) using Eq. (A-12).

From Eq. (A-12), the location where $\frac{c}{c_0} = 0.1$ occurs along the bisector is obtained:

$$x\big|_{c_{D=0.1}} = \frac{(vtK_T) + \sqrt{-K_L v^2 t^2 K_T - (K_T + K_L)\ln\left(\frac{4(0.1)\pi t\sqrt{K_L K_T}}{A}\right)(4K_L K_T t)}}{(k_T + K_L)}.$$

(A-13)

Similarly, for $c_D = 0.9$

$$x\big|_{c_{D=0.9}} \frac{(vtK_T) + \sqrt{-K_L v^2 t^2 K_T - (K_T + K_L)\ln\left(\frac{4(0.9)\pi t\sqrt{K_L K_T}}{A}\right)(4K_L K_T t)}}{(k_T + K_L)}.$$

(A-14)

In addition, if the longitudinal and transverse dispersion coefficients are assumed to be the same, the length of the mixing zone along the diagonal direction becomes

$$\Delta x = \sqrt{-\frac{v^2 t^2}{4} - 2Kt\ln\left(\frac{4(0.9)\pi tK}{A}\right)} - \sqrt{-\frac{v^2 t^2}{4} - 2Kt\ln\left(\frac{4(0.1)\pi tK}{A}\right)}.$$

(A-15)

The first term under radical sign in Eq. (A-15) can be eliminated in comparison with the second term as A is very small and the second term under the radical sign becomes much larger than the first term. Hence,

$$\Delta x = \sqrt{-2Kt\ln\left(\frac{4(0.9)\pi tK}{A}\right)} - \sqrt{-2Kt\ln\left(\frac{4(0.1)\pi tK}{A}\right)} \qquad \text{(A-16)}$$

Rearranging,

$$\Delta x = \sqrt{K\left[-2t\left(\ln(11.3t) + \ln K - \ln A\right)\right]} - \sqrt{K\left[-2t\left(\ln(1.25t) + \ln K - \ln A\right)\right]} \qquad \text{(A-17)}$$

lnK and lnA are usually very small compared to ln(11.3t) and ln(1.25 t); therefore, the length of the mixing zone along the diagonal direction (line $x = y$) is proportional to the square root of the dispersion coefficient,

$\Delta x \sim \sqrt{K}$.

(A-17)

Appendix B: Heterogeneity

With the probability distribution function *f(z)*, known for a continuous random variable *Z*, the r^{th} moment is defined as

$$\mu_r = \int_{-\infty}^{+\infty} z^r f(z)dz \quad , \tag{B-1}$$

where *r* is a non-negative integer. Hence, the first non-centered moment (*i.e.*, $r = 1$) is referred to as the expected value of *E(Z)* defined as

$$E(Z) = \int_{-\infty}^{+\infty} z\, f(z)dz \quad . \tag{B-2}$$

Similarly, the second-order centered moment, known as the variance, becomes

$$Var(Z) = \int_{-\infty}^{+\infty} (z - E(Z))^2 f(z)dz \tag{B-3}$$

or

$$Var(Z) = E(Z^2) - [E(Z)]^2 \quad . \tag{B-4}$$

In addition, the auto-covariance is a measure of how strongly a property *Z* (*e.g.*, permeability) at location x_i is related to *Z* at location x_j. In a spatially correlated medium, a strong relationship is expected for x_i and x_j that are close together. The auto-covariannce between data Z_i and Z_j is defined as

$$Cov(Z_i, Z_j) = E(Z_i Z_j) - E(Z_i)E(Z_j) \quad . \tag{B-5}$$

The correlation length is a measure of the auto-correlation extension so that a data set with a large range is strongly auto-correlated. As λ_{xD} and λ_{zD} approach zero, auto-correlation vanishes in both the longitudinal and transverse directions, respectively.

The auto-correlation coefficient between data Z_i and Z_j is the auto-covariance of Z_i and Z_j normalized by dividing by the variability of Z_i and Z_j (Jensen *et al.*, 2002):

$$\rho(Z_i, Z_j) = \frac{\mathrm{Cov}(Z_i, Z_j)}{\left[\mathrm{Var}(Z_i)\mathrm{Var}(Z_j)\right]^2}, \tag{B-6}$$

where $Cov(Z_i,Z_j)$ and $Var(Z_i)$ are the auto-covariance and variance, respectively.

Furthermore, the semi-variance (generalized variance) is defined as

$$2\gamma(Z_i, Z_j) = E(Z_i - Z_j)^2 \tag{B-7}$$

.

Assuming second-order stationary holds, all moments are invariant under translation and become independent of position. Therefore, the auto correlation and semi-variance measures become a function of a single argument:

$$\begin{aligned} &\gamma(Z_i, Z_{i+k}) = \gamma(k) = \gamma(k\Delta h) \\ &\mathrm{Cov}(Z_i, Z_{i+k}) = \mathrm{Cov}(k) = \mathrm{Cov}(k\Delta h) \\ &\rho(Z_i, Z_{i+k}) = \rho(k) = \rho(k\Delta h) \end{aligned}, \tag{B-8}$$

where $k\Delta h$ is the separation distance/lag distance. Second-order stationary allows a graphical representation of the autocorrelation measures. Furthermore, a simple relationship between the auto-covariance and the semi-variance is possible as

$$\gamma(h) = \sigma^2 - \mathrm{cov}(h) \tag{B-9}$$

.

Heterogeneity and variability are often used interchangeably. Heterogeneity is the property of the permeable medium that causes the flood front to distort and spread as the displacement proceeds. As permeability heterogeneity increases, distortion increases.

The common measure of permeability variation used in the petroleum industry is V_{DP}, the Dykstra-Parsons coefficient (Dykstra and Parsons, 1950):

$$V_{DP} = \frac{k_{50\%} - k_{16\%}}{k_{50\%}} \quad , \tag{B-10}$$

where $k_{50\%}$ is the median of permeability distribution and $k_{16\%}$ is the permeability value that is one standard deviation below $k_{50\%}$. V_{DP} is zero for homogeneous reservoirs and one for the hypothetical "infinitely" heterogeneous reservoir. V_{DP} is also called the coefficient of permeability variation; other definitions of V_{DP} involving permeability-porosity ratios are possible (Lake, 1989).

Appendix C: Scaling Analysis for Simultaneous Water-and-Gas Injection

This chapter presents the order-of-one o(1) scaling analysis and provides a unique set of dimensionless scaling groups to assess the displacement performance of simultaneous water and gas (SWAG) injection. For the first time, we consider the effects of water salinity, the dissolution of solvent in the aqueous phase, and the complexity of injection and production wells' configuration on the performance of miscible displacement; we can study their impacts on the performance of miscible displacements through a comparison of the obtained dimensionless groups.

Generally speaking, o(1) scaling analysis is useful when the objective is to identify approximations that are allowed for a particular transport phenomenon. The outcome of this study helps reduce the required number of parameters to be considered in the design process of SWAG injections.

We implement the o(1) scaling analysis into the system of governing equations using an eight-step procedure described by Krantz (2007). Each variable in the system of equations is replaced by an appropriate scale and reference factors. We further determine the scale and reference factors by ensuring that the resulting dimensionless scaling groups remain within o(1).

Our analysis suggests that o(1) scaling yields a unique set of 45 independent dimensionless groups for a three-phase five-component SWAG displacement in a two-dimensional anisotropic permeable medium. Through this study, several new

dimensionless groups are identified such as the salinity number, compressibility group, density-molecular weight group, viscosity-molecular weight and perforation groups.

MATHEMATICAL BASIS OF SCALING ANALYSIS

Scaling analysis is an application of a subset of the Lie group theory. In mathematics, group theory concerns the algebraic structures known as groups. Algebraic structures are defined as one or some sets (a collection of distinct objects), closed under one or more operations satisfying some axioms (from which other statements are logically derived). Furthermore, in mathematics, a set is defined to be closed under an operation if the performance of that operation on members of the set always produces a unique member of the same set; for more details on the Lie group theory, see Steeb (2007).

The basic idea in o(1) scaling analysis is to substitute dependent/independent variables in the governing equations with new terms. Therefore, a prerequisite of the scaling process is knowledge of the governing equations. The scaling yields interesting insight into the relations between the parameters and variables without solving the equations. The non-dimensionalizing process yields a system of dimensionless equations representing the minimum parametric description of the process; *i.e.*, the solution will be only a function of the dimensionless independent variables and the dimensionless groups generated by the scaling process.

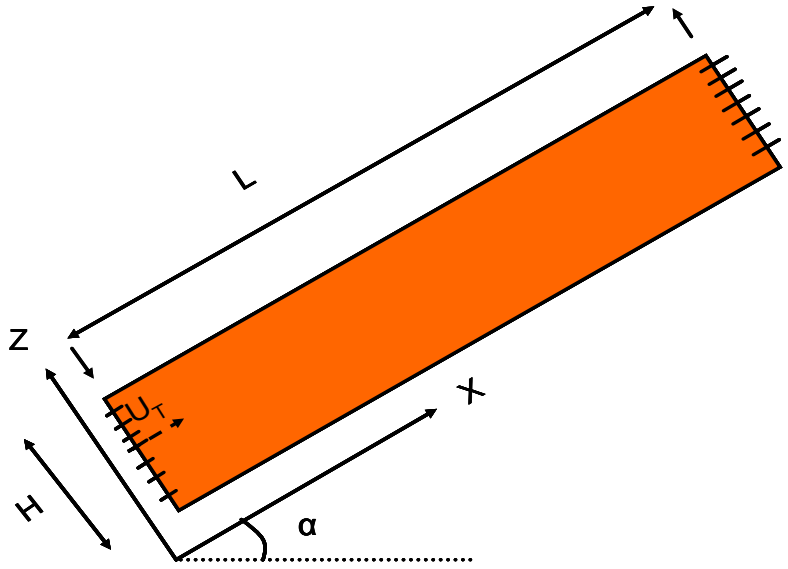

Figure C.1: Schematic of the displacement configuration (line-drive type) used by Wood *et al.* (2006)

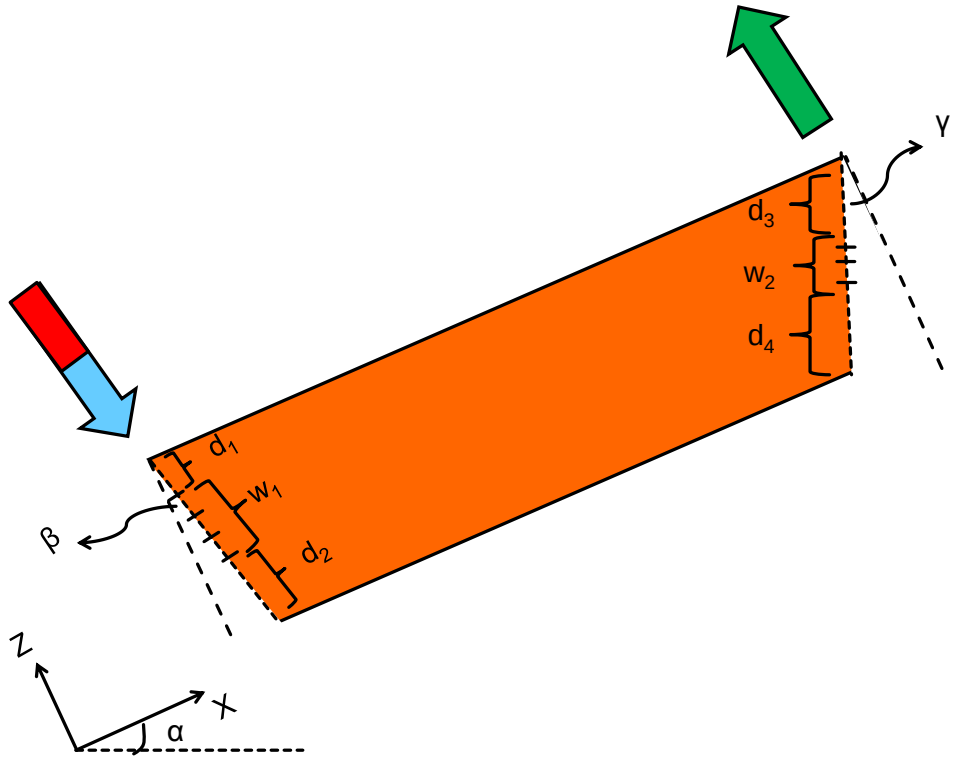

Figure C.2: Schematic of the SWAG displacement considered in this study

ASSUMPTIONS

In this chapter, SWAG scaling analysis will be presented through a stepwise procedure under the following premises:

1. Two-dimensional homogeneous, constant dip angle, anisotropic permeable medium (Figure C.2).
2. The model includes an injection well and a producer well, which may have a different orientation rather than just being parallel with the *z*-direction.
3. The injection and production wells can be partially perforated.

4. The injection well is assigned a constant rate.
5. The producer operates under a constant bottomhole pressure constraint.
6. Five components exist: two in the aqueous phase, two in the oleic phase, and one solvent (*e.g.,* CO_2).
7. The oil consists of pseudo-components 3 and 4. Component 3 (light oil component) may partition into the solvent phase, but component 4 (heavy oil component) always stays in the oil phase.
8. Both the injected and the resident water may contain some salinity.
9. No water vaporization into the solvent phase occurs.
10. The solubility of the solvent (*e.g.*, CO_2) in the aqueous phases occurs.
11. The maximum of three phases can exist simultaneously: the aqueous phase (subscript 1), oil phase, (subscript 3), and the solvent phase (subscript 2).
12. No sorption and no chemical reaction occur.
13. The pore space is assumed to be incompressible; *i.e.*, rock compressibility is assumed to be negligible.
14. Hydrodynamic dispersion is assumed to have the Fickian form; furthermore, molecular diffusion is negligible compared to the mechanical dispersion.

FORMULATION

The first step of scaling analysis is to determine the dimensional-describing equations (mass conservation equations) and their initial, boundary, and auxiliary conditions. The formulation for the mass conservation for simultaneous injection of CO_2 and water contains two fundamentally different forms: overall composition balances and the phase

conservation equations. We consider the overall mass conservation equation for N_c-*1* components, the continuity equation, and N_p-1 phase conservation equations; N_c and N_p are the number of components and the phases, respectively. It is required to ensure that the problem is completely determined. Two-dimensional five-component three-phase flow is governed by the following conservation, continuity, and constitutive equations.

Overall composition balances

The overall composition of component *i* represents the sum of component *i* in all phases. In this study, there are four overall compositional equations that are independent:

$$\phi\frac{\partial(\rho_1\omega_{11}S_1)}{\partial t}+\frac{\partial(\rho_1\omega_{11}U_{X1})}{\partial x}+\frac{\partial(\rho_1\omega_{11}U_{Z1})}{\partial z}-(\frac{\alpha_L U_{X1}^2+\alpha_T U_{Z1}^2}{U_1})\frac{\partial^2\rho_1\omega_{11}}{\partial x^2}-(\frac{\alpha_L U_{Z1}^2+\alpha_T U_{X1}^2}{U_1})\frac{\partial^2\rho_1\omega_{11}}{\partial z^2}=0. \quad \text{(C-1)}$$

$$\phi\frac{\partial(\rho_1\omega_{51}S_1)}{\partial t}+\frac{\partial(\rho_1\omega_{51}U_{X1})}{\partial x}+\frac{\partial(\rho_1\omega_{51}U_{Z1})}{\partial z}-(\frac{\alpha_L U_{X1}^2+\alpha_T U_{Z1}^2}{U_1})\frac{\partial^2\rho_1\omega_{51}}{\partial x^2}-(\frac{\alpha_L U_{Z1}^2+\alpha_T U_{X1}^2}{U_1})\frac{\partial^2\rho_1\omega_{51}}{\partial z^2}=0. \quad \text{(C-2)}$$

$$\phi\frac{\partial(\rho_3\omega_{43}S_3)}{\partial t}+\frac{\partial(\rho_3\omega_{43}U_{X3})}{\partial x}+\frac{\partial(\rho_3\omega_{43}U_{Z3})}{\partial z}-(\frac{\alpha_L U_{X3}^2+\alpha_T U_{Z3}^2}{U_3})\frac{\partial^2\rho_3\omega_{43}}{\partial x^2}-(\frac{\alpha_L U_{Z3}^2+\alpha_T U_{X3}^2}{U_3})\frac{\partial^2\rho_3\omega_{43}}{\partial z^2}=0. \quad \text{(C-3)}$$

$$\phi\frac{\partial(\rho_1\omega_{21}S_1+\rho_2\omega_{22}S_2)}{\partial t}+\frac{\partial(\rho_1\omega_{21}U_{X1}+\rho_2\omega_{22}U_{X2})}{\partial x}+\frac{\partial(\rho_1\omega_{21}U_{Z1}+\rho_2\omega_{22}U_{Z2})}{\partial z}-(\frac{\alpha_L U_{X1}^2+\alpha_T U_{Z1}^2}{U_1})\frac{\partial^2\rho_1\omega_{21}}{\partial x^2}$$
$$-(\frac{\alpha_L U_{X2}^2+\alpha_T U_{Z2}^2}{U_2})\frac{\partial^2\rho_2\omega_{22}}{\partial x^2}-(\frac{\alpha_L U_{Z1}^2+\alpha_T U_{X1}^2}{U_1})\frac{\partial^2\rho_1\omega_{21}}{\partial z^2}-(\frac{\alpha_L U_{Z2}^2+\alpha_T U_{X2}^2}{U_2})\frac{\partial^2\rho_2\omega_{22}}{\partial z^2}=0. \quad \text{(C-4)}$$

To facilitate the derivation procedure, we consider $c_{ij} = \rho_j \omega_{ij}$ for the remainder of this study. Hence, c_{ij} is defined as the mass of component *i* per volume of phase *j*.

Phase conservation equations

There are two independent phase conservation equations as

$$\phi \frac{\partial(\rho_1 S_1)}{\partial t} + \frac{\partial(\rho_1 U_{X1})}{\partial x} + \frac{\partial(\rho_1 U_{Z1})}{\partial z} = r_{m21}, \tag{C-5}$$

$$\phi \frac{\partial(\rho_2 S_2)}{\partial t} + \frac{\partial(\rho_2 U_{X2})}{\partial x} + \frac{\partial(\rho_2 U_{Z2})}{\partial z} = r_{m22} + r_{m32}, \tag{C-6}$$

where r_{mij} represents the rate of mass transfer between phases owing to condensation and vaporization.

Continuity equation

The continuity equation as the sum of all phase conservation equations is expressed as

$$\phi \frac{\partial\left[\rho_1 S_1 + \rho_2 S_2 + \rho_3 S_3\right]}{\partial t} + \frac{\partial(\rho_1 U_{X1} + \rho_2 U_{X2} + \rho_3 U_{X3})}{\partial x} + \frac{\partial(\rho_1 U_{Z1} + \rho_2 U_{Z2} + \rho_3 U_{Z3})}{\partial z} = 0. \tag{C-7}$$

Initial condition

The initial oil saturation in the reservoir is known; in addition, we assume that there is no solvent phase (gaseous phase) initially present in the reservoir. Moreover, the salinity of the resident brine and the composition of pseudo-component 4 (heavy oil) are known. Hence,

$$\begin{cases} \omega_{51} = \omega_{51}^{I} \\ \omega_{43} = \omega_{43}^{I} \\ S_3 = S_3^{I} \\ S_2 = 0 \ . \end{cases} \qquad @\ t = 0\ \forall x, z \tag{C-8}$$

Injection composition

At the injection inlet, we assume that the salinity of the injected water and the composition of the solvent in the gaseous phase are known.

$$\begin{cases} \omega_{51} = \omega_{51}^{J} \\ \omega_{22} = 1.0 \end{cases} \quad @ \quad \begin{cases} d_1 \, Sin\beta \le x \le (d_1 + w_1) Sin\beta \\ d_2 \, Cos\beta \le z \le (d_2 + w_1) Cos\beta \end{cases} \quad \text{and } t > 0 \ . \tag{C-9}$$

Definition of mass fraction and saturation

Following the definition, the summation of mass fractions (ω_{ij}) within each phase becomes unity; likewise, phase saturations add to one:

$$\begin{cases} S_1 + S_2 + S_3 = 1.0 \\ \omega_{11} + \omega_{51} + \omega_{21} = 1.0 \\ \omega_{22} = 1.0 \\ \omega_{23} + \omega_{33} + \omega_{43} = 1.0 \ . \end{cases} \tag{C-10}$$

Determined initial and injected phase viscosities

In addition, we assume that the fluids' viscosities are known at the initial and injected conditions:

$$\begin{cases} \mu_1 = \mu_1^{I} & @ t = 0 \\ \mu_3 = \mu_3^{I} & @ t = 0 \\ \mu_2 = \mu_2^{J} & @ t > 0 \,\&\, \text{injector} . \end{cases} \tag{C-11}$$

Salting-out effect

We assume that the salinity can be present in both injected and the resident aqueous phases. Furthermore, the solubility of injected solvent (CO_2) in water is considered as one of the miscibility-degrading factors as it reduces the solvent efficiency to extract oil.

The impact of an aqueous electrolyte phase on the solubility of a non-electrolyte gas is reported as the Sechenov salting-effect. The aqueous electrolyte may increase the gas activity coefficient and, thus, reduce the gas solubility. This phenomenon is called salt-out. The salt-in process is a similar phenomenon, but with an inverse impact that reduces the gas activity coefficient and increases the gas solubility. Sechnov (1889) proposed the following general empirical equation:

$$\log\left(\frac{H_{Pure}}{H_{brine}}\right) = K_{sal} M_{sal}\,, \tag{C-12}$$

where H_{brine} and H_{pure} are Henry constants for brine and pure water, respectively. K_{sal} is the Sechnov coefficient and M is the molality of the salt (solute).

Effect of pressure on the solubility of the solvent in the aqueous phase

The experimental results indicate that the solubility of CO_2 in an aqueous phase increases linearly with gas pressures greater than 2000 psi (Kumar, 2004; Hangx, 2005). Hence, the volume of dissolved CO_2 is linearly correlated with the gas pressure:

$$\frac{\omega_{21}}{\rho_2} = AP_2 + B, \tag{C-13}$$

where $\frac{\omega_{21}}{\rho_2}$ is the $\frac{\text{Vol. dissolved } CO_2}{\text{Mass Water}}$. Experimental results show that for T=160°F, A and B are 0.0016048 and 21.6, respectively. However, similar results are obtained for different temperatures. Therefore, the differential form of Eq. is expressed as

$$d\left(\frac{\omega_{21}}{\rho_2}\right) = A\, d(P_2) \quad \Rightarrow \quad \frac{d\left(\frac{\omega_{21}}{\rho_2}\right)}{d(P_2)} = A\,. \tag{C-14}$$

Top and bottom no flow boundaries

$$U_{jZ} = 0 \qquad \text{where } j = 1,..,N_P \quad @\ z = 0, z = H \qquad \forall\, x, t\ , \text{where } t > 0\,. \tag{C-15}$$

No flow boundary condition is applied at the bottom of the reservoir; therefore,

$$U_{1Z} = U_{2Z} = U_{3Z} = 0 \qquad @\ z = 0\, \forall\, x, t\ , \text{where } t > 0\ . \tag{C-16}$$

$$\begin{cases} U^*_{12Z} U_{1ZD} = 0 \\ U^*_{22Z} U_{2ZD} = 0 \\ U^*_{32Z} U_{3ZD} = 0 \end{cases} \qquad @\ Z^*_2\, Z_D = 0\ \ \forall\, x, t\ , \text{where } t > 0\,. \tag{C-17}$$

Likewise, the top of the reservoir is subjected to the no flow boundary condition:

$$U_{1Z} = U_{2Z} = U_{3Z} = 0 \qquad @\ z = H\, \forall\, x, t\ , \text{where } t > 0\ . \tag{C-18}$$

$$\begin{cases} U^*_{12Z} U_{1ZD} = 0 \\ U^*_{22Z} U_{2ZD} = 0 \\ U^*_{32Z} U_{3ZD} = 0 \end{cases} \qquad @\ Z_D = \left[\frac{H}{Z^*_2}\right]^{87}\ \forall\, x, t\ , \text{where } t > 0\,. \tag{C-19}$$

Constant pressure producer constraint

We assume a constant bottomhole pressure constraint for the producer.

$$P_j = P_{wf} + \bar{\rho}_j g C\,os\,\alpha(H - d_3 Cos\gamma - Z) \qquad @ \quad \begin{cases} L - (d_3 + w2)\,Sin\beta \le x \le L - d_3\,Sin\beta \\ d_4\,Cos\gamma \le z \le (d_4 + w_2)Cos\gamma \end{cases} \quad \text{and } t > 0,$$

(C-20)

where the average density is the flux average density in the production well:

$$\bar{\rho}_j u_{xj} = \frac{\int_{H-(d_3+w_2)\cos\gamma}^{H-d_3 Cos\gamma} \rho_j u_{xj} dz}{w_2 Cos\gamma} \quad \text{for } j = 1,2,3\,.$$

(C-21)

Capillary pressure equation

Using the Leverett J-function, a dimensionless function, the capillary pressure between phases are considered as

$$P_j - P_k = j(S)\delta_{jk}\sqrt{\frac{\phi}{k}} \quad \text{where } j,k = 1,..N_P \text{ and } j \ne k.$$

(C-22)

Constant rate injector

We further assume a constant rate constraint for the injector. Hence, the following relations between injection rates are defined:

$$\begin{cases} \left|\overrightarrow{u_1}\right| = U_1^J \\ \left|\overrightarrow{u_2}\right| = U_2^J \end{cases} \Rightarrow \begin{cases} u_{1x} = U_1^J Cos\beta \\ u_{1z} = U_1^J\,Sin\beta \end{cases} \quad \& \quad \begin{cases} u_{2x} = U_2^J Cos\beta \\ u_{2z} = U_2^J\,Sin\beta \end{cases} \quad @ \begin{cases} d_1\,Sin\beta \le x \le (d_1 + w_1)Sin\beta \\ d_2\,Cos\beta \le z \le (d_2 + w_1)Cos\beta \end{cases} \quad \text{and } t > 0\,.$$

(C-23)

Furthermore,

$$\frac{U_1^J}{U_2^J} = W_R, \qquad U_1^J + U_2^J = U_T,$$

(C-24)

where W_R is the WAG ratio defined as the ratio of injected water to that that of the gas phase expressed in reservoir units.

Darcy's law

We assume that Darcy's law is valid for multiphase flow:

$$\vec{u_j} = -\lambda_{rj}\,\vec{\vec{k}} \bullet (\vec{\nabla} Pj - \rho_j \vec{g}) \qquad \text{where} \quad j = 1,..N_P, \tag{C-25}$$

where,

$$\lambda_{rj}\vec{\vec{k}} = \frac{k_{rj}}{\mu_j}\vec{\vec{k}} = \frac{k^{\circ}_{rj}}{\mu_j} f_D(s_j)\vec{\vec{k}}, \tag{C-26}$$

Initial reservoir pressure

An initial pressure of P_i is considered for the oil phase at the datum z=0:

$$P_3 = Pi \qquad @\ t = 0 \ \text{and}\ z = 0. \tag{C-27}$$

Relative permeability

A typical form of relative permeability models consists of a constant endpoint, $k_{rj}°$, multiplied by an arbitrary dimensionless function of saturation as

$$k_{rj} = k^{\circ}_{rj} f_D(s_j) \quad \text{where} \quad j = 1,..N_P. \tag{C-28}$$

Fluid viscosity

We consider a constant value for viscosity of the aqueous phase and variable viscosities for the oil and gas phases. The viscosity of gas phase is usually much smaller than that of liquid phase; hence, the gas will tend to dominate the flow if it becomes mobile$\left(S_g > S_{gcrit}\right)$. However, the gas phase viscosity increases as the miscibility develops owing to the dissolution of oil component into the gaseous phase. The viscosity of gas phases increases until the gas and oil viscosities become equal. This is where

miscibility has been achieved. Therefore, we consider the following relation for the gas viscosity:

$$\mu_2 = \frac{\mu^{\circ}_{2,g}\chi_2\sqrt{M^{\circ}_2} + \mu^{\circ}_{3,g}\chi_3\sqrt{M^{\circ}_3}}{\chi_2\sqrt{M^{\circ}_2} + \chi_3\sqrt{M^{\circ}_3}}. \tag{C-29}$$

In this study, SWAG injection is considered as an isothermal process; therefore, we take the pure viscosity of components ($\mu^{\circ}_{i,g}$) as a parameter, not a variable.

On the other hand, the oil phase viscosity varies because of the mass transfer between phases. We consider the following logarithmic mixing rule for the oil viscosity:

$$\ln\mu_o = \sum_{i=1}^{N_c} x_i \ln\left(\mu^{\circ}_{i,o}\right) = \sum_{i=2}^{4} \chi_{i,3} \ln\left(\mu^{\circ}_{i,o}\right) = \chi_{23}\ln\left(\mu^{\circ}_{2,o}\right) + \chi_{33}\ln\left(\mu^{\circ}_{3,o}\right) + \chi_{43}\ln\left(\mu^{\circ}_{4,o}\right). \tag{C-30}$$

The pure viscosity of each component in the oleic phase $\mu^{\circ}_{i,o}$ can be measured directly or estimated from the existing correlations or tables.

Relations between mole and mass fractions

The mole fraction of component *i* in phase *j* has the following relation with the mass fraction of that component in the same phase:

$$\chi_{ij} = \frac{\overline{M_j}}{M^{\circ}_i}\omega_{ij}, \tag{C-31}$$

where the oil and gas average molecular weights are defined as

$$\overline{M_3} = \chi_{23}M^{\circ}_2 + \chi_{33}M^{\circ}_3 + \chi_{43}M^{\circ}_4, \tag{C-32}$$

$$\overline{M}_2 = \chi_{22} M_2^{\circ} + \chi_{32} M_3^{\circ}. \tag{C-33}$$

Mass Density

Liquid densities (water and oil) are obtained through the concept of an ideal mixture:

$$\frac{1}{\rho_1} = \sum_{i=1}^{N_{aq}} \frac{\omega_{i1}}{\rho_{i,w}} = \frac{\omega_{11}}{\rho_{11}^{\circ}} + \frac{\omega_{51}}{\rho_{51}^{\circ}} + \frac{\omega_{21}}{\rho_{21}^{\circ}},$$
$$\frac{1}{\rho_3} = \sum_{i=1}^{N_{oil}} \frac{\omega_{i3}}{\rho_{i,3}} = \frac{\omega_{23}}{\rho_{2,3}} + \frac{\omega_{33}}{\rho_{3,3}} + \frac{\omega_{43}}{\rho_{4,3}}. \tag{C-34}$$

Since the flow occurs the isothermal condition, the density of component *i* in the oleic phase is only affected by a change in the oleic phase pressure. The following relation represents the density variation because of the pressure change:

$$\rho_i = \rho_i^{\circ} (1 + c\Delta P), \qquad \text{where } i=3,4 \tag{C-35}$$

In addition, the density of water and salt components are assumed to be constant during the displacement.

Gas density can be calculated as:

$$\rho_2 = \frac{P_2 \overline{M_{Gas}}}{ZRT_{Gas}}. \tag{C-36}$$

The gas compressibility factor, *Z*, is a function of both temperature and pressure. However, it will be solely a function of pressure as here we study isothermal gas injection. Therefore,

$$Z = f(P_r, T_r) \xrightarrow{\text{Temp. cons.}} Z = f(P_r), \tag{C-37}$$

where P_r and T_r are reduced pressure and temperature, respectively. Furthermore,

$$\therefore$$
$$Z = Z^{\circ} f(P_r). \tag{C-38}$$

Mass transfer between phases

The following relations represent the mass transfer between phases:

$$\begin{aligned} r_{m21} &= \phi K_{21}(\rho_2 \omega_{22} S_2 - \rho_1 \omega_{21} S_1) \\ r_{m22} &= -\phi K_{21}(\rho_2 \omega_{22} S_2 - \rho_1 \omega_{21} S_1) - K_{23}(\rho_2 \omega_{22} S_2 - \rho_3 \omega_{23} S_3) \\ r_{m32} &= \phi K_{32}(\rho_3 \omega_{33} S_3 - \rho_2 \omega_{32} S_2), \end{aligned} \tag{C-39}$$

where K_{ij} is the mass transfer coefficient of component *i* in phase *j*. If the flow becomes fully immiscible, the mass transfer terms in the phase conservation equations will be zero.

IMPLEMENTATION OF THE TECHNIQUE

In step 2, we define a scale and a reference factor for each dependent and independent variable. These factors establish linear transformations from dimensional to dimensionless space.

Mass fraction of component *i* in phase *j*

$$\begin{cases} \omega_{11} = \omega^*_{112}\omega_{11D} + \omega^*_{111} \\ \omega_{21} = \omega^*_{212}\omega_{2D} + \omega^*_{211} \\ \omega_{51} = \omega^*_{512}\omega_{51D} + \omega^*_{511} \\ \omega_{22} = \omega^*_{222}\omega_{12D} + \omega^*_{221} \\ \omega_{32} = \omega^*_{322}\omega_{32D} + \omega^*_{321} \\ \omega_{23} = \omega^*_{232}\omega_{23D} + \omega^*_{231} \\ \omega_{33} = \omega^*_{332}\omega_{33D} + \omega^*_{331} \\ \omega_{43} = \omega^*_{432}\omega_{43D} + \omega^*_{431}. \end{cases} \tag{C-40}$$

Average molecular weight of phase *j*

$$\begin{cases} \overline{M}_1 = M^*_{12} M_{1D} + M^*_{11} \\ \overline{M}_2 = M^*_{22} M_{2D} + M^*_{21} \\ \overline{M}_3 = M^*_{32} M_{3D} + M^*_{31} \end{cases} . \tag{C-41}$$

Mass of component i per volume of phase *j*

$$\begin{cases} c_{11} = c^*_{112} c_{11D} + c^*_{111} \\ c_{21} = c^*_{212} c_{2D} + c^*_{211} \\ c_{51} = c^*_{512} c_{51D} + c^*_{511} \\ c_{22} = c^*_{222} c_{12D} + c^*_{221} \\ c_{32} = c^*_{322} c_{32D} + c^*_{321} \\ c_{23} = c^*_{232} c_{23D} + c^*_{231} \\ c_{33} = c^*_{332} c_{33D} + c^*_{331} \\ c_{43} = c^*_{432} c_{43D} + c^*_{431} \end{cases} . \tag{C-42}$$

Mole fraction of component *i* in phase *j*

$$\begin{cases} \chi_{11} = \chi^*_{112} \chi_{11D} + \chi^*_{111} \\ \chi_{21} = \chi^*_{212} \chi_{2D} + \chi^*_{211} \\ \chi_{51} = \chi^*_{512} \chi_{51D} + \chi^*_{511} \\ \chi_{22} = \chi^*_{222} \chi_{12D} + \chi^*_{221} \\ \chi_{32} = \chi^*_{322} \chi_{32D} + \chi^*_{321} \\ \chi_{23} = \chi^*_{232} \chi_{23D} + \chi^*_{231} \\ \chi_{33} = \chi^*_{332} \chi_{33D} + \chi^*_{331} \\ \chi_{43} = \chi^*_{432} \chi_{43D} + \chi^*_{431} \end{cases} . \tag{C-43}$$

Average molecular weight of phase *j*

$$\begin{cases} \overline{M}_1 = M^*_{12} M_{1D} + M^*_{11} \\ \overline{M}_2 = M^*_{22} M_{2D} + M^*_{21} \\ \overline{M}_3 = M^*_{32} M_{3D} + M^*_{31} \end{cases} . \tag{C-44}$$

Saturation of phase *j*

$$\begin{cases} S_1 = S_{12}^* S_{1D} + S_{11}^* \\ S_2 = S_{22}^* S_{2D} + S_{21}^* \\ S_3 = S_{32}^* S_{3D} + S_{31}^* \end{cases}. \tag{C-45}$$

Density of phase *j*

$$\begin{cases} \rho_1 = \rho_{12}^* \rho_{1D} + \rho_{11}^* \\ \rho_2 = \rho_{22}^* \rho_{2D} + \rho_{21}^* \\ \rho_3 = \rho_{32}^* \rho_{3D} + \rho_{31}^* \end{cases}. \tag{C-46}$$

Density of oil components in the oleic phase

$$\begin{cases} \rho_{33} = \rho_{332}^* \rho_{33D} + \rho_{331}^* \\ \rho_{43} = \rho_{432}^* \rho_{43D} + \rho_{431}^* \end{cases}. \tag{C-47}$$

Phase pressure

$$\begin{cases} P_1 = P_{12}^* P_{1D} + P_{11}^* \\ P_2 = P_{22}^* P_{2D} + P_{21}^* \\ P_3 = P_{32}^* P_{3D} + P_{31}^* \end{cases}. \tag{C-48}$$

Darcy velocity in the *x*-direction

$$\begin{cases} u_{1X} = u_{12X}^* u_{1XD} + u_{11X}^* \\ u_{2X} = u_{22X}^* u_{2XD} + u_{21X}^* \\ u_{3X} = u_{32X}^* u_{3XD} + u_{31X}^* \end{cases}. \tag{C-49}$$

Darcy velocity in the *z*-direction

$$\begin{cases} u_{1z} = u_{12Z}^* u_{1ZD} + u_{11Z}^* \\ u_{2z} = u_{22Z}^* u_{2ZD} + u_{21Z}^* \\ u_{3z} = u_{32Z}^* u_{3ZD} + u_{31Z}^* \end{cases}. \tag{C-50}$$

Injection rate

$$\begin{cases} U_1 = U_{12}^* U_{1D} + U_{11}^* \\ U_2 = U_{22}^* U_{2D} + U_{21}^* \\ U_3 = U_{32}^* U_{3D} + U_{31}^* \end{cases}. \tag{C-51}$$

Independent variables

$$\begin{cases} x = x_2^* x_D + x_1^* \\ z = z_2^* z_D + z_1^* \\ t = t_2^* t_D + t_1^* \end{cases}. \tag{C-52}$$

Phase viscosity

$$\begin{cases} \mu_1 = \mu_{12}^* \mu_{1D} \\ \mu_2 = \mu_{22}^* \mu_{2D} \\ \mu_3 = \mu_{32}^* \mu_{3D} \end{cases}. \tag{C-53}$$

Mass transfer rate between phases

$$\begin{cases} r_{m21} = r_{m212}^* r_{m21D} + r_{m211}^* \\ r_{m22} = r_{m222}^* r_{m22D} + r_{m221}^* \\ r_{m32} = r_{m322}^* r_{m32D} + r_{m321}^* \end{cases}. \tag{C-54}$$

Next, we determine reference factors for all variables (step 3). The parametric representation of the governing equations will involve an additional unnecessary dimensionless group if this step is not done properly; in other words, non-dimensionlizing should not change the original form of the equations. Hence, the dimensionless form of the variables becomes:

Mass fraction of component *i* in phase *j*

$$\begin{cases} \omega_{11} = \omega_{112}^{*}\omega_{11D} \\ \omega_{21} = \omega_{212}^{*}\omega_{2D} \\ \omega_{51} = \omega_{512}^{*}\omega_{51D} \\ \omega_{22} = \omega_{222}^{*}\omega_{12D} \\ \omega_{32} = \omega_{322}^{*}\omega_{32D} \\ \omega_{23} = \omega_{232}^{*}\omega_{23D} \\ \omega_{33} = \omega_{332}^{*}\omega_{33D} \\ \omega_{43} = \omega_{432}^{*}\omega_{43D} \end{cases}. \tag{C-55}$$

Phase pressure

$$\begin{cases} P_1 = P_{12}^{*}P_{1D} + P_{wf} \\ P_2 = P_{22}^{*}P_{2D} + P_{wf} \\ P_3 = P_{32}^{*}P_{3D} + P_{wf} \end{cases}. \tag{C-56}$$

Density of phase *j*

$$\begin{cases} \rho_1 = \rho_{12}^{*}\rho_{1D} + \rho_1^{I} \\ \rho_2 = \rho_{22}^{*}\rho_{2D} + \rho_2^{J} \\ \rho_3 = \rho_{32}^{*}\rho_{3D} + \rho_3^{I} \end{cases}. \tag{C-57}$$

Mass of component i per volume of phase *j*

$$\begin{cases} c_{11} = c^{*}_{112} c_{11D} \\ c_{21} = c^{*}_{212} c_{2D} \\ c_{51} = c^{*}_{512} c_{51D} \\ c_{12} = c^{*}_{122} c_{12D} \\ c_{22} = c^{*}_{222} c_{12D} \\ c_{32} = c^{*}_{322} c_{32D} \\ c_{23} = c^{*}_{232} c_{23D} \\ c_{33} = c^{*}_{332} c_{33D} \\ c_{43} = c^{*}_{432} c_{43D} \end{cases}. \tag{C-58}$$

Mole fraction of component *i* in phase *j*

$$\begin{cases} \chi_{11} = \chi^{*}_{112} \chi_{11D} \\ \chi_{21} = \chi^{*}_{212} \chi_{2D} \\ \chi_{51} = \chi^{*}_{512} \chi_{51D} \\ \chi_{12} = \chi^{*}_{122} \chi_{12D} \\ \chi_{22} = \chi^{*}_{222} \chi_{12D} \\ \chi_{32} = \chi^{*}_{322} \chi_{32D} \\ \chi_{23} = \chi^{*}_{232} \chi_{23D} \\ \chi_{33} = \chi^{*}_{332} \chi_{33D} \\ \chi_{43} = \chi^{*}_{432} \chi_{43D} \end{cases}. \tag{C-59}$$

Average molecular weight of phase *j*

$$\begin{cases} \overline{M}_1 = M^{*}_{12} M_{1D} \\ \overline{M}_2 = M^{*}_{22} M_{2D} \\ \overline{M}_3 = M^{*}_{32} M_{3D} \end{cases}. \tag{C-60}$$

Saturation of phase *j*

$$\begin{cases} S_1 = S_{12}^* S_{1D} + S_{1r} \\ S_2 = S_{22}^* S_{2D} \\ S_3 = S_{32}^* S_{3D} + S_{3r} \end{cases}. \tag{C-61}$$

Density of oil components in the oleic phase

$$\begin{cases} \rho_{33} = \rho_{332}^* \rho_{33D} \\ \rho_{43} = \rho_{432}^* \rho_{43D} \end{cases}. \tag{C-62}$$

Darcy velocity in the *x*-direction

$$\begin{cases} u_{1X} = u_{12X}^* u_{1XD} \\ u_{2X} = u_{22X}^* u_{2XD} \\ u_{3X} = u_{32X}^* u_{3XD} \end{cases}. \tag{C-63}$$

Darcy velocity in the *z*-direction

$$\begin{cases} u_{1z} = u_{12Z}^* u_{1ZD} \\ u_{2z} = u_{22Z}^* u_{2ZD} \\ u_{3z} = u_{32Z}^* u_{3ZD} \end{cases}. \tag{C-64}$$

Injection rate

$$\begin{cases} U_1 = U_{12}^* U_{1D} \\ U_2 = U_{22}^* U_{2D} \\ U_3 = U_{32}^* U_{3D} \end{cases}. \tag{C-65}$$

Independent variables

$$\begin{cases} x = x_2^* x_D \\ z = z_2^* z_D \\ t = t_2^* t_D \end{cases}. \tag{C-66}$$

Phase viscosity

$$\begin{cases} \mu_1 = \mu_{12}^{*}\,\mu_{1D} \\ \mu_2 = \mu_{22}^{*}\,\mu_{2D} \\ \mu_3 = \mu_{32}^{*}\,\mu_{3D} \end{cases}. \tag{C-67}$$

Mass transfer rate between phases

$$\begin{cases} r_{m21} = r_{m212}^{*}\, r_{m21D} \\ r_{m22} = r_{m222}^{*}\, r_{m22D} \\ r_{m32} = r_{m322}^{*}\, r_{m32D} \end{cases}. \tag{C-68}$$

In step 4, we incorporate scale and reference factors into the variables' expressions to determine dimensionless variables. Next, we introduce the derived dimensionless variables into the describing and constitutive equations (step 5). Through this process, we use the chain rule to recast the equations in terms of the dimensionless variables; the chain rule is used when a derivative of dimensionless variable is involved. Furthermore, we divide through by the dimensional coefficient of one of the terms in describing equations (step 6).

Overall composition balance for Component 1

$$\phi\frac{\partial(\rho_1\omega_{11}S_1)}{\partial t}+\frac{\partial(\rho_1\omega_{11}U_{X1})}{\partial x}+\frac{\partial(\rho_1\omega_{11}U_{Z1})}{\partial z}-\left(\frac{\alpha_L U_{X1}^2+\alpha_T U_{Z1}^2}{U_1}\right)\frac{\partial^2\rho_1\omega_{11}}{\partial x^2}-\left(\frac{\alpha_L U_{Z1}^2+\alpha_T U_{X1}^2}{U_1}\right)\frac{\partial^2\rho_1\omega_{11}}{\partial z^2}=0 \tag{C-69}$$

The substitution of $\rho_1\omega_{11}$ with c_{11} yields

$$\phi\frac{\partial(c_{11}S_1)}{\partial t}+\frac{\partial(c_{11}U_{X1})}{\partial x}+\frac{\partial(c_{11}U_{Z1})}{\partial z}-\left(\frac{\alpha_L U_{X1}^2+\alpha_T U_{Z1}^2}{U_1}\right)\frac{\partial^2 c_{11}}{\partial x^2}-\left(\frac{\alpha_L U_{Z1}^2+\alpha_T U_{X1}^2}{U_1}\right)\frac{\partial^2 c_{11}}{\partial z^2}=0 \tag{C-70}$$

Incorporating the dimensionless form of the variables into Eq. gives

$$\begin{aligned}
&\frac{\phi c_{112}^{*} S_{12}^{*}}{t_2^{*}} \frac{\partial (c_{11D} S_{1D})}{\partial t_D} + \frac{\phi c_{112}^{*} S_{11}^{*}}{t_2^{*}} \frac{\partial (c_{11D})}{\partial t_D} \\
&+ \frac{c_{112}^{*} U_{X12}^{*}}{x_2^{*}} \frac{\partial (c_{11D} U_{X1D})}{\partial x_D} + \frac{c_{112}^{*} U_{Z12}^{*}}{z_2^{*}} \frac{\partial (c_{11D} U_{Z1D})}{\partial z} \\
&- \frac{c_{112}^{*} U_{X12}^{*\,2} \alpha_L}{x_2^{*2} U_{12}^{*}} \left(\frac{U_{X1D}^2}{U_{1D}}\right) \frac{\partial^2 c_{11D}}{\partial x_D^{\,2}} - \frac{c_{112}^{*} U_{Z12}^{*\,2} \alpha_T}{x_2^{*2} U_{12}^{*}} \left(\frac{U_{Z1D}^2}{U_{1D}}\right) \frac{\partial^2 c_{11D}}{\partial x_D^{\,2}} \\
&- \frac{c_{112}^{*} U_{Z12}^{*\,2} \alpha_L}{z_2^{*2} U_{12}^{*}} \left(\frac{U_{Z1D}^2}{U_{1D}}\right) \frac{\partial^2 c_{11D}}{\partial z_D^{\,2}} - \frac{c_{112}^{*} U_{X12}^{*\,2} \alpha_{T2}}{z_2^{*2} U_{12}^{*}} \left(\frac{U_{X1D}^2}{U_{1D}}\right) \frac{\partial^2 c_{11D}}{\partial z_D^{\,2}} = 0
\end{aligned} \qquad \text{(C-71)}$$

Dividing through all terms in the equation by the first term gives

$$\begin{aligned}
&\frac{\partial (C_{11D} S_{1D})}{\partial t_D} + \frac{\phi t_2^{*} C_{112}^{*} S_{11}^{*}}{\phi t_2^{*} C_{112}^{*} S_{12}^{*}} \frac{\partial (C_{11D})}{\partial t_D} \\
&+ \frac{t_2^{*} C_{112}^{*} U_{X12}^{*}}{\phi C_{112}^{*} S_{12}^{*} x_2^{*}} \frac{\partial (C_{11D} U_{X1D})}{\partial x_D} + \frac{t_2^{*} C_{112}^{*} U_{Z12}^{*}}{\phi C_{112}^{*} S_{12}^{*} z_2^{*}} \frac{\partial (C_{11D} U_{Z1D})}{\partial z} \\
&- \frac{t_2^{*} U_{X12}^{*\,2} \alpha_L}{\phi S_{12}^{*} x_2^{*2} U_{12}^{*}} \left(\frac{U_{XD}^2}{U_{1D}}\right) \frac{\partial^2 C_{11D}}{\partial x_D^{\,2}} - \frac{t_2^{*} U_{Z12}^{*\,2} \alpha_T}{\phi S_{12}^{*} x_2^{*2} U_{12}^{*}} \left(\frac{U_{ZD}^2}{U_{1D}}\right) \frac{\partial^2 C_{11D}}{\partial x_D^{\,2}} \\
&- \frac{t_2^{*} U_{Z12}^{*\,2} \alpha_L}{\phi S_{12}^{*} z_2^{*2} U_{12}^{*}} \left(\frac{U_{ZD}^2}{U_{1D}}\right) \frac{\partial^2 C_{11D}}{\partial z_D^{\,2}} - \frac{t_2^{*} U_{X12}^{*\,2} \alpha_T}{\phi S_{12}^{*} z_2^{*2} U_{12}^{*}} \left(\frac{U_{XD}^2}{U_{1D}}\right) \frac{\partial^2 C_{11D}}{\partial z_D^{\,2}} = 0
\end{aligned} \qquad \text{(C-72)}$$

The following identify scaling groups:

$$\begin{aligned}
&\frac{\partial (C_{11D} S_{1D})}{\partial t_D} + \frac{S_{11}^{*}}{S_{12}^{*}} \frac{\partial (C_{11D})}{\partial t_D} \\
&+ \frac{t_2^{*} C_{112}^{*} U_{X12}^{*}}{\phi C_{112}^{*} S_{12}^{*} x_2^{*}} \frac{\partial (C_{11D} U_{X1D})}{\partial x_D} + \frac{t_2^{*} C_{112}^{*} U_{Z12}^{*}}{\phi C_{112}^{*} S_{12}^{*} z_2^{*}} \frac{\partial (C_{11D} U_{Z1D})}{\partial z} \\
&- \frac{t_2^{*} C_{112}^{*} U_{X12}^{*\,2} \alpha_L}{\phi C_{112}^{*} S_{12}^{*} x_2^{*2} U_{12}^{*}} \left(\frac{U_{X1D}^2}{U_{1D}}\right) \frac{\partial^2 C_{11D}}{\partial x_D^{\,2}} - \frac{t_2^{*} C_{112}^{*} U_{Z12}^{*\,2} \alpha_T}{\phi C_{112}^{*} S_{12}^{*} x_2^{*2} U_{12}^{*}} \left(\frac{U_{Z1D}^2}{U_{1D}}\right) \frac{\partial^2 C_{11D}}{\partial x_D^{\,2}} \\
&- \frac{t_2^{*} C_{112}^{*} U_{Z12}^{*\,2} \alpha_L}{\phi C_{112}^{*} S_{12}^{*} z_2^{*2} U_{12}^{*}} \left(\frac{U_{Z1D}^2}{U_{1D}}\right) \frac{\partial^2 C_{11D}}{\partial z_D^{\,2}} - \frac{t_2^{*} C_{112}^{*} U_{X12}^{*\,2} \alpha_T}{\phi C_{112}^{*} S_{12}^{*} z_2^{*2} U_{12}^{*}} \left(\frac{U_{X1D}^2}{U_{1D}}\right) \frac{\partial^2 C_{11D}}{\partial z_D^{\,2}} = 0
\end{aligned} \qquad \text{(C-73)}$$

The derived dimensionless groups will be

$$\frac{\partial(C_{11D}S_{1D})}{\partial t_D}+\overbrace{\left[\frac{S^*_{11}}{S^*_{12}}\right]}^{1}\frac{\partial(C_{11D})}{\partial t_D}$$
$$+\overbrace{\left[\frac{t^*_2U^*_{X12}}{\phi S^*_{12}x^*_2}\right]}^{2}\frac{\partial(C_{11D}U_{X1D})}{\partial x_D}+\overbrace{\left[\frac{t^*_2U^*_{Z12}}{\phi S^*_{12}z^*_2}\right]}^{3}\frac{\partial(C_{11D}U_{Z1D})}{\partial z}$$
$$-\overbrace{\left[\frac{t^*_2U^{*\,2}_{X12}\alpha_L}{\phi S^*_{12}x^{*2}_2U^*_{12}}\right]}^{4}\left(\frac{U^2_{X1D}}{U_{1D}}\right)\frac{\partial^2C_{11D}}{\partial x_D^{\,2}}-\overbrace{\left[\frac{t^*_2U^{*\,2}_{Z12}\alpha_T}{\phi S^*_{12}x^{*2}_2U^*_{12}}\right]}^{5}\left(\frac{U^2_{Z1D}}{U_{1D}}\right)\frac{\partial^2C_{11D}}{\partial x_D^{\,2}} \qquad \text{(C-74)}$$
$$-\overbrace{\left[\frac{t^*_2U^{*\,2}_{Z12}\alpha_L}{\phi S^*_{12}z^{*2}_2U^*_{12}}\right]}^{6}\left(\frac{U^2_{Z1D}}{U_{1D}}\right)\frac{\partial^2C_{11D}}{\partial z_D^{\,2}}-\overbrace{\left[\frac{t^*_2U^{*\,2}_{X12}\alpha_T}{\phi S^*_{12}z^{*2}_2U^*_{12}}\right]}^{7}\left(\frac{U^2_{X1D}}{U_{1D}}\right)\frac{\partial^2C_{11D}}{\partial z_D^{\,2}}=0 .$$

Overall composition balance for Component 5

$$\phi\frac{\partial(\rho_1\omega_{51}S_1)}{\partial t}+\frac{\partial(\rho_1\omega_{51}U_{X1})}{\partial x}+\frac{\partial(\rho_1\omega_{51}U_{Z1})}{\partial z}-\left(\frac{\alpha_LU^2_{X1}+\alpha_TU^2_{Z1}}{U_1}\right)\frac{\partial^2\rho_1\omega_{51}}{\partial x^2}-\left(\frac{\alpha_LU^2_{Z1}+\alpha_TU^2_{X1}}{U_1}\right)\frac{\partial^2\rho_1\omega_{51}}{\partial z^2}=0 .$$

(C-75)

The substitution of $\rho_5\omega_{51}$ with c_{51} yields

$$\phi\frac{\partial(c_{51}S_1)}{\partial t}+\frac{\partial(c_{51}U_{X1})}{\partial x}+\frac{\partial(c_{51}U_{Z1})}{\partial z}-\left(\frac{\alpha_LU^2_{X1}+\alpha_TU^2_{Z1}}{U_1}\right)\frac{\partial^2c_{51}}{\partial x^2}-\left(\frac{\alpha_LU^2_{Z1}+\alpha_TU^2_{X1}}{U_1}\right)\frac{\partial^2c_{51}}{\partial z^2}=0 . \qquad \text{(C-76)}$$

Incorporating the dimensionless form of the variables into Eq. gives

$$\frac{\phi c^*_{512}S^*_{12}}{t^*_2}\frac{\partial(c_{51D}S_{1D})}{\partial t_D}+\frac{\phi c^*_{512}S^*_{11}}{t^*_2}\frac{\partial(c_{51D})}{\partial t_D}$$
$$+\frac{c^*_{512}U^*_{X12}}{x^*_2}\frac{\partial(c_{51D}U_{X1D})}{\partial x_D}+\frac{c^*_{512}U^*_{Z12}}{z^*_2}\frac{\partial(c_{51D}U_{Z1D})}{\partial z}$$
$$-\frac{c^*_{512}U^{*\,2}_{X12}\alpha_L}{x^{*2}_2U^*_{12}}\left(\frac{U^2_{X1D}}{U_{1D}}\right)\frac{\partial^2c_{51D}}{\partial x_D^{\,2}}-\frac{c^*_{512}U^{*\,2}_{Z12}\alpha_T}{x^{*2}_2U^*_{12}}\left(\frac{U^2_{Z1D}}{U_{1D}}\right)\frac{\partial^2c_{51D}}{\partial x_D^{\,2}} \qquad \text{(C-77)}$$
$$-\frac{c^*_{512}U^{*\,2}_{Z12}\alpha_L}{z^{*2}_2U^*_{12}}\left(\frac{U^2_{Z1D}}{U_{1D}}\right)\frac{\partial^2c_{51D}}{\partial z_D^{\,2}}-\frac{c^*_{512}U^{*\,2}_{X12}\alpha_{T2}}{z^{*2}_2U^*_{12}}\left(\frac{U^2_{X1D}}{U_{1D}}\right)\frac{\partial^2c_{51D}}{\partial z_D^{\,2}}=0 .$$

Dividing through all terms in the equation by the first term gives

$$\frac{\partial(c_{51D}S_{1D})}{\partial t_D}+\frac{\phi t_2^* c_{512}^* S_{11}^*}{\phi t_2^* c_{512}^* S_{12}^*}\frac{\partial(c_{51D})}{\partial t_D}$$
$$+\frac{t_2^* c_{512}^* U_{X12}^*}{\phi c_{512}^* S_{12}^* x_2^*}\frac{\partial(c_{51D}U_{X1D})}{\partial x_D}+\frac{t_2^* c_{512}^* U_{Z12}^*}{\phi c_{512}^* S_{12}^* z_2^*}\frac{\partial(c_{11D}U_{Z1D})}{\partial z}$$
$$-\frac{t_2^* U_{X12}^{*2}\alpha_L}{\phi S_{12}^* x_2^{*2} U_{12}^*}\left(\frac{U_{XD}^2}{U_{1D}}\right)\frac{\partial^2 c_{51D}}{\partial x_D^2}-\frac{t_2^* U_{Z12}^{*2}\alpha_T}{\phi S_{12}^* x_2^{*2} U_{12}^*}\left(\frac{U_{ZD}^2}{U_{1D}}\right)\frac{\partial^2 c_{51D}}{\partial x_D^2} \qquad \text{(C-78)}$$
$$-\frac{t_2^* U_{Z12}^{*2}\alpha_L}{\phi S_{12}^* z_2^{*2} U_{12}^*}\left(\frac{U_{ZD}^2}{U_{1D}}\right)\frac{\partial^2 c_{51D}}{\partial z_D^2}-\frac{t_2^* U_{X12}^{*2}\alpha_T}{\phi S_{12}^* z_2^{*2} U_{12}^*}\left(\frac{U_{XD}^2}{U_{1D}}\right)\frac{\partial^2 c_{51D}}{\partial z_D^2}=0$$

.

Rearranging the equations gives

$$\frac{\partial(c_{51D}S_{1D})}{\partial t_D}+\frac{S_{11}^*}{S_{12}^*}\frac{\partial(c_{51D})}{\partial t_D}$$
$$+\frac{t_2^* c_{512}^* U_{X12}^*}{\phi c_{512}^* S_{12}^* x_2^*}\frac{\partial(c_{51D}U_{X1D})}{\partial x_D}+\frac{t_2^* c_{512}^* U_{Z12}^*}{\phi c_{512}^* S_{12}^* z_2^*}\frac{\partial(c_{51D}U_{Z1D})}{\partial z}$$
$$-\frac{t_2^* c_{512}^* U_{X12}^{*2}\alpha_L}{\phi c_{512}^* S_{12}^* x_2^{*2} U_{12}^*}\left(\frac{U_{X1D}^2}{U_{1D}}\right)\frac{\partial^2 c_{51D}}{\partial x_D^2}-\frac{t_2^* c_{512}^* U_{Z12}^{*2}\alpha_T}{\phi c_{512}^* S_{12}^* x_2^{*2} U_{12}^*}\left(\frac{U_{Z1D}^2}{U_{1D}}\right)\frac{\partial^2 c_{51D}}{\partial x_D^2} \qquad \text{(C-79)}$$
$$-\frac{t_2^* c_{512}^* U_{Z12}^{*2}\alpha_L}{\phi c_{512}^* S_{12}^* z_2^{*2} U_{12}^*}\left(\frac{U_{Z1D}^2}{U_{1D}}\right)\frac{\partial^2 c_{51D}}{\partial z_D^2}-\frac{t_2^* c_{512}^* U_{X12}^{*2}\alpha_T}{\phi c_{512}^* S_{12}^* z_2^{*2} U_{12}^*}\left(\frac{U_{X1D}^2}{U_{1D}}\right)\frac{\partial^2 c_{51D}}{\partial z_D^2}=0$$

.

Identifying dimensionless scaling groups,

$$\frac{\partial(C_{51D}S_{1D})}{\partial t_D}+\overbrace{\left[\frac{S_{11}^*}{S_{12}^*}\right]}^{8}\frac{\partial(C_{51D})}{\partial t_D}$$
$$+\overbrace{\left[\frac{t_2^* U_{X12}^*}{\phi S_{12}^* x_2^*}\right]}^{9}\frac{\partial(C_{51D}U_{X1D})}{\partial x_D}+\overbrace{\left[\frac{t_2^* U_{Z12}^*}{\phi S_{12}^* z_2^*}\right]}^{10}\frac{\partial(C_{51D}U_{Z1D})}{\partial z}$$
$$-\overbrace{\left[\frac{t_2^* U_{X12}^{*2}\alpha_L}{\phi S_{12}^* x_2^{*2} U_{12}^*}\right]}^{11}\left(\frac{U_{X1D}^2}{U_{1D}}\right)\frac{\partial^2 C_{51D}}{\partial x_D^2}-\overbrace{\left[\frac{t_2^* U_{Z12}^{*2}\alpha_T}{\phi S_{12}^* x_2^{*2} U_{12}^*}\right]}^{12}\left(\frac{U_{Z1D}^2}{U_{1D}}\right)\frac{\partial^2 C_{51D}}{\partial x_D^2} \qquad \text{(C-80)}$$
$$-\overbrace{\left[\frac{t_2^* U_{Z12}^{*2}\alpha_L}{\phi S_{12}^* z_2^{*2} U_{12}^*}\right]}^{13}\left(\frac{U_{Z1D}^2}{U_{1D}}\right)\frac{\partial^2 C_{51D}}{\partial z_D^2}-\overbrace{\left[\frac{t_2^* U_{X12}^{*2}\alpha_T}{\phi S_{12}^* z_2^{*2} U_{12}^*}\right]}^{14}\left(\frac{U_{X1D}^2}{U_{1D}}\right)\frac{\partial^2 C_{51D}}{\partial z_D^2}=0$$

.

Overall composition balance for Component 4

$$\phi\frac{\partial(\rho_3\omega_{43}S_3)}{\partial t}+\frac{\partial(\rho_3\omega_{43}U_{X3})}{\partial x}+\frac{\partial(\rho_3\omega_{43}U_{Z3})}{\partial z}-(\frac{\alpha_L U_{X3}^2+\alpha_T U_{Z3}^2}{U_3})\frac{\partial^2\rho_3\omega_{43}}{\partial x^2}-(\frac{\alpha_L U_{Z3}^2+\alpha_T U_{X3}^2}{U_3})\frac{\partial^2\rho_3\omega_{43}}{\partial z^2}=0 \quad \text{(C-81)}$$

The substitution of $\rho_3\omega_{43}$ with c_{43} yields

$$\frac{\partial(\phi c_{43}S_3)}{\partial t}+\frac{\partial(c_{43}U_{X3})}{\partial x}+\frac{\partial(c_{43}U_{Z3})}{\partial z}-(\frac{\alpha_L U_{X3}^2+\alpha_T U_{Z3}^2}{U_3})\frac{\partial^2 c_{43}}{\partial x^2}-(\frac{\alpha_L U_{Z3}^2+\alpha_T U_{X3}^2}{U_3})\frac{\partial^2 c_{43}}{\partial z^2}=0 \quad \text{(C-82)}$$

Incorporating the dimensionless form of the variables into Eq. gives

$$\begin{aligned}&\frac{\phi c_{432}^* S_{32}^*}{t_2^*}\frac{\partial(c_{43D}S_{3D})}{\partial t_D}+\frac{\phi c_{432}^* S_{31}^*}{t_2^*}\frac{\partial(c_{43D})}{\partial t_D}\\&+\frac{c_{432}^* U_{X32}^*}{x_2^*}\frac{\partial(c_{43D}U_{X3D})}{\partial x_D}+\frac{c_{432}^* U_{X32}^*}{x_2^*}\frac{\partial(U_{X3D})}{\partial x_D}\\&+\frac{c_{432}^* U_{Z32}^*}{z_2^*}\frac{\partial(c_{43D}U_{Z3D})}{\partial z}+\frac{c_{432}^* U_{Z32}^*}{z_2^*}\frac{\partial(U_{Z3D})}{\partial z}\\&-\frac{c_{432}^* U_{X32}^{*2}\alpha_L}{x_2^{*2}U_{32}^*}(\frac{U_{X3D}^2}{U_{3D}})\frac{\partial^2 c_{43D}}{\partial x_D^2}-\frac{c_{432}^* U_{Z32}^{*2}\alpha_T}{x_2^{*2}U_{32}^*}(\frac{U_{Z3D}^2}{U_{3D}})\frac{\partial^2 c_{43D}}{\partial x_D^2}\\&-\frac{c_{432}^* U_{Z32}^{*2}\alpha_L}{z_2^{*2}U_{32}^*}(\frac{U_{Z3D}^2}{U_{3D}})\frac{\partial^2 c_{43D}}{\partial z_D^2}-\frac{c_{432}^* U_{X32}^{*2}\alpha_T}{z_2^{*2}U_{32}^*}(\frac{U_{X3D}^2}{U_{3D}})\frac{\partial^2 c_{43D}}{\partial z_D^2}=0\end{aligned} \quad \text{(C-83)}$$

Dividing through all terms in the equation by the first term gives

$$\begin{aligned}&\frac{\partial(C_{43D}S_{3D})}{\partial t_D}+\frac{S_{31}^*}{S_{32}^*}\frac{\partial(C_{43D})}{\partial t_D}\\&+\frac{t_2^* C_{432}^* U_{X12}^*}{\phi C_{432}^* S_{12}^* x_2^*}\frac{\partial(C_{43D}U_{X3D})}{\partial x_D}+\frac{t_2^* C_{431}^* U_{X32}^*}{\phi C_{432}^* S_{32}^* x_2^*}\frac{\partial(U_{X3D})}{\partial x_D}\\&+\frac{t_2^* C_{432}^* U_{Z32}^*}{\phi C_{432}^* S_{32}^* z_2^*}\frac{\partial(C_{43D}U_{Z3D})}{\partial z}+\frac{t_2^* C_{431}^* U_{Z32}^*}{\phi C_{432}^* S_{32}^* z_2^*}\frac{\partial(U_{Z3D})}{\partial z}\\&-\frac{t_2^* C_{432}^* U_{X32}^{*2}\alpha_L}{\phi C_{432}^* S_{12}^* x_2^{*2}U_{32}^*}(\frac{U_{X3D}^2}{U_{3D}})\frac{\partial^2 C_{43D}}{\partial x_D^2}-\frac{t_2^* C_{432}^* U_{Z32}^{*2}\alpha_T}{\phi C_{432}^* S_{32}^* x_2^{*2}U_{32}^*}(\frac{U_{Z3D}^2}{U_{3D}})\frac{\partial^2 C_{43D}}{\partial x_D^2}\\&-\frac{t_2^* C_{432}^* U_{Z32}^{*2}\alpha_L}{\phi C_{432}^* S_{12}^* z_2^{*2}U_{32}^*}(\frac{U_{Z3D}^2}{U_{3D}})\frac{\partial^2 C_{43D}}{\partial z_D^2}-\frac{t_2^* C_{432}^* U_{X32}^{*2}\alpha_T}{\phi C_{432}^* S_{32}^* z_2^{*2}U_{32}^*}(\frac{U_{X3D}^2}{U_{3D}})\frac{\partial^2 C_{43D}}{\partial z_D^2}=0\end{aligned} \quad \text{(C-84)}$$

The following identify the scaling groups

$$\frac{\partial(C_{43D}S_{3D})}{\partial t_D}+\overbrace{\left[\frac{S_{31}^*}{S_{32}^*}\right]}^{15}\frac{\partial(C_{43D})}{\partial t_D}$$
$$+\overbrace{\left[\frac{t_2^*U_{X32}^*}{\phi S_{32}^* x_2^*}\right]}^{16}\frac{\partial(C_{43D}U_{X3D})}{\partial x_D}$$
$$+\overbrace{\left[\frac{t_2^*U_{Z32}^*}{\phi S_{32}^* z_2^*}\right]}^{17}\frac{\partial(C_{43D}U_{Z3D})}{\partial z} \qquad \text{(C-85)}$$
$$-\overbrace{\left[\frac{t_2^*U_{X32}^{*\,2}\alpha_L}{\phi S_{32}^* x_2^{*2}U_{32}^*}\right]}^{18}\left(\frac{U_{X3D}^2}{U_{3D}}\right)\frac{\partial^2 C_{43D}}{\partial x_D^{\,2}}-\overbrace{\left[\frac{t_2^*U_{Z32}^{*\,2}\alpha_T}{\phi S_{32}^* x_2^{*2}U_{32}^*}\right]}^{19}\left(\frac{U_{Z3D}^2}{U_{3D}}\right)\frac{\partial^2 C_{43D}}{\partial x_D^{\,2}}$$
$$-\overbrace{\left[\frac{t_2^*U_{Z32}^{*\,2}\alpha_L}{\phi S_{32}^* z_2^{*2}U_{32}^*}\right]}^{20}\left(\frac{U_{Z3D}^2}{U_{3D}}\right)\frac{\partial^2 C_{43D}}{\partial z_D^{\,2}}-\overbrace{\left[\frac{t_2^*U_{X32}^{*\,2}\alpha_T}{\phi S_{32}^* z_2^{*2}U_{32}^*}\right]}^{21}\left(\frac{U_{X3D}^2}{U_{3D}}\right)\frac{\partial^2 C_{43D}}{\partial z_D^{\,2}}=0 \;.$$

Overall composition balance for Component 2

$$\phi\frac{\partial(\rho_1\omega_{21}S_1+\rho_2\omega_{22}S_2)}{\partial t}+\frac{\partial(\rho_1\omega_{21}U_{X1}+\rho_2\omega_{22}U_{X2})}{\partial x}+\frac{\partial(\rho_1\omega_{21}U_{Z1}+\rho_2\omega_{22}U_{Z2})}{\partial z}$$
$$-\left(\frac{\alpha_L U_{X1}^2+\alpha_T U_{Z1}^2}{U_1}\right)\frac{\partial^2\rho_1\omega_{21}}{\partial x^2}-\left(\frac{\alpha_L U_{X2}^2+\alpha_T U_{Z2}^2}{U_2}\right)\frac{\partial^2\rho_2\omega_{22}}{\partial x^2}$$
$$-\left(\frac{\alpha_L U_{Z1}^2+\alpha_T U_{X1}^2}{U_1}\right)\frac{\partial^2\rho_1\omega_{21}}{\partial z^2}-\left(\frac{\alpha_L U_{Z2}^2+\alpha_T U_{X2}^2}{U_2}\right)\frac{\partial^2\rho_2\omega_{22}}{\partial z^2}=0 \;. \qquad \text{(C-86)}$$

The substitution of $\rho_1\omega_{21}$ and $\rho_2\omega_{22}$ with c_{21} and c_{22} yields

$$\frac{\partial(\phi C_{21}S_1+\phi C_{22}S_2)}{\partial t}+\frac{\partial(C_{21}U_{X1}+C_{22}U_{X2})}{\partial x}+\frac{\partial(C_{21}U_{Z1}+C_{22}U_{Z2})}{\partial z}$$
$$-\left(\frac{\alpha_L U_{X1}^2+\alpha_T U_{Z1}^2}{U_1}\right)\frac{\partial^2 C_{21}}{\partial x^2}-\left(\frac{\alpha_L U_{X2}^2+\alpha_T U_{Z2}^2}{U_2}\right)\frac{\partial^2 C_{22}}{\partial x^2}$$
$$-\left(\frac{\alpha_L U_{Z1}^2+\alpha_T U_{X1}^2}{U_1}\right)\frac{\partial^2 C_{21}}{\partial z^2}-\left(\frac{\alpha_L U_{Z2}^2+\alpha_T U_{X2}^2}{U_2}\right)\frac{\partial^2 C_{22}}{\partial z^2}=0 \;. \qquad \text{(C-87)}$$

Incorporating the dimensionless form of the variables into Eq. gives

$$\frac{\phi C^*_{212} S^*_{12}}{t^*_2}\frac{\partial(C_{21D}S_{1D})}{\partial t_D}+\frac{\phi C^*_{212} S^*_{11}}{t^*_2}\frac{\partial(C_{21D})}{\partial t_D}+\frac{\phi C^*_{222} S^*_{22}}{t^*_2}\frac{\partial(C_{22D}S_{2D})}{\partial t_D}$$
$$+\frac{C^*_{212} U^*_{X12}}{x^*_2}\frac{\partial(C_{21D}U_{X1D})}{\partial x_D}+\frac{C^*_{222} U^*_{X22}}{x^*_2}\frac{\partial(C_{22D}U_{X2D})}{\partial x_D}$$
$$+\frac{C^*_{212} U^*_{Z12}}{z^*_2}\frac{\partial(C_{21D}U_{Z1D})}{\partial z_D}+\frac{C^*_{222} U^*_{Z22}}{z^*_2}\frac{\partial(C_{22D}U_{Z2D})}{\partial z_D}$$
$$-\frac{C^*_{212} {U^*_{X12}}^2\alpha_L}{{x^*_2}^2 U^*_{12}}\left(\frac{U^2_{X1D}}{U_{1D}}\right)\frac{\partial^2 C_{21D}}{\partial {x_D}^2}-\frac{C^*_{222} {U^*_{X22}}^2\alpha_L}{{x^*_2}^2 U^*_{22}}\left(\frac{U^2_{X2D}}{U_{2D}}\right)\frac{\partial^2 C_{22D}}{\partial {x_D}^2}$$
$$-\frac{C^*_{212} {U^*_{Z12}}^2\alpha_T}{{x^*_2}^2 U^*_{12}}\left(\frac{U^2_{Z1D}}{U_{1D}}\right)\frac{\partial^2 C_{21D}}{\partial {x_D}^2}-\frac{C^*_{222} {U^*_{Z22}}^2\alpha_T}{{x^*_2}^2 U^*_{22}}\left(\frac{U^2_{Z2D}}{U_{2D}}\right)\frac{\partial^2 C_{22D}}{\partial {x_D}^2}$$
$$-\frac{C^*_{212} {U^*_{Z12}}^2\alpha_L}{{z^*_2}^2 U^*_{12}}\left(\frac{U^2_{Z1D}}{U_{1D}}\right)\frac{\partial^2 C_{21D}}{\partial {z_D}^2}-\frac{C^*_{222} {U^*_{Z22}}^2\alpha_L}{{z^*_2}^2 U^*_{22}}\left(\frac{U^2_{Z2D}}{U_{2D}}\right)\frac{\partial^2 C_{22D}}{\partial {z_D}^2}$$
$$-\frac{C^*_{212} {U^*_{X12}}^2\alpha_T}{{z^*_2}^2 U^*_{12}}\left(\frac{U^2_{X1D}}{U_{1D}}\right)\frac{\partial^2 C_{21D}}{\partial {z_D}^2}-\frac{C^*_{222} {U^*_{X22}}^2\alpha_T}{{z^*_2}^2 U^*_{22}}\left(\frac{U^2_{X2D}}{U_{2D}}\right)\frac{\partial^2 C_{22D}}{\partial {z_D}^2}\quad=0\quad. \tag{C-88}$$

Dividing through all terms in the equation by the first term gives

$$\frac{t^*_2\phi C^*_{212} S^*_{12}}{t^*_2\phi C^*_{212} S^*_{12}}\frac{\partial(C_{21D}S_{1D})}{\partial t_D}+\frac{t^*_2\phi C^*_{212} S^*_{11}}{\phi C^*_{212} S^*_{12} t^*_2}\frac{\partial(C_{21D})}{\partial t_D}+\frac{t^*_2\phi C^*_{222} S^*_{22}}{\phi C^*_{212} S^*_{12} t^*_2}\frac{\partial(C_{22D}S_{2D})}{\partial t_D}$$
$$+\frac{t^*_2 C^*_{212} U^*_{X12}}{\phi C^*_{212} S^*_{12} x^*_2}\frac{\partial(C_{21D}U_{X1D})}{\partial x_D}+\frac{t^*_2 C^*_{222} U^*_{X22}}{\phi C^*_{212} S^*_{12} x^*_2}\frac{\partial(C_{22D}U_{X2D})}{\partial x_D}$$
$$+\frac{t^*_2 C^*_{212} U^*_{Z12}}{\phi C^*_{212} S^*_{12} z^*_2}\frac{\partial(C_{21D}U_{Z1D})}{\partial z_D}+\frac{t^*_2 C^*_{222} U^*_{Z22}}{\phi C^*_{212} S^*_{12} z^*_2}\frac{\partial(C_{22D}U_{Z2D})}{\partial z_D}$$
$$-\frac{t^*_2 C^*_{212} {U^*_{X12}}^2\alpha_L}{\phi C^*_{212} S^*_{12} {x^*_2}^2 U^*_{12}}\left(\frac{U^2_{X1D}}{U_{1D}}\right)\frac{\partial^2 C_{21D}}{\partial {x_D}^2}-\frac{t^*_2 C^*_{222} {U^*_{X22}}^2\alpha_L}{\phi C^*_{212} S^*_{12} {x^*_2}^2 U^*_{22}}\left(\frac{U^2_{X2D}}{U_{2D}}\right)\frac{\partial^2 C_{22D}}{\partial {x_D}^2}$$
$$-\frac{t^*_2 C^*_{212} {U^*_{Z12}}^2\alpha_T}{\phi C^*_{212} S^*_{12} {x^*_2}^2 U^*_{12}}\left(\frac{U^2_{Z1D}}{U_{1D}}\right)\frac{\partial^2 C_{21D}}{\partial {x_D}^2}-\frac{t^*_2 C^*_{222} {U^*_{Z22}}^2\alpha_T}{\phi C^*_{212} S^*_{12} {x^*_2}^2 U^*_{22}}\left(\frac{U^2_{Z2D}}{U_{2D}}\right)\frac{\partial^2 C_{22D}}{\partial {x_D}^2}$$
$$-\frac{t^*_2 C^*_{212} {U^*_{Z12}}^2\alpha_L}{\phi C^*_{212} S^*_{12} {z^*_2}^2 U^*_{12}}\left(\frac{U^2_{Z1D}}{U_{1D}}\right)\frac{\partial^2 C_{21D}}{\partial {z_D}^2}-\frac{t^*_2 C^*_{222} {U^*_{Z22}}^2\alpha_L}{\phi C^*_{212} S^*_{12} {z^*_2}^2 U^*_{22}}\left(\frac{U^2_{Z2D}}{U_{2D}}\right)\frac{\partial^2 C_{22D}}{\partial {z_D}^2}$$
$$-\frac{t^*_2 C^*_{212} {U^*_{X12}}^2\alpha_T}{\phi C^*_{212} S^*_{12} {z^*_2}^2 U^*_{12}}\left(\frac{U^2_{X1D}}{U_{1D}}\right)\frac{\partial^2 C_{21D}}{\partial {z_D}^2}-\frac{t^*_2 C^*_{222} {U^*_{X22}}^2\alpha_T}{\phi C^*_{212} S^*_{12} {z^*_2}^2 U^*_{22}}\left(\frac{U^2_{X2D}}{U_{2D}}\right)\frac{\partial^2 C_{22D}}{\partial {z_D}^2}=0\,. \tag{C-89}$$

The following identify the scaling groups:

$$\frac{\partial(C_{21D}S_{1D})}{\partial t_D}+\overbrace{\left[\frac{S^*_{11}}{S^*_{12}}\right]}^{22}\frac{\partial(C_{21D})}{\partial t_D}+\overbrace{\left[\frac{C^*_{222}S^*_{22}}{C^*_{212}S^*_{12}}\right]}^{23}\frac{\partial(C_{22D}S_{2D})}{\partial t_D}$$
$$+\overbrace{\left[\frac{t^*_2U^*_{X12}}{\phi S^*_{12}x^*_2}\right]}^{24}\frac{\partial(C_{21D}U_{X1D})}{\partial x_D}+\overbrace{\left[\frac{t^*_2C^*_{222}U^*_{X22}}{\phi C^*_{212}S^*_{12}x^*_2}\right]}^{25}\frac{\partial(C_{22D}U_{X2D})}{\partial x_D}$$
$$+\overbrace{\left[\frac{t^*_2U^*_{Z12}}{\phi S^*_{12}z^*_2}\right]}^{26}\frac{\partial(C_{21D}U_{Z1D})}{\partial z_D}+\overbrace{\left[\frac{t^*_2C^*_{222}U^*_{Z22}}{\phi C^*_{212}S^*_{12}z^*_2}\right]}^{27}\frac{\partial(C_{22D}U_{Z2D})}{\partial z_D}$$
$$-\overbrace{\left[\frac{t^*_2U^{*2}_{X12}\alpha_L}{\phi S^*_{12}x^{*2}_2U^*_{12}}\right]}^{28}\left(\frac{U^2_{X1D}}{U_{1D}}\right)\frac{\partial^2C_{21D}}{\partial x_D^2}-\overbrace{\left[\frac{t^*_2C^*_{222}U^{*2}_{X22}\alpha_L}{\phi C^*_{212}S^*_{12}x^{*2}_2U^*_{22}}\right]}^{29}\left(\frac{U^2_{X2D}}{U_{2D}}\right)\frac{\partial^2C_{22D}}{\partial x_D^2}$$
$$-\overbrace{\left[\frac{t^*_2U^{*2}_{Z12}\alpha_T}{\phi S^*_{12}x^{*2}_2U^*_{12}}\right]}^{30}\left(\frac{U^2_{Z1D}}{U_{1D}}\right)\frac{\partial^2C_{21D}}{\partial x_D^2}-\overbrace{\left[\frac{t^*_2C^*_{222}U^{*2}_{Z22}\alpha_T}{\phi C^*_{212}S^*_{12}x^{*2}_2U^*_{22}}\right]}^{31}\left(\frac{U^2_{Z2D}}{U_{2D}}\right)\frac{\partial^2C_{22D}}{\partial x_D^2}$$
$$-\overbrace{\left[\frac{t^*_2U^{*2}_{Z12}\alpha_L}{\phi S^*_{12}z^{*2}_2U^*_{12}}\right]}^{32}\left(\frac{U^2_{Z1D}}{U_{1D}}\right)\frac{\partial^2C_{21D}}{\partial z_D^2}-\overbrace{\left[\frac{t^*_2C^*_{222}U^{*2}_{Z22}\alpha_L}{\phi C^*_{212}S^*_{12}z^{*2}_2U^*_{22}}\right]}^{33}\left(\frac{U^2_{Z2D}}{U_{2D}}\right)\frac{\partial^2C_{22D}}{\partial z_D^2}\quad .$$
$$-\overbrace{\left[\frac{t^*_2U^{*2}_{X12}\alpha_T}{\phi S^*_{12}z^{*2}_2U^*_{12}}\right]}^{34}\left(\frac{U^2_{X1D}}{U_{1D}}\right)\frac{\partial^2C_{21D}}{\partial z_D^2}-\overbrace{\left[\frac{t^*_2C^*_{222}U^{*2}_{X22}\alpha_T}{\phi C^*_{212}S^*_{12}z^{*2}_2U^*_{22}}\right]}^{35}\left(\frac{U^2_{X2D}}{U_{2D}}\right)\frac{\partial^2C_{22D}}{\partial z_D^2}=0$$

(C-90)

Conservation equation for Phase 1

$$\phi\frac{\partial(\rho_1S_1)}{\partial t}+\frac{\partial(\rho_1U_{X1})}{\partial x}+\frac{\partial(\rho_1U_{Z1})}{\partial z}=r_{m21}$$

. (C-91)

Incorporating the dimensionless form of the variables into Eq. gives

$$\phi\frac{\partial\left[(\rho^*_{12}\rho_{1D})(S^*_{12}S_{1D}+S^*_{11})\right]}{\partial(t^*_2t_{2D})}+\frac{\partial\left[(\rho^*_{12}\rho_{1D})(U^*_{X12}U_{X1D})\right]}{\partial x^*_2x_D}+\frac{\partial\left[(\rho^*_{12}\rho_{1D})(U^*_{Z12}U_{Z1D})\right]}{\partial z^*_2z_D}=r^*_{m212}r_{m21D}$$

. (C-92)

Rearranging the equations gives,

$$\left[\frac{\phi\rho_{12}^{*}S_{12}^{*}}{t_2^{*}}\right]\frac{\partial\rho_{1D}S_{1D}}{\partial t_{2D}}+\left[\frac{\phi\rho_{12}^{*}S_{11}^{*}}{t_2^{*}}\right]\frac{\partial\rho_{1D}}{\partial t_{2D}}+\left[\frac{\rho_{12}^{*}U_{X12}^{*}}{x_2^{*}}\right]\frac{\partial\rho_{1D}U_{X1D}}{\partial x_D}+\left[\frac{\rho_{12}^{*}U_{Z12}^{*}}{z_2^{*}}\right]\frac{\partial\rho_{1D}U_{Z1D}}{\partial z_D}=r_{m212}^{*}r_{m21D} \quad . \tag{C-93}$$

Dividing through all terms in the equation by the first term gives

$$\left[\frac{\phi\rho_{12}^{*}S_{12}^{*}}{t_2^{*}}\frac{t_2^{*}}{\phi\rho_{12}^{*}S_{12}^{*}}\right]\frac{\partial\rho_{1D}S_{1D}}{\partial t_{2D}}+\left[\frac{\phi\rho_{12}^{*}S_{11}^{*}}{t_2^{*}}\frac{t_2^{*}}{\phi\rho_{12}^{*}S_{12}^{*}}\right]\frac{\partial\rho_{1D}}{\partial t_{2D}}+\left[\frac{\rho_{12}^{*}U_{X12}^{*}}{x_2^{*}}\frac{t_2^{*}}{\phi\rho_{12}^{*}S_{12}^{*}}\right]\frac{\partial\rho_{1D}U_{X1D}}{\partial x_D}$$
$$+\left[\frac{\rho_{12}^{*}U_{Z12}^{*}}{z_2^{*}}\frac{t_2^{*}}{\phi\rho_{12}^{*}S_{12}^{*}}\right]\frac{\partial\rho_{1D}U_{Z1D}}{\partial z_D}=\left[r_{m212}^{*}\frac{t_2^{*}}{\phi\rho_{12}^{*}S_{12}^{*}}\right]r_{m21D} \quad . \tag{C-94}$$

The following identify the scaling groups

$$\frac{\partial\rho_{1D}S_{1D}}{\partial t_{2D}}+\overbrace{\left[\frac{S_{11}^{*}}{S_{12}^{*}}\right]}^{36}\frac{\partial\rho_{1D}}{\partial t_{2D}}+\overbrace{\left[\frac{U_{X12}^{*}t_2^{*}}{\phi S_{12}^{*}x_2^{*}}\right]}^{37}\frac{\partial\rho_{1D}U_{X1D}}{\partial x_D}+\overbrace{\left[\frac{U_{Z12}^{*}t_2^{*}}{z_2^{*}\phi S_{12}^{*}}\right]}^{38}\frac{\partial\rho_{1D}U_{Z1D}}{\partial z_D}=\overbrace{\left[\frac{r_{m212}^{*}t_2^{*}}{\phi\rho_{12}^{*}S_{12}^{*}}\right]}^{39}r_{m21D} \quad . \tag{C-95}$$

Conservation equation for Phase 2

$$\phi\frac{\partial(\rho_2S_2)}{\partial t}+\frac{\partial(\rho_2U_{X2})}{\partial x}+\frac{\partial(\rho_2U_{Z2})}{\partial z}=r_{m22}+r_{m32} \quad . \tag{C-96}$$

Incorporating the dimensionless form of the variables into Eq. gives

$$\phi\frac{\partial\left[(\rho_{22}^{*}\rho_{2D})(S_{22}^{*}S_{2D})\right]}{\partial(t_2^{*}t_{2D})}+\frac{\partial\left[(\rho_{22}^{*}\rho_{2D})(U_{X22}^{*}U_{X2D})\right]}{\partial x_2^{*}x_D}+\frac{\partial\left[(\rho_{22}^{*}\rho_{2D})(U_{Z22}^{*}U_{Z2D})\right]}{\partial z_2^{*}z_D}=r_{m222}^{*}r_{m22D}+r_{m322}^{*}r_{m32D} \quad . \tag{C-97}$$

Dividing through all terms in the equation by the first term gives

$$\left[\frac{\phi\rho_{22}^{*}S_{22}^{*}}{t_2^{*}}\right]\frac{\partial\rho_{2D}S_{2D}}{\partial t_{2D}}+\left[\frac{\rho_{22}^{*}U_{X22}^{*}}{x_2^{*}}\right]\frac{\partial\rho_{2D}U_{X2D}}{\partial x_D}+\left[\frac{\rho_{22}^{*}U_{Z22}^{*}}{z_2^{*}}\right]\frac{\partial\rho_{2D}U_{Z2D}}{\partial z_D}=r_{m222}^{*}r_{m22D}+r_{m322}^{*}r_{m32D}$$

Rearranging the equations gives,

$$\left[\frac{\phi\rho_{22}^{*}S_{22}^{*}}{t_2^{*}}\frac{t_2^{*}}{\phi\rho_{22}^{*}S_{22}^{*}}\right]\frac{\partial\rho_{2D}S_{2D}}{\partial t_{2D}}+\left[\frac{\rho_{22}^{*}U_{X22}^{*}}{x_2^{*}}\frac{t_2^{*}}{\phi\rho_{22}^{*}S_{22}^{*}}\right]\frac{\partial\rho_{2D}U_{X2D}}{\partial x_D}+\left[\frac{\rho_{22}^{*}U_{Z22}^{*}}{z_2^{*}}\frac{t_2^{*}}{\phi\rho_{22}^{*}S_{22}^{*}}\right]\frac{\partial\rho_{2D}U_{Z2D}}{\partial z_D}$$
$$=\left[\frac{r_{m222}^{*}t_2^{*}}{\phi\rho_{22}^{*}S_{22}^{*}}\right]r_{m22D}+\left[\frac{r_{m322}^{*}t_2^{*}}{\phi\rho_{22}^{*}S_{22}^{*}}\right]r_{m32D}\quad.\qquad\text{(C-98)}$$

The following identify the scaling groups

$$\frac{\partial\rho_{2D}S_{2D}}{\partial t_{2D}}+\overbrace{\left[\frac{U_{X22}^{*}t_2^{*}}{\phi S_{22}^{*}x_2^{*}}\right]}^{40}\frac{\partial\rho_{2D}U_{X2D}}{\partial x_D}+\overbrace{\left[\frac{U_{Z22}^{*}t_2^{*}}{z_2^{*}\phi S_{22}^{*}}\right]}^{41}\frac{\partial\rho_{2D}U_{Z2D}}{\partial z_D}=\overbrace{\left[\frac{r_{m222}^{*}t_2^{*}}{\phi\rho_{22}^{*}S_{22}^{*}}\right]}^{42}r_{m22D}+\overbrace{\left[\frac{r_{m322}^{*}t_2^{*}}{\phi\rho_{22}^{*}S_{22}^{*}}\right]}^{43}r_{m32D}$$

Continuity equation

$$\phi\frac{\partial\left[\rho_1S_1+\rho_2S_2+\rho_3S_3\right]}{\partial t}+\frac{\partial(\rho_1U_{X1}+\rho_2U_{X2}+\rho_3U_{X3})}{\partial x}+\frac{\partial(\rho_1U_{Z1}+\rho_2U_{Z2}+\rho_3U_{Z3})}{\partial z}=0$$

. (C-99)

Incorporating the dimensionless form of the variables into Eq. gives

$$\phi\frac{\partial\left[(\rho_{12}^{*}\rho_{1D}+\rho_1^{I})(S_{12}^{*}S_{1D}+S_{11}^{*})+(\rho_{22}^{*}\rho_{2D}+\rho_2^{J})(S_{22}^{*}S_{1D})+(\rho_{32}^{*}\rho_{3D}+\rho_3^{I})(S_{32}^{*}S_{3D}+S_{31}^{*})\right]}{\partial t_2^{*}t_D}$$
$$+\frac{\partial\left[(\rho_{12}^{*}\rho_{1D}+\rho_1^{I})(U_{X1}^{*}U_{X1D})+(\rho_{22}^{*}\rho_{2D}+\rho_2^{J})(U_{X2}^{*}U_{X2D})+(\rho_{32}^{*}\rho_{3D}+\rho_3^{I})(U_{X3}^{*}U_{X3D})\right]}{\partial(x_2^{*}x_D)}$$
$$+\frac{\partial\left[(\rho_{12}^{*}\rho_{1D}+\rho_1^{I})(U_{Z1}^{*}U_{Z1D})+(\rho_{22}^{*}\rho_{2D}+\rho_2^{J})(U_{Z2}^{*}U_{Z2D})+(\rho_{32}^{*}\rho_{3D}+\rho_3^{I})(U_{Z3}^{*}U_{Z3D})\right]}{\partial(z_2^{*}z_D)}=0$$

. (C-100)

Rearranging the equations gives,

$$\frac{\phi\rho_{12}^{*}S_{12}^{*}}{t_2^{*}}\frac{\partial(\rho_{1D}S_{1D})}{\partial t_D}+\frac{\phi\rho_{12}^{*}S_{11}^{*}}{t_2^{*}}\frac{\partial(\rho_{1D})}{\partial t_D}+\frac{\phi\rho_1^{I}S_{12}^{*}}{t_2^{*}}\frac{\partial(S_{1D})}{\partial t_D}$$
$$+\frac{\phi\rho_{22}^{*}S_{22}^{*}}{t_2^{*}}\frac{\partial(\rho_{2D}S_{2D})}{\partial t_D}+\frac{\phi\rho_2^{J}S_{22}^{*}}{t_2^{*}}\frac{\partial(S_{2D})}{\partial t_D}$$
$$+\frac{\phi\rho_{32}^{*}S_{32}^{*}}{t_2^{*}}\frac{\partial(\rho_{3D}S_{3D})}{\partial t_D}+\frac{\phi\rho_{32}^{*}S_{31}^{*}}{t_2^{*}}\frac{\partial(\rho_{3D})}{\partial t_D}+\frac{\phi\rho_3^{I}S_{32}^{*}}{t_2^{*}}\frac{\partial(S_{3D})}{\partial t_D}$$
$$+\frac{\rho_{12}^{*}U_{X12}^{*}}{x_2^{*}}\frac{\partial(\rho_{1D}U_{X1D})}{\partial x_D}+\frac{\rho_1^{I}U_{X12}^{*}}{x_2^{*}}\frac{\partial(U_{X1D})}{\partial x_D}$$
$$+\frac{\rho_{22}^{*}U_{X22}^{*}}{x_2^{*}}\frac{\partial(\rho_{2D}U_{X2D})}{\partial x_D}+\frac{\rho_2^{J}U_{X22}^{*}}{x_2^{*}}\frac{\partial(U_{X2D})}{\partial x_D}$$
$$+\frac{\rho_{32}^{*}U_{X32}^{*}}{x_2^{*}}\frac{\partial(\rho_{3D}U_{X3D})}{\partial x_D}+\frac{\rho_3^{I}U_{X32}^{*}}{x_2^{*}}\frac{\partial(U_{X3D})}{\partial x_D}$$
$$+\frac{\rho_{12}^{*}U_{Z12}^{*}}{z_2^{*}}\frac{\partial(\rho_{1D}U_{Z1D})}{\partial z_D}+\frac{\rho_1^{I}U_{Z12}^{*}}{z_2^{*}}\frac{\partial(U_{Z1D})}{\partial z_D}$$
$$+\frac{\rho_{22}^{*}U_{Z22}^{*}}{z_2^{*}}\frac{\partial(\rho_{2D}U_{Z2D})}{\partial z_D}+\frac{\rho_2^{J}U_{Z22}^{*}}{z_2^{*}}\frac{\partial(U_{Z2D})}{\partial z_D}$$
$$+\frac{\rho_{32}^{*}U_{Z32}^{*}}{z_2^{*}}\frac{\partial(\rho_{3D}U_{Z3D})}{\partial z_D}+\frac{\rho_3^{I}U_{Z32}^{*}}{z_2^{*}}\frac{\partial(U_{Z3D})}{\partial z_D}=0\quad . \tag{C-101}$$

Dividing through all terms in Eq. (C-101) by the first term gives

$$\left[\frac{\phi\rho_{12}^{*}S_{12}^{*}}{t_2^{*}}\frac{t_2^{*}}{\phi\rho_{12}^{*}S_{12}^{*}}\right]\frac{\partial(\rho_{1D}S_{1D})}{\partial t_D}+\left[\frac{\phi\rho_{12}^{*}S_{11}^{*}}{t_2^{*}}\frac{t_2^{*}}{\phi\rho_{12}^{*}S_{12}^{*}}\right]\frac{\partial(\rho_{1D})}{\partial t_D}+\left[\frac{\phi\rho_{1}^{I}S_{12}^{*}}{t_2^{*}}\frac{t_2^{*}}{\phi\rho_{12}^{*}S_{12}^{*}}\right]\frac{\partial(S_{1D})}{\partial t_D}$$
$$+\left[\frac{\phi\rho_{22}^{*}S_{22}^{*}}{t_2^{*}}\frac{t_2^{*}}{\phi\rho_{12}^{*}S_{12}^{*}}\right]\frac{\partial(\rho_{2D}S_{2D})}{\partial t_D}+\left[\frac{\phi\rho_{2}^{J}S_{22}^{*}}{t_2^{*}}\frac{t_2^{*}}{\phi\rho_{12}^{*}S_{12}^{*}}\right]\frac{\partial(S_{2D})}{\partial t_D}$$
$$+\left[\frac{\phi\rho_{32}^{*}S_{32}^{*}}{t_2^{*}}\frac{t_2^{*}}{\phi\rho_{12}^{*}S_{12}^{*}}\right]\frac{\partial(\rho_{3D}S_{3D})}{\partial t_D}+\left[\frac{\phi\rho_{32}^{*}S_{31}^{*}}{t_2^{*}}\frac{t_2^{*}}{\phi\rho_{12}^{*}S_{12}^{*}}\right]\frac{\partial(\rho_{3D})}{\partial t_D}+\left[\frac{\phi\rho_{3}^{I}S_{32}^{*}}{t_2^{*}}\frac{t_2^{*}}{\phi\rho_{12}^{*}S_{12}^{*}}\right]\frac{\partial(S_{3D})}{\partial t_D}$$
$$+\left[\frac{\rho_{12}^{*}U_{X12}^{*}}{x_2^{*}}\frac{t_2^{*}}{\phi\rho_{12}^{*}S_{12}^{*}}\right]\frac{\partial(\rho_{1D}U_{X1D})}{\partial x_D}+\left[\frac{\rho_{1}^{I}U_{X12}^{*}}{x_2^{*}}\frac{t_2^{*}}{\phi\rho_{12}^{*}S_{12}^{*}}\right]\frac{\partial(U_{X1D})}{\partial x_D}$$
$$+\left[\frac{\rho_{22}^{*}U_{X22}^{*}}{x_2^{*}}\frac{t_2^{*}}{\phi\rho_{12}^{*}S_{12}^{*}}\right]\frac{\partial(\rho_{2D}U_{X2D})}{\partial x_D}+\left[\frac{\rho_{2}^{J}U_{X22}^{*}}{x_2^{*}}\frac{t_2^{*}}{\phi\rho_{12}^{*}S_{12}^{*}}\right]\frac{\partial(U_{X2D})}{\partial x_D}$$
$$+\left[\frac{\rho_{32}^{*}U_{X32}^{*}}{x_2^{*}}\frac{t_2^{*}}{\phi\rho_{12}^{*}S_{12}^{*}}\right]\frac{\partial(\rho_{3D}U_{X3D})}{\partial x_D}+\left[\frac{\rho_{3}^{I}U_{X32}^{*}}{x_2^{*}}\frac{t_2^{*}}{\phi\rho_{12}^{*}S_{12}^{*}}\right]\frac{\partial(U_{X3D})}{\partial x_D}$$
$$+\left[\frac{\rho_{12}^{*}U_{Z12}^{*}}{z_2^{*}}\frac{t_2^{*}}{\phi\rho_{12}^{*}S_{12}^{*}}\right]\frac{\partial(\rho_{1D}U_{Z1D})}{\partial z_D}+\left[\frac{\rho_{1}^{I}U_{Z12}^{*}}{z_2^{*}}\frac{t_2^{*}}{\phi\rho_{12}^{*}S_{12}^{*}}\right]\frac{\partial(U_{Z1D})}{\partial z_D}$$
$$+\left[\frac{\rho_{22}^{*}U_{Z22}^{*}}{z_2^{*}}\frac{t_2^{*}}{\phi\rho_{12}^{*}S_{12}^{*}}\right]\frac{\partial(\rho_{2D}U_{Z2D})}{\partial z_D}+\left[\frac{\rho_{2}^{J}U_{Z22}^{*}}{z_2^{*}}\frac{t_2^{*}}{\phi\rho_{12}^{*}S_{12}^{*}}\right]\frac{\partial(U_{Z2D})}{\partial z_D}$$
$$+\left[\frac{\rho_{32}^{*}U_{Z32}^{*}}{z_2^{*}}\frac{t_2^{*}}{\phi\rho_{12}^{*}S_{12}^{*}}\right]\frac{\partial(\rho_{3D}U_{Z3D})}{\partial z_D}+\left[\frac{\rho_{3}^{I}U_{Z32}^{*}}{z_2^{*}}\frac{t_2^{*}}{\phi\rho_{12}^{*}S_{12}^{*}}\right]\frac{\partial(U_{Z3D})}{\partial z_D}=0\ .$$

(C-102)

The following identify scaling groups

$$\frac{\partial(\rho_{1D}S_{1D})}{\partial t_D}+\overbrace{\left[\frac{S^*_{11}}{S^*_{12}}\right]}^{44}\frac{\partial(\rho_{1D})}{\partial t_D}+\overbrace{\left[\frac{\rho^I_1}{\rho^*_{12}}\right]}^{45}\frac{\partial(S_{1D})}{\partial t_D}$$
$$+\overbrace{\left[\frac{\rho^*_{22}S^*_{22}}{\rho^*_{12}S^*_{12}}\right]}^{46}\frac{\partial(\rho_{2D}S_{2D})}{\partial t_D}+\overbrace{\left[\frac{\rho^J_2S^*_{22}}{\rho^*_{12}S^*_{12}}\right]}^{47}\frac{\partial(S_{2D})}{\partial t_D}$$
$$+\overbrace{\left[\frac{\rho^*_{32}S^*_{32}}{\rho^*_{12}S^*_{12}}\right]}^{48}\frac{\partial(\rho_{3D}S_{3D})}{\partial t_D}+\overbrace{\left[\frac{\rho^*_{32}S^*_{31}}{\rho^*_{12}S^*_{12}}\right]}^{49}\frac{\partial(\rho_{3D})}{\partial t_D}+\overbrace{\left[\frac{\rho^I_3S^*_{32}}{\rho^*_{12}S^*_{12}}\right]}^{50}\frac{\partial(S_{3D})}{\partial t_D}$$
$$+\overbrace{\left[\frac{U^*_{X12}t^*_2}{x^*_2\phi S^*_{12}}\right]}^{51}\frac{\partial(\rho_{1D}U_{X1D})}{\partial x_D}+\overbrace{\left[\frac{\rho^I_1U^*_{X12}t^*_2}{x^*_2\phi\rho^*_{12}S^*_{12}}\right]}^{52}\frac{\partial(U_{X1D})}{\partial x_D}$$
$$+\overbrace{\left[\frac{\rho^*_{22}U^*_{X22}t^*_2}{x^*_2\phi\rho^*_{12}S^*_{12}}\right]}^{53}\frac{\partial(\rho_{2D}U_{X2D})}{\partial x_D}+\overbrace{\left[\frac{\rho^J_2U^*_{X22}t^*_2}{x^*_2\phi\rho^*_{12}S^*_{12}}\right]}^{54}\frac{\partial(U_{X2D})}{\partial x_D}$$
$$+\overbrace{\left[\frac{\rho^*_{32}U^*_{X32}t^*_2}{x^*_2\phi\rho^*_{12}S^*_{12}}\right]}^{55}\frac{\partial(\rho_{3D}U_{X3D})}{\partial x_D}+\overbrace{\left[\frac{\rho^I_3U^*_{X32}t^*_2}{x^*_2\phi\rho^*_{12}S^*_{12}}\right]}^{56}\frac{\partial(U_{X3D})}{\partial x_D}$$
$$+\overbrace{\left[\frac{U^*_{Z12}t^*_2}{z^*_2\phi S^*_{12}}\right]}^{57}\frac{\partial(\rho_{1D}U_{Z1D})}{\partial z_D}+\overbrace{\left[\frac{\rho^I_1U^*_{Z12}t^*_2}{z^*_2\phi\rho^*_{12}S^*_{12}}\right]}^{58}\frac{\partial(U_{Z1D})}{\partial z_D}$$
$$+\overbrace{\left[\frac{\rho^*_{22}U^*_{Z22}t^*_2}{z^*_2\phi\rho^*_{12}S^*_{12}}\right]}^{59}\frac{\partial(\rho_{2D}U_{Z2D})}{\partial z_D}+\overbrace{\left[\frac{\rho^J_2U^*_{Z22}t^*_2}{z^*_2\phi\rho^*_{12}S^*_{12}}\right]}^{60}\frac{\partial(U_{Z2D})}{\partial z_D}$$
$$+\overbrace{\left[\frac{\rho^*_{32}U^*_{Z32}t^*_2}{z^*_2\phi\rho^*_{12}S^*_{12}}\right]}^{61}\frac{\partial(\rho_{3D}U_{Z3D})}{\partial z_D}+\overbrace{\left[\frac{\rho^I_3U^*_{Z32}t^*_2}{z^*_2\phi\rho^*_{12}S^*_{12}}\right]}^{62}\frac{\partial(U_{Z3D})}{\partial z_D}=0\ .$$

(C-103)

Initial condition

Incorporating the dimensionless form of the variables into the initial condition and rearranging them, yields

$$\begin{cases} \omega_{51D} = \overbrace{\left[\frac{\omega_{51}^{I}}{\omega_{512}^{*}}\right]}^{63} \\ \omega_{43D} = \overbrace{\left[\frac{\omega_{43}^{I}}{\omega_{432}^{*}}\right]}^{64} \\ S_{3D} = \overbrace{\left[\frac{S_3^{I} - S_{3r}}{S_{32}^{*}}\right]}^{65} \\ S_{22}^{*} S_{2D} = 0 \end{cases} \quad @\ t_D t_2^{*} = 0 \,\forall x, z \tag{C-104}$$

Injection composition

Incorporating the dimensionless form of the variables into injection condition and rearranging them, yields

$$\begin{cases} \omega_{51D} = \overbrace{\left[\frac{\omega_{51}^{J}}{\omega_{512}^{*}}\right]}^{66} \\ \omega_{22D} = \overbrace{\left[\frac{1.0}{\omega_{222}^{*}}\right]}^{67} \end{cases} \quad @ \quad \begin{cases} \overbrace{\left[\frac{d_1 \mathrm{Sin}\beta}{x_2^{*}}\right]}^{68} \le x_D \le \overbrace{\left[\frac{d_1 \mathrm{Sin}\beta}{x_2^{*}}\right]}^{} + \overbrace{\left[\frac{w_1 \mathrm{Sin}\beta}{x_2^{*}}\right]}^{69} \\ \overbrace{\left[\frac{d_2 \mathrm{Cos}\beta}{z_2^{*}}\right]}^{70} \le z_D \le \overbrace{\left[\frac{d_2 \mathrm{Cos}\beta}{z_2^{*}}\right]}^{} + \overbrace{\left[\frac{w_1 \mathrm{Cos}\beta}{z_2^{*}}\right]}^{71} \end{cases} \text{and } t_2^{*} t_D > 0$$

(C-105)

Definition of mass fraction and saturation

Incorporating the dimensionless form of the variables into the corresponding equations and rearranging them, yields

$$\begin{cases} S_{1D} + \overbrace{\left[\frac{S^*_{22}}{S^*_{12}}\right]}^{72} S_{2D} + \overbrace{\left[\frac{S^*_{32}}{S^*_{12}}\right]}^{73} S_{3D} = \overbrace{\left[\frac{(1 - S_{1r} - S_{3r})}{S^*_{12}}\right]}^{74} \\ \omega_{11D} + \overbrace{\left[\frac{\omega^*_{512}}{\omega^*_{112}}\right]}^{75} \omega_{51D} + \overbrace{\left[\frac{\omega^*_{212}}{\omega^*_{112}}\right]}^{76} \omega_{21D} = \overbrace{\left[\frac{1.0}{\omega^*_{112}}\right]}^{77} \\ \omega_{22} = \overbrace{\left[\frac{1.0}{\omega^*_{222}}\right]}^{78} \\ \omega_{23D} + \overbrace{\left[\frac{\omega^*_{332}}{\omega^*_{232}}\right]}^{79} \omega_{33D} + \overbrace{\left[\frac{\omega^*_{432}}{\omega^*_{232}}\right]}^{80} \omega_{43} = \overbrace{\left[\frac{1.0}{\omega^*_{232}}\right]}^{81} \end{cases} \quad \text{(C-106)}$$

Salting-out effect

Incorporating the dimensionless form of the variables into Eq. and rearranging them, yields

$$\log\left(\frac{H_{brine}}{H_{pure}}\right) = K_{sal} M_{sal} . \quad \text{(C-107)}$$

$$\log\left(\frac{\frac{\chi^{brine}_{21}}{\chi_{22}}}{\frac{\chi_{21}^{fresh\ water}}{\chi_{22}}}\right) = K_{sal} M_{sal} . \quad \text{(C-108)}$$

Since χ_{22}=1.0,

$$\log\left(\frac{\chi^{brine}_{21}}{\chi^{fresh\ water}_{21}}\right) = K_{sal} M_{sal} \ , \quad \text{(C-109)}$$

where K_{sal} is the salt-effect parameter and M_{sal} is the molality of the dissolved salt. Furthermore, we can rewrite Eq. as the following to convert the molality to the solute's mole fraction:

$$\log\left(\frac{\chi_{21}^{\text{brine}}}{\chi_{21}^{\text{fresh water}}}\right) = \frac{K_{sal}}{55.55}\,\chi_{51}\,. \tag{C-110}$$

The Taylor series of expansion for the exponential function, e^x, is expressed as

$$e^x = 1 + \frac{x^1}{1!} + \frac{x^2}{2!} + \frac{x^3}{3!} + \ldots \tag{C-111}$$

Taking the logarithm of Eq. gives

$$\frac{\chi_{21}^{\text{brine}}}{\chi_{21}^{\text{fresh water}}} = \exp\left(\frac{K_{sal}}{55.55}\chi_{51}\right). \tag{C-112}$$

Incorporating Eq. into Eq. gives

$$\frac{(\chi_{212}^{*}\chi_{21D})}{(\chi_{212}^{*}\chi_{21D})} = \left[\left(\frac{K_{sal}}{55.55}\right)\frac{\chi_{512}^{*}\chi_{51D}}{1!} + \left(\frac{K_{sal}}{55.55}\right)^2\frac{(\chi_{512}^{*}\chi_{51D})^2}{2!} + \left(\frac{K_{sal}}{55.55}\right)^3\frac{(\chi_{512}^{*}\chi_{51D})^3}{3!} + ..\right]. \tag{C-113}$$

The following identify scaling groups,

$$\frac{(\chi_{212}^{*}\chi_{21D})}{(\chi_{212}^{*}\chi_{21D})} = \left[\overbrace{\left[\frac{K_{sal}\chi_{512}^{*}}{55.55}\right]}^{82}\frac{\chi_{51D}}{1!} + \overbrace{\left[\frac{K_{sal}\chi_{512}^{*}}{55.55}\right]}^{83\ 2}\frac{(\chi_{51D})^2}{2!} + \overbrace{\left[\frac{K_{sal}\chi_{512}^{*}}{55.55}\right]}^{84\ 3}\frac{(\chi_{51D})^3}{3!} + ..\right] \tag{C-114}$$

The effect of pressure on the solubility

Inserting the corresponding scaling and reference factors into Eq. , yields

$$\frac{d\left(\frac{\omega_{212}^{*}\omega_{21D}}{\rho_{22}^{*}\rho_{2D+}\rho_2^{J}}\right)}{d(P_{22}^{*}P_{2D} + P_{wf})} = A \quad \Rightarrow \quad \frac{d\left(\frac{\omega_{21D}}{\rho_{2D+}\frac{\rho_2^{J}}{\rho_{22}^{*}}}\right)}{d(P_{2D})} = \frac{\rho_{22}^{*}P_{22}^{*}A}{\omega_{212}^{*}}\,. \tag{C-115}$$

The following identify the dimensionless scaling groups

$$\frac{d\left(\begin{array}{c}\frac{\omega_{21D}}{85}\\ \rho_{2D+}\left[\frac{\rho_2^J}{\rho_{22}^*}\right]\end{array}\right)}{d(P_{2D})}=\overbrace{\left[\frac{\rho_{22}^*P_{22}^*A}{\omega_{212}^*}\right]}^{86}. \qquad \text{(C-116)}$$

Note that the coefficients of Eq.(C-116), *A* and *B*, will not be constant for a thick reservoir as the temperature difference between the top and bottom of the reservoir is substantial. Likewise, coefficients that are not fixed values for cases where CO_2 is injected at a temperature significantly different from that of the reservoir.

Top and bottom no flow boundaries

$$\begin{cases} U_{12Z}^* U_{1ZD} = 0 \\ U_{22Z}^* U_{2ZD} = 0 \qquad @\ Z_D = \overbrace{\left[\frac{H}{Z_2^*}\right]}^{87} \ \forall\, x, t\ , \text{where}\, t > 0 \\ U_{32Z}^* U_{3ZD} = 0 \end{cases} \qquad \text{(C-117)}$$

.

Constant BHP producer

We assume a constant bottomhole pressure constraint for the producer.

$$P_j = P_{wf} + \rho_j g \text{Cos}\alpha (H - d_3 \text{Cos}\gamma - Z) \qquad @ \quad \begin{cases} L - (d_3 + w_2)\,\text{Sin}\beta \le x \le L - d_3\,\text{Sin}\beta \\ d_4\,\text{Cos}\gamma \le z \le (d_4 + w_2)\text{Cos}\gamma \end{cases} \quad \text{and } t > 0, \qquad \text{(C-118)}$$

where the average density is the flux average density in the production well:

$$\begin{cases} P_j = P_{wf} + \rho_j g \mathrm{Cos}\alpha (H - d_3 \mathrm{Cos}\gamma - Z) & @ \quad \begin{cases} L - (d_3 + w_2)\mathrm{Sin}\beta \le x_2^* x_D \le L - d_3 \mathrm{Sin}\beta \\ d_4 \mathrm{Cos}\gamma \le z_2^* z_D \le (d_4 + w_2)\mathrm{Cos}\gamma \end{cases} \quad \text{and } t_2^* t_D > 0 \\ P_{12}^* P_{1D} + P_{wf} = P_{wf} + (\rho_{12}^* \rho_{1D} + \rho_1^I)\, g \cos\alpha\, (H - d_3 \mathrm{Cos}\gamma - Z_2^* Z_D) \\ P_{22}^* P_{2D} + P_{wf} = P_{wf} + (\rho_{22}^* \rho_{1D} + \rho_2^J)\, g \cos\alpha\, (H - d_3 \mathrm{Cos}\gamma - Z_2^* Z_D) \\ P_{32}^* P_{3D} + P_{wf} = P_{wf} + (\rho_{32}^* \rho_{1D} + \rho_3^I)\, g \cos\alpha\, (H - d_3 \mathrm{Cos}\gamma - Z_2^* Z_D). \end{cases}$$

(C-119)

Next,

$$\begin{cases} P_j = P_{wf} + \rho_j g (H - d_3 \mathrm{Cos}\gamma - Z) & @ \quad \begin{cases} \left[\frac{L - (d_3 + w_2)\mathrm{Sin}\beta}{x_2^*}\right] \le x_D \le \left[\frac{L - d_3 \mathrm{Sin}\beta}{x_2^*}\right] \\ \left[\frac{d_4 \mathrm{Cos}\gamma}{z_2^*}\right] \le z_D \le \left[\frac{(d_4 + w_2)\mathrm{Cos}\gamma}{z_2^*}\right] \end{cases} \quad \text{and } t_2^* t_D > 0 \\ P_{1D} = \left[\frac{z_2^* \rho_{12}^* g \cos\alpha}{P_{12}^*}\right] (\rho_{1D} + \left[\frac{\rho_1^I}{\rho_{12}^*}\right]) \left(\left[\frac{H - d_3 \mathrm{Cos}\gamma}{Z_2^*}\right] - Z_D\right) \\ P_{2D} = \left[\frac{z_2^* \rho_{22}^* g \cos\alpha}{P_{22}^* w_2 \mathrm{Cos}\gamma}\right] (\rho_{2D} + \left[\frac{\rho_2^J}{\rho_{22}^*}\right]) \left(\left[\frac{H - d_3 \mathrm{Cos}\gamma}{Z_2^*}\right] - Z_D\right) \\ P_{3D} = \left[\frac{z_2^* \rho_{32}^* g \cos\alpha}{P_{32}^* w_2 \mathrm{Cos}\gamma}\right] (\rho_{1D} + \left[\frac{\rho_3^I}{\rho_{32}^*}\right]) \left(\left[\frac{H - d_3 \mathrm{Cos}\gamma}{Z_2^*}\right] - Z_D\right). \end{cases}$$

(C-120)

Therefore,

$$\begin{cases} P_j = P_{wf} + \rho_j g (H - d_3 \mathrm{Cos}\gamma - Z) & @ \quad \begin{cases} \overbrace{\left[\frac{L - d_3 \mathrm{Sin}\beta}{x_2^*}\right]}^{88} - \overbrace{\left[\frac{w_2 \mathrm{Sin}\beta}{x_2^*}\right]}^{89} \le x_D \le \overbrace{\left[\frac{L - d_3 \mathrm{Sin}\beta}{x_2^*}\right]}^{90} \\ \overbrace{\left[\frac{d_4 \mathrm{Cos}\gamma}{z_2^*}\right]}^{91} \le z_D \le \overbrace{\left[\frac{d_4 \mathrm{Cos}\gamma}{z_2^*}\right]}^{} + \overbrace{\left[\frac{w_2 \mathrm{Cos}\gamma}{z_2^*}\right]}^{92} \end{cases} \quad \text{and } t_2^* t_D > 0 \\ P_{1D} = \overbrace{\left[\frac{z_2^* \rho_{12}^* g \cos\alpha}{P_{12}^*}\right]}^{93} (\rho_{1D} + \overbrace{\left[\frac{\rho_1^I}{\rho_{12}^*}\right]}^{}) \overbrace{\left(\left[\frac{H - d_3 \mathrm{Cos}\gamma}{Z_2^*}\right] - Z_D\right)}^{94} \\ P_{2D} = \overbrace{\left[\frac{z_2^* \rho_{22}^* g \cos\alpha}{P_{22}^*}\right]}^{95} (\rho_{2D} + \overbrace{\left[\frac{\rho_2^J}{\rho_{22}^*}\right]}^{97}) \left(\left[\frac{H - d_3 \mathrm{Cos}\gamma}{Z_2^*}\right] - Z_D\right) \\ P_{3D} = \overbrace{\left[\frac{z_2^* \rho_{32}^* g \cos\alpha}{P_{32}^*}\right]}^{96} (\rho_{1D} + \overbrace{\left[\frac{\rho_3^I}{\rho_{32}^*}\right]}^{}) \left(\left[\frac{H - d_3 \mathrm{Cos}\gamma}{Z_2^*}\right] - Z_D\right). \end{cases}$$

(C-121)

Capillary pressure equations

$$P_2 - P_1 = j(s)\delta_{21}\sqrt{\frac{\phi}{k}}$$

$$P^*_{22}P_{2D} - P^*_{12}P_{1D} = j(s)\delta_{21}\sqrt{\frac{\phi}{k_x}}$$

$$(P_{2D} - \overbrace{\left[\frac{P^*_{12}}{P^*_{22}}\right]}^{98} P_{1D}) = j(s_1)\overbrace{\left[\frac{\delta_{21}}{P^*_{22}}\sqrt{\frac{\phi}{k_x}}\right]}^{99}$$

. (C-122)

Similarly,

$$(P_{3D} - \overbrace{\left[\frac{P^*_{12}}{P^*_{32}}\right]}^{100} P_{1D}) = j(s_1)\overbrace{\left[\frac{\delta_{31}}{P^*_{32}}\sqrt{\frac{\phi}{k_x}}\right]}^{101}, \quad \text{(C-123)}$$

where $j(S_1)$ is a dimensionless function of saturations.

Constant injection rate

We further assume a constant rate constraint for the injector. Hence, the following relations between injection rates are defined:

$$\begin{cases} u_{1x} = U^J_1 \text{Cos}\beta \\ u_{1z} = U^J_1 \text{Sin}\beta \end{cases} \quad \& \quad \begin{cases} u_{2x} = U^J_2 \text{Cos}\beta \\ u_{2z} = U^J_2 \text{Sin}\beta \end{cases} \quad @ \quad \begin{cases} d_1 \text{Sin}\beta \le x \le (d_1 + w_1)\text{Sin}\beta \\ d_2 \text{Cos}\beta \le z \le (d_2 + w_1)\text{Cos}\beta \end{cases} \quad \text{and } t > 0.$$

(C-124)

Furthermore,

$$\begin{cases} \left|\overrightarrow{u_1}\right| = U_1^J \\ \left|\overrightarrow{u_2}\right| = U_2^J \end{cases} \quad \therefore \quad \begin{cases} u_{1x} = U_1^J \mathrm{Cos}\beta \\ u_{1z} = U_1^J \mathrm{Sin}\beta \end{cases} \quad \& \quad \begin{cases} u_{2x} = U_2^J \mathrm{Cos}\beta \\ u_{2z} = U_2^J \mathrm{Sin}\beta \end{cases} \quad @ \quad \begin{cases} d_1 \mathrm{Sin}\beta \le x \le (d_1 + w_1)\mathrm{Sin}\beta \\ d_2 \mathrm{Cos}\beta \le z \le (d_2 + w_1)\mathrm{Cos}\beta \end{cases} \quad \text{and } t > 0$$

$$\frac{U_1^J}{U_2^J} = W_R, \qquad U_{12}^* U_{1D} + U_{22}^* U_{2D} = U_T \quad \Rightarrow \qquad \frac{U_{12}^*}{U_{12}^*} U_{1D} + \frac{U_{22}^*}{U_{12}^*} U_{2D} = \frac{U_T}{U_{12}^*} \Rightarrow$$

$$U_{1D} + \overbrace{\left[\frac{U_{22}^*}{U_{12}^*}\right]}^{102} U_{2D} = \overbrace{\left[\frac{U_T}{U_{12}^*}\right]}^{103}.$$

(C-125)

Implementing the definition of SWAG ratio, we re-write the equations as

$$\begin{cases} u_{1x} = \dfrac{W_R}{W_R + 1} U_T \mathrm{Cos}\beta \\ u_{1z} = \dfrac{W_R}{W_R + 1} U_T \mathrm{Sin}\beta \\ u_{2x} = \dfrac{U_T}{W_R + 1} \mathrm{Cos}\beta \\ u_{2z} = \dfrac{U_T}{W_R + 1} \mathrm{Sin}\beta \ . \end{cases} \qquad @ \quad \begin{cases} d_1 \mathrm{Sin}\beta \le x \le (d_1 + w_1)\mathrm{Sin}\beta \\ d_2 \mathrm{Cos}\beta \le z \le (d_2 + w_1)\mathrm{Cos}\beta \end{cases} \quad \text{and } t > 0$$

(C-126)

Next, we substitute the corresponding linear transformation of each variable:

$$\begin{cases} u_{1xD} = \overbrace{\left[\dfrac{W_R}{W_R + 1} \dfrac{U_T}{u_{1x2}^*} \mathrm{Cos}\beta\right]}^{104} \\ u_{1zD} = \overbrace{\left[\dfrac{W_R}{W_R + 1} \dfrac{U_T}{u_{1z2}^*} \mathrm{Sin}\beta\right]}^{105} \\ u_{2xD} = \overbrace{\left[\dfrac{U_T \mathrm{Cos}\beta}{W_R + 1} \dfrac{1}{u_{2x2}^*}\right]}^{106} \\ u_{2zD} = \overbrace{\left[\dfrac{U_T \mathrm{Sin}\beta}{W_R + 1} \dfrac{1}{u_{2z2}^*}\right]}^{107}. \end{cases} \qquad @ \quad \begin{cases} \overbrace{\left[\dfrac{d_1 \mathrm{Sin}\beta}{x_2^*}\right]}^{108} \le x_D \le \overbrace{\left[\dfrac{d_1 \mathrm{Sin}\beta}{x_2^*}\right]}^{} + \overbrace{\left[\dfrac{w_1 \mathrm{Sin}\beta}{x_2^*}\right]}^{109} \\ \overbrace{\left[\dfrac{d_2 \mathrm{Cos}\beta}{z_2^*}\right]}^{110} \le z_D \le \overbrace{\left[\dfrac{d_2 \mathrm{Cos}\beta}{z_2^*}\right]}^{} + \overbrace{\left[\dfrac{w_1 \mathrm{Cos}\beta}{z_2^*}\right]}^{111} \end{cases} \quad \text{and } t > 0$$

(C-127)

Darcy equations

We write the Darcy's law for multiphase flow as

Phase 1:

$$u_{X1D} = -\overbrace{\left[\frac{k^{\circ}_{r1}k_x P^*_{12}}{\mu^*_{12}u^*_{x12}x^*_2}\right]}^{112}\frac{f_D(s_1)}{\mu_{1D}}\left(\frac{\partial P_{1D}}{\partial x_D}+\overbrace{\left[\frac{\rho^*_{12}g\ x^*_2\sin\alpha}{P^*_{12}}\right]}^{113}\rho_{1D}\right)$$
$$u_{Z1D} = -\overbrace{\left[\frac{k^{\circ}_{r1}k_Z P^*_{12}}{\mu^*_{12}u^*_{z12}z^*_2}\right]}^{114}\frac{f_D(s_1)}{\mu_{1D}}\left(\frac{\partial P_{1D}}{\partial z_D}+\overbrace{\left[\frac{\rho^*_{12}gz^*_2\cos\alpha}{P^*_{12}}\right]}^{115}\rho_{1D}\right). \quad \text{(C-128)}$$

Phase 2:

$$u_{X2D} = -\overbrace{\left[\frac{k^{\circ}_{r2}k_x P^*_{22}}{\mu^*_{22}u^*_{x22}x^*_2}\right]}^{116}\frac{f_D(s_2)}{\mu_{2D}}\left(\frac{\partial P_{2D}}{\partial x_D}+\overbrace{\left[\frac{\rho^*_{22}g\ x^*_2\sin\alpha}{P^*_{22}}\right]}^{117}\rho_{2D}\right)$$
$$u_{Z2D} = -\overbrace{\left[\frac{k^{\circ}_{r2}k_z P^*_{22}}{\mu^*_{22}u^*_{z22}z^*_2}\right]}^{118}\frac{f_D(s_2)}{\mu_{2D}}\left(\frac{\partial P_{2D}}{\partial z_D}+\overbrace{\left[\frac{\rho^*_{22}g\ z^*_2\cos\alpha}{P^*_{22}}\right]}^{119}\rho_{2D}\right). \quad \text{(C-129)}$$

Phase 3:

$$u_{X3D} = -\overbrace{\left[\frac{k^{\circ}_{r3}k_x P^*_{32}}{\mu^*_{32}u^*_{x32}x^*_2}\right]}^{120}\frac{f_D(s_3)}{\mu_{3D}}\left(\frac{\partial P_{3D}}{\partial x_D}+\overbrace{\left[\frac{\rho^*_{32}g\ x^*_2\sin\alpha}{P^*_{32}}\right]}^{121}\rho_{3D}\right)$$
$$u_{Z3D} = -\overbrace{\left[\frac{k^{\circ}_{r3}k_Z P^*_{32}}{\mu^*_{32}u^*_{z32}z^*_2}\right]}^{122}\frac{f_D(s_3)}{\mu_{3D}}\left(\frac{\partial P_{3D}}{\partial z_D}+\overbrace{\left[\frac{\rho^*_{32}g\ z^*_2\cos\alpha}{P^*_{32}}\right]}^{123}\rho_{3D}\right). \quad \text{(C-130)}$$

Fluid viscosity

Gas viscosity:

$$\mu_2 = \frac{\mu^{\circ}_{2,2}\chi_{22}\sqrt{M^{\circ}_2} + \mu^{\circ}_{3,2}\chi_{32}\sqrt{M^{\circ}_3}}{\chi_{22}\sqrt{M^{\circ}_2} + \chi_{32}\sqrt{M^{\circ}_3}} \quad \text{(C-131)}$$

Substituting the scale factors results in

$$\mu_{2D}\,\mu^{*}_{22} = \frac{\mu^{\circ}_{2,2}\chi^{*}_{222}\sqrt{M^{\circ}_2}\chi_{2D} + \mu^{\circ}_{3,2}\chi^{*}_{322}\sqrt{M^{\circ}_3}\chi_{3D}}{\chi^{*}_{222}\sqrt{M^{\circ}_2}\chi_{2D} + \chi_3\sqrt{M^{\circ}_3}\chi_{3D}} \quad \text{(C-132)}$$

Rearranging the equation gives

$$\mu_{2D} = \frac{\chi_{2D}}{\overbrace{\left[\frac{\mu^{*}_{22}}{\mu^{\circ}_{2,2}}\right]}^{124}\chi_{2D} + \overbrace{\left[\frac{\mu^{*}_{22}\chi^{*}_{322}\sqrt{M^{\circ}_3}}{\mu^{\circ}_{2,2}\chi^{*}_{222}\sqrt{M^{\circ}_2}}\right]}^{125}\chi_{3D}} + \frac{\chi_{3D}}{\overbrace{\left[\frac{\mu^{*}_{22}}{\mu^{\circ}_{3,2}}\right]}^{126}\chi_{3D} + \overbrace{\left[\frac{\mu^{*}_{22}\chi^{*}_{222}\sqrt{M^{\circ}_2}}{\mu^{\circ}_{3,2}\chi^{*}_{322}\sqrt{M^{\circ}_3}}\right]}^{127}\chi_{2D}} \quad \text{(C-133)}$$

Oil viscosity:

$$\ln\mu_o = \sum_{i=1}^{N_c} x_i \ln\left(\mu^{\circ}_{i,o}\right) = \sum_{i=2}^{4} \chi_{i,3} \ln\left(\mu^{\circ}_{i,o}\right) = \chi_{23}\ln\left(\mu^{\circ}_{2,o}\right) + \chi_{33}\ln\left(\mu^{\circ}_{3,o}\right) + \chi_{43}\ln\left(\mu^{\circ}_{4,o}\right) \quad \text{(C-134)}$$

To conduct o(1) scaling analysis and to use linear transformation for this equation, we consider the logarithm of the viscosity of pure components in the oil phase ($\ln\mu^{\circ}_{i,o}$) and viscosity of the oil mixture as new parameters:

$$\begin{cases} \ln\mu^{\circ}_{2,o} = \mu^{\circ}_{2,3} \\ \ln\mu^{\circ}_{2,o} = \mu^{\circ}_{2,3} \\ \ln\mu^{\circ}_{2,o} = \mu^{\circ}_{2,3} \\ \ln\mu_o = \mu_3 \end{cases}$$

$\Rightarrow$

$$\mu_3 = \chi_{23}\left(\mu^{\circ}_{2,3}\right) + \chi_{33}\left(\mu^{\circ}_{3,3}\right) + \chi_{43}\left(\mu^{\circ}_{4,3}\right) \quad \text{(C-135)}$$

Substituting the scale factors in Eq. (C-135) results in

$$\mu^{*}_{32}\mu_{3D} = \chi^{*}_{232}\chi_{23D}\left(\mu^{\circ}_{2,3}\right) + \chi^{*}_{332}\chi_{33D}\left(\mu^{\circ}_{3,3}\right) + \chi^{*}_{432}\chi_{43D}\left(\mu^{\circ}_{4,3}\right) \quad \text{(C-136)}$$

Therefore,

$$\mu_{3D} = \overbrace{\left[\frac{\chi^{*}_{232}\mu^{\circ}_{2,3}}{\mu^{*}_{32}}\right]}^{128}\chi_{23D} + \overbrace{\left[\frac{\chi^{*}_{332}\mu^{\circ}_{3,3}}{\mu^{*}_{32}}\right]}^{129}\chi_{33D} + \overbrace{\left[\frac{\chi^{*}_{432}\mu^{\circ}_{4,3}}{\mu^{*}_{32}}\right]}^{130}\chi_{43D} \quad \text{(C-137)}$$

Co-relation between mole fractions and weight fractions

$$\chi_{ij} = \frac{\overline{M_j}}{M_i}\omega_{ij} \quad \text{(C-138)}$$

The mole fraction of component 2 in phase 2 has the following relation with the weight fraction of component 2 in that phase:

$$\chi^{*}_{222}\chi_{22D} = \frac{\overline{M^{*}_{22}}}{M^{\circ}_{2}}\omega^{*}_{222}\omega_{22D}\overline{M_{2D}} \quad \text{(C-139)}$$

We define the scaling group as:

$$\chi_{22D} = \overbrace{\left[\frac{\overline{M^{*}_{22}}}{M^{\circ}_{2}}\frac{\omega^{*}_{222}}{\chi^{*}_{222}}\right]}^{131}\omega_{22D}\overline{M_{2D}} \quad \text{(C-140)}$$

Similarly, for the other components:

Component 2 in phase 1:

$$\chi_{21D} = \overbrace{\left[\frac{\overline{M^{*}_{12}}}{M^{\circ}_{2}}\frac{\omega^{*}_{212}}{\chi^{*}_{212}}\right]}^{132}\omega_{21D}\overline{M_{1D}} \quad \text{(C-141)}$$

Component 2 in phase 3:

$$\chi_{23D} = \overbrace{\left[\frac{\overline{M^{*}_{32}}}{M^{\circ}_{2}}\frac{\omega^{*}_{232}}{\chi^{*}_{232}}\right]}^{133}\omega_{23D}\overline{M_{3D}} \quad \text{(C-142)}$$

Component 3 in phase 2:

$$\chi_{32D} = \overbrace{\left[\frac{\overline{M^*_{22}}}{M^\circ_3}\frac{\omega^*_{322}}{\chi^*_{322}}\right]}^{134}\omega_{32D}\overline{M_{2D}} \quad \text{(C-143)}$$

.

Component 3 in phase 3:

$$\chi_{33D} = \overbrace{\left[\frac{\overline{M^*_{32}}}{M^\circ_3}\frac{\omega^*_{332}}{\chi^*_{332}}\right]}^{135}\omega_{33D}\overline{M_{3D}} \quad \text{(C-144)}$$

.

Component 4 in phase 3:

$$\chi_{43D} = \overbrace{\left[\frac{\overline{M^*_{32}}}{M^\circ_4}\frac{\omega^*_{432}}{\chi^*_{432}}\right]}^{136}\omega_{43D}\overline{M_{3D}} \quad \text{(C-145)}$$

.

Component 1 in phase 1:

$$\chi_{11D} = \overbrace{\left[\frac{\overline{M^*_{12}}}{M^\circ_1}\frac{\omega^*_{112}}{\chi^*_{112}}\right]}^{137}\omega_{11D}\overline{M_{1D}} \quad \text{(C-146)}$$

.

Component 5 in phase 1:

$$\chi_{51D} = \overbrace{\left[\frac{\overline{M^*_{12}}}{M^\circ_5}\frac{\omega^*_{512}}{\chi^*_{512}}\right]}^{138}\omega_{51D}\overline{M_{1D}} \quad \text{(C-147)}$$

.

However, the aqueous, oleic, and gaseous average molecular weights are defined as

$$\overline{M^*_{12}}\,\overline{M_{1D}} = \chi^*_{112}M^\circ_1\chi_{11D} + \chi^*_{512}M^\circ_5\chi_{51D} + \chi^*_{212}M^\circ_2\chi_{21D}\,. \quad \text{(C-148)}$$

Defining the scaling groups gives

$$\overline{M}_{1D} = \overbrace{\left[\frac{\chi^{*}_{112} M^{\circ}_{1}}{\overline{M}^{*}_{12}}\right]}^{139} \chi_{11D} + \overbrace{\left[\frac{\chi^{*}_{512} M^{\circ}_{5}}{\overline{M}^{*}_{12}}\right]}^{140} \chi_{51D} + \overbrace{\left[\frac{\chi^{*}_{212} M^{\circ}_{2}}{\overline{M}^{*}_{12}}\right]}^{141} \chi_{21D} \quad \text{(C-149)}$$

Similarly,

$$\overline{M}_{2D} = \overbrace{\left[\frac{\chi^{*}_{222} M^{\circ}_{2}}{\overline{M}^{*}_{22}}\right]}^{142} \chi_{22D} + \overbrace{\left[\frac{\chi^{*}_{322} M^{\circ}_{3}}{\overline{M}^{*}_{22}}\right]}^{143} \chi_{32D} \quad \text{(C-150)}$$

$$\overline{M}_{3D} = \overbrace{\left[\frac{\chi^{*}_{232} M^{\circ}_{1}}{\overline{M}^{*}_{32}}\right]}^{144} \chi_{23D} + \overbrace{\left[\frac{\chi^{*}_{332} M^{\circ}_{3}}{\overline{M}^{*}_{32}}\right]}^{145} \chi_{33D} + \overbrace{\left[\frac{\chi^{*}_{432} M^{\circ}_{4}}{\overline{M}^{*}_{32}}\right]}^{146} \chi_{43D} \quad \text{(C-151)}$$

Mass density

Liquid densities (water and oil) are obtained through the concept of the ideal mixture:

$$\begin{aligned} \frac{1}{\rho_1} &= \sum_{i=1}^{N_{aq}} \frac{\omega_{i1}}{\rho_{i,w}} = \frac{\omega_{11}}{\rho^{\circ}_{11}} + \frac{\omega_{51}}{\rho^{\circ}_{51}} + \frac{\omega_{21}}{\rho_2} \\ \frac{1}{\rho_3} &= \sum_{i=1}^{N_{oil}} \frac{\omega_{i3}}{\rho_{i,3}} = \frac{\omega_{23}}{\rho_{2,3}} + \frac{\omega_{33}}{\rho_{3,3}} + \frac{\omega_{43}}{\rho_{4,3}} \end{aligned} \quad \text{(C-152)}$$

$$\begin{cases} \dfrac{1}{\rho^{*}_{12}\rho_{1D} + \rho^{*}_{11}} = \displaystyle\sum_{i=1}^{N_{aq}} \frac{\omega_{i1}}{\rho_{i,w}} = \frac{\omega^{*}_{112}\omega_{11D}}{\rho^{\circ}_{11}} + \frac{\omega^{*}_{512}\omega_{51D}}{\rho^{\circ}_{51}} + \frac{\omega^{*}_{212}\omega_{21D}}{\rho^{*}_{22}\rho_{2D}} \Rightarrow \\ \dfrac{1}{\rho_{1D} + \left[\dfrac{\rho^{I}_{1}}{\rho^{*}_{12}}\right]} = \overbrace{\left[\frac{\rho^{*}_{12}\omega^{*}_{112}}{\rho^{\circ}_{11}}\right]}^{147} \omega_{11D} + \overbrace{\left[\frac{\rho^{*}_{12}\omega^{*}_{512}}{\rho^{\circ}_{51}}\right]}^{148} \omega_{51D} + \overbrace{\left[\frac{\rho^{*}_{12}\omega^{*}_{212}}{\rho^{*}_{22}}\right]}^{149} \frac{\omega_{21D}}{\rho_{2D}} \end{cases} \quad \text{(C-153)}$$

Furthermore, we assume that the pure density of water and salt ($\rho_{1,W}$, $\rho_{5,W}$) are fixed for oil component 3:

$$\frac{1}{\rho_{3D}+\left[\frac{\rho_3^I}{\rho_{32}^*}\right]}=\overbrace{\left[\frac{\rho_{32}^*\omega_{332}^*}{\rho_{332}^*}\right]}^{151}\frac{\omega_{33D}}{\rho_{33D}}+\overbrace{\left[\frac{\rho_{32}^*\omega_{432}^*}{\rho_{432}^*}\right]}^{152}\frac{\omega_{43D}}{\rho_{43D}}+\overbrace{\left[\frac{\rho_{32}^*\omega_{232}^*}{\rho_{22}^*}\right]}^{153}\frac{\omega_{23D}}{\rho_{23D}} \qquad \text{(C-154)}$$

Also we consider the oil components 3 and 4 as slightly compressible fluids with a constant compressibility factor of *c*:

$$\rho_{33}=\rho_{33}^{\circ}\,(1+c\Delta P)\,. \qquad \text{(C-155)}$$

Incorporating the dimensionless variables into Eq. (C-155) gives

$$\rho_{332}^*\rho_{33D}^*=\rho_{33}^{\circ}\,(1+cP_{32}^*\Delta P_{3D}) \qquad \text{(C-156)}$$

The following identify the dimensionless scaling groups,

$$\rho_{33D}^*=\overbrace{\left[\frac{\rho_{33}^{\circ}}{\rho_{332}^*}\right]}^{154}+\overbrace{\left[\frac{\rho_{33}^{\circ}cP_{32}^*}{\rho_{332}^*}\right]}^{155}\Delta P_{3D} \qquad \text{(C-157)}$$

Similarly, for oil component 4:

$$\rho_{43D}^*=\overbrace{\left[\frac{\rho_{43}^{\circ}}{\rho_{432}^*}\right]}^{156}+\overbrace{\left[\frac{\rho_{43}^{\circ}cP_{32}^*}{\rho_{432}^*}\right]}^{157}\Delta P_{3D} \qquad \text{(C-158)}$$

In addition, gas density is calculated as

$$\rho_2=\frac{P_2\overline{M_{gas}}}{ZRT_{Gas}} \qquad \text{(C-159)}$$

Incorporating dimensionless variables into Eq. (C-159) gives

$$\rho_{2D}\rho_{22}^*+\rho_{21}^*=\frac{P_{22}^*\overline{M_{22}^*}}{Z^{\circ}RT_{Gas}}\frac{P_{2D}\overline{M_{2D}}}{f(P_r)} \qquad \text{(C-160)}$$

$$\frac{\rho_{2D} f(P_r)}{P_{2D}\overline{M_{2D}}} + \left[\frac{\rho_2^J}{\rho_{22}^*}\right] = \overbrace{\left[\frac{P_{22}^*\overline{M_{22}^*}}{\rho_{22}^* Z^\circ R T_{Gas}}\right]}^{158}. \qquad \text{(C-161)}$$

Mass transfer among phases

$$\begin{cases} r_{m21}^* r_{m21D} = \phi K_{21}(\rho_{22}^*\rho_{2D}\omega_{222}^*\omega_{22D}S_{22}^*S_{2D} - \rho_{12}^*\rho_{1D}\omega_{212}^*\omega_{21D}S_{12}^*S_{1D} + (\rho_2^J S_{22}^* S_{2D} - \rho_1^I S_{12}^* S_{1D}) \Rightarrow \\ r_{m21D} = \overbrace{\left[\frac{\phi K_{21}\rho_{22}^*\omega_{222}^* S_{22}^*}{r_{m212}^*}\right]}^{159}\rho_{2D}\omega_{22D}S_{2D} - \overbrace{\left[\frac{\phi K_{21}\rho_{12}^*\omega_{212}^* S_{12}^*}{r_{m212}^*}\right]}^{160} S_{1D}\rho_{1D}\omega_{21D} \\ \quad + \overbrace{\left[\frac{\phi K_{21}\rho_2^J S_{22}^*}{r_{m212}^*}\right]}^{161} S_{2D} - \overbrace{\left[\frac{\phi K_{21}\rho_1^I S_{12}^*}{r_{m212}^*}\right]}^{162} S_{1D}. \end{cases}$$

(C-162)

Similarly,

$$r_{m22D} = -\overbrace{\left[\frac{\phi K_{21}\rho_{22}^*\omega_{222}^* S_{22}^*}{r_{m222}^*}\right]}^{163} S_{2D}\rho_{2D}\omega_{22D} - \overbrace{\left[\frac{\phi K_{23}\rho_{22}^*\omega_{222}^* S_{22}^*}{r_{m222}^*}\right]}^{164} S_{2D}\rho_{2D}\omega_{22D} + \overbrace{\left[\frac{\phi K_{21}\rho_{12}^*\omega_{212}^* S_{12}^*}{r_{m222}^*}\right]}^{165} S_{1D}\rho_{1D}\omega_{21D}$$
$$+ \overbrace{\left[\frac{\phi K_{23}\rho_{32}^*\omega_{232}^* S_{32}^*}{r_{m222}^*}\right]}^{166} S_{3D}\rho_{3D}\omega_{23D} - \overbrace{\left[\frac{\phi K_{21}\rho_2^J S_{22}^*}{r_{m222}^*}\right]}^{167} S_{2D} + \overbrace{\left[\frac{\phi K_{21}\rho_1^I S_{12}^*}{r_{m222}^*}\right]}^{168} S_{1D} - \overbrace{\left[\frac{\phi K_{23}\rho_2^J S_{22}^*}{r_{m222}^*}\right]}^{169} S_{2D} + \overbrace{\left[\frac{\phi K_{23}\rho_3^I S_{32}^*}{r_{m222}^*}\right]}^{170} S_{3D}$$

(C-163)

$$r_{m32D} = \overbrace{\left[\frac{\phi K_{23}\rho_{32}^*\omega_{332}^* S_{32}^*}{r_{m322}^*}\right]}^{171} S_{3D}\rho_{3D}\omega_{33D} - \overbrace{\left[\frac{\phi K_{23}\rho_{22}^*\omega_{322}^* S_{22}^*}{r_{m322}^*}\right]}^{172} S_{2D}\rho_{2D}\omega_{32D} + \overbrace{\left[\frac{\phi K_{23}\rho_3^I S_{32}^*}{r_{m322}^*}\right]}^{173} S_{3D} - \overbrace{\left[\frac{\phi K_{23}\rho_2^J S_{22}^*}{r_{m322}^*}\right]}^{174} S_{2D}.$$

(C-164)

Initial and injection conditions

$$\begin{cases} \mu_{1D} = \overbrace{\left[\dfrac{\mu_1^I}{\mu_{12}^*}\right]}^{175} & @\, t = 0 \\ \mu_{3D} = \overbrace{\left[\dfrac{\mu_3^I}{\mu_{13}^*}\right]}^{176} & @\, t = 0 \\ \mu_{2D} = \overbrace{\left[\dfrac{\mu_2^J}{\mu_{22}^*}\right]}^{177} & @\, t > 0 \,\&\, \text{injector well} \end{cases} \qquad \text{(C-165)}$$

Step 7 determines the scaling factors such that all dimensionless groups remain in the same order of magnitude, unity, in our study. This step is a trial-and-error procedure through which primary dimensionless groups are set to unity or zero.

Step 8 is the desired end result of the analysis as the unique minimum primary scaling factors based on the problem parameters; this is the critical step. Once the primary scaling factors are determined through step 7, the last step is to apply them and obtain the remaining dimensionless groups.

There is no restriction on choosing the primary dimensionless groups as well as the value to which we set them except that the remaining scaling groups should stay in the same order of magnitude as the primary groups. This is also true when we directly set values to primary factors. For instance, we set all $S_{j2}^*, \chi_{ij2}^* (\text{except for } i = 5), C_{ij2}^*$ equal to unity in this study.

The following dimensionless groups are set to unity:

2, 45, 72, 73, 74, 82, 86, 87, 102, 103, 112, 116, 120, 131,132, 133, 134, 135, 136, 137, 139, 142, 146, 147, 150, 154, 156, 158, 162, 168, 173, 175, 176, and 177.

The following values are considered for the scaling factors:

$$\begin{cases} u^*_{Xj2} = U_T \\ u^*_{zj2} = U_T \\ U^*_{j2} = U_T \end{cases} \quad \text{Where } j\text{=1, 2, and 3} \tag{C-166}$$

Also,

$$\begin{cases} x^*_2 = L \\ z^*_2 = H \end{cases} . \tag{C-167}$$

Incorporating the above scaling factors yields the remaining scaling factors. Also, inserting the assigned and the derived scaling factors into the dimensionless groups, the dimensionless scaling groups are obtained:

$$G_1 = \frac{S_{1r}}{1 - S_{1r} - S_{3r}} . \tag{C-168}$$

$$G_2 = \frac{L}{H} . \tag{C-169}$$

$$G_3 = \frac{\alpha_L}{L} . \tag{C-170}$$

$$G_4 = \frac{\alpha_T}{L} . \tag{C-171}$$

$$G_5 = \frac{L}{H^2}\alpha_L . \tag{C-172}$$

$$G_6 = \frac{L}{H^2}\alpha_T . \tag{C-173}$$

$$G_7 = \frac{S_{3r}}{1 - S_{1r} - S_{3r}} . \tag{C-174}$$

$$G_8 = \frac{K_{21}\phi(1 - S_{1r} - S_{3r})L}{U_T}. \quad \text{(C-175)}$$

$$G_9 = \frac{K_{21}\phi\rho_1^I(1 - S_{1r} - S_{3r})K_{r2}^{\circ} K_x Z^{\circ} RT_{Gas}}{\mu_2^J U_T{}^2 M_2^{\circ}}. \quad \text{(C-176)}$$

$$G_{10} = \frac{K_{23}\phi\rho_3^I(1 - S_{1r} - S_{3r})K_{r2}^{\circ} K_x Z^{\circ} RT_{Gas}}{\mu_2^J U_T{}^2 M_2^{\circ}}. \quad \text{(C-177)}$$

$$G_{11} = \frac{\mu_2^J U_T L M_2^{\circ}}{K_{r2}^{\circ} K_x Z^{\circ} RT_{Gas}\rho_1^I}. \quad \text{(C-178)}$$

$$G_{12} = \frac{\rho_2^J}{\rho_3^I}. \quad \text{(C-179)}$$

$$G_{13} = \frac{\rho_2^J}{\rho_1^I}. \quad \text{(C-180)}$$

$$G_{14} = \frac{\rho_3^I}{\rho_1^I}. \quad \text{(C-181)}$$

$$G_{15} = \frac{\rho_3^I S_{3r}}{\rho_1^I}. \quad \text{(C-182)}$$

$$G_{16} = \frac{\mu_2^J U_T L^2 M_2^{\circ}}{K_{r2}^{\circ} K_x Z^{\circ} RT_{Gas}\rho_1^I H}. \quad \text{(C-183)}$$

$$G_{17} = \frac{\rho_2^J}{\rho_1^I}\frac{L}{H}. \quad \text{(C-184)}$$

$$G_{18} = \frac{\rho_3^I}{\rho_1^I}\frac{L}{H}. \quad \text{(C-185)}$$

$$G_{19} = \omega_{51}^{I} \frac{M_1^{\circ}}{M_5^{\circ}} K_{sal} \quad \text{(C-186)}$$

$$G_{20} = \omega_{43}^{I} \quad \text{(C-187)}$$

$$G_{21} = \frac{S_3^{I} - S_{3r}}{1 - S_{1r} - S_{3r}} \quad \text{(C-188)}$$

$$G_{22} = \omega_{51}^{J} \frac{M_1^{\circ}}{M_5^{\circ}} K_{sal} \quad \text{(C-189)}$$

$$G_{23} = \frac{d_1 \mathrm{Sin}\beta}{L} \quad \text{(C-190)}$$

$$G_{24} = \frac{w_1 \mathrm{Sin}\beta}{L} \quad \text{(C-191)}$$

$$G_{25} = \frac{d_2 \mathrm{Cos}\beta}{H} \quad \text{(C-192)}$$

$$G_{26} = \frac{w_1 \mathrm{Cos}\beta}{H} \quad \text{(C-193)}$$

$$G_{27} = \frac{1}{K_{sal}} \frac{M_5^{\circ}}{M_1^{\circ}} \quad \text{(C-194)}$$

$$G_{28} = \frac{M_2^{\circ}}{Z^{\circ} R T_{Gas}} \left(\frac{\mu_2^{J} U_T L}{K_{r2}^{\circ} K_x} \right)^2 A \quad \text{(C-195)}$$

$$G_{29} = \frac{M_3^{\circ}}{M_2^{\circ}} \quad \text{(C-196)}$$

$$G_{30} = \frac{M_4^{\circ}}{M_2^{\circ}} \quad \text{(C-197)}$$

$$G_{31} = \frac{d_3 \mathrm{Sin}\beta}{L} \quad \text{(C-198)}$$

$$G_{32} = \frac{w_2 \mathrm{Sin}\beta}{L} \quad . \tag{C-199}$$

$$G_{33} = \frac{d_4 \mathrm{Cos}\gamma}{H} \quad . \tag{C-200}$$

$$G_{34} = \frac{w_2 \mathrm{Cos}\gamma}{H} \quad . \tag{C-201}$$

$$G_{35} = \frac{d_3 \mathrm{Cos}\gamma}{H} \quad . \tag{C-202}$$

$$G_{36} = \frac{H\rho_1^I g\,\mathrm{Cos}\alpha K_{r1}^{\circ} K_x}{\mu_1^I U_T L} \quad . \tag{C-203}$$

$$G_{37} = \frac{H\rho_3^I g\,\mathrm{Cos}\alpha K_{r3}^{\circ} K_x}{\mu_3^I U_T L} \quad . \tag{C-204}$$

$$G_{38} = \frac{H M_2^{\circ} g\,\mathrm{Cos}\alpha}{Z^{\circ} R T_{Gas}} \quad . \tag{C-205}$$

$$G_{39} = \frac{\rho_2^J Z^{\circ} R T_{Gas} K_{r2}^{\circ} K_x}{\mu_2^J U_T L M_2^{\circ}} \quad . \tag{C-206}$$

$$G_{40} = \frac{\mu_1^I K_{r2}^{\circ}}{\mu_2^J K_{r1}^{\circ}} \quad . \tag{C-207}$$

$$G_{41} = \frac{\delta_{21} K_{r2}^{\circ}}{\mu_2^J U_T L} \sqrt{K_x \phi} \quad . \tag{C-208}$$

$$G_{42} = \frac{\mu_1^I K_{r3}^{\circ}}{\mu_3^J K_{r1}^{\circ}} \quad . \tag{C-209}$$

$$G_{43} = \frac{\delta_{31} K_{r3}^{\circ}}{\mu_3^I U_T L} \sqrt{K_x \phi} \quad . \tag{C-210}$$

$$G_{44} = \frac{W_R}{1+W_R} Cos\beta \quad . \tag{C-211}$$

$$G_{45} = \frac{W_R}{1+W_R} Sin\beta \quad . \tag{C-212}$$

$$G_{46} = \frac{1}{1+W_R} Cos\beta \quad . \tag{C-213}$$

$$G_{47} = \frac{1}{1+W_R} Sin\beta \quad . \tag{C-214}$$

$$G_{48} = \frac{\rho_1^I g Sin\alpha}{\mu_1^I U_T} K_{r1}^{\circ} K_x \quad . \tag{C-215}$$

$$G_{49} = \frac{L}{H} \frac{K_z}{K_x} \quad . \tag{C-216}$$

$$G_{50} = \frac{\rho_1^I g Cos\alpha H}{\mu_1^I U_T L} K_{r1}^{\circ} K_x \quad . \tag{C-217}$$

$$G_{51} = \frac{M_2^{\circ} g L Sin\alpha}{Z^{\circ} R T_{Gas}} \quad . \tag{C-218}$$

$$G_{52} = \frac{M_2^{\circ} g H Cos\alpha}{Z^{\circ} R T_{Gas}} \quad . \tag{C-219}$$

$$G_{53} = \frac{\rho_3^I g Sin\alpha}{\mu_3^I U_T} K_{r3}^{\circ} K_x \quad . \tag{C-220}$$

$$G_{54} = \frac{\rho_3^I g Cos\alpha H}{\mu_3^I U_T L} K_{r3}^{\circ} K_x \quad . \tag{C-221}$$

$$G_{55} = \frac{\mu_2^J}{\mu_{2,2}^{\circ}} \quad . \tag{C-222}$$

$$G_{56} = \frac{\mu_2^J \sqrt{M_3^\circ}}{\mu_{2,2}^\circ \sqrt{M_2^\circ}} . \quad \text{(C-223)}$$

$$G_{57} = \frac{\mu_2^J \sqrt{M_2^\circ}}{\mu_{3,2}^\circ \sqrt{M_3^\circ}} . \quad \text{(C-224)}$$

$$G_{58} = \frac{\mu_{2,3}^\circ}{\mu_3^I} . \quad \text{(C-225)}$$

$$G_{59} = \frac{\mu_{3,3}^\circ}{\mu_3^I} . \quad \text{(C-226)}$$

$$G_{60} = \frac{\mu_{4,3}^\circ}{\mu_3^I} . \quad \text{(C-227)}$$

$$G_{61} = \frac{M_5^\circ}{M_1^\circ K_{sal}} . \quad \text{(C-228)}$$

$$G_{62} = \left(\frac{\mu_2^J U_T L}{K_{r2}^\circ K_x} \right)^2 \frac{A}{Z^\circ RT_{Gas}} M_2^\circ . \quad \text{(C-229)}$$

$$G_{63} = \frac{M_3^\circ}{M_2^\circ} . \quad \text{(C-230)}$$

$$G_{64} = \frac{M_1^\circ}{M_4^\circ} . \quad \text{(C-231)}$$

$$G_{65} = \frac{M_3^\circ}{M_4^\circ} . \quad \text{(C-232)}$$

$$G_{66} = \frac{\rho_1^I}{\rho_{11}^\circ} . \quad \text{(C-233)}$$

$$G_{67} = \frac{\rho_1^I}{\rho_{51}^\circ} \frac{1}{K_{sal}} \frac{M_5^\circ}{M_1^\circ} . \quad \text{(C-234)}$$

$$G_{68} = \rho_1^I \frac{\mu_2^J U_T L}{K_{r2}^\circ K_x} A \quad \text{(C-235)}$$

$$G_{69} = \frac{\rho_3^I}{\rho_{33}^\circ} \frac{M_3^\circ}{M_4^\circ} \quad \text{(C-236)}$$

$$G_{70} = \frac{\rho_3^I}{\rho_{43}^\circ} \quad \text{(C-237)}$$

$$G_{71} = \frac{\rho_3^I K_{r2}^\circ K_x}{\mu_2^J U_T L} \frac{Z^\circ RT_{Gas}}{M_4^\circ} \quad \text{(C-238)}$$

$$G_{72} = \frac{c\mu_3^I U_T L}{K_{r3}^\circ K_x} \quad \text{(C-239)}$$

$$G_{73} = \frac{\mu_2^J U_T L M_2^\circ}{K_{r2}^\circ K_x Z^\circ RT_{Gas} \rho_1^I} \quad \text{(C-240)}$$

$$G_{74} = \frac{K_{23} \mu_2^J U_T L M_2^\circ}{K_{21} K_{r2}^\circ K_x Z^\circ RT_{Gas} \rho_1^I} \quad \text{(C-241)}$$

$$G_{75} = \frac{K_{23}\ \rho_3^I M_2^\circ}{K_{21} \rho_1^I M_4^\circ} \quad \text{(C-242)}$$

$$G_{76} = \frac{K_{23}\ \rho_2^J}{K_{21} \rho_1^I} \quad \text{(C-243)}$$

$$G_{77} = \frac{K_{23}\ \rho_3^I}{K_{21} \rho_1^I} \quad \text{(C-244)}$$

$$G_{78} = \frac{\mu_2^J U_T L M_3^\circ}{K_{r2}^\circ K_x Z^\circ RT_{Gas} \rho_3^I} \quad \text{(C-245)}$$

The last step of o(1) scaling analysis is to determine the minimum number of dimensionless groups describing the process. The scaling analysis produces dimensionless parameters that are not always independent. Therefore, we use the same method introduced by Shook *et al.* (1992) to minimize the number of scaling groups.

We consider all dimensionless groups as a system of equations (G_1 through G_{78}). Hence, taking the logarithm from both sides of these equations yields a linear system of equations. This gives a set of 78 equations in 62 parameters. Furthermore, the elements of the resulting matrix are the exponents of the involved parameters in the remaining 78 dimensionless groups. In addition, the rank of the coefficient matrix is 47, which illustrates the minimum number of independent dimensionless groups.

Now, we use a linear transformation technique to convert the coefficient matrix to the reduced form. We use MATLAB ® to determine the linearly independent dimensionless groups as the following:

$$G_1 = \frac{S_{1r}}{1 - S_{1r} - S_{3r}} . \qquad \text{(C-246)}$$

$$G_2 = \frac{L}{H} . \qquad \text{(C-247)}$$

$$G_3 = \frac{\alpha_L}{L} . \qquad \text{(C-248)}$$

$$G_4 = \frac{\alpha_T}{L} . \qquad \text{(C-249)}$$

$$G_7 = \frac{S_{3r}}{1 - S_{1r} - S_{3r}} . \qquad \text{(C-250)}$$

$$G_8 = \frac{K_{21}\phi(1 - S_{1r} - S_{3r})L}{U_T} \quad . \qquad \text{(C-251)}$$

$$G_9 = \frac{K_{21}\phi\rho_1^I(1 - S_{1r} - S_{3r})K_{r2}^{\circ} K_x Z^{\circ} RT_{Gas}}{\mu_2^J U_T{}^2 M_2^{\circ}} \quad . \qquad \text{(C-252)}$$

$$G_{10} = \frac{K_{23}\phi\rho_3^I(1 - S_{1r} - S_{3r})K_{r2}^{\circ} K_x Z^{\circ} RT_{Gas}}{\mu_2^J U_T{}^2 M_2^{\circ}} \quad . \qquad \text{(C-253)}$$

$$G_{12} = \frac{\rho_2^J}{\rho_3^I} \quad . \qquad \text{(C-254)}$$

$$G_{14} = \frac{\rho_3^I}{\rho_1^I} \quad . \qquad \text{(C-255)}$$

$$G_{15} = \frac{\rho_3^I S_{3r}}{\rho_1^I} \quad . \qquad \text{(C-256)}$$

$$G_{19} = \omega_{51}^I \frac{M_1^{\circ}}{M_5^{\circ}} K_{sal} \quad . \qquad \text{(C-257)}$$

$$G_{20} = \omega_{43}^I \quad . \qquad \text{(C-258)}$$

$$G_{21} = \frac{S_3^I - S_{3r}}{1 - S_{1r} - S_{3r}} \quad . \qquad \text{(C-259)}$$

$$G_{22} = \omega_{51}^J \frac{M_1^{\circ}}{M_5^{\circ}} K_{sal} \quad . \qquad \text{(C-260)}$$

$$G_{23} = \frac{d_1 \mathrm{Sin}\beta}{L} \quad . \qquad \text{(C-261)}$$

$$G_{24} = \frac{w_1 \mathrm{Sin}\beta}{L} \quad . \qquad \text{(C-262)}$$

$$G_{25} = \frac{d_2 \mathrm{Cos}\beta}{H} \quad . \qquad \text{(C-263)}$$

$$G_{26} = \frac{w_1 \mathrm{Cos}\beta}{H} \quad . \tag{C-264}$$

$$G_{27} = \frac{1}{K_{sal}} \frac{M_5^{\circ}}{M_1^{\circ}} \quad . \tag{C-265}$$

$$G_{28} = \frac{M_2^{\circ}}{Z^{\circ} R T_{Gas}} \left(\frac{\mu_2^J U_T L}{K_{r2}^{\circ} K_x} \right)^2 A \quad . \tag{C-266}$$

$$G_{29} = \frac{M_3^{\circ}}{M_2^{\circ}} \quad . \tag{C-267}$$

$$G_{30} = \frac{M_4^{\circ}}{M_2^{\circ}} \quad . \tag{C-268}$$

$$G_{31} = \frac{d_3 \mathrm{Sin}\beta}{L} \quad . \tag{C-269}$$

$$G_{32} = \frac{w_2 \mathrm{Sin}\beta}{L} \quad . \tag{C-270}$$

$$G_{33} = \frac{d_4 \mathrm{Cos}\gamma}{H} \quad . \tag{C-271}$$

$$G_{34} = \frac{w_2 \mathrm{Cos}\gamma}{H} \quad . \tag{C-272}$$

$$G_{36} = \frac{H \rho_1^I g \, \mathrm{Cos}\alpha K_{r1}^{\circ} K_x}{\mu_1^I U_T L} \quad . \tag{C-273}$$

$$G_{37} = \frac{H \rho_3^I g \, \mathrm{Cos}\alpha K_{r3}^{\circ} K_x}{\mu_3^I U_T L} \quad . \tag{C-274}$$

$$G_{38} = \frac{H M_2^{\circ} g \, \mathrm{Cos}\alpha}{Z^{\circ} R T_{Gas}} \quad . \tag{C-275}$$

$$G_{41} = \frac{\delta_{21} \overset{\circ}{K}_{r2}}{\mu_2^J U_T L} \sqrt{K_x \phi} \quad . \tag{C-276}$$

$$G_{43} = \frac{\delta_{31} \overset{\circ}{K}_{r3}}{\mu_3^I U_T L} \sqrt{K_x \phi} \quad . \tag{C-277}$$

$$G_{44} = \frac{W_R}{1 + W_R} \mathrm{Cos}\beta \quad . \tag{C-278}$$

$$G_{46} = \frac{1}{1 + W_R} \mathrm{Cos}\beta \quad . \tag{C-279}$$

$$G_{48} = \frac{\rho_1^I g \mathrm{Sin}\alpha}{\mu_1^I U_T} \overset{\circ}{K}_{r1} K_x \quad . \tag{C-280}$$

$$G_{49} = \frac{L}{H} \frac{K_z}{K_x} \quad . \tag{C-281}$$

$$G_{55} = \frac{\mu_2^J}{\overset{\circ}{\mu}_{2,2}} \quad . \tag{C-282}$$

$$G_{57} = \frac{\mu_2^J \sqrt{\overset{\circ}{M}_2}}{\overset{\circ}{\mu}_{3,2} \sqrt{\overset{\circ}{M}_3}} \quad . \tag{C-283}$$

$$G_{58} = \frac{\overset{\circ}{\mu}_{2,3}}{\mu_3^I} \quad . \tag{C-284}$$

$$G_{59} = \frac{\overset{\circ}{\mu}_{3,3}}{\mu_3^I} \quad . \tag{C-285}$$

$$G_{60} = \frac{\overset{\circ}{\mu}_{4,3}}{\mu_3^I} \quad . \tag{C-286}$$

$$G_{64} = \frac{\overset{\circ}{M}_1}{\overset{\circ}{M}_4} \quad . \tag{C-287}$$

$$G_{66} = \frac{\rho_1^I}{\overset{\circ}{\rho}_{11}} . \tag{C-288}$$

$$G_{67} = \frac{\rho_1^I}{\overset{\circ}{\rho}_{51}} \frac{1}{K_{sal}} \frac{\overset{\circ}{M}_5}{\overset{\circ}{M}_1} . \tag{C-289}$$

$$G_{69} = \frac{\rho_3^I}{\overset{\circ}{\rho}_{33}} \frac{\overset{\circ}{M}_3}{\overset{\circ}{M}_4} . \tag{C-290}$$

$$G_{70} = \frac{\rho_3^I}{\overset{\circ}{\rho}_{43}} . \tag{C-291}$$

$$G_{72} = \frac{c\mu_3^I U_T L}{\overset{\circ}{K}_{r3} K_x} . \tag{C-292}$$

Furthermore, subtracting G_{15} from G_{14} and G_{22} from G_{19} yields 45 independent dimensionless scaling groups as

$$G_1 = \frac{S_{1r}}{1 - S_{1r} - S_{3r}} . \tag{C-293}$$

$$G_2 = \frac{L}{H} . \tag{C-294}$$

$$G_3 = \frac{\alpha_L}{L} . \tag{C-295}$$

$$G_4 = \frac{\alpha_T}{L} . \tag{C-296}$$

$$G_5 = \frac{S_{3r}}{1 - S_{1r} - S_{3r}} . \tag{C-297}$$

$$G_6 = \frac{K_{21}\phi(1 - S_{1r} - S_{3r})L}{U_T} . \tag{C-298}$$

$$G_7 = \frac{K_{21}\phi\rho_1^I(1 - S_{1r} - S_{3r})\overset{\circ}{K}_{r2} K_x \overset{\circ}{Z} RT_{Gas}}{\mu_2^J U_T{}^2 \overset{\circ}{M}_2} . \tag{C-299}$$

$$G_8 = \frac{K_{23}\phi\rho_3^I(1-S_{1r}-S_{3r})K_{r2}^{\circ}K_x Z^{\circ} RT_{Gas}}{\mu_2^J U_T{}^2 M_2^{\circ}} . \quad \text{(C-300)}$$

$$G_9 = \frac{\rho_2^J}{\rho_3^I} . \quad \text{(C-301)}$$

$$G_{10} = \frac{\rho_3^I(1-S_{3r})}{\rho_1^I} . \quad \text{(C-302)}$$

$$G_{11} = (\omega_{51}^I - \omega_{51}^J)\frac{M_1^{\circ}}{M_5^{\circ}} K_{sal} . \quad \text{(C-303)}$$

$$G_{12} = \omega_{43}^I . \quad \text{(C-304)}$$

$$G_{13} = \frac{S_3^I - S_{3r}}{1-S_{1r}-S_{3r}} . \quad \text{(C-305)}$$

$$G_{14} = \frac{d_1 Sin\beta}{L} . \quad \text{(C-306)}$$

$$G_{15} = \frac{w_1 Sin\beta}{L} . \quad \text{(C-307)}$$

$$G_{16} = \frac{d_2 Cos\beta}{H} . \quad \text{(C-308)}$$

$$G_{17} = \frac{w_1 Cos\beta}{H} . \quad \text{(C-309)}$$

$$G_{18} = \frac{1}{K_{sal}}\frac{M_5^{\circ}}{M_1^{\circ}} . \quad \text{(C-310)}$$

$$G_{19} = \frac{M_2^{\circ}}{Z^{\circ} RT_{Gas}}\left(\frac{\mu_2^J U_T L}{K_{r2}^{\circ} K_x}\right)^2 A . \quad \text{(C-311)}$$

$$G_{20} = \frac{M_3^{\circ}}{M_2^{\circ}} . \quad \text{(C-312)}$$

$$G_{21} = \frac{M_4^{\circ}}{M_2^{\circ}} \quad \text{(C-313)}$$

$$G_{22} = \frac{d_3 \mathrm{Sin}\beta}{L} \quad \text{(C-314)}$$

$$G_{23} = \frac{w_2 \mathrm{Sin}\beta}{L} \quad \text{(C-315)}$$

$$G_{24} = \frac{d_4 \mathrm{Cos}\gamma}{H} \quad \text{(C-316)}$$

$$G_{25} = \frac{w_2 \mathrm{Cos}\gamma}{H} \quad \text{(C-317)}$$

$$G_{26} = \frac{H\rho_1^I g \mathrm{Cos}\alpha K_{r1}^{\circ} K_x}{\mu_1^I U_T L} \quad \text{(C-318)}$$

$$G_{27} = \frac{H\rho_3^I g \mathrm{Cos}\alpha K_{r3}^{\circ} K_x}{\mu_3^I U_T L} \quad \text{(C-319)}$$

$$G_{28} = \frac{H M_2^{\circ} g \mathrm{Cos}\alpha}{Z^{\circ} R T_{Gas}} \quad \text{(C-320)}$$

$$G_{29} = \frac{\delta_{21} K_{r2}^{\circ}}{\mu_2^J U_T L} \sqrt{K_x \phi} \quad \text{(C-321)}$$

$$G_{30} = \frac{\delta_{31} K_{r3}^{\circ}}{\mu_3^I U_T L} \sqrt{K_x \phi} \quad \text{(C-322)}$$

$$G_{31} = \frac{W_R}{1 + W_R} \mathrm{Cos}\beta \quad \text{(C-323)}$$

$$G_{32} = \frac{1}{1 + W_R} \mathrm{Cos}\beta \quad \text{(C-324)}$$

$$G_{33} = \frac{\rho_1^I g \mathrm{Sin}\alpha}{\mu_1^I U_T} K_{r1}^{\circ} K_x \quad \text{(C-325)}$$

$$G_{34} = \frac{L}{H}\frac{K_z}{K_x} \quad \text{(C-326)}$$

$$G_{35} = \frac{\mu_2^J}{\overset{\circ}{\mu}_{2,2}} \quad \text{(C-327)}$$

$$G_{36} = \frac{\mu_2^J \sqrt{\overset{\circ}{M}_2}}{\overset{\circ}{\mu}_{3,2}\sqrt{\overset{\circ}{M}_3}} \quad \text{(C-328)}$$

$$G_{37} = \frac{\overset{\circ}{\mu}_{2,3}}{\mu_3^I} \quad \text{(C-329)}$$

$$G_{38} = \frac{\overset{\circ}{\mu}_{3,3}}{\mu_3^I} \quad \text{(C-330)}$$

$$G_{39} = \frac{\overset{\circ}{\mu}_{4,3}}{\mu_3^I} \quad \text{(C-331)}$$

$$G_{40} = \frac{\overset{\circ}{M}_1}{\overset{\circ}{M}_4} \quad \text{(C-332)}$$

$$G_{41} = \frac{\rho_1^I}{\overset{\circ}{\rho}_{11}} \quad \text{(C-333)}$$

$$G_{42} = \frac{\rho_1^I}{\overset{\circ}{\rho}_{51}}\frac{1}{K_{sal}}\frac{\overset{\circ}{M}_5}{\overset{\circ}{M}_1} \quad \text{(C-334)}$$

$$G_{43} = \frac{\rho_3^I}{\overset{\circ}{\rho}_{33}}\frac{\overset{\circ}{M}_3}{\overset{\circ}{M}_4} \quad \text{(C-335)}$$

$$G_{44} = \frac{\rho_3^I}{\overset{\circ}{\rho}_{43}} \quad \text{(C-336)}$$

$$G_{45} = \frac{c\mu_3^I U_T L}{\overset{\circ}{K}_{r3} K_x} \quad \text{(C-337)}$$

DISCUSSION

In this study, an eight-step procedure was outlined to determine the minimum parametric representation of SWAG displacement for scaling purposes. One of the main features of this method is that all derived dimensionless groups are bounded within o(1). Hence, the o(1) scaling analysis is used to evaluate the importance of a specific mechanism in a particular transport phenomenon. In other words, this procedure is useful when one is seeking to determine what approximations are allowed for a particular transport phenomenon. For instance, if the magnitude of a dimensionless group that is multiplied by the dispersion flux in the describing equations is an order of magnitude smaller than the rest of the dimensionless groups (for given parameters), the error incurred from dropping the dispersion term will be approximately 10%. This is not something that we get through dimensional analysis (*e.g.*, Pi theorem).

However, in some cases the objective is to obtain a minimum parametric representation of the describing equations for dimensional analysis purposes. In fact, scaling analysis can be used to resolve the issues encountered when the Pi theorem is implemented. For more information, see Krantz (2007).

NOMENCLATURE

k_{r1} = Water relative permeability

k_{r2} = Oil relative permeability

k_{r3} = Gas relative permeability

ω_{51}^{I} = Salt mass fraction of the resident aqueous phase

ω_{51}^{J} = Salt mass fractions of the injected aqueous phase

ω_{43}^{I} = Initial mass fraction of pseudo-component 4

c_{ij} = Mass fraction of component *i* per pore volume

L = Length of the permeable medium

H = Height of the permeable medium

W_1 = Perforated interval of the injection well

W_2 = Perforated interval of the production well

d_1 = The distance between the shallowest perforation of the injection well and the top of the reservoir

d_2 = The distance between the deepest perforation of the injection well and the bottom of the reservoir

d_3 = The distance between the shallowest perforation of the production well and the top of the reservoir

d_4 = The distance between the deepest perforation of the production well and the bottom of the reservoir

γ = Deviation of the production well from the *z*-direction

α = Reservoir dip angle

β = Deviation of the injection well from the *z*-direction

k_x = Permeability in the *x*-direction

k_z = Permeability in the *z*-direction

ϕ = Porosity

Z° = Compressibility factor of the injected gas at T_{ref} and P_{ref}

R = The universal gas constant

T_{Gas} = Temperature of the injected gas

W_R = SWAG ratio

j(s) = Leverett J-function

U_T = Total injection rate (volume-based)

U_{κ}^{J} = Injection rate of phase k

K_{salt} = Sechenov salting-effect parameter

K_{ij} = Mass transfer coefficient of component *i* in phase *j*

A = Solubility coefficient used in Eq.(C-14)

g = Gravitational constant

σ_{jk} = Interfacial tension between phase *j* and *k*

c = Isothermal compressibility of the oleic phase

α_L = Longitudinal dispersivity coefficient

α_T = Transverse dispersivity coefficient

S_{1r} = Irreducible water saturation

S_{3r} = Residual oil saturation

S_{gcrit} = Critical gas saturation

$S_3^I - S_{3r}$ = Initial movable oil saturation

$1 - S_{1r} - S_{3r}$ = Fraction of pore volume that is open to flow

ρ_1^I = Mass density of the resident aqueous phase

ρ_2^J = Mass density of the injected gaseous phase

ρ_3^I = Mass density of the initial oleic phase

ρ_{11}° = Mass density of pure water

ρ_{33}° = Mass density of pure light oil in oleic phase (pseudo-component 3) at T_{ref} and P_{ref}

ρ_{43}° = Mass density of pure heavy oil in oleic phase (pseudo-component 4) at Tref and Pref

ρ_{51}° = Mass density of salt

M_1° = Molecular weight of water component

M_2° = Molecular weight of the pure solvent

M_3° = Molecular weight of the light oil (pseudo-component 3)

M_4° = Molecular weight of the heavy oil (pseudo-component 4)

μ_1^I = Viscosity of the resident aqueous phase

μ_3^I = Initial oleic phase viscosity

μ_2^J = Viscosity of the injected gaseous phase

μ_{22}° = Viscosity of the solvent in the gaseous phase

μ_{32}° = Viscosity of the light oil (pseudo-component 3) in the gaseous phase

μ_{43}° = Viscosity of the heavy oil (pseudo-component 4) in the oleic phase

References

Arya, A., Hewett, T.A., Larson, R.G., and Lake, L.W. 1988. Dispersion and Reservoir Heterogeneity. *SPE Res Eng* **4** (1):139-148.

Bachu, S., Gunther, W.D., and Perkins, E. H. 1994. Aquifer Disposal of CO_2: Hydrodynamic and Mineral Trapping. *Energy Conv. Management*. **34** (4): 269-279.

Bachu, S., Bonijoly, D., Bradshaw, J., Burruss, R., Holloway, S., Christensen, N. P., and Mathiassen, O. M. 2007. CO_2 Storage Capacity Estimation: Methodology and Gaps. *Intl J. Greenhouse Gas Control.* **1** (4): 430–443.

Barnes, E.W. 1908. A New Development in the Theory of the Hypergeometric Functions. *Proc. London Math. Soc.* **6**: 141-177.

Batycky, R.P. 1997. A Three-Dimensional Two-Phase Field Scale Streamline Simulator. PhD dissertation, Stanford University, Stanford, California.

Bear, J. 1972. *Dynamics of Fluids in Porous Media*. New York City: American Elsevier Publishing Company.

Benson, D.A., Wheatcraft, S.W., and Meerschaert, M.M. 2000. Application of a Fractional Advection-Dispersion Equation. *Water Resources Research* **36** (6): 1403-1412.

Berentsen, C.W.J., Van Kruijsdijk, C.P.J.W., and Verlaan, M.L. 2007. Upscaling, Relaxation and Reversibility of Dispersive Flow in Stratified Porous Media. *Transport in Porous Media* **68** (2): 187-218.

Berentsen, C.W.J., Verlaan, M.L., and van Kruijsdijk, C.P.J.W. 2005. Upscaling and Reversibility of Taylor Dispersion in Heterogeneous Porous Media. *Physical Review E, Statistical, Nonlinear and Soft Matter Physics* **71** (4): 046308.

Berkowitz, B. and Scher, H. 1995. On Characterization of Anomalous Dispersion in Porous and Fracture Media. *Water Resources Research* **31** (6): 1461–1466.

Berkowitz, B., Klafter, J., Metzler, R., and Scher, J. 2002. Physical Pictures of Transport in Heterogeneous Media: Advection-Dispersion, Random-Walk, and Fractional Derivative Formulations. *Water Resources Research* **38** (10): 1191-1203.

Bourdarot, G. 1998. *Well Testing: Interpretation Methods*. Editions Technip, Paris

Box, G.E.P. and Behnken, D.W. 1960. Some New Three Level Designs for the Study of Quantitative Variables. *Technometrics* **2**:455–475.

Bradshaw, J., Bachu, S., Bonijoly, D., Burruss, R., Holloway, S., Christensen, N.P., and Mathiassen, O.M. 2007. CO_2 Storage Capacity Estimation: Issues and Development of Standards. *Intl. J. Greenhouse Gas Control* **1**: 62-68.

Bridgman, P.W. 1922. *Dimensional Analysis*. Yale University Press. New Haven, CT.

Buckley, S.E. and Leverett, M.C. 1942. Mechanism of Fluid Displacement in Sands. *Trans.*, AIME **146**:107-116.

Burton, M., Kumar, N., Bryant, S.2008. Time-Dependent Injectivity during CO_2 Storage in Aquifers. Paper SPE 113927 at the SPE/DOE Improved Oil Recovery Symposium, Tulsa, Oklahoma, 19-23 April.

Carslaw, H.S. and Jaeger, J.C. 1959. *Conduction of Heat in Solids*. Oxford University Press.

Caudle, B.H. and Dyes, A.B. 1959. Improving Miscible Displacement by Gas-Water Injection. *Trans*., AIME **213**:281–284.

Chang, H.I., Lo, T.S., and Ring, W.W. 1993. The Effects of Injectant-Enrichment Level on Oil recovery in Horizontal, Gravity-Tongue Dominated Enriched Gas Drives. Paper SPE 26084 presented at the western regional meeting, Anchorage, Alaska.

Chang, Y.B., Chang, M.T., Lim, M.T., Pope, G.A., and Sepehrnoori, K. 1994. CO_2 Flow Patterns under Multiphase Flow: Heterogeneous Field-Scale Conditions. *SPE Res Eng* **9**(3): 208-216.

Cheng, L., Kam, S.I., Delshad, M., Rossen, W.R. 2002. Simulation of Dynamic Foam-Acid Diversion Processes. *SPE J.* **7** (3):316-324.

Claridge, E.L. 1972. Prediction of Recovery in Unstable Miscible Flooding. *SPE J.* **12**(2): 143-155.

Coats, K.H., Whitson, C.H.,and Thomas, L.K. 2009. Modeling Conformance as Dispersion. *SPEREE* **12** (1): 33-47. SPE 90390-PA.

Cortis, A., Gallo, C., Scher, H., and Berkowitz, B. 2004. Numerical Simulation of Non-Fickian Transport in Geological Formations with Multiple-Scale Heterogeneities. *Water Resources Research* **40 (3)**: W04209.

Courant, R., and D. Hilbert .1962. *Methods of Mathematical Physics*. Interscience, New York.

Craig, F., Jr. 1993. *The Reservoir Engineering Aspects of Water Flooding*. Monograph Series, SPE, Richardson, Texas.

Dagan, G. 1984. Solute Transport in Heterogeneous Porous Formations. *Journal of Fluid Mechanics* **145**: 151-177.

Darman, N.H., Durlofsky, L.J., Sorbie, K.S., and Pickup, G.E. 2001. Upscaling Immiscible Gas Displacements: Quantitative Use of Fine-Grid Flow Data in Grid-Coarsening Schemes. *SPE J* **6** (1): 47-56.

Design-Expert, Version 6.0.11, Stat-Ease, Inc., 2005.

Dindoruk, B. 1992. Analytical Theory of Multiphase, Multicomponent Displacement in Porous Media. PhD thesis, Stanford University, Stanford, California.

Dumore, J.M., Hagoort, J., and Risseeuw, A.S. 1984. An Analytical Model for One-Dimensional, Three-Component Condensing and Vaporizing Gas Drives. *SPEJ* **24**(2):169-179.

Dykstra, H. and Parsons, R.L. 1950. The Prediction of Oil Recovery by Waterflood. Secondary Recovery of Oil in the United States, 2nd Edition. new York: American Petroleum Institute

Earlougher, R.C., Jr. 1977. *Advances in Well Test Analysis*. Monograph Series, SPE, Richardson, Texas **5**: 125-140.

Ennis-King, J. and Paterson, L. 2005. Role of Convective Mixing in the Long-Term Storage of Carbon Dioxide in Deep Saline Formations. *SPE J*. **10**(3): 349–356.

Fanchi, J.R. 1983. Multidimensional Numerical Dispersion. *SPEJ* **23**(1):143-151. SPE-9018-PA.

Fayers, F.J., Jouaux, F., and Tchelepi, H.A. 1994. An Improved Macroscopic Model for Viscous Fingering and Its Validation for 2D and 3D Flows-I Non-Gravity Flows. *In Situ***18** (1):43–78.

Gardner, J.W., Orr, F.M., and Patel, P.D. 1981. The Effect of Phase Behavior on CO_2-Flood Displacement Efficiency. *J. Pet Tech* **33** (11): 2067-2081.

Garmeh, G. and Johns, R.T. 2010. Upscaling of Miscible Floods in Heterogeneous Reservoirs Considering Reservoir Mixing. *SPE Res Eval & Eng* **13**(5):747-763.

Garmeh, G., Johns, R.T., and Lake, L.W. 2009. Pore-Scale Simulation of Dispersion in Porous Media. *SPEJ* **14**(4). SPE-110228-PA.

Gelhar, L.W. 1993. *Stochastic Subsurface Hydrology*. New Jersey: Prentice Hall, Englewood Cliffs.

Gelhar, L.W. and Axness, C.L. 1983. Three Dimensional Stochastic Analysis of Macro-Dispersion in Aquifers. *Water Resources Research* **19** (1): 161–180.

GEM Advanced Compositional Reservoir Simulator, Version 2009, Calgary, Alberta: CMG.

Ghanbarnezhad Moghanloo, R. and Lake, L.W. 2010. Simultaneous Water-Gas-Injection Performance under Loss of Miscibility. Paper SPE 129966 presented at SPE Improved Oil Recovery Symposium, Tulsa, Oklahoma, USA, 24-28 April.

Ghanbarnezhad Moghanloo, R. and Lake, L.W. 2011. Applying Fractional Flow Theory to Determine CO2 Storage Capacity of a Deep Saline Aquifer. Paper SPE 144493 presented at SPE Western North American Region Meeting , Anchorage, Alaska, USA, 7-11 May 2011.

Ghanbarnezhad Moghanloo, R. 2011. Numerical Dispersion Impact on Local Mixing in Heterogeneous Reservoirs. Paper SPE 149420 presented at the SPE Eastern Regional Meeting, Colombus, Ohio, USA, 17–19 August.

Ghanbarnezhad Moghanloo, R. 2011. A Regime Indicator for Flow Through Heterogeneous Permeable Media.2011. Paper SPE 146370 presented at the SPE Annual Technical Conference and Exhibition, Denver, Colorado, USA, 30 October-2 November.

Gharbi, R., Peters, E.J., and Elkamel A. 1998. Scaling Miscible Fluid Displacements in Porous Media. *Energy & Fuels* **12**:801-811.

Ghomian, Y. 2008. Reservoir Simulation Studies for Coupled CO_2 Sequestration and Enhanced Oil Recovery. PhD dissertation, University of Texas, Austin, Texas.

Greenkorn, R.A. and Kessler, D.P. 1969. Dispersion in Heterogeneous No uniform Anisotropic Porous Media. *Industrial and Engineering and Chemistry*, 61: 14-32.

Greenkorn, A.R. 1983. *Flow Phenomena in Porous Media*. New York City: Marcel Decker, Inc.

Gunter, W.D., Wiwchar, B., and Perkins, E.H. 1997. Aquifer Disposal of CO_2-Rich Greenhouse Gases: Extension of the Time Scale of Experiment for CO_2-Sequestering Reactions by Geochemical Modeling. *Miner. Pet*. **59** (2): 121–140.

Haajizadeh, M., Fayers, F.J., Cockin, A.P., Roffey, M., and Bond, D.J. 1999. On the Importance of Dispersion and Heterogeneity in the Compositional Simulation of the Miscible Gas Processes. Paper SPE 57264 presented at the SPE Asia Pacific Improved Oil Recovery Conference, Kuala Lumpur, Malaysia, 25–26 October.

Haajizadeh, M., Fayers, F.J., and Cockin, A.P. 2000. Effects of Phase Behavior, Dispersion and Girding on Sweep Patterns for Nearly Miscible Gas Displacement. Paper SPE 62995 presented at the SPE Annual Technical Conference and Exhibition, Dallas, TX.

Hangx. S.J.T. 2005. Behaviour of the CO_2-H_2O system and Preliminary Mineralization Model and Experiments. Utrecht University.

Hankins, N. P., Harwell, H.H.2003. Application of Coherence Theory to Reservoir Enhanced Oil Recovery Simulator. *Journal of Petroleum Science and Engineering* **42**(1): 29-55.

Helfferich, F. and Klein, G. 1970. *Multicomponent Chromatography*. New York City: Marcel Dekker Publishing Co.

Helfferich, F.G. 1981. Theory of Multicomponent, Multiphase Displacement in Porous Media. *SPE J.* **21** (1):52-62.

Heller, J.P. 1972. Observations of Mixing and Diffusion in Porous Media. Paper presented at the International Symposium on Fundamentals of Transport Phenomena in Porous Media, Guelph University, Ontario.

Hill, S. 1952. Channeling in Packed Columns. *Chem. Eng. Society* **1**: 247–253.

IPCC. 2005. *Special Report on Carbon Dioxide Capture and Storage*. Cambridge University Press.

IPCC. 2007. *Climate Change: The physical Science Basis*. Fourth assessment report.

Javandel, I., Doughty, C., and Tsang, C.F. 1984. *Groundwater Transport: Handbook of Mathematical Models*, No. 10. Washington, DC: Water Resources Monograph, American Geophysical Union.

Jennings, J.W., Ruppel, S.C., and Ward, W.B. 2002. Geostatistical Analysis of Permeability Data and Modeling of Fluid-Flow Effects in Carbonate Outcrops. *SPE Res Eval & Eng* **3** (4):292-303.

Jensen, J.L., Lake, L.W., Corbett, P.W., and Goggin, D.J. 1998. *Statistics for Petroleum Engineers and Geosciences.* New Jersey: Prentice Hall.

Jensen, J.L., Lake, L.W., Corbett, P.W., and Goggin, D.J. 2003. *Statistics for Petroleum Engineers and Geosciences.* New Jersey: Prentice Hall.

Jessen, K. and Orr, F.M., Jr. 2002. Compositional Streamline Simulation. Paper SPE 77379 presented at the 2002 SPE Annual Technical Conference and Exhibition, San Antonio, TX, September 29-October 2.

Jessen, K., Stenby, E.H., and Orr, F.M. 2002. Interplay of Phase Behavior and Numerical Dispersion in Finite Difference Compositional Simulation. Paper SPE 75134 presented at the SPE/DOE Symposium on Improved Oil Recovery, Tulsa, OK.

Jha, R.K. 2008. Investigation of Local Mixing and Its Influence on Core Scale Mixing (Dispersion). PhD dissertation, University of Texas, Austin, Texas.

Jha, R.K., Bryant, S.L., Lake, L.W., and John, A.K. 2006. Investigation of Pore-Scale (Local) Mixing. Paper SPE 99782 presented at the SPE Improved Oil Recovery Symposium, Tulsa, OK.

John, A.K. 2008. Dispersion in Large Scale Permeable Media. PhD dissertation, University of Texas, Austin, Texas.

Johns, R.T. 1992. Analytical Theory of Multicomponent Gas Drives with Two-Phase Mass Transfer. PhD dissertation, Stanford University, Stanford, California.

Johns, R.T., B. Dindoruk, and Orr, F.M., Jr. 1993. Analytical Theory of Combined Condensing/Vaporizing Gas Drives. *SPE Advanced Technology Series.***1** (2):7-16.

Johns, R.T., Sah, P., and Solano, R. 2002. Effect of Dispersion on Local Displacement Efficiency for Multicomponent Enriched-Gas Floods Above the Minimum Miscibility Enrichment. *SPE Res Eval & Eng* **5** (1): 4–10. SPE-75806-PA.

Juanes R., Spiteri, E.J., Orr, F.M. Jr., and Blunt, M.J. 2006. Impact of relative permeability hysteresis on geological CO_2 storage. *Water Resource. Research*. 42: W12418.

Juanes, R., and MacMinn, C.W. 2010. The Footprint of the CO_2 Plume During Carbon Dioxide Storage in Saline Aquifers: Storage Efficiency for Capillary Trapping at the Basin Scale. *Transp Porous Med.* **30**: 19-30.

Kumar, A., Ozah, R., Noh, M., Pope, G.A., Bryant, S., Sepehrnoori, K., and Lake, L.W. 2005. Reservoir Simulation of CO_2 Storage in Deep Saline Aquifers. *SPE J.* **10** (3):

Krantz, W.B. 2007. *Scaling Analysis in Modeling Transport and Reaction Processes: A Systematic Approach to Model Building and the Art of Approximation*. John Wiley & Sons, Inc., Hoboken, New Jersey.

Koval, E.J. 1963. A Method for Predicting the Performance of Unstable Miscible Displacement in Heterogeneous Media. *SPE J*. **3** (2):145–154**.**

Kumar. A.B. 2004. A Simulation Study of Carbon Sequestration In Deep Saline Aquifers. Thesis, The University of Texas at Austin, Austin, Texas.

Lake, L.W. 1989. *Enhanced Oil Recovery*. Englewood Cliffs, New Jersey: Prentice Hall.

Lake, L.W. and Walsh, M. 2003. *Generalized Approach To Primary Hydrocarbon Recovery Of Petroleum Exploration & Production.* Elsevier Science B. V., Amsterdam.

Lake, L.W. and Hirasaki, G.J. 1981. Taylor's Dispersion in Stratified Porous Media. *SPEJ* **21**(4): 459–468. SPE-8436-PA.

LaForce, T. and Jessen, K. 2010. Analytical and Numerical Investigation of Multicomponent Multiphase WAG Displacement. *Computational Geoscience* **14** (4):745-754

LaForce, T. and Orr, F.M., Jr. 2009. Four-Component Gas/Water/Oil Displacements in One Dimension: Part iii: Development of Miscibility. *Transp. Porous Media* **79**(2): 225–247

Lange, E.A. 1998. Correlation and Prediction of Residual Oil Saturation for Gas-Injection-Enhanced Oil-Recovery Processes. *SPE Res Eval & Eng* **1** (2):127-133.

Lantz, R.B. 1971. Quantitative Evaluation of Numerical Dispersion (Truncation Error). *SPE J*.**11** (3):315–320.

Li, Dachang and Lake, L.W. 1995. Scaling Fluid Flow through Heterogeneous Permeable Media. *SPE Advanced Technology Series.* **3**(1): 188-197.

Mahadevan, J., Lake, L.W., and Johns, R.T. 2003. Estimation of True Dispersivity in Field-Scale Permeable Media. *SPEJ* **8** (3): 272–279. SPE-86303-PA.

Matheron, G. and De Marsily, G. DE. 1980. Is Transport in Porous Media Always Diffusive A Counterexample. *Water Resour. Res.* **16** (5): 901-917.

Nghiem, L. 2002. Compositional Simulator for Carbon Dioxide Sequestration. Computer Modeling Group Ltd.

Oruganti, Y. D. 2010. Geological CO2 Storage: Understanding Pressure Perturbations and Estimating Risk Due to Pressure Buildup. M Sc. Thesis, University of Texas, Austin, Texas.

Orr, F.M.J. 2007. *The Theory of gas Injection Processes*. Copenhagen, Denmark: Tie-Line Publications.

Pande, K.K. 1988. Interaction of Phase Behaviour with Nonuniform Flow. PhD dissertation, Stanford University, Stanford, California.

Pande, K.K., Ramey, Jr., Brigham, W.E., and Orr, Jr. 1987. Frontal Advance Theory for Flow in Heterogeneous Porous Media. Paper SPE 16344 presented at the SPE California Regional Meeting, Ventura, California, 8-10 April.

Perkins, T.K. and Johnston, O.C. 1963. A Review of Diffusion and Dispersion in Porous Media. *SPEJ* **3** (1): 70–84; *Trans.,* AIME, 228. SPE-480-PA.

Riaz, A., Hesse, M., Tchelepi, H.A., and Orr, F.M. Jr. 2006. Onset of Convection in a Gravitationally Unstable, Diffusive Boundary Layer in Porous Media. *J. Fluid Mech.* **548**: 87–111.

Raghavan, R. 1993. *Well Test Analysis*. New Jersey: Prentice Hall.

Rhee, H., Aris, R. and Amundson, N.R. 1986. *First-Order Partial Differential Equations: Volume I.* Prentice-Hall, Englewood Cliffs, New Jersey.

Rhee, H., Aris, R. and Amundson, N.R. 1986. *First-Order Partial Differential Equations: Volume II.* Prentice-Hall, Englewood Cliffs, New Jersey.

Saadatpoor, E., Bryant, S.L., and Sepehrnoori, K. 2010. New Trapping Mechanism in Carbon Sequestration. *Transp Porous Med*. **82**(3): 3-17.

Schulze-Makuch, D. 2005. Longitudinal Dispersivity data and Implications for Scaling Behavior. *Ground Water*, **43** : 443-456

Setchenow, I.M. 1989. *Z. Physical Chemistry* **4**:117.

Shook, M., Lake, L.W., and Li, D. 1992. Scaling Immiscible Flow Through Permeable Media by Inspectional Analysis. *In Situ* 16 (4): 311-349.

Sifuentes, W., Blunt, M. J., and Giddins, M. A. 2009. Modeling CO_2 Storage in Aquifers: Assessing the Key Contributors to Uncertainty. Paper SPE presented at the Offshore Europe Oil & Gas Conference & Exhibition, Aberdeen, UK, 8-11 September.

Solano, R. 2001. Evaluation of the Effects of Heterogeneity, Grid Refinement, and Capillary Pressure on Recovery for Miscible-Gas Injection Processes. Paper SPE 71602 presented at the SPE Annual Technical Conference and Exhibition, New Orleans, 27-30 September.

Sorbie K.S., Feghi, F., Pickup, G.E., Ringrose P.S., and Jensen, J.L. 1994. Flow Regimes in Miscible Displacements in Heterogeneous Correlated Random Fields. *SPE Advanced Technology Series* **2**(2): 78:87. SPE-24140-PA.DOI: 10.2118/57469-PA.

Sorbie, K.S., Pickup, S., Ringrose, P.S., and Jensen, J.L. 1994. Flow Regimes in Miscible Displacements in Heterogeneous Correlated Random Fields. *SPE Advanced Technology Series* **2** (2): 78-87.

Stalkup, F.I. 1983. *Miscible Flooding Fundamentals*. Monograph Series, SPE, Richardson, Texas.

STARS. Steam, Thermal, and Advanced Processes Reservoir Simulator, Version 2009, Calgary, Alberta: CMG.

Steeb, W, H. 2007. *Continuous Symmetries, Lie algebras, Differential Equations and Computer Algebra*. Second edition, World Scientific Publishing, ISBN 981-270-809-X.

Sternberg, S. 2004. Dispersion Measurements in Highly Heterogeneous Laboratory Scale Porous Media. *Transport in Porous Media* **54** (1): 107–124.

Sternberg, S., Cushman, J.H., and Greenkorn, R.A. 1996. Laboratory Observation of Non Local Dispersion. *Transport in Porous Media* **23** (2): 135–151.

Sternberg, S.P.K. and Greenkorn, R.A. 1994. An Experimental Investigation of Dispersion in Layered Porous Media. *Transport in Porous Media* **15** (1): 15–30.

Su, N., Sander, G.C., Liu, F., Anh, V., and Barry, D.A. 2005. Similarity Solutions for Solute Transport in Fractal Porous Media Using a Time and Scale Dependent Dispersivity. *Applied Mathematical Modeling* **29**: 852-870.

Szulczewski, M. and Juanes, R. 2009. A simple but Rigorous Model for Calculating CO_2 Storage Capacity in Deep Saline Aquifers at the Basin Scale. *Energy Procedia* (Proc. GHGT-9) **1** (1): 3307–3314.

Taku Ide, S., Jessen, K., and Orr, F.M.J. 2007. Storage of CO_2 in Saline Aquifers: Effects of Gravity, Viscous, and Capillary Forces on Amount and Timing of Trapping. *International Journal of Greenhaouse Gas Control I*. **1**(4):481-491.

Taylor, G.I. 1922. Diffusion by Continuous Movements. Proceedings of the London Mathematical Society, series 2, 20: 196-212.

Taylor, G.I. 1953. Dispersion of Soluble Matter in Solvent Flowing Slowly Through a Tube. Proceedings of the Royal Society of London, Series A: Mathematical and Physical Sciences 219: 186-203.

Taylor, G.I. 1954. The Dispersion of Matter in Turbulent Flow Through a Pipe. Proceedings of the Royal Society of London, Series A: Mathematical and Physical Sciences 223: 446-468.

Taylor, A.R., Hintetiong, G.H., and Kumar, K.H. 1998. West Welch CO_2 Flood Simulation with an Equation of State and Mixed Wettability. Paper SPE 39808 presented at the SPE Permian Basin Oil and Gas Recovery Conference, Midland, Texas, 25-27 March.

Thiele, M.R. 1994. Modeling Multiphase Flow in Heterogeneous Media Using Streamtubes. PhD dissertation, Stanford University, Stanford, California.

Todd, M.R., and Longstaff, W.J. 1972. The Development, Testing, and Application of a Numerical Simulator for Predicting Miscible Flood Performance. *J. Pet Tech* **24** (7):874 -.882.

Van Poolen H.K. 1964. Radius of Drainage and Stabilization Time Equations. *Oil and Gas Journal* **14**: 138-146.

Vanderborght, J. and Vereecken, H. 2007. Review of Dispersivity for Transport Modeling in Soils. *Vadose Zone Journal* **6**:29-52.

Vasco, D. W., Yoon, S., and Datta-Gupta, A. 1999. Integrating Dynamic Data into High-Resolution Reservoir Models Using Streamline-Based Analytic Sensitivity Coefficients. *SPE J.*, **4** : 389– 399.

Vasco, D.W., Keers, H., and Karasaki, K. 2000. Estimation of Reservoir Properties Using Transient Pressure Data: An asymptotic Approach. *Water Resour. Res.*, **36**(12): 3447– 3465, DOI:10.1029/2000WR900179.

Vasco, D. W. 2011.On the Propagation of A Coupled Saturation and Pressure Front. *Water Resour. Res*. , 47, W03526, doi:10.1029/2010WR009740.

Waggoner, J.R., Castillo, J.R., and Lake, L.W. 1992. Simulation of EOR processes in Stochastically Generated Permeable Media. *SPE Form Eval* **7** (2): 173-180.

Walsh, M.P. 1989. An Analysis of Miscible Flooding Chase- Fluid Design Practices: Part 2-Strategies Involving Interference. Paper SPE 19669 presented at the SPE Annual Technical Conference and Exhibition, San Antonio, Texas, 28-30 October.

Walsh, B.W. and Orr, F.M., Jr. 1990. Prediction of Miscible Flood Performance: The Effect of Dispersion on Composition Paths in Ternary Systems. *In Situ* **14** (1):19-47.

Walsh, M.P. and Lake, L.W. 1989. Applying Fractional Flow Theory to Solvent Flooding and Chase Fluids. *J. Petroleum Science and Eng.* **2**(4): 281-303.

Walsh, M.P. and Moon G.M. 1991. An Analysis of Gravity-Dominated, Immiscible Flows in Dipping Reservoirs. Paper SPE presented at the Production Operations Symposium, Oklaham city, Oklahama, April 7-9.

Welge, H.J., Johnson, E.F., Ewing, S.P. and Brinkman, F.H. 1961. The Linear Displacement of Oil from Porous Media by Enriched Gas. *J. Pet Tech* **13** (8):787-796.

Welge, H.J. 1952. A Simplified Method for Computing Oil Recovery by Gas or Water Drive. *Trans.*, AIME **195**: 91-98.

WINPROP Phase Behavior Program, Version 2009 User Guide. 2006. Calgary, Alberta: CMG.

Wood, D.J., Lake, L.W., Johns, R.T., and Nunez, V. 2008. A Screening Model for CO_2 Flooding and Storage in Gulf Coast Reservoirs Based on Dimensionless Groups. *SPE Res Eval & Eng* **11** (3): 513-520.

Yang, A.P. 1990. Stochastic Heterogeneity and Dispersion. Ph.D. Thesis, The University of Texas at Austin, Austin, Texas.

Zhou, Q., Liu, H.H., Molz, F.J., Zhang, Y., and Bodvarsson, G.S.2007. Field-Scale Effective Matrix Diffusion Coefficient for Fractured Rock: results From Literature Survey. *Journal of Contaminant Hydrology* **93**: 161-187.

Zuluaga, E. and Lake, L. W. 2008. Modeling of Experiments on Water Vaporization for Gas Injection Using Traveling Waves. *SPE J*.**13**(2): 248-256.